BIOMECHANICAL SIMULATIONS OF HEART VALVE BIOMATERIALS

by

Wei Sun

BS, Harbin Institute of Technology, 1991

MS, Shanghai Jiao Tong University, 1993

Submitted to the Graduate Faculty of

the School of Engineering in partial fulfillment

of the requirements for the degree of

Doctor of Philosophy

University of Pittsburgh

2003

UNIVERSITY OF PITTSBURGH

SCHOOL OF ENGINEERING

This dissertation was presented

by

Wei Sun

It was defended on

Oct 23, 2003

and approved by

William S. Slaughter, Associate Professor, Department of Mechanical Engineering

David A. Vorp, Associate Professor, Department of Surgery and Bioengineering

Michael J. Scott, Director of R&D, Orqis Medical, Lake Forest, CA

James F. Antaki, Associate Professor, Department of Biomedical Engineering and Computer Science, Carnegie Mellon University

Dissertation Director: Michael S. Sacks, Associate Professor, Department of Bioengineering

ABSTRACT

BIOMECHANICAL SIMULATIONS OF HEART VALVE BIOMATERIALS

Wei Sun, Ph.D.

University of Pittsburgh, 2003

For more than 40 years, replacement of diseased natural heart valves with prosthetic devices has dramatically extended the quality and length of the lives of millions of patients worldwide. However, as in many medical therapies today, replacement valves are never as good as natural, healthy valves. Bioprosthetic heart valves (BHV) continue to fail due to structural failure, a result of both poor tissue durability and faulty design. Clearly, an in-depth understanding of the biomechanical behavior of the BHV at both the tissue- and functional prosthesis levels is essential to improving BHV design and the mechanisms of failure.

The goal of this research effort was to develop and evaluate a complete process for biomechanical simulations of heart valve biomaterials, with an emphasis on numerical stability and experimental validation. This process started from the collection of appropriate experimental data, formulating and validating a constitutive model, obtaining and refining material parameters, finite element implementation and validation of a constitutive model, and finally finite element simulation of valve deformation.

The results of this study indicated that explicit expression of shear behavior was required for proper computational implementation of the exponential Fung pseudo-elastic model and thus, biaxial testing with extension only did not provide sufficient information to constitute a strain energy function for computational implementation. This study also demonstrated that a set of model constraints imposed by the convexity of strain energy function and condition number of elasticity tensor were necessary for numerical stability. When applied to an intact valve, the finite element model demonstrated an overall discrepancy of only 0.0187 strain when compared to experimental validation data, which was within the experimental error. This result underscored the need for rigorous experimentation and constitutive modeling to allow a close match between FE and experiment output. The present study is, to our knowledge, the most rigorously developed and validated model available to date for characterizing valve deformation. It is hoped that the developed approaches will be a valuable tool for evaluating various valve design parameters and will greatly facilitate optimal BHV design.

TABLE OF CONTENTS

LIST OF TABLES

LIST OF FIGURES

PREFACE

I am truly grateful to everyone who has directly or indirectly supported and helped me complete this Ph.D. dissertation. First and foremost, I would like to thank my advisor Dr. Sacks, for his advice, mentoring, and financial support for my Ph.D. study. I will always be impressed by the depth and breadth of his technical expertise and his persistence for academic excellence. This dissertation would not be possible without his help and effort.

I would like to thank to my committee members: Dr. David Vorp, Dr. Michael Scott, Dr. James Antaki and Dr. William Slaughter for their assistance, advice, and careful review of the dissertation. Besides research, I also learned from their teaching, I took Biomechanics class from Dr. Vorp, Advanced Elasticity class from Dr. Slaughter and I was a teaching assistant for Dr. Antaki for Bioengineering Senior Design class.

I am indebted particularly to Dr. Scott not only for his coming all the way from California to attend my defense but also for the care and guidance he gave to me during my two summer interns at Edwards Lifesciences. In this respect, I would like to express my gratitude to all the friends in Edwards Lifesciences who made my short stays in California so enjoyable. Also special thanks to Dr. Claudio Argento and Dr. Milton DeHerrera for the enlightening discussion on the finite element method.

I was also very fortunate to have the opportunity to work with a group of energetic, talented people in the Engineered Tissue Mechanics Lab, they are Jiro Nagatomi, Ph.D., Ali Mirnajafi, Ph.D., David Merryman, George C. Engelmayr, Shadow Huang, Tiffany Sellaro, Jon Grashow, Daniel Hildebrand and Thanh V. Lam. They are my friends and I have enjoyed every moment we worked together and I appreciated all their help. I want especially to thank lab alumni Dr. Claire Gloeckner, whom I called "a useful resource for everything you don't know," her help to me was boundless. Also I would like to thank Hiroatsu Sugimoto, a recent graduated M.S. student, for his help in performing the valve deformation experiments and digitization of the images.

Finally, I thank my family, parents, Guiyun Zhu and Wentang Sun, wife, Bixia, and daughter, Christina and son, Bill, for their belief in me and whole-hearted love. They are an endless source of support and purpose. This dissertation is dedicated to them.

1.0 INTRODUCTION

"The heart, consequently, is the beginning of life; the sun of the microcosm, even as the sun in his turn might well be designated the heart of the world; for it is the heart by whose virtue and pulse the blood is moved, perfected, and made nutrient, and is preserved from corruption and coagulation" – William Harvey (1578-1657)

Before 1900, most people made their living primarily through manual labor and had relatively short live spans, and thus very few people died of heart disease. After the Industrial Revolution, the age of technology has made life easier and the increased lifespan made people more prone to heart disease. The combination of a sedentary lifestyle and a rich diet led to an increase in clogged blood vessels, heart attacks, and strokes. Heart disease became commonplace. The rate of heart disease increased so sharply between 1940 and 1967 that the World Health Organization called it the world's most serious epidemic. Since then, heart disease has become the number one killer in the United States. Today, many causes of heart disease are known. To a certain extent, so are the cures. Through the years, tools and techniques for treating heart disease have also evolved to meet the increased need[1] (See Milestones in Cardiology at http://sln.fi.edu/biosci/history/firsts.html). However, much remains to be done.

Heart valve disease, a kind of heart disease caused by rheumatic fever, birth defects, aneurysms, and other ailments, is a significant cause of morbidity and mortality. Currently, the treatment of aortic valve disease is usually complete valve replacement. Worldwide, there are ~300,000 people each year who undergo heart valve replacement surgery. Approximately one-half of heart valve patients receive mechanical heart valves, which are composed of rigid, synthetic materials. The other half receives bioprosthetic heart valve (BHV) replacements, which are composed of biologically derived tissues. In general, BHV have good hemodynamics and do not require the anti-coagulation therapy necessary for mechanical heart valves. However, BHV continue to fail from calcification and mechanical damage [2]. Recent work on explanted BHV suggested that *mechanical damage to collagen could occur independent of calcification [3], indicating that mechanical damage alone can be a major clinical cause of failure.* Clearly, an in-depth understanding of the biomechanical behavior of the BHV at both the tissue- and functional prosthesis levels is essential to improving our understanding of BHV failure.

Improving BHV durability is an ongoing and challenging research area. It is the goal of this dissertation to provide better understanding of BHV biomechanical behaviors and to aid in the design of novel heart valve biomaterials. In this chapter, a brief overview of heart valve replacement, experiment techniques, constitutive models and numerical simulations will be presented. However, where appropriate, more detailed reviews on theories and previous studies may be presented in the introduction section of the associated chapters. Nonetheless, this chapter begins with a brief look at the heart and its four valves.

1.1 INTRODUCTION TO THE HEART AND ITS FOUR VALVES

Heart is a pumping muscle that works nonstop to keep the body supplied with oxygen-rich blood. Four one-way heart valves keep blood moving in one direction through the heart. The heart is divided into four chambers. The upper chambers are called atria and the lower chambers are called ventricles. The heart muscle contracts blood from chamber to chamber. With each contraction, the one-way valves open to let blood through to the next chamber. The valves then close to stop blood from moving backward. In this way, the valves keep blood moving through the heart and out to the body. The valves and the parts of the heart are shown in Figure 1-1.

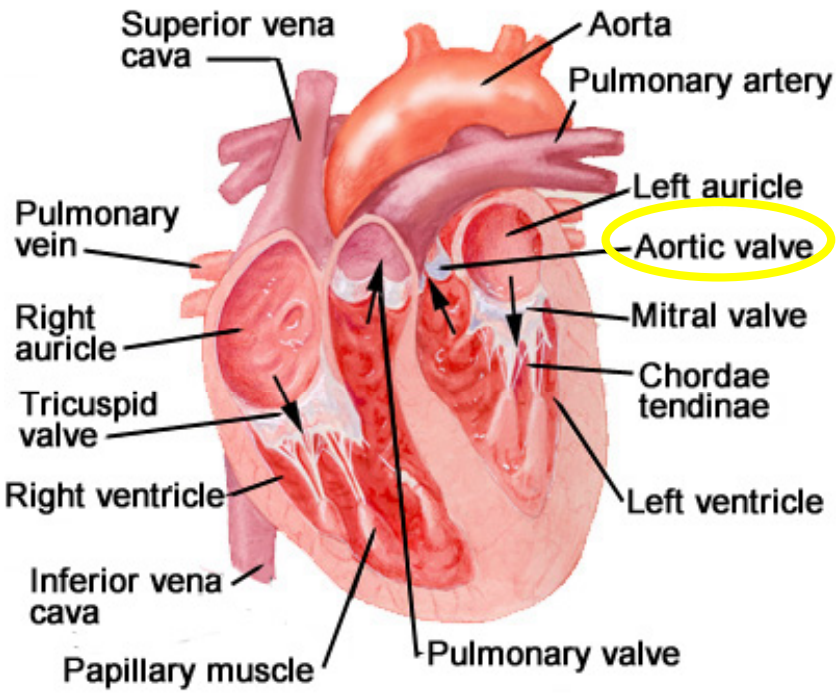

Figure 1-1 Anatomical structure of the heart and the heart valves (Image courtesy of www.surgery.com)

The **tricuspid** valve is located between the right atrium and right ventricle. The **pulmonary** or **pulmonic** valve is between the right ventricle and the pulmonary artery. The **mitral** valve is between the left atrium and left ventricle. The **aortic** valve is between the left ventricle and the aorta.

Each valve has a set of flaps (also called leaflets or cusps). When working properly, the heart valves open and close fully. But a heart valve can be damaged. A person can be born with an abnormal heart valve, a type of congenital heart defect. A valve can become damaged by

- Infections such as infective endocarditis
- Rheumatic fever
- Changes in valve structure in the elderly

Disease can affect these valves in two ways, stenosis and regurgitation. Stenosis is a narrowing of the valve so that blood cannot move through as freely as necessary. Regurgitation is a failure of the one-way valve so that blood flows back through the valve in the wrong direction.

The valves most commonly affected by disease are the mitral valve, which controls flow of the blood from the left upper chamber (atrium) to the left lower chamber, and the aortic valve, which controls blood flow out of the left ventricle to the rest of the body. The study in this dissertation will focus on the aortic valve replacement.

1.2 BIOMECHANICS AND FUNCTION OF NATURAL AORTIC VALVE

Development of tissue valve substitutes depends on an understanding of the fundamental mechanisms limiting the durability of previous and current tissue valves. This in turn necessitates an understanding of the structure-function of the natural aortic valve, in particular from the biomechanical prospective.

The aortic valve cusps are mostly (90%) water, but contain other components that give it unique mechanical properties. The connective tissue proteins collagen and elastin are the main structural components, while the roles of glycosaminoglycans and a small population of cells are poorly understood. The cusp consists of three layers of morphologically distinct tissue in the Figure 1-2 below: the fibrosa, spongiosa and ventricularis.

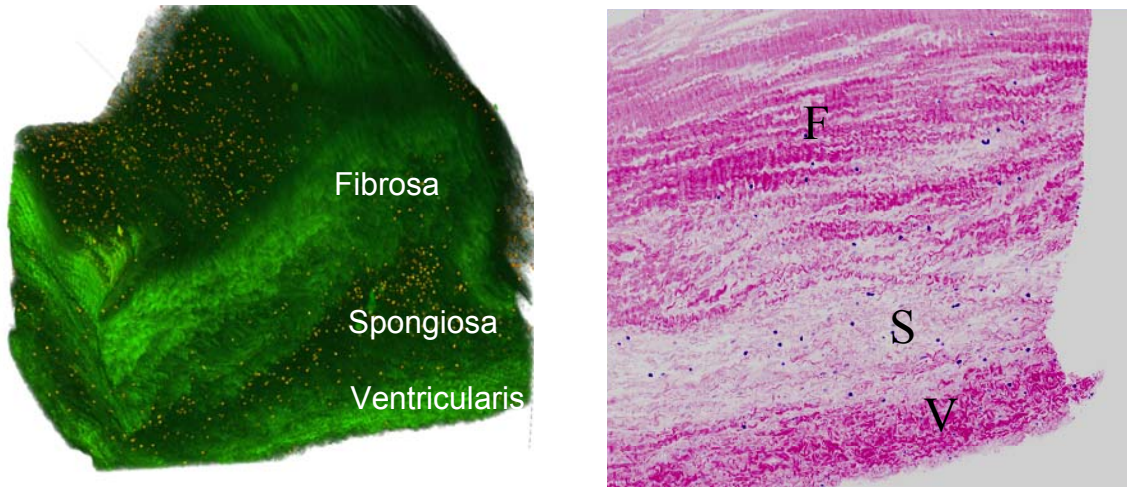

Figure 1-2 Three layers of aortic cusp: fibrosa(F), spongiosa(S) and ventricularis(V).

The fibrosa consists mainly of collagen, arranged in a circumferential direction to transmit the forces imposed on the leaflets to the aortic wall, in a corrugated manner that enables the leaflets to expand radially, typically to 50% strain. During valve

loading, the radial expansion enables the three leaflets to mate together and seal off the orifice. The stiffening induced by fully extended collagen crimp, flattened corrugations, and taut collagen cords prevents exaggerated sag of the cusp centers when the valve is shut, thereby preserving maximum coaptation (Figure 1-3).

The ventricularis consists mainly of sheet elastin and provides the tensile recoil necessary to retain the folded shape of the fibrosa. This relationship between the fibrosa and the ventricularis requires the fibrosa to remain preloaded in compression (to retain its corrugated state) and the ventricularis to remain in tension (to hold the fibrosa in compression). The elastin of the ventricularis expands when the cusps stretch to enlarge the coaptation area, but recoils to make the cusp smaller in the open phase (Figure 1-3).

The spongiosa consists mainly of collagen, elastin, proteoglycans and mucopolysaccharides, behaves as a buffer zone that enables the localized movement and shearing between the fibrosa and the ventricularis during loading and unloading. Shear stresses caused by the differential movement of the layers and the shock of valve closure are dissipated in the spongiosa, whose hydrophilic GAGs readily absorb water, swell to form a gel and resist compression forces[4].

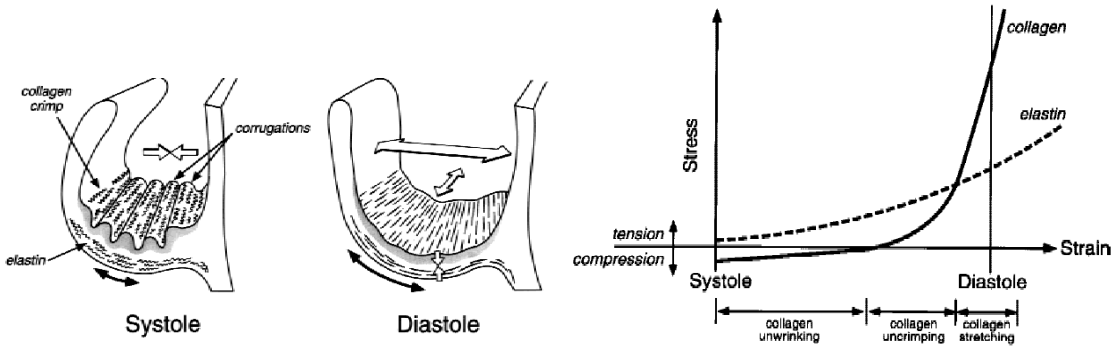

(a) (b)

Figure 1-3 (a) Schematic representation of cuspal configuration and architecture of collagen and elastin in systole and diastole. (b) Schematic representation of biomechanical cooperatively between elastin and collagen during valve motion. During opening, elastin extends at minimal load during extension of collagen crimp and corrugations. Near full closure, when the collagen has fully unfolded, the load-bearing element shifts from elastin to collagen, and stress rises steadily while coaptation is maintained. In systole, elastin restores the contracted configuration of the cusp. Adapted from Schoen and Levy [4].

In addition to layer-to-layer differences, valve cusps also exhibit heterogeneity of tissue structure with region-to-region variation. Those regions include free edge, commissures, coaptation surface, nodulus, belly and annulus (Figure 1-4a). These functionally different regions not only have varied thickness [5] but also varied preferred fiber orientations (Figure 1-4b) [6]. When mapped with stress-strain data, those regions exhibited a profound mechanical property difference, for example, between the nodulus and central belly region (Figure 1-5) [7].

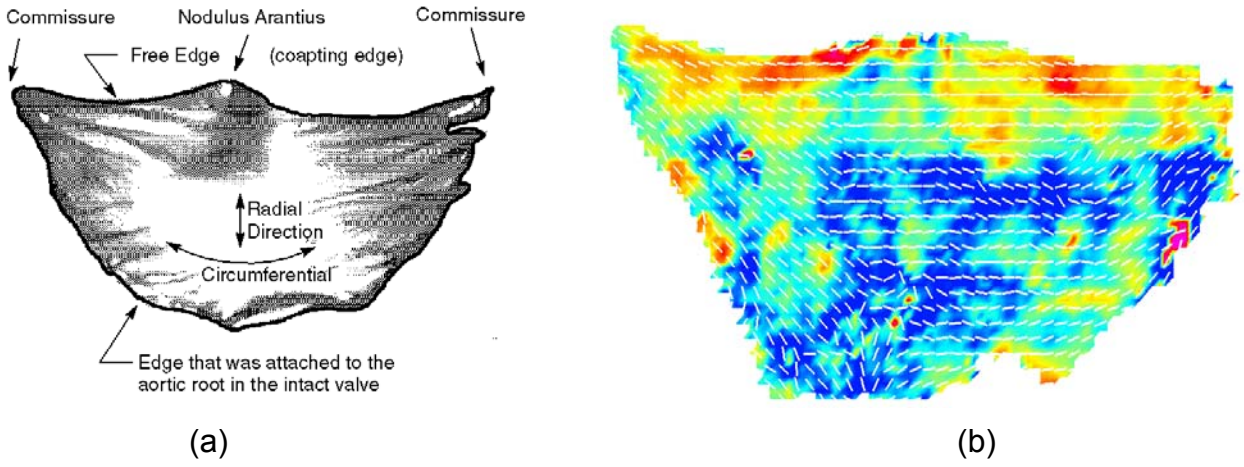

Figure 1-4 (a) cuspal from porcine aortic valve, b) corresponding SALS data. The white vectors represent the local preferred fiber orientations. The background color shading indicates the degree of orientation (warmer color = more highly aligned fiber population).

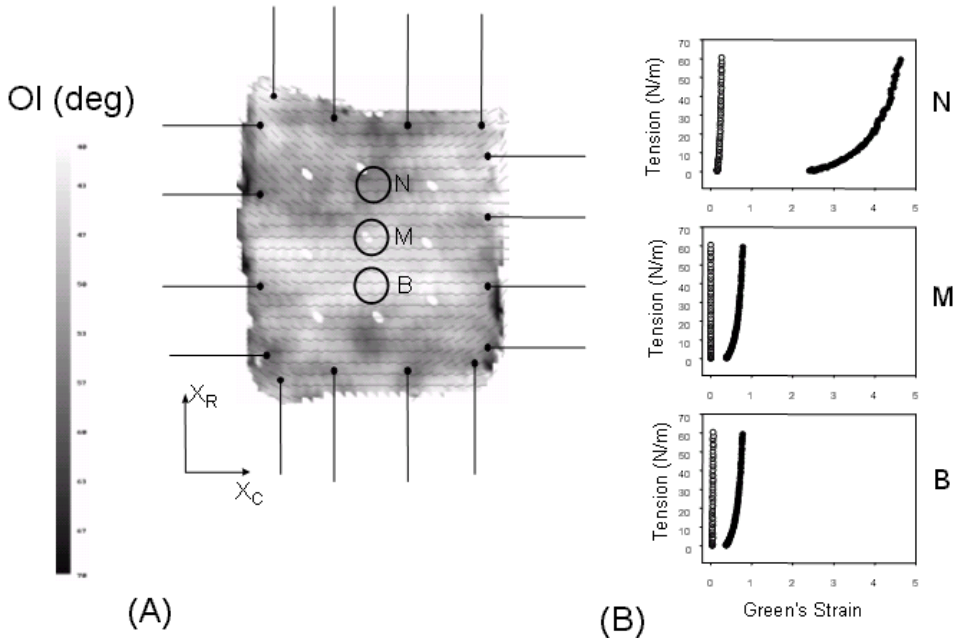

Figure 1-5 (a) Tissue leaflet under biaxial testing. Letters denote the location of local stress-strain curve. (b) Stress strain curve from three locations on the valve. Light circles are in circumferential direction. and dark circles are in radial direction. OI, orientation index; N, nodulus; M midregion; B, belly. Adapted from Billiar and Sacks [7, 8].

1.3 HEART VALVE REPLACEMENT

First performed successfully in 1960, surgical replacement of diseased human heart valves by valve prostheses is now commonplace and enhances survival and quality of life for many patients. Currently it is estimated that about 82,000 valve replacements are performed in the United States and about 300,000 worldwide each year[9]. The state-of-the-art prosthetic valves clinically used include mechanical valves and tissue valves (xenografts and homografts) [9]. Mechanical prostheses are fabricated from synthetic materials, mainly pyrolytic carbon leaflets mounted in a metal frame. Bioprosthetic valves (BHV) are fabricated from either porcine aortic valve or bovine pericardium, chemically treated with glutaraldehyde, and usually mounted onto a flexible metal frame (stent) that is covered with cloth to facilitate surgical implementation (Figure 1-6).

(a)

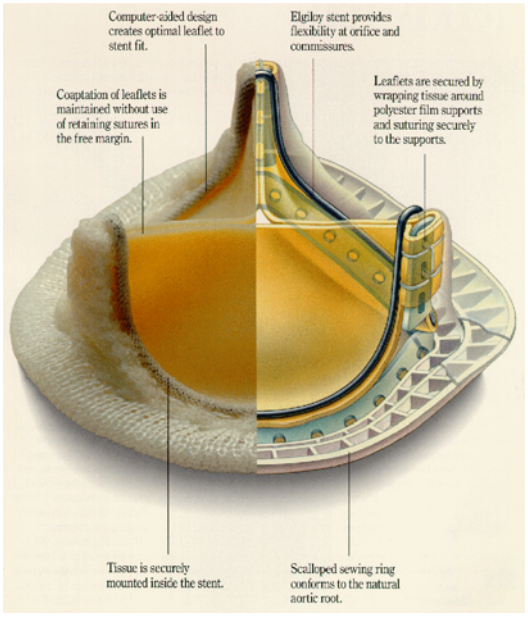

(b)

Figure 1-6 (a) Starr-Edwards Silastic Ball valve prosthesis; (b) Edwards - Perimount® tissue valve. (Images courtesy of Edwards Lifesciences)

In general, BHV has the advantage of low rates of thromboembolic complications without chronic anticoagulation therapy (and its associated morbidity and mortality risks) required for mechanical prostheses. However, they suffer high rates of late structural dysfunction owing to tissue degradation [4, 10]. The principal processes that account for BHV tissue degradation *in vivo* are widely considered to be 1) cuspal mineralization, causing cuspal stiffening with or without tearing, and 2) non-calcific cuspal damage, including mechanical fatigue and possibly proteolytic degradation of the collagenous extracellular matrix, causing cuspal tears and perforations [4, 10].

Of the two major BHV designs, BHV fabricated from chemically (glutaraldehyde) treated bovine pericardium (GLBP) has greater design flexibility, since

the anatomy of the porcine aortic valve and root limit the range of valve designs. Although early pericardial BHV were poorly designed, resulting in high failure rates, current designs have a level of durability comparable to or higher than their porcine aortic valve counterparts [11-15]. However, all BHV continue to suffer from limited durability due to structural failure [2, 16] and are generally restricted to patients ~60 years or older, limiting their clinical applicability.

There have been many attempts to improve BHV durability through novel chemical treatments [17-21]. For example, dye-mediated photo-oxidation has been shown to be resistant to mineralization and *in vitro* chemical and enzymatic degradation, supportive to endothelial cell growth, and to be stabile *in vivo* [22-25]. However, BHV made utilizing this chemical treatment have met with poor clinical outcomes exclusively due to structural failures, a result of both faulty valve design and poor tissue durability [26]. Recent work on explanted BHV indicated that mechanical damage to collagen could occur independent of calcification [3], indicating that *mechanical damage alone can be a major clinical cause of failure*. Clearly, an in-depth understanding of the mechanical behavior of the BHV at both the tissue- and functional prosthesis levels is essential to improving our understanding of BHV failure.

1.4 MECHANICAL TESTING OF NATURAL AND BIOPROSTHETIC VALVE

Experimental biomechanics is a challenging and important discipline unto itself; experiments provide information that is essential for formulating constitutive relations,

evaluating broader theoretical concepts as well as for solving many boundary value and initial value problems. The most commonly used experimental tests for characterizing mechanical properties of soft tissue include uniaxial test, biaxial test, bending test (three- or four-point bending), membrane inflation test, and accelerated durability fatigue test.

1.4.1 Uniaxial Test

Mechanical investigations of tissue valve biomaterials have usually been confined to *uniaxial* studies because of the difficulties in controlling two or even three-dimensional boundary conditions. In simple elongation at a constant strain rate, collagenous tissue usually exhibits "strain-stiffening" J-shaped stress-strain curves. It is an important characteristic of soft tissue that an initial large extension is achieved with relatively low levels of stress and becomes subsequently stiffer at higher levels of extension. Biomechanically, it is widely accepted that this phenomenon is associated with the recruitment of collagen fibers as they become uncrimped and reach their natural lengths, whereupon their significant stiffness comes into play and overrides that of the underlying matrix material.

Broom (1978) reported early uniaxial stress-strain data from porcine pulmonary valves, tested in both the circumferential and radial direction. [27] Morphology of collagen crimp was found to correlate with a nonlinear stress-strain response. Kunzelman *et al.* [28] conducted uniaxial tests on the mitral valve and found different stress-strain responses between the circumferential and radial directions. However, due

to anisotropy, uniaxial data cannot be used to extrapolate to the fully generalized three-dimensional constitutive equations, even if multidimensional strain data from the uniaxial experiment is available.

1.4.2 Inflation of Membrane Tissues

There have been investigations using *inflation of circular membranes*, which is intended to test thin-walled tissues, such as pleura, dura mater, mesentery, urinary bladder, in a more natural way. However, experiments were performed under an assumption of isotropy can provide necessary experimental data [29, 30], which is usually not applicable [31]. The experiment requires small markers to be affixed to the membrane surface and two CCD cameras are used to trace the marker motion to infer the associated inflation and membrane strain. The difficulty of performing such experiments lies in the accurate 3D reconstruction of the inflated surface, because the markers sometimes are out of focus during the inflation. If local strain within a particular small region delimited by 3 or 4 markers is required, meticulous care needs to be given in digitizing the marker locations from the images. Further, when attempting to determine material constants for complex material models, *biaxial testing* methods are required that include complex testing protocols that allow large variations in stress and strain states for full characterization [7, 32-34].

1.4.3 Biaxial Test

Biaxial experiments on soft biological tissues, as illustrated on Figure 1-7, are generally difficult to perform and present challenges unique to biological tissues. Just a few of the experimental problems include: small specimen sizes, structural and compositional heterogeneity, difficulty in gripping (without causing damage), dramatic effects of different gripping techniques, e.g. St. Venant–like effects (will be addressed in detail in Chapter 4), difficulty in precisely identifying material axes, difficulty in assuring constant forces along specimen edges, large specimen-to-specimen variability, time-dependent changes due to biological degradation, and unknown levels of pre-stress in tissue layers. In addition, determination of homogeneity of deformation within the specimen is paramount. These issues can often frustrate the application of even the most straightforward attempts to develop a constitutive model [34].

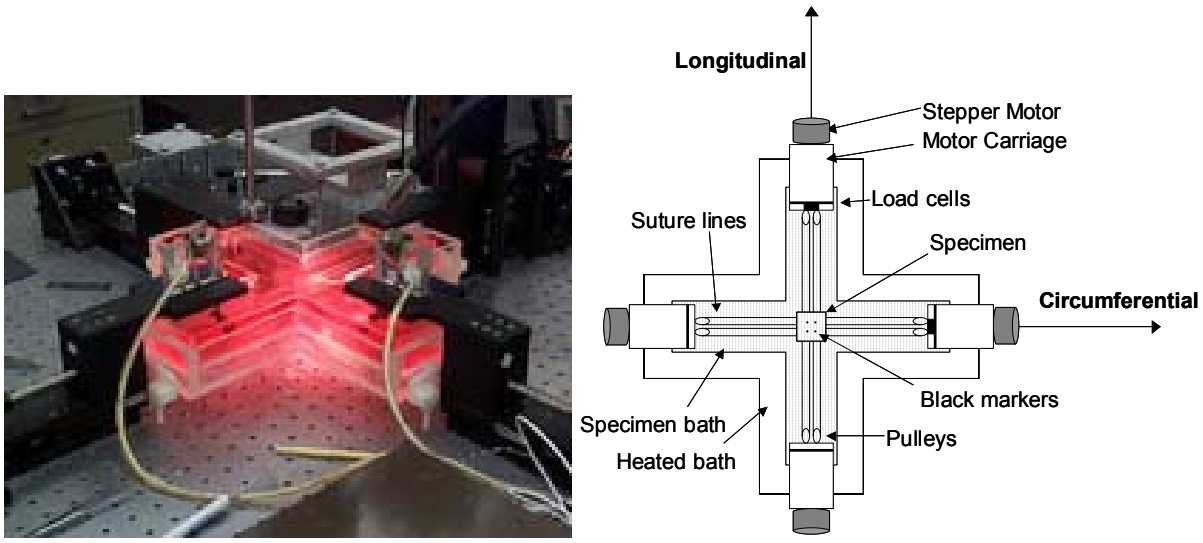

(a) (b)

Figure 1-7 Actual (a) and schematic (b) biaxial testing setup. The specimen is submerged in an appropriate physiologic solution, marked with four black graphite particles (optical markers for strain measurement) and attached to the device via four hooks at each side.

The first investigators to develop and utilize planar biaxial testing for soft biological tissues were Lanir and Fung in 1974 [32, 35] who investigated the mechanical properties of rabbit skin. The techniques were quickly adapted for testing of other tissues, for example, lung parenchyma [36], pericardium [37-39], myocardium [40-42].

Biaxial testing has recently been used to characterize valve tissues. May-Newman *et al.* [43, 44] reported biaxial testing results of anterior and posterior leaflets from excised porcine mitral valves. They showed that both anterior and posterior leaflets were less extensible in the circumferential than in the radial direction under equibiaxial stretch, with aspect stress ratios of 5.7 and 4.3. The experimental data ware later modeled with a transversely isotropic model. To induce shear, which is essential for a

finite element formulation, Sacks [38] introduced a method to induce a combined state of in-plane biaxial normal and shear strains. The method takes advantage of rotation of the test specimen's material axis to the test axes and requires only modest modifications to the biaxial testing device [45] to allow the specimen to undergo unrestricted shear deformations [34]. The experimental method was later adapted in Sun *et al.* [39] for stress-controlled biaxial testing. High in-plane shear response of heart valve biomaterials was characterized (will be further elaborated in Chapter 2).

1.4.4 Accelerated Durability Fatigue Test

Another mode of mechanical testing, which will be addressed in detail in Chapter 6, is the fatigue testing of heart valve biomaterials. Only vague references are available for the possible processes of wear or tissue fatigue of valve biomaterials. Lee *et al*. have performed extensive physical studies on GLBP behaviors [46-51]. Recently they detected that fatigue damage accelerates enzymatic degradation of GLBP [52]. Hilbert *et al*. [53] used polarized light optics to characterize damage to the BHV collagen fiber architecture due to accelerated testing. For bovine pericardium, they measured an initial collagen fiber crimp period of 17.1±3.2 microns, which increased to 23.5±3.4 microns after 360×10^6 cycles. Purinya *et al*. [54] found ~50% reduction in strength in human implanted BHV after only 48 months of in-vivo operation.

For candidate BHV biomaterials, current methods to assess their durability are mainly through costly and time-consuming accelerated durability testing, animal implantation studies, and clinical trials. Accelerated durability tests can cause some

forms of tissue damage that might or might not approximate the tissue stress fields for a intact valve. Nonetheless, the mechanisms of such damage are difficult to analyze due to the complexity of the BHV leaflet deformations and the confounding influences of the specific valve design. Broom *et al*. [55] conducted the first efforts to characterize the tissue behavior under combined tensile and buckling fatigue studies. However, to fully characterize the mechanisms of tissue degeneration, isolation of the individual mechanical loading states (e.g. tension, flexure) is a necessary first step in understanding the fatigue process as a whole.

1.5 CONSTITUTIVE MODELING OF MECHANICAL PROPERTIES OF SOFT TISSUE

For both natural biological tissues and tissue-derived soft biomaterials, there exist many physiological, surgical, and medical device applications where rigorous constitutive models are required. Examples include skin, myocardium, tendons, natural and prosthetic heart valves, and blood vessels. For these biological materials particular challenges in constitutive modeling are encountered due to their complex mechanical behavior. For example, because of their oriented fibrous structures they often exhibit pronounced mechanical anisotropy. In addition, they exhibit highly nonlinear stress-strain relationships, large deformations, viscoelasticity, and strong axial coupling. Taken as whole, soft biomaterials defy simple material models [31].

Determination of a constitutive relation that describes well the behavior exhibited by a complex nonlinear, anisotropic soft tissue is very challenging, even under limited conditions. Fortunately, however, the search for the possible forms of such relations has been simplified considerably by the continuum "principles", for which the materials can be reasonable assumed to behave. Those principles are included in the theory of finite elasticity, in particular, the principles of determinism, local action, equipresence, and material frame indifference – in addition to conservation of mass, balance of linear and angular momentum, balance of energy and the second law of thermodynamics – each restricts the possible forms of constitutive relations.

The concept of pseudo-elasticity was introduced by Y. C. Fung [56] following the observation that most tissues exhibit repeatable (elastic) behavior under cyclic loading. This allowed the use of the theoretic framework of hyperelasticity, originally developed for isotropic rubber-like materials, to be used to describe the mechanical response of soft tissues. Hyperelasticity implies that material behavior can be described via a strain (stored) energy function. Over the last few decades, various strain energy functions have been developed for soft tissues. Among them are the nonlinear isotropic model [57, 58], transversely isotropic model [41, 42, 59, 60], and anisotropic exponential models [39, 56, 61-63]. Among all these constitutive models, the exponential model proposed by Fung [56] is perhaps the most widely used constitutive model for characterizing biaxial responses of soft biological tissues, as well as other loading states. More detailed discussion of the constitutive theory for cardiovascular biomechanics and soft tissue biomechanics in general can be found in the treaties of Fung [56, 64, 65]. Some basic concepts will be restated

in Chapter 2 and finite element implementation of a general pseudo-elastic Fung model will be addressed in detail in Chapter 3.

1.6 COMPUTATIONAL METHODS

It is suggested that there were three major events in history necessary before the study of modern biomechanics of soft tissues could evolve [66]; one of them is the development of the *finite element method* in the 1950s*. Because of the complex nature of soft tissues, such as heart valves, computational methods are necessary to model their biomechanical response. Computational methods therefore offer a powerful way to integrate structural properties quantitatively measured *in vitro* and predict physiological functions *in vivo*.

Accurate computational modeling of the nonlinear, anisotropic mechanical properties of soft tissues remains an important and challenging area. Although various strain energy functions have been proposed in the literature for soft tissues, finite element implementation has been rather limited. Lack of finite element implementations of soft tissue constitutive models could be of many reasons. Among them are a lack of appropriate experimental data (for both formulating constitutive models and validation of numerical simulations) and computational difficulties in

* The other two major events are the development of the nonlinear field theory of mechanics during the 1950s and the rapid advances in computer technology.

incorporating these models into available finite element codes. In particular, problems with solution convergence can result in a numerically unstable model that may lead to either inaccurate results or fail to converge.

Among various constitutive models developed, the exponential model proposed by Fung [56] is perhaps the most widely used. Although it has been in the literature over several decades, the implementation of this model into finite element simulations has been very limited. The main reason is due to the high nonlinearity of the model that leads to numerical unstable in finite element simulations. We will address this issue in Chapter 3 and illustrate our approaches of restricting the model necessary to achieve numerical stability.

Finite element analysis has been the most popular method for the stress analysis of the valve leaflets with the blood pressure applied as the load. Numerical analysis and simulation of BHV has made some headway into understanding true valve behavior. Particular challenges encountered in numerical simulation of BHV include modeling of complex leaflets and stent geometry, modeling of the associated (nonlinear anisotropic) mechanical properties, contact of leaflets, and experiment validation of numerical results. The importance of experimental validation of finite element results cannot be over-emphasized. However, many finite element studies offered no experiment validation [67-70] or simple validations, such as comparison between images taken from pulse duplicator to that of a finite element output[71, 72]. In Chapter 5 we will further elaborate the issue and present a rigorous experiment validation of our BHV simulation.

The most crucial factor affecting the accuracy of a BHV simulation is probably the material model of the valve leaflets. Some of the studies used the linear isotropic models [73, 74], others used nonlinear isotropic models [67-69, 72, 75, 76]. However, utilizing a full nonlinear anisotropic model, such as the Fung model that will be described in Chapter 3, in a BHV simulation has not yet been seen in the literature. In Chapter 5, we will construct a more accurate finite element valve model and simulate its deformations under 120mmHg trans-valvular pressure. Once the results of such simulations are validated with experimental data, parametric studies with geometrical changes of the leaflets and material property changes of the leaflets as well as trans-valvular pressure conditions can be carried out inexpensively.

1.7 MOTIVATION OF THE STUDY

Replacement of diseased natural heart valves with prosthetic replacements has been life saving for millions of patients. However, as in so much of medicine today, the replacements valves are never as good as natural, healthy valves. Tissue engineering of heart valves is an evolving research field. Multidisciplinary approaches for designing and growing viable heart valves identical to the native heart valves have begun and offers a promising future. However, in the immediate future, BHV fabricated from heterograft biomaterials will continue to be extensively used [4]. GLBP will still be one of the most favorite tissue candidates. Hence comprehensive studies of chemically treated tissue behaviors under both quasi-static and dynamic loading conditions will enhance

our understanding to the BHV failure. Incorporating those experimentally-derived material properties into finite element models and simulating valve deformations under various conditions will ultimately improve BHV design and consequently its durability.

Our long-term goal is to develop a comprehensive understanding of BHV biomechanics to provide insight into tissue mechanical damage and to aid in the design of novel heart valve biomaterials. To achieve these aims, we believe that 1) rigorous experimentation is necessary to fully quantify biomaterial mechanical properties; 2) robust constitutive models are required for accurate modeling of tissue behaviors; 3)numerical simulations need to be conducted to analyze BHV function and optimally design BHV. In this dissertation, *our aim is to develop and evaluate a complete process for biomechanical simulations of heart valve biomaterials, with an emphasis on accurate material model, numerical stability and experimental validation*. This process includes:

- Formulating a constitutive model
- Collection of appropriate experimental data
- Obtaining and refining material parameters
- Finite element implementation and validation of the constitutive model
- Finite element simulations of BHV deformation

2.0 CHARACTERIZATION OF MECHANICAL PROPERTIES OF HEART VALVE BIOMATERIALS[†]

"Physical theory must be based on experience, but experiment comes after, rather than before, theory. Without theoretical concepts one would neither know what experiments to perform nor be able to interpret their outcome" - Truesdell and Noll, 1965

Utilization of novel biologically-derived biomaterials in bioprosthetic heart valves requires robust constitutive models to predict the mechanical behavior under generalized loading states. Thus, it is necessary to perform rigorous experimentation involving the functional deformations to obtain both the form and material constants of a strain-energy density function. In this chapter, we will apply a novel stress-control biaxial testing method to generate a comprehensive biaxial mechanical dataset that includes a high in-plane shear state for heart valve biomaterials (sections 2.2.1 - 2.2.3). To develop the appropriate model, we developed an interpolation technique for the

---

[†] Some of the results of this chapter are published in:

M. S. Sacks and W. Sun, "Multiaxial mechanical behavior of biological materials", ***Annual Reviews of Biomedical Engineering,*** vol. 5, pp.251-284, 2003.

W. Sun, M.S. Sacks, T.L. Sellaro, W.S. Slaughter, and M.J. Scott, "Biaxial mechanical response of bioprosthetic heart valve biomaterials to high in-plane shear", ***Journal of Biomechanical Engineering,*** vol. 125, pp. 372-380, 2003.

pseudo-elastic response to guide the final model form (sections 2.3.3 and 2.3.4). Finally, some concerns during our experiment and modeling will be discussed in section 2.4, including the rationales of using stress-controlled protocol, effects of chemical fixation on the mechanical properties. We will begin the chapter with a brief review of the biaxial testing method, kinematics and the associated stress and strain energy functions.

2.1 INTRODUCTION

2.1.1 Basic Techniques for Biaxial Testing of Soft Biological Materials

In general, biaxial testing of biological tissues are performed using thin specimens, which are either a membrane in its native form or a thin section prepared from a thick tissue slab. The specimen is mounted to the biaxial device in trampoline-like fashion using thin threads, which allows the edges to expand freely in the lateral direction. Testing is generally performed with the specimen completely immersed in phosphate buffered normal saline (pH 7.4) at room or body (37 °C) temperature. The central target region must be sufficiently small and located away from the outer edges to avoid the tethering effects. Thus, in the central target region the stress and strain field is generally considered homogeneous.

2.1.2 Kinematics of a Biaxial Test

The following is a brief summary of the most important aspects of the kinematics of a biaxial mechanical test. For further details, the interested reader is referred to Sacks

2002[34]. We consider deformation of membrane tissues under a biaxial stress state, including non-zero in-plane shear stresses. For this case, we let Ω_0 and Ω be the (fixed) reference and deformed configurations of the continuous body, respectively. We consider the general mapping $\chi : \Omega_0 \to \mathbb{R}^3$, which transforms a material point $\mathbf{X} \in \Omega_0$ to a position $\mathbf{x} = \chi(\mathbf{X}) \in \Omega$ in the deformed configuration. For planar homogeneous deformations that occur during a biaxial test, this mapping reduces to

$$x_1 = \lambda_1 X_1 + \kappa_1 X_2, \;\; x_2 = \lambda_2 X_2 + \kappa_2 X_1, \;\; x_3 = \lambda_3 X_3 \tag{2.1}$$

where λ_i are the axial stretch ratios and κ_i measures of in-plane shear. λ_i and κ_i are also components of the deformation gradient tensor $\mathbf{F}$, which for deformation described in eqn. 2.1 is $\mathbf{F} = \mathrm{Grad}(\mathbf{x})$ or

$$\mathbf{F} = \begin{bmatrix} \frac{\partial x_1}{\partial X_1} & \frac{\partial x_1}{\partial X_2} & \frac{\partial x_1}{\partial X_3} \\ \frac{\partial x_2}{\partial X_1} & \frac{\partial x_2}{\partial X_2} & \frac{\partial x_2}{\partial X_3} \\ \frac{\partial x_3}{\partial X_1} & \frac{\partial x_3}{\partial X_2} & \frac{\partial x_3}{\partial X_3} \end{bmatrix} = \begin{bmatrix} \lambda_1 & \kappa_1 & 0 \\ \kappa_2 & \lambda_2 & 0 \\ 0 & 0 & \lambda_3 \end{bmatrix} \tag{2.2}$$

where the out-of-plane stretch $\lambda_3 = h/H$ is the ratio of deformed (h) to the undeformed thickness (H) of specimen. $\mathbf{F}$ is a critical mathematical quantity since it completely describes the deformation state. Since soft tissues are composed primarily of water and have negligible permeability [56], they can be considered incompressible so that $J = \det\mathbf{F} = 1$. From $\mathbf{F}$ the right Cauchy-Green deformation tensor is defined as $\mathbf{C} = \mathbf{F}^T \cdot \mathbf{F}$, from which the components of the in-plane Green-Lagrange strain tensor $\mathbf{E} = \frac{1}{2}(\mathbf{C} - \mathbf{I})$,

where **I** is the identity tensor. **E** is the most common finite strain measure in the soft tissue literature due to the simplicity of the constitutive formulations. In practice the components of **E** are computed more directly using:

$$\mathbf{E} = \frac{1}{2}(\mathbf{F}^{T}\mathbf{F} - 1) = \frac{1}{2}\begin{bmatrix} \lambda_1^2 + k_2^2 - 1 & \lambda_1 k_1 + \lambda_2 k_2 & 0 \\ \lambda_1 k_1 + \lambda_2 k_2 & \lambda_2^2 + k_1^2 - 1 & 0 \\ 0 & 0 & \lambda_3^2 - 1 \end{bmatrix} \tag{2.3}$$

The components of **F** are determined optically to avoid any mechanical interference with the specimen. This is typically done by tracking the position of markers mounted on the upper specimen surface that delimit the central target region using optical tracking software [45, 77]. In both our laboratory [45] and in others [78, 79], finite element shape functions are used to approximate the position vector field within the central target regions. This can include linear and quadratic variations in strain [7].

2.1.3 Forces and Stress

As mentioned above, biaxial testing of biological tissues is performed using thin specimens (no more than ~3 mm, usually <1 mm) and acted on by only in-plane loads. A state of plane stress is thus assumed so that the components t_{i3} (i=1,2,3) of the Cauchy stress **t** (force/deformed area) are 0. During actual experiments one can directly measure only the initial specimen dimensions, so that the Lagrangian stresses **T** (force/unit original cross-sectional area) are used for convenience. The components of **T** are computed from the measured axial forces **P** using

$$T_{11} = \frac{P_1}{hL_2}, \quad T_{22} = \frac{P_2}{hL_1} \tag{2.4}$$

where h is the specimen thickness and L_i are the specimen lengths. Since experimentally applied loads are normal to the edges, $T_{12}=T_{21}=0$. The 2nd Piola-Kirchhoff stress tensor **S** is the most commonly utilized stress tensor for soft tissue constitutive theories, and is determined using $\mathbf{S}=\mathbf{T}\bullet\mathbf{F}^{-1}$. The Cauchy stress tensor **t** is determined using $\mathbf{t}=\mathbf{F}\bullet\mathbf{T}/J$, which in component form is given by (with $T_{12}=T_{21}=0$):

$$t_{11} = \lambda_1 T_{11},\ t_{22} = \lambda_2 T_{22},\ t_{12} = \kappa_1 T_{22},\ t_{21} = \kappa_2 T_{11} \tag{2.5}$$

In the case where there is negligible shear strain (i.e. $E_{12}\sim 0$), the normal components of the two stress tensors are related by:

$$S_{11} = T_{11}/\lambda_1,\ S_{22} = T_{22}/\lambda_2 \tag{2.6}$$

2.1.4 Constitutive Modeling

Perhaps the best way to introduce characterization and modeling for the multi-axial behavior of soft tissues is to summarize the pioneering work on elastomers of Treloar [80] and Rivlin [81-83]. In addition to describing methods for multi-axial testing and modeling, the integrated mathematical-experimental approach of Rivlin is an excellent example on how to conduct material modeling in general. For this class of materials, we assume they are *hyperelastic*, which is defined as the existence of a strain energy function $W = W(\mathbf{F})$. W completely describes the change in internal (mechanical) energy of the material due to the application of external forces.

Since elastomeric materials are assumed to be isotropic, W is assumed be a function of the following strain coordinate invariants I_1 and I_2, defined as:

$$\begin{aligned} I_1 &= \mathrm{tr}\mathbf{C} = \mathrm{tr}\mathbf{B} \\ I_2 &= \frac{1}{2}\left[\left(\mathrm{tr}\mathbf{C}\right)^2 - \mathrm{tr}\mathbf{C}^2 \right] = \frac{1}{2}\left[\left(\mathrm{tr}\mathbf{B}\right)^2 - \mathrm{tr}\mathbf{B}^2 \right] \\ \mathbf{C} &= \mathbf{F}^T\mathbf{F},\ \mathbf{B} = \mathbf{F}\mathbf{F}^T \end{aligned} \tag{2.7}$$

where $\mathbf{C}$ and $\mathbf{B}$ are known as the right and left Cauchy-Green deformation tensors, respectively [84]. In this formulation W is thus still a function of $\mathbf{F}$, but is restricted to isotropic materials through the coordinate invariance of I_1 and I_2. When there is no shear, $\kappa_1=\kappa_2=0$.

Rivlin *et al*. [82] developed the following generalized strain energy formulation:

$$W = \sum_{i=0}^{\infty}\ \sum_{j=0}^{\infty} C_{ij}\left(I_1-3\right)^i\left(I_2-3\right)^j,\ C_{00}=0 \tag{2.8}$$

where C_{ij} are material constants to be determined by fitting the model to experimental data. In most practical applications, the upper limits for the sums in eqn. 2.8 are i=j=3. For the homogenous deformation described by eqn. 2.1, the general constitutive model for isotropic elastomeric materials with $W=W(I_1,I_2)$ is expressed as [83]:

$$t_{(ii)} = 2\left(\lambda_i^2 \frac{\partial W}{\partial I_1} - \frac{1}{\lambda_i^2}\frac{\partial W}{\partial I_2} \right) + p, \qquad i = 1,2,3 \tag{2.9}$$

where p is a Lagrange multiplier that physically represents an arbitrary hydrostatic pressure, and the (ii) subscript indicates no component summation.

In addition to handling incompressibility explicitly using the Lagrange multiplier approach, one can also take advantage of the boundary conditions of a biaxial test to re-express the normal Cauchy stress components. Specifically, with $t_{33}=0$

(upper and lower surfaces are traction free) and employing $\lambda_1\lambda_2\lambda_3=1$ to impose incompressibility, the two remaining Cauchy components are:

$$t_{11} = 2\left(\lambda_1^2 - \frac{1}{\lambda_1^2\lambda_2^2}\right)\left(\lambda_1^2\frac{\partial W}{\partial I_1} - \frac{1}{\lambda_2^2}\frac{\partial W}{\partial I_2}\right)$$
$$t_{22} = 2\left(\lambda_2^2 - \frac{1}{\lambda_1^2\lambda_2^2}\right)\left(\lambda_2^2\frac{\partial W}{\partial I_1} - \frac{1}{\lambda_1^2}\frac{\partial W}{\partial I_2}\right) \quad (2.10)$$

Where the partial derivatives $W_1 = \frac{\partial W}{\partial I_1}$ and $W_2 = \frac{\partial W}{\partial I_2}$ are the response functions. Rather than assume an a-priori form, Rivlin noted that response functions can be directly determined from the experimental measured variables using

$$\frac{\partial W}{\partial I_1} = \frac{\frac{\lambda_1^2 t_{11}}{\lambda_1^2 - \frac{1}{\lambda_1^2\lambda_2^2}} - \frac{\lambda_2^2 t_{22}}{\lambda_2^2 - \frac{1}{\lambda_1^2\lambda_2^2}}}{2\left(\lambda_1^2 - \lambda_2^2\right)} \qquad \frac{\partial W}{\partial I_2} = \frac{\frac{t_{11}}{\lambda_1^2 - \frac{1}{\lambda_1^2\lambda_2^2}} - \frac{t_{22}}{\lambda_2^2 - \frac{1}{\lambda_1^2\lambda_2^2}}}{2\left(\lambda_2^2 - \lambda_1^2\right)} \quad (2.11)$$

Note well that by conducting constant invariant biaxial tests, the functional form of W can be directly determined from the experimental data. This approach can avoid much of the ambiguity inherent in constitutive modeling of elastomeric materials.

2.1.5 Previous Biaxial Testing Experiments

The first investigators to develop and utilize planar biaxial testing for soft biological tissues were Lanir and Fung in 1974 [32, 35] who investigated the mechanical properties of rabbit skin. Briefly, a 3 cm to 6 cm square skin specimen was mounted in a trampoline-like fashion with up to 68 individual attachments distributed equally over the four specimen sides (17/side). Similar to Rivlin [82], the tension on each line could be

individually adjusted to ensure a reasonably uniform stress was applied to each specimen side. Actuator motion was controlled utilizing a function generator. To avoid the effects of local stress concentrations of the suture attachments, bi-directional tissue strain was measured in a central region by monitoring the distance between pairs of lines separated by ~5 mm along each axis video dimensional analyzers (VDA) [85]. Experimental results demonstrated that skin exhibited a nonlinear, orthotropic stress-strain response, whose material axis depended on the specimen's anatomic orientation. While differences between the loading and unloading curves were observed due to hysteresis, the loading and unloading stress-strain responses were essentially independent of strain rate. It is important to note that these results underscore the major phenomenon found in all subsequent biaxial mechanical investigations of soft planar tissues [86].

Another group active in the developing multi-axial constitutive relationships was Vito and co-workers. Among the technical improvements of their device were the use of multi-particle tracking to allow computation of the complete in-plane strain tensor and the use of real-time computer control [87]. Perhaps their main contribution was the development of a technique to identify the specimen's material axis [37]. Generally, identification of a material axis is based on observations of the gross specimen shape (e.g. long axis of a blood vessel) or gross fiber architecture (e.g. myocardium). However, in many tissues the fibers are too small to be visually observed and up to the time of the study there were no rapid, non-destructive techniques for quantification of fiber architecture [31].

To quantify planar tissue fibrous structure, Sacks *et al*. [88] have developed a small angle light scattering technique (SALS). SALS allows for rapid quantification of the angular distribution of fibers at each point in the tissue, from which the preferred fiber direction and degree of orientation can be determined. A SALS based tissue sorting procedure was used to guide the selection of bovine pericardial specimens to minimize structural variability [45]. Note that the designations preferred fiber (PD) and cross-preferred fiber (XD) were used for the x_1 and x_2 axes, respectively. An extensive biaxial test protocol was then used and the resulting stress-strain data fitted to an exponential strain energy function developed by Choi and Vito [37]. Results indicated that this equation was able to reproduce the mechanical response of chemically treated bovine pericardium over a wide range of biaxial test protocols. Most importantly, the high structural uniformity resulted in both a consistent mechanical response and low variability in the material constants [31].

2.1.6 Limitation of Previous Studies

In order for novel biomaterials to be optimally utilized in BHV designs, robust constitutive models are required for accurate numerical simulations. In the formulation and parameter estimation of any constitutive model, rigorous experimentation involving all multi-axial deformations within the functional range of the tissue is necessary [34]. In previous biaxial mechanical studies, specimen deformation was restricted to extensional strains only, i.e., no shear [45, 89]. This approach cannot be used

in in-depth material analyses or finite element simulations since it cannot predict the anisotropic tissue's response to the presence of shear strains.

2.1.7 Motivation of This Study

We have developed a straightforward technique that produces a combined state of in-plane biaxial extensional and shear strains [38]. However, peak nominal stresses in that study were limited to ~250 kPa and peak shear stresses to ±40 kPa. Novel heart valve biomaterials may be more compliant than traditional aldehyde-based approaches [45], and are thus likely to be subjected to larger in-plane shear strains during valve operation. Clearly, a robust constitutive model for heart valve biomaterials requires a comprehensive experimental data set that spans the estimated normal operational stress range. To allow for accurate simulation of abnormal valve function, such a constitutive model should also be accurate to stress levels two to three fold normal operational stress levels.

The present study was undertaken to produce biaxial mechanical experimental data for heart valve biomaterials subjected to a wide range of normal and shear stresses. This was achieved by modifying our strain-based biaxial testing protocol to a stress-based one using peak stresses of 1 MPa. We utilized glutaraldehyde-treated bovine pericardium (GLBP) as the representative heart valve biomaterial.

2. 2 MATERIALS AND METHODS

2.2.1 Specimen Preparation

The methods used to prepare structurally consistent biaxial specimens from the bovine pericardial sac using SALS have been previously described [38, 45]. Briefly, large sections of fresh bovine pericardium were stored in phosphate buffered saline (pH 7.4) at 4 °C. These sections were split into two groups, one kept in the native state and the other chemically treated with 0.625% glutaraldehyde for a minimum of 72 hours prior to SALS testing and designated as the GLBP group. In order to make the bovine pericardium sheets transparent for SALS measurements, the sections were first processed through a graded series of dehydration in 25%, 50%, 75% and 100% sugar-based hyper-osmotic solution for 1 hour each dehydration step. Due to the biological stabilization effects of the hyper-osmotic dehydration, no time limit was set between dehydration and SALS testing, but this period seldom exceeded one week.

Next, each bovine pericardium section was mounted flat in a thin vertical glass well free floating in the hyper-osmotic solution, and SALS tests performed over the entire section using a 2.54mm rectilinear sampling grid. From the resulting structural data, 25 x 25 mm test specimens exhibiting a high degree of structural uniformity suitable for biaxial testing were selected. Pilot biaxial mechanical studies of specimens before and after a dehydration/rehydration cycle indicated no detectable change in properties (Sacks, unpublished data). As in our previous study [38], the collagen fiber

preferred cross-preferred directions were taken to be the material axes (X_1-X_2 in Figure 2-1a), oriented at θ=45°±1° with respect to the specimen axes (X'_1-X'_2 in Figure 2-1a). A total of five specimens were prepared in the fresh state. A second group of ten GLBP biaxial specimens were prepared as described above and tested only in the chemically treated state.

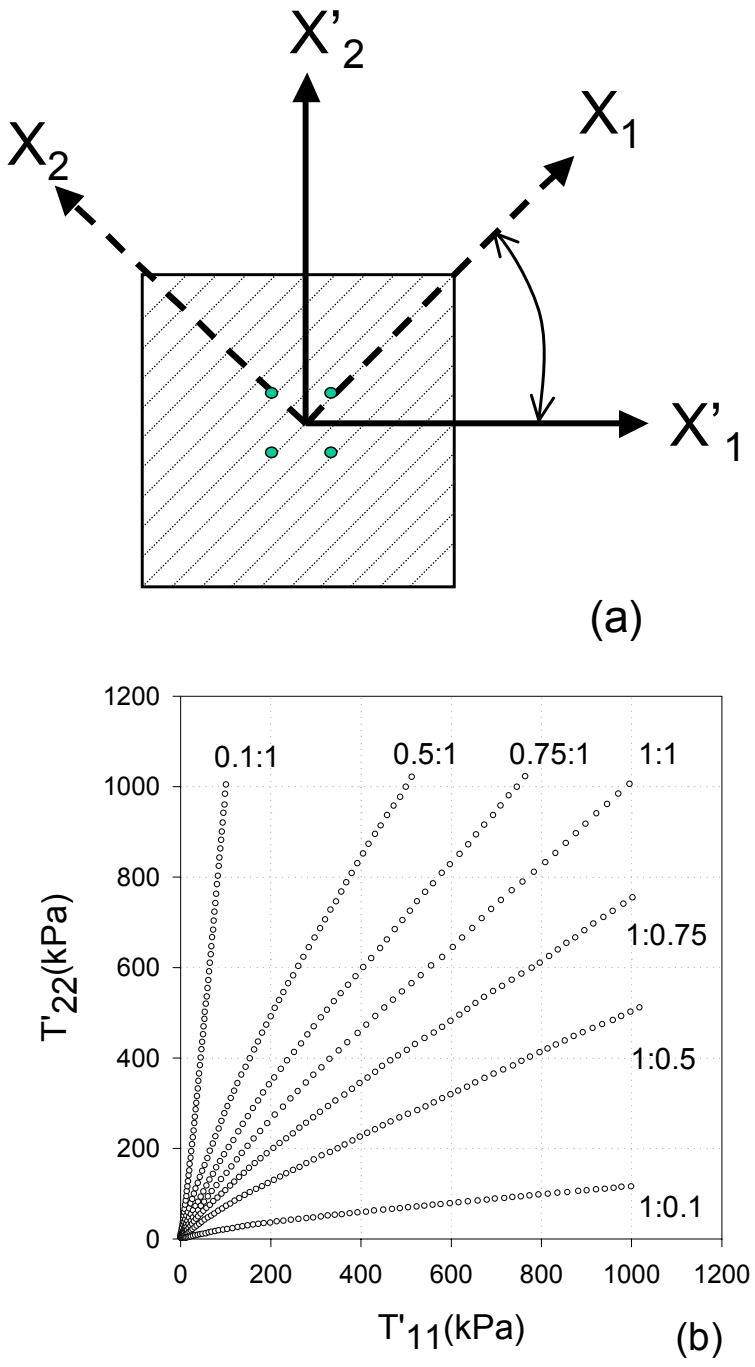

Figure 2-1 (a) A schematic of the biaxial specimen showing the specimen axes (**X'**$_1$-**X'**$_2$ axes) and material axes (i.e. **X**$_1$-**X**$_2$ axes), which were aligned at a 45° angle with respect to the specimen axes; (b) Experimental protocols of stress-control biaxial testing, where the labels indicate the ratios of the normal Lagrangian stress in the specimen axes coordinate system (T'_{11}: T'_{22}).

2.2.2 Biaxial Mechanical Testing

Biaxial mechanical testing methods for testing native and chemically treated pericardium have been previously described [38, 45]. Briefly, testing was performed with the specimen immersed in phosphate buffered normal saline (pH 7.4) at room temperature. As a modification to our previous studies a *stress* controlled test protocol was utilized, wherein the ratio of the normal Lagrangian stress components T'_{11}:T'_{22} was kept constant with $T'_{12}=T'_{21}=0$. To fully capture the response over the functional range a maximum stress level of 1 MPa was used, which is estimated to be four times the nominal stresses of 250 kPa in the BHV [67, 72]. For the first testing phase, an equi-biaxial stress state (i.e. T'_{11}:T'_{22} = 1:1) was used. A total of 15 contiguous cycles were run with a stress rate of 5 MPa/sec. Next, seven successive protocols were performed using ratios T'_{11}:T'_{22} = 1:0.1, 1:0.5, 1:0.75, 1:1, 0.75:1, 0.5:1, and 0.1:1 (Figure 2-1b). This range was chosen for extensive coverage of the in-plane strain state.

2.2.3 Effects of Chemical Treatment

After initial biaxial testing, native specimens were allowed to mechanically re-equilibrate by storing them in a stress-free state at 4 °C for 24 hours. Next, these specimens were treated with glutaraldehyde as described above, then biaxially tested using same protocol. This was done to characterize the effects of chemical fixation on the biaxial mechanical properties, and in particular the high in-plane shear properties.

2.2.4 Constitutive Modeling

Following our previous in-plane shear study [38], we assumed that both native pericardium and GLBP behave as hyperelastic membranes following the concept of pseudo-elasticity [56]. Thus, **S** can be derived from a scalar strain energy function W through:

$$\mathbf{S} = \frac{\partial W}{\partial \mathbf{E}} \tag{2.12}$$

We utilized a function W previously used for GLBP [38]:

$$W = \frac{c}{2}[e^{Q} - 1] \tag{2.13}$$

where $Q = A_{ijkl}E_{ij}E_{kl}$ and **A** and c are constants. In our previous study, we developed a five parameter version of eqn. 2.13 [38]. However, due to the more complex in-plane shear response observed in initial pilot studies, we chose to directly utilize the full seven parameter form. Utilizing symmetry of **E** (i.e. $E_{12}=E_{21}$), Q can be expressed as:

$$Q = A_1E_{11}^2 + A_2E_{22}^2 + 2A_3E_{11}E_{22} + A_4E_{12}^2 + 2A_5E_{12}E_{11} + 2A_6E_{12}E_{22} \tag{2.14}$$

2.2.5 Parameter Estimation

Values for the material constants were determined using SYSTAT (SPSS Inc) with the Marquardt-Levenberg algorithm, with the experimental data from all protocols fitted simultaneously to reduce the effects of multiple collinearities [90]. As the residual errors about the regression curve were generally not Gaussian distributed, a non-

parametric bootstrapping technique was used to estimate the uniqueness of the parameter values. Thirty additional sets of simulated parameters were generated per specimen. In addition, a robust regression procedure was used to down-weight the influence of outliers in experiment data [91]. Finally, parameter constraints based on basic physical requirements of the strain energy function W were used to provide parameter bounds during nonlinear regression (see appendix A).

2.3 RESULTS

2.3.1 Biaxial Mechanical Response

The stress-controlled biaxial protocol covered a wide range of strain-stress space (Figure 2-2). Of particular note are the high in-plane shear stresses generated (peak ~400 kPa) at a peak shear strain of ±0.10 (Figure 2-2b), which are comparable in magnitude to the corresponding normal stress and extensional strain components (Figure 2-2a,c). A feature of the GLBP biaxial response we have not previously observed was that the responses to the T'_{11}: T'_{22}=1:0.1 and 0.1:1 "outer" protocols were different from the "inner" five protocols (T'_{11}: T'_{22} = 1:0.5, 1:0.75, 1:1, 0.75:1, 0.5:1, Figure 2-1b). The outer two protocols exhibited not only large shear response, but also less extensibility for the normal components. This behavior suggested a substantial change in mechanical behavior under the extreme T'_{11}:T'_{22} ratios, where the shear stresses were greater by approximately two-fold or more compared to the other test protocols.

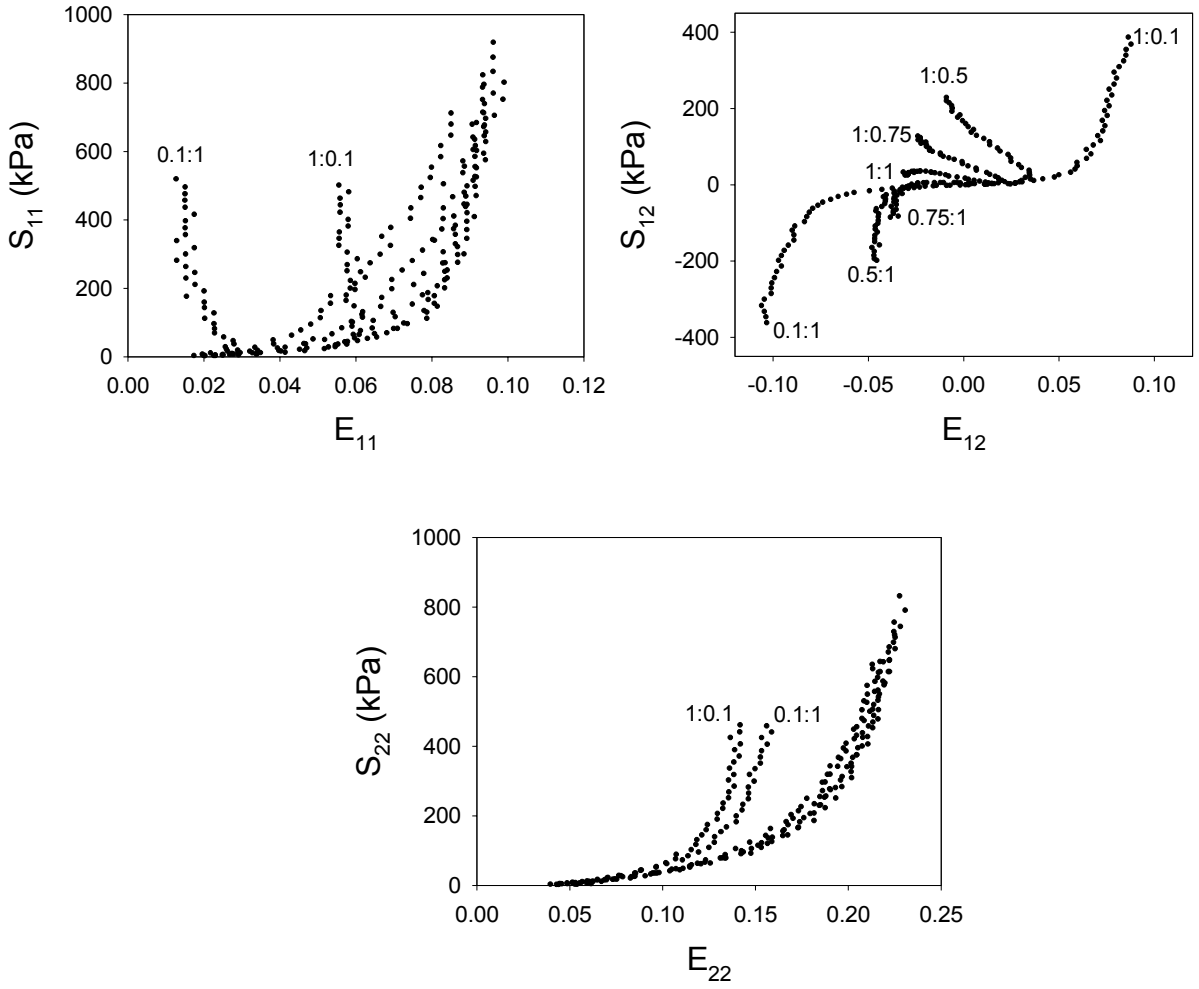

Figure 2-2 A representative biaxial mechanical response for each component, with peak shear stresses of 400 kPa and peak shear strains of ±0.10. One novel feature observed was that the mechanical response to the T'_{11}: T'_{22}=1:0 and 0:1 were quite different from the other protocols. Labels indicate the ratios of the normal Lagrangian stress in the specimen axes coordinate system (T'_{11}: T'_{22}).

2.3.2 Effects of Chemical Treatment

Glutaraldehyde chemical treatment induced a tissue contraction of 9.6±1.3% from the native state in the cross-fiber direction, and 1.8±1.7% in the preferred fiber direction. Generally, chemical fixation was observed to affect the low-stress region

(<200 kPa), whereas the remaining high stress region responses were comparable. This was also true for the in-plane shear component, where the differences between native and chemically treated were small at the higher stress levels (Figure 2-3).

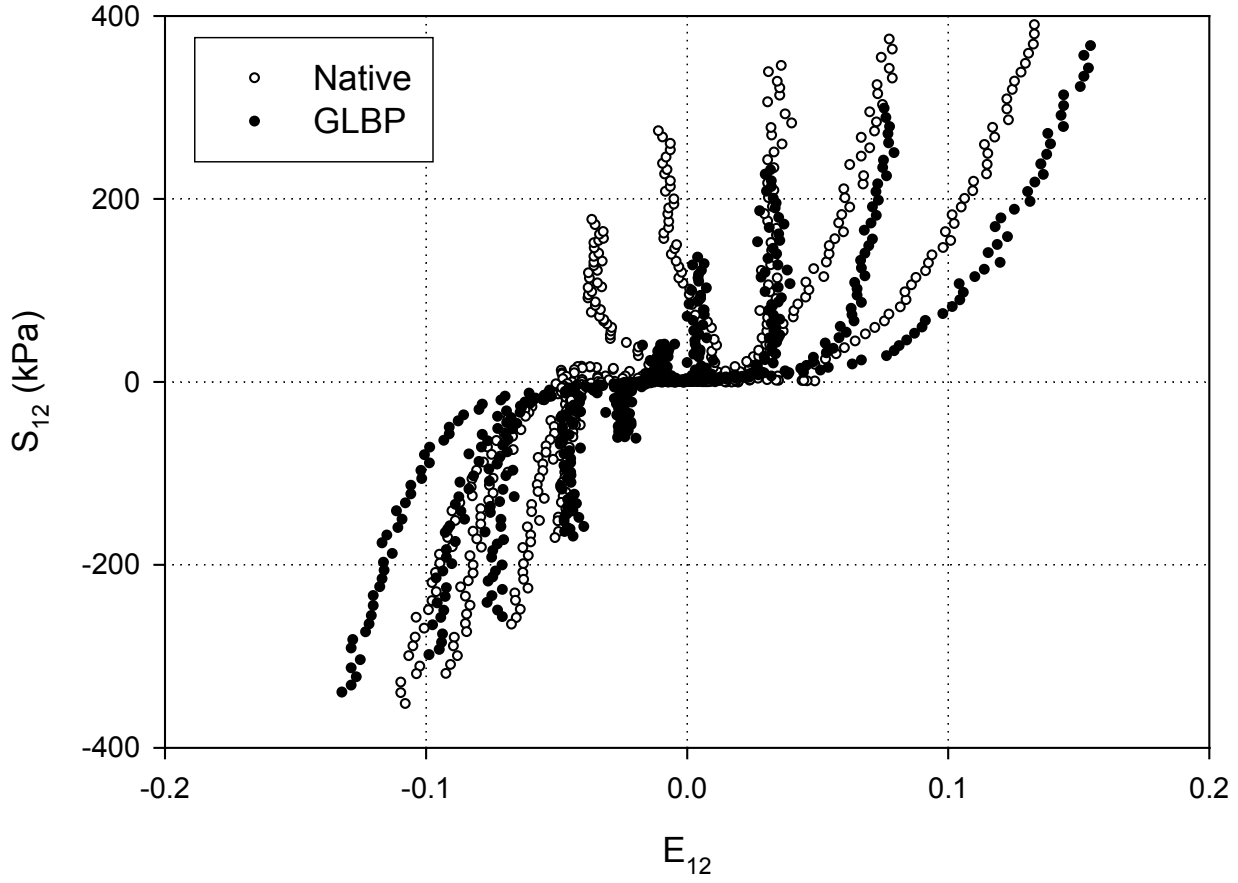

Figure 2-3 Representative biaxial response for the in-plane shear response before and after glutaraldehyde fixation, which affected the low-stress (<250 kPa), whereas the remaining higher stress region were comparable.

2.3.3 Initial Constitutive Modeling Results

Given the substantially more complex tissue response using the stress-controlled protocol, it was not surprising that eqn. 2.14, albeit containing two additional degrees of

freedom from our earlier model [38], was still not sufficiently improved. In particular, eqn. 2.14 had difficulties with the shear response of the 1:0.1 and 0.1:1 protocols.

Based on our current observations (Figure 2-2), we hypothesized that the high shear state occurring in the outer two protocols was a primary factor in our poor fit results. We therefore subdivided the experimental data into two sets: Set I composed of the "inner" five protocols: T'_{11}:T'_{22}=1:0.5, 1:0.75, 1:1, 0.75:1, 0.5:1 protocols and Set II composed of the "outer" two protocols: T'_{11}:T'_{22}= 0.1:1 and 1:0.1. Next, we applied this approach using eqn. 2.14, which was able to describe each individual data set well (Figure 2-4), with Set I r^2= 0.980 and Set II r^2= 0.963. These results suggest that a Fung-type model using eqn. 2.14 was adequate using two separate sets of material constants for the low/moderate and high shear states.

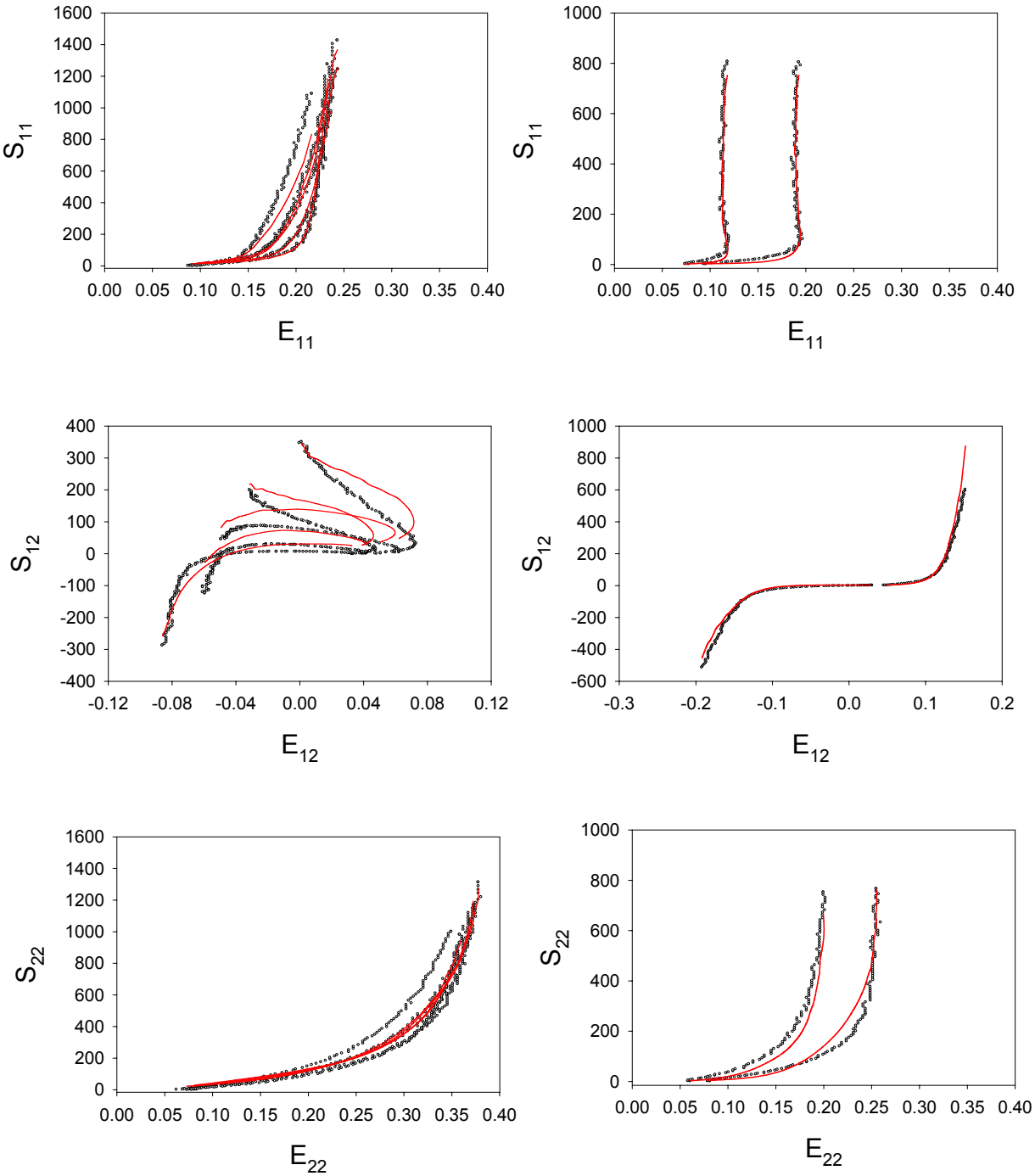

Figure 2-4 Results for the seven parameter Fung model (Q_7) applied to a) the sub-divided data set I demonstrating a very good fit (r^2= 0.980) and data set II demonstrating a very good fit (r^2= 0.963).

2.3.4 Further Modifications to the Standard Fung Model

While able to fit the biaxial data, a single analytical expression was clearly preferable to this two parameter set result.. This was underscored by the limited predictive abilities of the subdivided model. For example, we expected that eqn. 2.14 could predict the Set I response using the Set II parameters reasonably well, since the Set I strain range lie within the Set II strain space. However, the results for this interpolation were poor (Figures. 2-5). Given the complexity of the strain space, improper subdivision could lead to highly erroneous stress predictions.

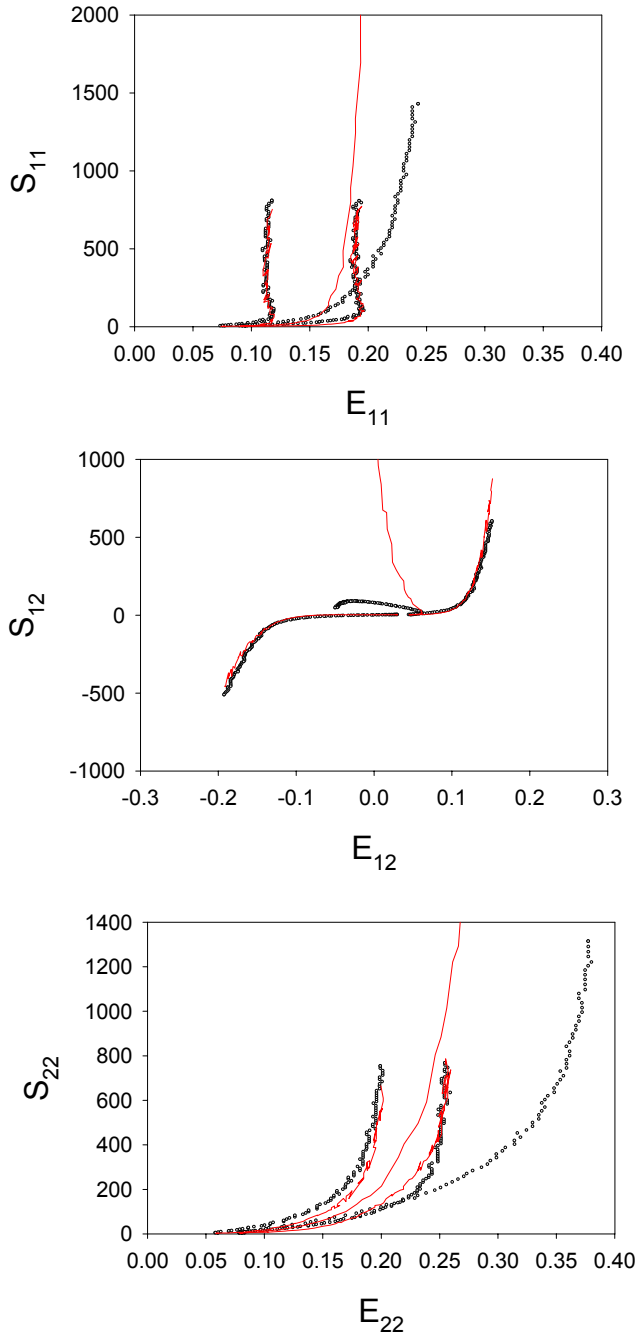

Figure 2-5 Predictive capability results for the equal-biaxial protocol 1:1 by fitting the seven parameter model (Q_7) to the T'_{11}:T'_{22}=1:0.1 and 0.1:1 protocols only. Even though equal-biaxial protocol lies within the stress and strain ranges used for parameter determination, the interpolated result is poor. For illustration purposes the peak values of S_{11}, S_{12} and S_{22}, which were 1.4e+5, 0.4E+5, and 1.2E+5 kPa, respectively, were truncated.

To develop a single model for all protocols, we expanded the eqn. 2.14 as follows. To minimize the number of parameters, we choose to modify Q only through the addition of terms greater than quadratic order $E_{ij}E_{kl}$. Although cubic order terms of the general form $E_{ij}E_{kl}^2$ could have been added, from our experience quartic functions of the form $E_{ij}^2E_{kl}^2$ would be able to capture the mechanical responses with fewer parameters. Thus, the final generalized form for the expanded Q in eqn. 2.14 (incorporating symmetry of **E**) is given by

$$\begin{aligned} Q = {} & A_1E_{11}^2 + A_2E_{22}^2 + 2A_3E_{11}E_{22} + A_4E_{12}^2 + 2A_5E_{12}E_{11} + 2A_6E_{12}E_{22} \\ & + B_1E_{11}^4 + B_2E_{22}^4 + B_3E_{11}^2E_{22}^2 + B_4E_{12}^4 + B_5E_{12}^2E_{11}^2 + B_6E_{12}^2E_{22}^2 \end{aligned} \tag{2.15}$$

where A_i and B_i are the material constants.

As in any nonlinear constitutive model, the number of term additions needs to be minimized to avoid numerical instability issues in computational implementations. To provide a rationale for adding the additional quartic terms in eqn. 2.15, we developed the following interpolation method to estimate the strain energy response functions with respect to each strain component directly from our stress-controlled biaxial test data. Each **S** component from the loading data was expressed as a function of two strain components, while the third component was kept at a constant value. This allowed us to simulate the pseudo-elastic loading response of each **S** component against various combinations of **E** and guide the choice of the functional form of **Q**. Interpolations were restricted over the strain space of the actual experimental data.

Details of the approach are presented in Appendix B. All together, nine response functions were generated; three for each stress component.

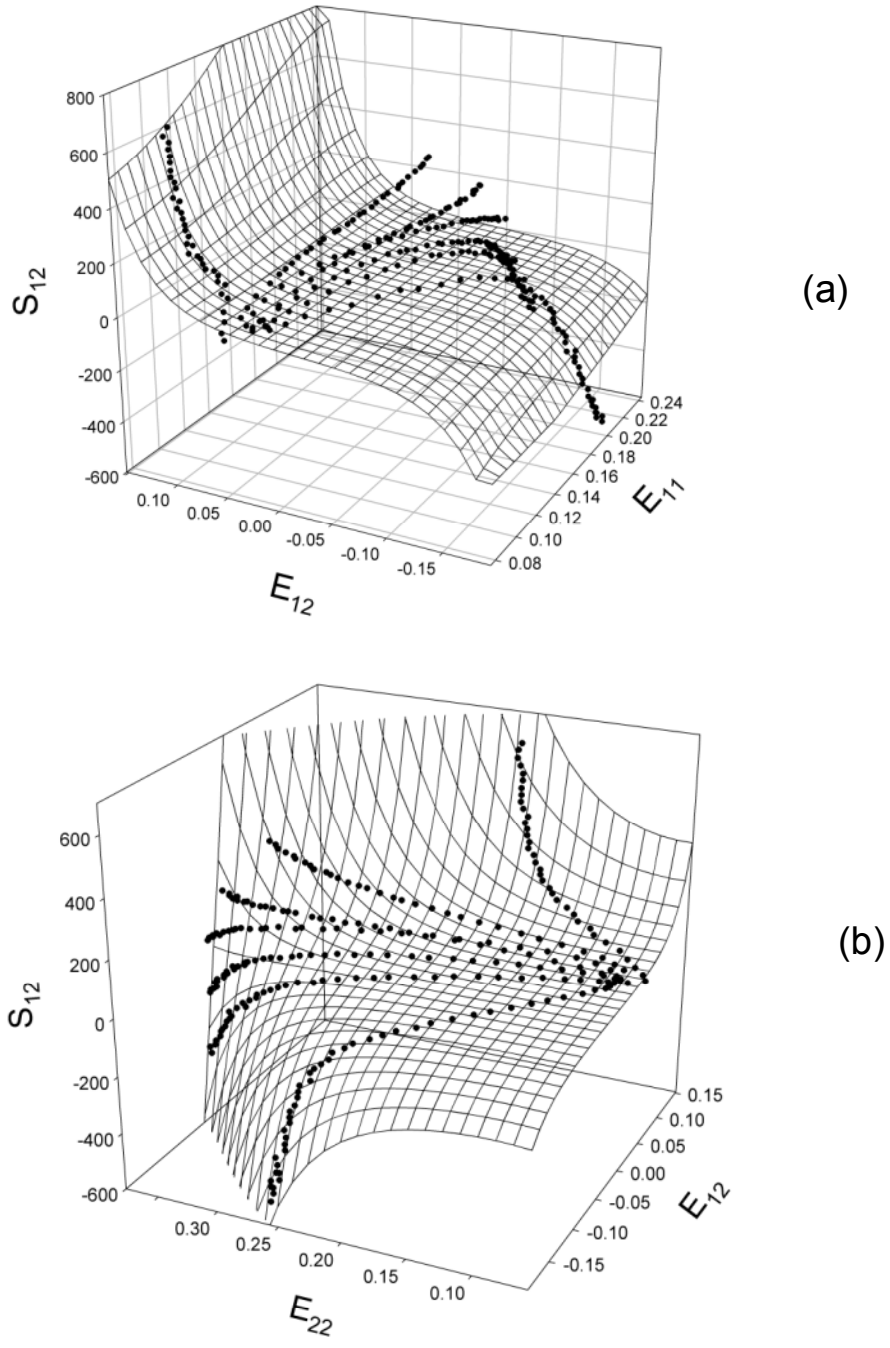

Figure 2-6 Representative response functions for (a) S_{12} vs. E_{11} and E_{12}, with E_{22}=0.2, indicating that S_{12} had a relatively weak dependence on E_{11}. In contrast, the S_{12} vs. E_{12} and E_{22} with E_{11}=0.18 responses shown in (b) indicated that S_{12} had a strong dependence on both E_{12} and E_{22}.

Representative response functions are shown in Figure 2-6a for S_{12}, where E_{11} and E_{12} were varied and E_{22} was held at 0.2. In this case, the response function indicated that S_{12} had a relatively weak dependence on E_{11}. This indicated that additional terms did not require E_{11}, so that B_1, B_3 and B_5 =0. Also shown in Figure 2-6b for S_{12} where E_{11} and E_{22} were varied and E_{11} was held at 0.18. The response function indicated that S_{12} had a strong dependence on E_{12} and E_{22}. Based on the more gradual increase in stress of the stress-strain curves, we determined that inclusion of quartic powers for individual strain component (i.e. E_{ij}^4) was unnecessary, thus B_2 = B_4 =0, leaving only the term $B_6E_{12}^2E_{22}^2$. Replacing B_6 with B, we derived the following eight parameter form for the expanded Fung-type model:

$$Q = A_1E_{11}^2 + A_2E_{22}^2 + 2A_3E_{11}E_{22} + A_4E_{12}^2 + 2A_5E_{12}E_{11} + 2A_6E_{12}E_{22} + BE_{12}^2E_{22}^2 \qquad (2.16)$$

Eqn. 2.16 was found to describe the biaxial mechanical response for all seven protocols well, with a mean r^2=0.94 (Table 2-1). Bootstrapping results indicated that the parameters were highly clustered for the simulated datasets, giving further confidence in the uniqueness of the model parameter values and model robustness. The predictive capability of eqn. 2.16 was evaluated by fitting the Set I data only (Table 2-2) and then extrapolating Set II (Figure 2-7a). As expected, eqn. 2.16 demonstrated a better fit to Set I alone (Figure 2-7a) then when Sets I and II were fit simultaneously (Figure 2-7b), especially the in-plane shear response. Interestingly, this approach also demonstrated good predictive capabilities (Figure 2-7a). Overall, eqn. 2.16 was able to faithfully

reproduce the complete high in-plane response, and predict the tissue response outside the range used for parameter determination.

Table 2-1 The parameters for eqn. 2.16 fit to all biaxial protocols (sets I and II).

Specimen	c (kPa)	A_1	A_2	A_3	A_4	A_5	A_6	B	r^2
sb111	5.52	60.00	46.99	41.12	85.01	3.58	59.37	3961.66	0.95
sb131	4.16	48.00	43.00	42.66	28.58	0.10	0.62	8146.80	0.93
sb51	3.46	62.11	30.85	-20.59	29.40	4.70	9.42	442.40	0.94
sb52	9.84	13.62	9.90	5.84	9.25	0.13	0.04	241.00	0.95
sb53	3.02	26.10	21.16	1.12	34.11	1.12	1.52	654.64	0.92
sb61	4.10	41.42	33.51	28.22	66.81	1.50	3.16	4803.09	0.93
sb62	3.94	66.07	33.00	20.65	78.62	24.96	15.44	2424.58	0.95
sb71	4.51	28.00	18.41	10.88	37.77	8.43	26.09	527.83	0.95
sb31	8.73	25.00	17.80	15.51	14.75	0.20	8.76	1778.22	0.94
sb132	2.25	70.49	27.00	17.20	52.86	21.95	20.88	1609.34	0.94
Mean	**4.95**	**44.08**	**28.16**	**16.26**	**43.72**	**6.67**	**14.53**	**2458.96**	**0.94**
Std. Err	**0.78**	**6.37**	**3.68**	**5.97**	**8.25**	**2.92**	**5.72**	**797.65**	**0.003**

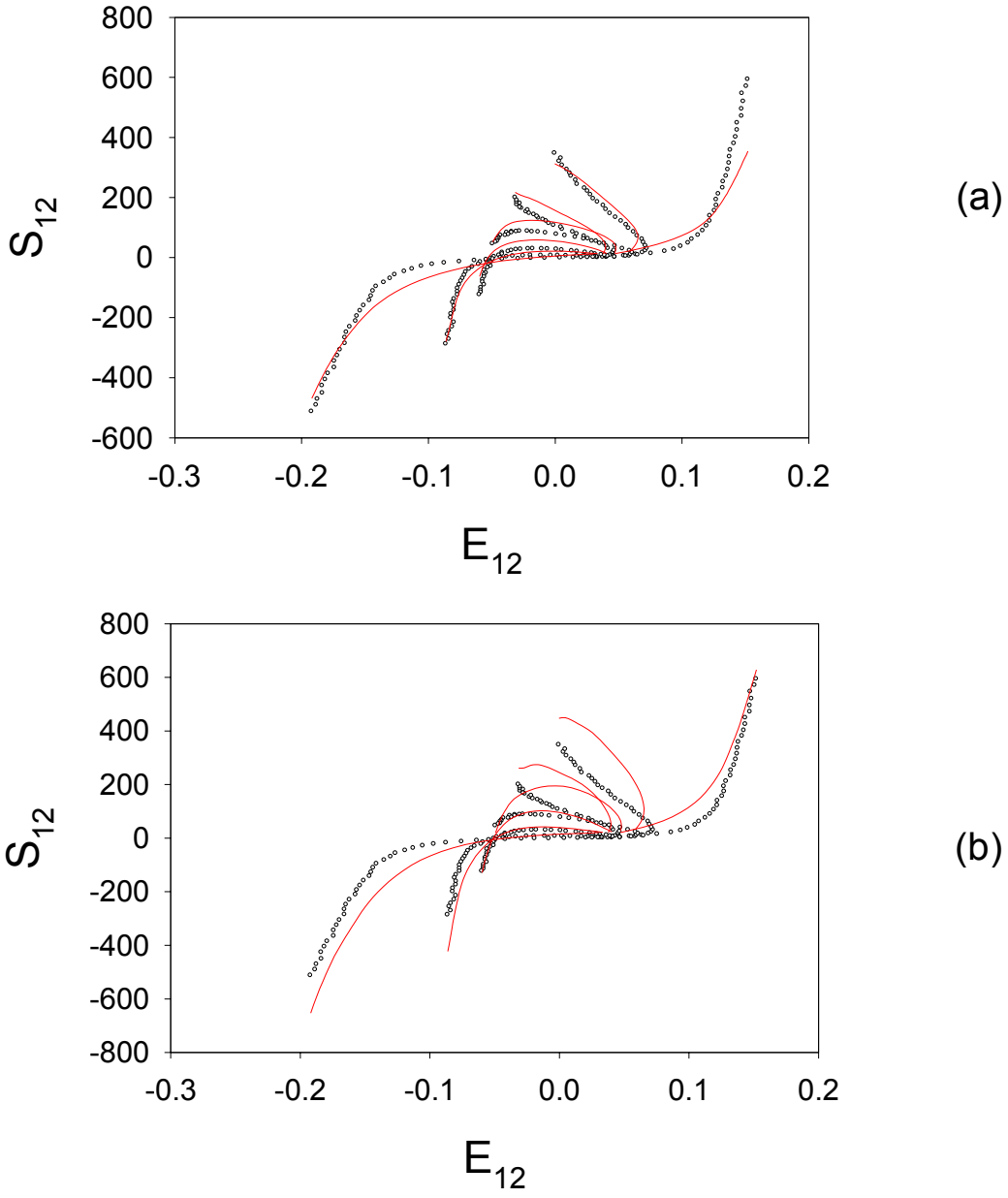

Figure 2-7 In-plane shear fit results for the eight parameter model (eqn. 2.16) fit to (a) data set I only and predicting the set II response, and (b) all protocols simultaneously. As expected, the fit to set I only demonstrated a better fit to both the inner test protocols (set I), but also demonstrated reasonable predictive capabilities.

Table 2-2 The parameters for eqn. 2.16 for Set I biaxial protocols only.

Specimen	c (kPa)	A_1	A_2	A_3	A_4	A_5	A_6	B	r^2
sb111	6.01	56.00	43.36	33.87	74.93	1.00	38.67	1826.93	0.96
sb131	8.41	96.69	47.02	6.21	34.94	2.07	1.00	4154.36	0.95
sb51	4.36	51.56	26.90	-15.53	30.38	1.98	6.74	181.94	0.97
sb52	5.34	29.42	17.39	-2.66	7.96	2.00	0.40	124.00	0.94
sb53	5.95	13.04	11.91	8.61	10.00	1.00	2.00	284.39	0.96
sb61	5.81	63.59	39.37	7.78	30.41	2.00	1.00	4106.12	0.96
sb62	4.89	41.00	29.60	25.08	73.75	2.12	17.65	1169.28	0.98
sb71	3.41	28.91	20.00	10.09	53.36	9.24	19.61	194.13	0.98
sb31	7.16	28.93	19.00	14.65	1.00	2.00	5.29	1460.87	0.98
sb132	2.43	50.44	23.80	23.72	152.08	41.15	8.78	0.71	0.97
Mean	**5.38**	**45.96**	**27.84**	**11.18**	**46.88**	**6.46**	**10.11**	**1350.27**	**0.97**
Std. Err	**0.55**	**7.45**	**3.75**	**4.50**	**14.25**	**3.93**	**3.84**	**504.34**	**0.004**

2.4 DISCUSSION

2.4.1 Strain Vs. Stress Control

In our original technique to apply in-plane shear in a biaxial test [38], control of the normal Green's strain components alone was used while the shear strain component E_{12} was allowed to vary freely. While this approach allowed for the application of in-plane shear, the range of stresses and strains was limited. This limitation restricts the ability to accurately simulate heart valve stresses, since they can exhibit strains outside those used in Sacks (1999)[38] during normal valve function. Use of Lagrangian stress-control

biaxial tests allowed for a wider range of stress and strain, especially in generating a negative strain state that is difficult to reproduce in a strain-controlled test. Also, physiologically native and bioprosthetic heart valve tissues are loaded by transvalvular pressure, which is more accurately simulated in a stress-control test.

2.4.2 Effects of Chemical Treatment

Overall, it was observed that chemical fixation induced directionally dependent tissue shrinkage, with greater tissue contraction found along the cross-preferred fiber direction. This result suggested that cross-linking compacted the collagen fiber network, whereas the fiber lengths were not appreciably reduced. More interestingly, the presence of exogenous cross-links resulting from glutaraldehyde treatment did not appreciably affect the biaxial mechanical response at high stress levels (>250 kPa), including the shear (Figure 2-3). Thus, chemical fixation appears to affect the planar biaxial mechanical stress-strain response at stress values below ~250 kPa.

While definitive evidence is still outstanding, our biaxial mechanical data suggest that chemical fixation primarily produces strong inter-fiber bonding, yet does not affect intrinsic collagen fiber stiffness at high stresses. This is supported by tensile failure properties for native and chemically treated bovine pericardium, which demonstrated little or no differences in ultimate failure strength between the chemically treated and native groups [92]. If chemical fixation only affected inter-fiber bonding, this would suggest that at stresses >250 kPa most of the collagen fibers are uncrimped and bearing stress. This is also in agreement with our hypothesis that the unusual high in-

plane shear for GLBP is due to large rotations of the collagen fibers under high shear strain, as opposed to the effects of chemical fixation. Chemical fixation is utilized extensively in biologically-derived biomaterials, and future studies are required to further explore this important area.

2.4.3 Use of Response Functions to Guide Functional Forms

The response function method developed in the current study is derived from approaches developed for isotropic rubber-like materials [82] and transversely-isotropic and orthotropic soft biological tissues [42, 93]. For soft tissues, the basic concept is to probe the pseudo-elastic response in a controlled manner to deduce the functional form of the strain energy function. Ideally, experimental protocols are designed in accordance with an assumed form of the strain energy function, so that a single strain component can be varied independent of the other two components.

Experimentally, these conditions are sometimes difficult to realize. In addition, one cannot take full advantage of stress-controlled tests without a complementary strain energy density function, which would have the additional restriction to be of an invertible form. The approach presented herein avoids some of these complications by allowing for interpolation of the pseudo-elastic response without a-priori assumptions of the functional form of the strain-energy function. In our experience with the biaxial mechanical properties of biological tissues [34], we have found that stress-controlled tests were easier to both generate data over the functional range of the tissue and to perform. Thus, the current approach, although theoretically equivalent to the previous

approaches cited above, allows for more straightforward implementation for soft tissue constitutive modeling.

2.4.4 Additional Constitutive Modeling Considerations

In the current study, several novel modeling problems were encountered, mainly due the presence of high shear stresses. First, we were not able to able to fit our current dataset to the general Fung-type model used previously [38], even though we utilized identical biomaterials. This result underscores the need to obtain mechanical testing data over the entire physiological range (and operational ranges in the case of bioprosthetic biomaterials). Our initial solution to sub-divide the strain region is not uncommon in solid mechanics, and is analogous to bi-modular material approaches [94]. However, for completeness, a single analytical expression is always preferable. More critically, the inability to accurately predict responses substantially outside the data range used for parameter determination (Figure 2-5) makes this approach clearly untenable for soft tissue analyses.

Even after a final model is obtained, the fitted parameter set must also produce physically reasonable solutions in addition to an accurate fit to the data. Otherwise, it is possible that under certain conditions the predicted response could be physically unreasonable. This problem may be especially acute in cases of nonlinear constitutive laws under heterogeneous multidimensional deformations where such errors may be difficult to detect[95, 96].

In the current work, we applied several parameter restrictions based on physically consistency to simple deformation states (Appendix A). However, these should not be construed as exhaustive. Many constitutive model restrictions for physical plausibility have been previously proposed, including the Baker-Ericksen inequalities, generalized Coleman-Noll condition [97], and polyconvexity [98]. In spite of its apparent fundamental importance, only limited attention has been given to the issue of plausibility in constitutive equations for biological and biologically-derived materials [42, 95, 96]. Generalized applicability to soft anisotropic biological materials is largely unexplored, and more theoretical work in this area is clearly warranted.

2.4.5 3D Stress Space

The current approach of describing tissue response at 45-degree material axes is an improvement to the traditional way of describing tissue response at specimen axes. However, by examining the entire possible stress space, it can be seen that the approach still covers limited stress space. We will illustrate the reason of why we make such a statement as below:

The components of Lagrangian stress tensor **T** in material axes can be obtained by transforming the components of Lagrangian stress tensor **T'** in specimen axes to the material axes using the $\mathbf{T}=\mathbf{Q}\mathbf{T}'\mathbf{Q}^{\mathsf{T}}$, where $\mathbf{Q}=\begin{bmatrix} \cos\theta & \sin\theta \\ -\sin\theta & \cos\theta \end{bmatrix}$ [84]. It can be explicitly expressed as:

$$T_{11}=T'_{11}\cos^2\theta+T'_{22}\sin^2\theta \tag{2.17}$$

$$T_{22}=T'_{11}\sin^2\theta+T'_{22}\cos^2\theta \tag{2.18}$$

$$T_{12}=(T'_{22}-T'_{11})\sin\theta\cos\theta \tag{2.19}$$

In our stress-control biaxial tests, we can see that $T'_{11}\geq 0$ and $T'_{22}\geq 0$ (Figure 2-1). It leads to that $T_{11}\geq 0$ and $T_{22}\geq 0$ by eqn. 2.17 and eqn. 2.18. We will prove $|T_{12}|\leq\sqrt{T_{11}T_{22}}$ is also satisfied.

From the difference of eqn. 2.17 and eqn. 2.18, we have

$$T_{11}-T_{22}=T'_{11}(\cos^2\theta-\sin^2\theta)+T'_{22}(\sin^2\theta-\cos^2\theta) \tag{2.20}$$

similarly from the sum of eqn. 2.17 and eqn. 2.18, we have

$$T_{11}+T_{22}=T'_{11}+T'_{22} \tag{2.21}$$

Eqns 2.20 and 2.19 can be re-expressed as

$$T_{11}-T_{22}=(T'_{11}-T'_{22})\cos 2\theta \tag{2.22}$$

$$T_{12}=(T'_{22}-T'_{11})\frac{\sin 2\theta}{2} \tag{2.23}$$

Square eqn. 2.22 and eqn. 2.23, and add them together, we find that

$$(T_{11}-T_{22})^2+4T_{12}^2=(T'_{11}-T'_{22})^2 \tag{2.24}$$

and re-express it as

$$(T_{11}+T_{22})^2-4T_{11}T_{22}+4T_{12}^2=(T'_{11}+T'_{11})^2-4T'_{11}T'_{22} \tag{2.25}$$

Due to eqn. 2.21, it is reduced to

$$-4T_{11}T_{22}+4T_{12}^2=-4T_{11}^{'}T_{22}^{'} \tag{2.26}$$

Because $-T_{11}^{'}T_{22}^{'} \le 0$, we have $-4T_{11}T_{22}+4T_{12}^2 \le 0$, hence, $|T_{12}| \le \sqrt{T_{11}T_{22}}$. Therefore the inequalities are:

$$T_{11} \ge 0,\ T_{22} \ge 0 \text{ and } |T_{12}| \le \sqrt{T_{11}T_{22}} \tag{2.27}$$

Eqn 2.27 is the bounds restricting the possible stress domain that the stresses could fall into (Figure 2-8). However, due to our material axes are at 45-degree angle, from eqn. 2.17 and eqn. 2.18, it can be easily deduced that T_{11} is always equal to T_{22}.‡ Consequently, our stress space is limited by

$$T_{11}=T_{22} \tag{2.28}$$

within the domain restricted by eqn 2.27 (Figure 2-8).

‡ Note here the stresses are the Lagrangian stresses. For Cauchy stresses, t_{11} may not be equal to t_{22} because the deformation gradient **F** is taken into the calculation of the Cauchy stresses.

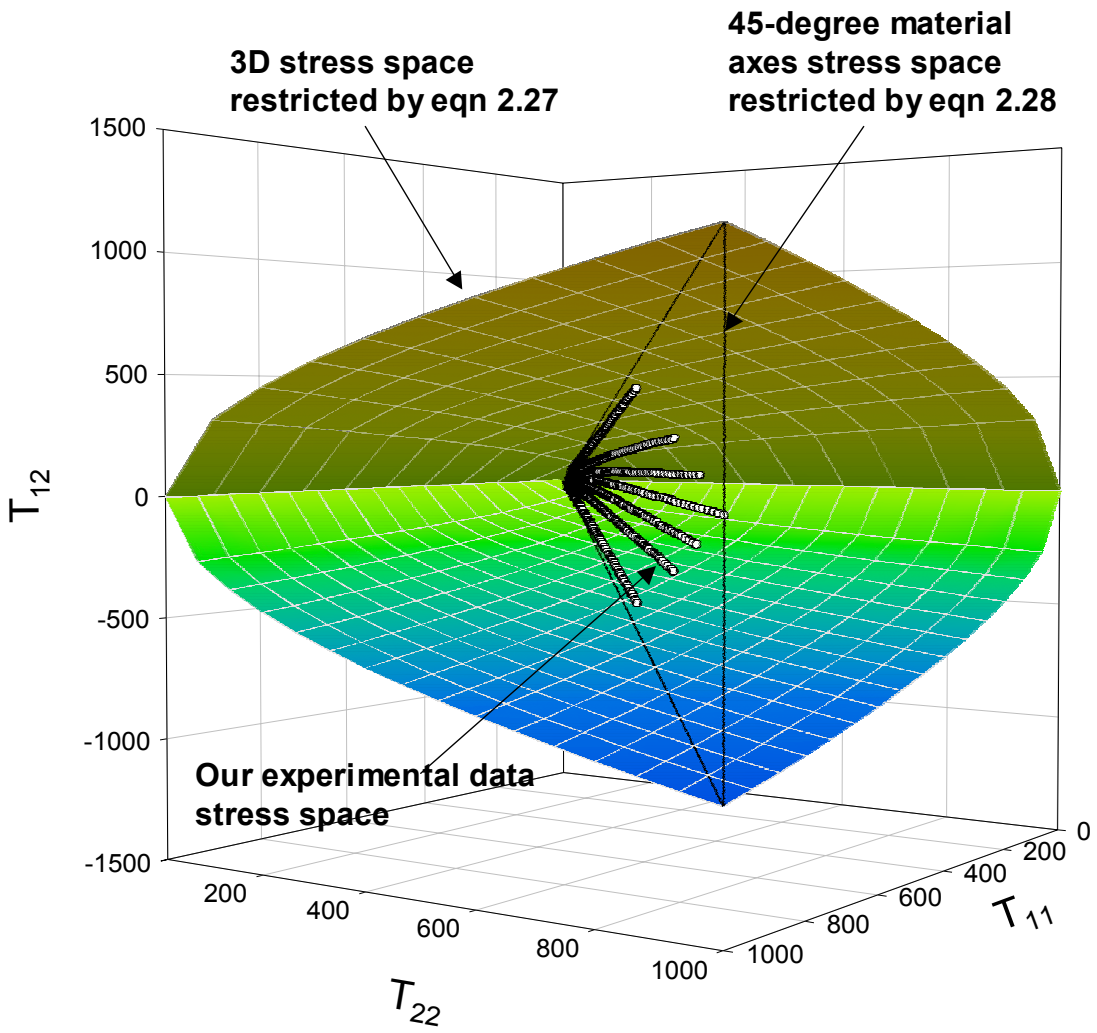

Figure 2-8 The 3D stress space. The color surface embraces the 3D stress space restricted by eqn 2.27. The 45-degree material axes stress space is a plane intersecting the color surface by eqn 2.28. Our experimental data are shown in white dots within the domain restricted by eqn 2.28.

2.5 SUMMARY

A comprehensive experimental biaxial mechanical dataset that included a high in-plane shear state for heart valve biomaterials was presented. We found that our original five parameter Fung model developed for GLBP was unable to fit the new

extended dataset. To develop the appropriate model, we developed an interpolation technique for the pseudo-elastic response to guide the final model form. An eight parameter model utilizing a single additional quartic term was found to fit the complete dataset well, with the model parameters satisfying physical plausibility.

3.0 FINITE ELEMENT IMPLEMENTATION OF A FUNG ELASTIC MODEL FOR PLANAR ANISOTROPIC BIOLOGICAL MATERIALS

From this chapter and onwards, we will study a fascinating area of biomechanics, the *finite element* simulations of soft tissue behaviors. We will in this chapter focus on the finite element implementation of material models, in particularly the Fung pseudo-elastic model, whereas the applications of simulating tissue and bioprosthesis behaviors will be presented in Chapters 4 and 5. In this chapter, we will go through finite element issues particular to soft tissue, i.e., the method of nonlinear finite element solution (section 3.1.1) and the procedure of defining a user-defined material model in a finite element code (section 3.1.2). An in depth study on the Fung model implementation will be given in sections 3.2.1 to 3.3.2 with emphasis on the method of forming the model with numerical stability. Also numerical accuracy is rigorously validated against experimental data. Throughout the study, ABAQUS (Pawtucket, RI) is used as the finite element implementation platform due to its wide availability and thus, the methods developed here can be adapted easily for other applications.

3.1 INTRODUCTION

Given the complex geometries and material properties inherent to the cardiovascular system, sophisticated numerical methods often become essential for accurate stress-strain analysis and prosthesis design. One of the most powerful numerical tools available today is the *finite element method*, which quickly proved indispensable in biomechanics [59, 99-101].

3.1.1 Nonlinear Finite Element Solution Procedure

As a brief introduction of the basic concepts, in the finite element method one seeks to divide the domain of interest into a finite number of non-overlapping but contiguous sub domains, called elements and thus, a boundary value problem or initial value problem is reduced to a system of equations of the form:

$$[\mathbf{K}]\{\mathbf{u}\}=\{\mathbf{F}\} \tag{3.1}$$

where **[K]** is the (structural) stiffness matrix, **{u}** the vector of unknowns (such as displacements) and **{F}** the boundary loads. When **[K]** depends on **{u}**, the system of equations is *nonlinear* and thereby requires special consideration for solution (e.g. Newton-Raphson method).

Finite element simulations of soft tissues are in general nonlinear and a finite element model can involve from a few to many variables. In terms of these variables the equilibrium equations obtained by discretizing the virtual work equation can be written symbolically as

$$F^N(\mu^M) = 0 \tag{3.2}$$

where F^N is the force component conjugate to the N^{th} variable in the problem and μ^M is the value of the M^{th} variable. The basic problem is to solve eqn. 3.2 for the μ^M throughout the history of interest.

Many of the problems are time or history-dependent, so the solution must be developed by a series of "small" increments. Two issues arise: how the discrete equilibrium statement eqn. 3.2 is to be solved at each increment, and how the increment size is chosen. Generally Newton's method is used as a numerical technique for solving the nonlinear equilibrium equations. The motivation for this choice is primarily the quadratic convergence rate obtained by using Newton's method compared to the convergence rates exhibited by alternate methods (usually modified Newton or quasi-Newton methods) for the nonlinear problems. The basic formalism of Newton's method is as follows [102]. Assume that, after iteration i, an approximation μ_i^M, to the solution has been obtained. Let c_{i+1}^M be the difference between this solution and the exact solution to the discrete equilibrium equation eqn. 3.2. This means that

$$F^N(\mu_i^M + c_{i+1}^M) = 0 \tag{3.3}$$

Expanding the left-hand side of this equation in a Taylor series about the approximate solution μ_i^M then gives

$$F^N(\mu_i^M) + \frac{\partial F^N}{\partial \mu^P}(\mu_i^M)c_{i+1}^P + \frac{\partial^2 F^N}{\partial \mu^P \partial \mu^Q}(\mu_i^M)c_{i+1}^P c_{i+1}^Q + \ldots = 0 \tag{3.4}$$

If μ_i^M is a close approximation to the solution, the magnitude of each c_{i+1}^M will be small, and so all but the first two terms above can be neglected giving a linear system of equations:

$$\frac{\partial F^N}{\partial \mu^P}(\mu_i^M)c_{i+1}^P = -F^N(\mu_i^M) \tag{3.5}$$

The next approximation to the solution is then

$$\mu_{i+1}^M = \mu_i^M + c_{i+1}^M \tag{3.6}$$

and the iteration continues.

Convergence of Newton's method is best measured by ensuring that all entries in F_i^N and all entries in c_{i+1}^M are sufficiently small. Both these criteria are checked by default in a finite element code, for example, ABAQUS.

Even though many finite element codes are commercially available, frequently they are misused in biomechanics, and one is cautioned to understand, or at least appreciate, the underlying mechanics prior to implementation. Therefore, most significant contributions continue to be realized via custom codes [101].

3.1.2 Finite Element Implementation of a User-defined Strain Energy Function

To incorporate a user-defined material mode into a commercial available code, one generally needs to follow the procedure in Figure 3-1. ABAQUS will be used as a platform for numerical implementation, user-defined constitutive laws will be incorporated into ABAQUS through its user subroutine UMAT.

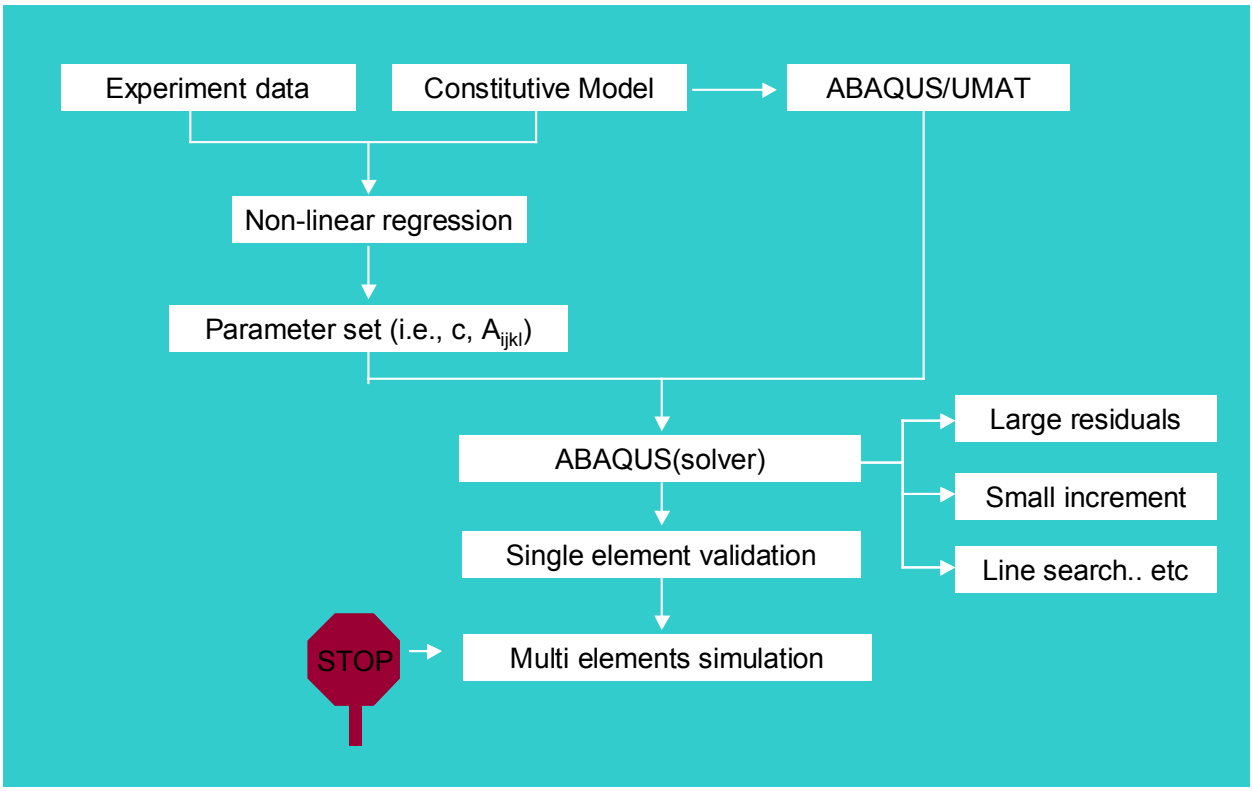

Figure 3-1 A flow chart for finite element implementation of a user-defined material model

- Fitting the experimental data to the constitutive model through a nonlinear regression software package, such as SYSTAT10 or SigmaStat (SPSS Inc), to obtain the parameter estimates for the constitutive model.
- Code the constitutive model into ABAQUS/UMAT by Fortran software.
- Conduct a single element test to test the correctness of UMAT coding. That is to build a simple single element ABAQUS input file, calling the parameters and the UMAT (the constitutive model), with a simple loading condition. Compare the ABAQUS output with the prediction from the constitutive model. If it matches, then it indicates that the UMAT programming is correct. If it does not match then examine the UMAT coding.

- With correct UMAT coding, one can continue to use the material model into his application, i.e., complex multi-element simulation.
- If multi-element simulation does not converge, one can:
  - Examine the ABAQUS solver, which is based on Newton's methods for nonlinear solution, to find possible, user specific causes of non-convergence, and modify the convergence criteria. The corresponding techniques provided by ABAQUS include: allow large residuals; reduce increment step, and Line search, RIKS methods.
  - Reforming the model by either using another form of constitutive model, or controlling parameters of the model.

3.1.3 Previous Studies, Limitations and Purpose of This Study

Various nonlinear strain energy functions have been developed for soft tissues, including isotropic [57, 58], transversely isotropic [41, 42, 59, 60], anisotropic models [39, 56, 61-63, 103, 104], and structural models [8, 96, 105]. Among all these constitutive models, the exponential model proposed by Fung [56] is perhaps the most widely used.

Although these strain energy functions have been in the literature for several years, finite element implementation has been rather limited. Lack of finite element implementations of soft tissue constitutive models are a result of a lack of appropriate experimental data (for both formulating constitutive models and validation of numerical simulations), and computational difficulties in incorporating these models into available finite element codes. In particular, problems with solution convergence

can result in a numerically unstable model that may lead to either inaccurate results or failure to converge.

Holzapfel *et al*. [100] presented a theoretical framework for biological membranes and finite element implementation of a four parameter unconstrained Fung model. The simulation was conducted with single element and shear response was ignored. Later Holzapfel *et al*.[106] addressed imposing physical constrains in constructing an experimentally-driven hyperelastic model for arteries. Similar physical plausibility considerations for soft tissue models had also been addressed by Lanir *et al*. [95, 96] and Humphrey [107]. However, their importance related to computational requirements has largely been unexplored.

In the present study, we developed a generalized approach for finite element implementation of a nonlinear anisotropic Fung pseudo-elastic constitutive model that incorporated the effects of in-plane shear. Experimental data was obtained from a previous study [39] of biaxial mechanical evaluation of pericardium. Moreover, we present restrictions of the model parameters necessary to achieve numerical solution convergence. Finite element results were validated with both theoretical solutions and experimental data.

3.2 METHODS

3.2.1 Constitutive Models

It is assumed that biological tissues behave as hyperelastic materials following the concept of pesudoelasticity [56]. Thus **S** can be derived from a two-dimensional strain energy function W through:

$$\mathbf{S} = \frac{\partial W}{\partial \mathbf{E}} \tag{3.7}$$

We utilize a Fung elastic model with full expansion of quadric terms of Q and with the ability to characterize in-plane shear response [38]:

$$W = \frac{c}{2}\left[e^{Q} - 1\right]$$

$$Q = A_1E_{11}^2 + A_2E_{22}^2 + 2A_3E_{11}E_{22} + A_4E_{12}^2 + 2A_5E_{12}E_{11} + 2A_6E_{12}E_{22} \tag{3.8}$$

where c and A_i are material constants.

Note that we chose eqn. 3.8 instead of eqn. 2.16 for our simulations based on the following considerations: For finite element simulation, if using eqn. 2.16, for each finite element increment, the deformation gradient **F'** from global coordinate system needs to be transformed first to local material axes coordinate system as **F** and stress tensor **S** is calculated by eqn. 2.16, then the stress **S** needs to be transformed back to the global coordinate system as **S'** for consequently equilibrium calculations. This process increases the numerical complexity. In finite element simulations, we could use material

models described either on material axes or specimen axes. For numerical convenience, in this study we use eqn. 3.8 to describe experimental data obtained on the specimen axes (X_1'-X_2' axes of Figure 2-1a). Thus we do not need to rotate the stress-strain tensor to material axes. Note all finite element formulations in this dissertation are based on specimen axes description.

To evaluate the effects of mechanical anisotropy, we also implemented the following Ogden constitutive model for elastomeric materials [108]. The Ogden strain energy function W can be expressed as:

$$W = \sum_{i=1}^{N} \frac{2\mu_i}{a_i^2}(\hat{\lambda}_1^{a_i} + \hat{\lambda}_2^{a_i} + \hat{\lambda}_3^{a_i} - 3) \tag{3.9}$$

where μ_i and a_i are material constants and $\hat{\lambda}_i$ are the principle stretches. For N=3 the Lagrangian stress components are T_B for an equibiaxial stress experiment can be expressed as

$$T_B = \sum_{i=1}^{3} \frac{2\mu_i}{a_i^2}(\hat{\lambda}_B^{a_i-1} - \hat{\lambda}_B^{-2a_i-1}) \tag{3.10}$$

where $\hat{\lambda}_B = \hat{\lambda}_1 = \hat{\lambda}_2$, representing the stretch under equibiaxial stress condition.

3.2.2 Experiment Data

For this study, the constitutive model parameters for eqn. 3.8 were obtained utilizing biaxial mechanical data of GLBP described on specimen axes with tissue material axes at 45-degree. To obtain model parameters for the Ogden model, we

created an isotropic response of GLBP by averaging the stress and strain response of equibiaxial test (T_{11}:T_{22} =1:1) of GLBP and fit the synthetic data set to the eqn. 3.10.

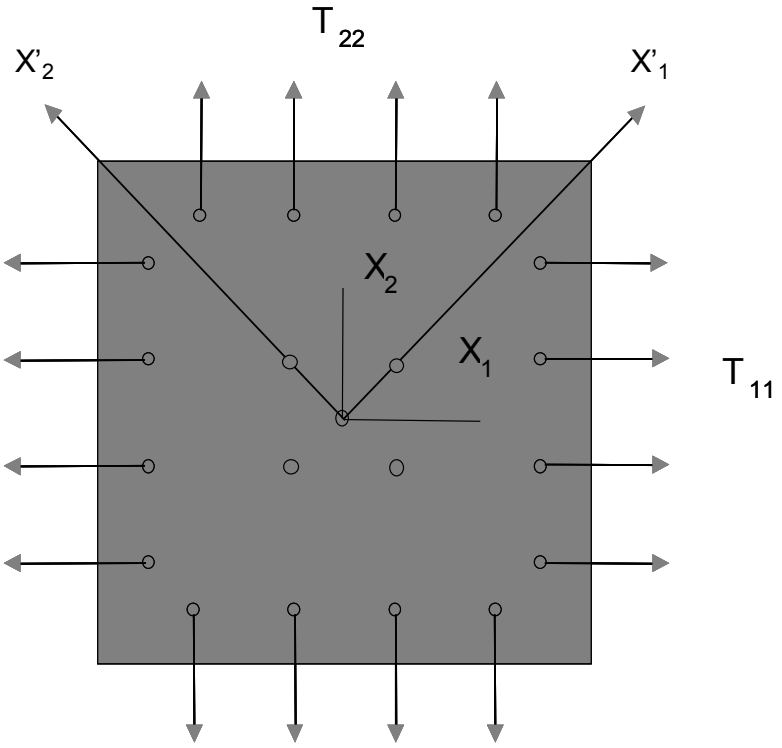

Figure 3-2 Specimen loading approach for biaxial testing. T_{11} and T_{22} of 1 MPa Lagrangian stress are imposed on each side of the sample, by the four evenly spaced suture attachments on two stretching axes X_1 and X_2. Specimens were tested with material axes (X'_1-X'_2), determined by small angle light scattering (SALS), inclined to a 45-degree angle with respect to the biaxial device stretching axes (X_1-X_2).

3.2.3 Finite Element Formulation

In nonlinear finite element analysis, the equilibrium equations are obtained by discretizing the virtual work equation. In the following, we largely follow Holzapfel *et al*. [100, 109] for formulation for hyperelastic membranes. Let the virtual work contribution from the internal forces in an element in Lagrangian form be

$$\delta W_I(\mathbf{E}) = \int_{\partial\Omega_0} (\delta\mathbf{E} : \mathbf{S}) H dS \tag{3.11}$$

where W_I denotes the internal work and S denotes the undeformed membrane surface encompassed by the boundary $\partial\Omega_0$. The material linearization operator $\Delta\{\cdot\}$ (Gateaux operator) is defined by the following [98]

$$\Delta\{\cdot\}(\mathbf{u}, \Delta\mathbf{u}) := \frac{d}{d\varepsilon}\{\cdot\}(\mathbf{u} + \varepsilon\Delta\mathbf{u})\big|_{\varepsilon=0} \tag{3.12}$$

where $\mathbf{u}$ is the displacement field. Linearization of internal energy variation is given by,

$$\Delta\delta W_I = \int_{\partial\Omega_0} (\mathbf{S} : \Delta\delta\mathbf{E} + \delta\mathbf{E} : \Delta\mathbf{S}) H dS \tag{3.13}$$

Linearization of the second Piola-Kirchhoff stress tensor is obtained by using chain rule:

$$\Delta\mathbf{S} = \frac{\partial\mathbf{S}}{\partial\mathbf{E}} : \Delta\mathbf{E} = \mathbb{C} : \Delta\mathbf{E} \tag{3.14}$$

where $\mathbb{C}$ is the elasticity tensor in material description. Hence, the eqn. 3.13 may be re-expressed in index notation as[109]

$$\Delta\delta W_I = \int_{\partial\Omega_0} \left(\frac{\partial\delta u_a}{\partial X_B}(\delta_{ab} S_{BD} + F_{aA} F_{bC} C_{ABCD})\frac{\partial\Delta u_b}{\partial X_D}\right) H dS \tag{3.15}$$

where δ_{ab} denotes the Kronecker delta.

Eqn. 3.15 describes the fully nonlinear finite deformation case. The term $\delta_{ab} S_{BD} + F_{aA} F_{bC} C_{ABCD}$ represents the effective tangential elasticity tensor, the first term S_{BD} is the geometrical stress contribution and the second term is the so-called material

contribution to the linearization. Note here that linearization of the principle of virtual work in spatial description can be obtained by the push-forward operation [109] of the linearized terms in eqn. 3.15 and may be written as

$$\Delta\delta W_l = \int_{\partial\Omega} \left(\frac{\partial \delta u_a}{\partial x_b}(\delta_{ab}\sigma_{bd} + c_{abcd})\frac{\partial \Delta u_b}{\partial x_d}\right) h\, ds \tag{3.16}$$

where $c_{abcd} = F_{aA}F_{bB}F_{cC}F_{dD}C_{ABCD}$ and s denotes the deformed membrane surface encompassed by the boundary $\partial\Omega$. Incremental/iterative solution technique of Newton-Raphson's method is used by ABAQUS for solving the nonlinear equilibrium equations.

The 4th order elasticity tensor $\mathbb{C}$ usually has 81 components, however, due to our two-dimensional application, it reduces to 16 components, furthermore, to respect symmetry of $\mathbb{C}$ and $S_{12}=S_{21}$(because $E_{12}=E_{21}$), it reduces to 9 components, from which only 6 components need to be determined. It may be written in matrix form as

$$\mathbb{C} = \frac{c}{2} e^{Q} \begin{bmatrix} 2A_1+\zeta_1^2 & 2A_3+\zeta_1\zeta_2 & 2A_5+\zeta_1\zeta_3 \\ & 2A_2+\zeta_2^2 & 2A_6+\zeta_2\zeta_3 \\ \text{sym} & & 2A_4+\zeta_3^2 \end{bmatrix} \tag{3.17}$$

where:

$$\zeta_1 = 2A_1E_{11}+2A_3E_{22}+2A_5E_{12},\ \zeta_2 = 2A_2E_{22}+2A_3E_{11}+2A_6E_{12},\ \zeta_3 = 2A_4E_{12}+2A_5E_{11}+2A_6E_{22}.$$

3.2.4 Biaxial Testing Simulations

The biaxial testing simulation model consisted of 400 plane stress elements (ABAQUS element type CPS8R) describing a specimen geometry of 25 mm x 25 mm x 0.4 mm (Figure 3-2). Four evenly spaced node forces, with 5 mm between two adjacent nodes and 2.5mm inside the specimen edge, were imposed on each side (Figure 3-2). Each node force was 2.5 N, imposing 1 MPa Lagrangian stress on each edge. Similar to the actual biaxial testing setup, only the central region was used for stress-strain measurements. This was accomplished by averaging the stress and strain tensor components for sixteen elements located in the center of the finite element model, delimiting a 5 mm x 5 mm region.

3.2.5 Enforcement of Convexity Condition

Conventionally, biaxial experimentally measured stresses are fit to the predicted stress by the constitutive model, with parameter estimates obtained using nonlinear regression techniques to obtain model parameter values [34]. However, the resulting model may be numerically unstable for computational implementation, and thus will not lead to convergent solutions. Moreover, physical plausibility of the resultant constitutive model must be enforced [39, 101, 109]. However, mathematical techniques enforcing these constraints from computational perspective have largely been unexplored.

In most commercial finite element codes, the Newton-Raphson method is used to evaluate the material stiffness matrix, which is a function of $\mathbb{C}$. If $\mathbb{C}$ is positive definite (as well as full rank and well-conditioned), then the numerical solution of the equilibrium equations (eqn. 3.16) will be stable and accurate. From eqns. 3.7 and 3.14, it can be seen that elasticity tensor $\mathbb{C}$ is the second partial derivative, or Hessian, of W. We know that whenever the Hessian of a function is positive definite, the corresponding function will be convex. Thus, by requiring the elasticity tensor $\mathbb{C}$ be positive definite, the convexity of the generalized Fung pseudo-elastic constitutive model is enforced.

For planar biaxial loading of biomembranes, strict convexity physically implies that the projections of the contours of W on the E_{11}-E_{22}, E_{11}-E_{12}, and E_{22}-E_{12} planes form convex surfaces [106]. To impose convexity on the current strain energy function (eqn. 3.8), we examined elasticity tensor $\mathbb{C}$ in the reference configuration (where $E_{11} = E_{22} = E_{12}=0$):

$$\mathbb{C}=\frac{c}{2}\begin{bmatrix} 2A_1 & 2A_3 & 2A_5 \\ 2A_3 & 2A_2 & 2A_6 \\ 2A_5 & 2A_6 & 2A_4 \end{bmatrix} \tag{3.18}$$

From eqn. 3.18 we obtained the following parameter constraints by satisfying $\mathbb{C}$ be positive definite in the reference configuration $E_{11}=E_{22}=E_{12}=0$:

$$c>0,\ A_1>|A_3|,\ A_2>|A_3| \text{ and } \quad A_1A_2A_4+2A_3A_6A_5-A_5^2A_2-A_6^2A_1-A_3^2A_4>0 \tag{3.19}$$

However, the above constraints for eqn. 3.19 are not sufficient to guarantee $\mathbb{C}$ is positive definite over the entire strain range. Rather, we consider these to be a necessary condition that if parameter constraints fail to satisfy these constraints, convexity will be violated. It is therefore necessary that $\mathbb{C}$ be evaluated at every point in the anticipated strain range to verify that positive definiteness is always satisfied.

3.2.6 Requirement for the Condition Number of $\mathbb{C}$

The condition number of $\mathbb{C}$ is defined as

$$\Re = \| \mathbb{C} \| \cdot \| \mathbb{C}^{-1} \| \tag{3.20}$$

where the norm of $\mathbb{C}$ is defined as $\| \mathbb{C} \| = \max_{1 \le j \le n} \sum_{i=1}^{n} | C_{ij} |$. We evaluated the condition number of elasticity tensor $\mathbb{C}$ over the experimental strain ranges. Theoretically, the lower the condition number, the better the numerical stability. In our experience, for the Fung pseudo-elastic constitutive model we found that a condition number ≤ 200 was acceptable for numerical convergence. Note that we do not have analytic bounds similar to the eqn. 3.19 for the condition number inequality. This is due to the fact that solving the condition number inequality through matrix manipulation leads to a very complex formulation and further simplification for nonlinear regression bounds is difficult to obtain. Thus we only examined if a condition number ≤ 200 is satisfied once the model parameters were obtained.

3.2.7 Finite Element Implementation

Eqn. 3.15 was incorporated into finite element software package ABAQUS through its user subroutine UMAT. An 8-node biquadratic, reduced integration plane stress element (ABAQUS element type CPS8R) was used for all simulations, using the updated Lagrangian formulation. Static simulations allowing for nonlinearity arising from both the constitutive law and the large geometric deformation were performed.

3.2.8 Finite Element Model Validation

To ensure that the stress update and tangent stiffness were properly implemented into the ABAQUS, displacement-controlled single-element tests were performed. Briefly, node displacements of the single-element were prescribed as boundary condition to control the element deformation. The resulting FE updated strains were used as input to the constitutive model of Eqn (5) to calculate the theoretical updated stresses. This was done in a spreadsheet. The theoretical updated stresses were compared with the FE updated stresses to validate the correctness of the model implementation. Note that for anisotropic materials the resulting asymmetry of the model requires that full element simulations be used, precluding the use of partial models (i.e. quarter models) that require material and geometric symmetry.

3.3 RESULTS

3.3.1 Parameter Values

Nonlinear regression results for the Fung model, with and without enforcing eqn. 3.19, are illustrated in Figure 3-3 and parameter values listed in Table 3-I. Further, with the bounds imposed the elasticity tensor $\mathbb{C}$ satisfied the positive definiteness requirement over the experimental ranges, and W satisfied the convexity condition (Figure 3-4d-f, Table 3-2). As a comparison (Figure 3-4), without the bounds, the elasticity tensor $\mathbb{C}$ failed to be positive definite (Table 3-2) and the strain energy function was not convex (Figure 3-4a, b, c). For illustration purposes, another set of parameters that meet the requirement of a positive definite elasticity tensor $\mathbb{C}$ is listed Table 3-2. However, in this case $\mathbb{C}$ had a high condition number. It is interesting to note that with the same finite element configuration, one parameter set (with positive definite $\mathbb{C}$ and low condition number) achieved numerical convergence while the other two sets failed. For the Ogden model (eqn. 3.16), the parameters estimates are illustrated in Figure 3-3 and listed in Table 3-1, respectively.

Table 3-1 Constitutive model (eqn. 3.8) parameter results for the Fung pseudo-elastic model with and without the bounds of eqn. 3.19, and with low or high condition numbers (CN).

Fung model & constraints	C	A_1	A_2	A_3	A_4	A_5	A_6	r^2
without bounds	4.25	56.55	86.27	-16.76	-76.08	-9.07	-22.29	0.97
with bounds and low CN	5.12	60.12	86.34	2	203.16	43.05	42.14	0.96
with bounds and high CN	4.16	60.09	90.58	-13.76	2.1	6.57	-5.97	0.97

Ogden model	μ_1	α_1	μ_2	α_2	μ_3	α_2	-	r^2
Parameters	3.87	56.11	3.87	56.11	3.87	56.11	-	0.99

Table 3-2 The positive definiteness and condition numbers (CN) for the elasticity tensor $\mathbb{C}$ for the Fung pseudo-elastic model (eqn. 3.8) with and without the bounds of eqn. 3.19, and with low or high condition numbers (CN). The condition numbers values are between the maximum and minimum numbers in the table.

Projection plane	Positive definite		Condition number			
			Fung w/ bounds, low CN		Fung w/ bounds, high CN	
	Fung w/ bounds	Fung w/o bounds	Max	Min	Max	Min
E_{11}-E_{22}, E_{12}=0.0	yes	yes	18.31	2.3	682.2	49.7
E_{11}-E_{12}, E_{22}=0.1	yes	no	31.5	2.71	246.03	106.24
E_{22}-E_{12}, E_{11}=0.1	yes	no	35.85	2.3	478.77	69.17

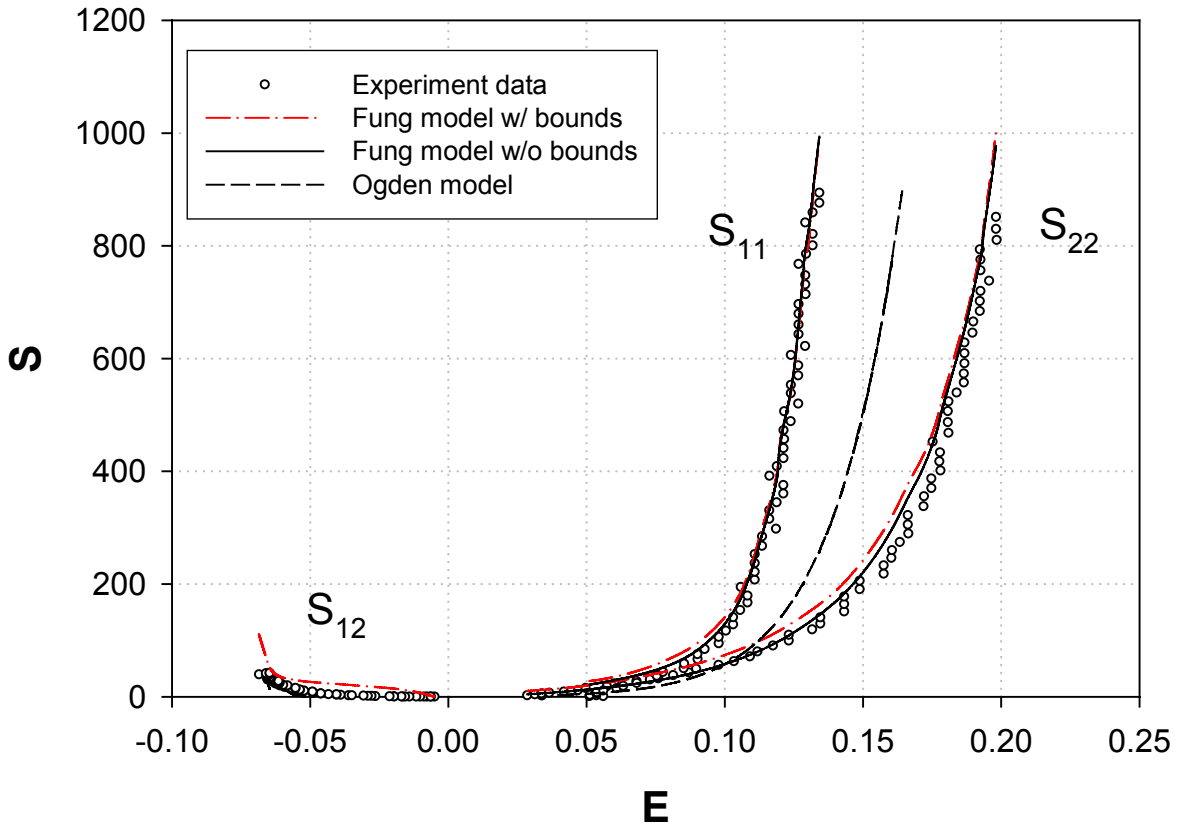

Figure 3-3 Nonlinear regression fitting results for the Fung elastic model of eqn. 3.8 with and without the bounds of eqn. 3.19 and for the isotropic Ogden model of eqn. 3.9.

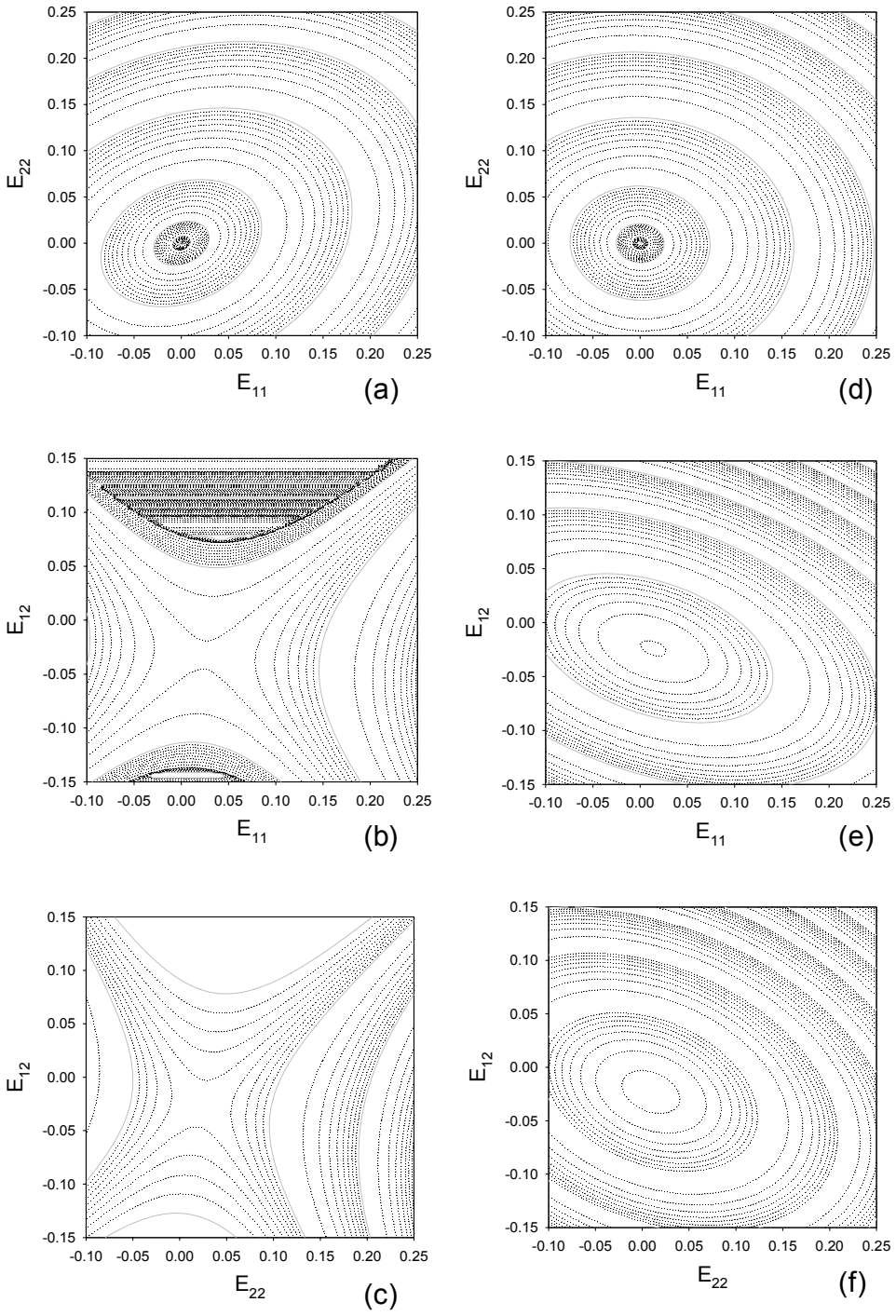

Figure 3-4 The projections of the strain energy function potential contour plots in the a) E_{11}-E_{22}, b) E_{11}-E_{12} and c) E_{22}-E_{12} planes without convexity condition imposed; the projections of the strain energy function potential contour plots in the d) E_{11}-E_{22}, e) E_{11}-E_{12} and f) E_{22}-E_{12} planes with convexity condition imposed.

3.3.2 Single Element and Biaxial Test Specimen Simulations

The results of single-element test for equibiaxial protocol are shown in Figure 3-5, where exact agreements between the theoretical and finite element solutions were obtained. It indicated that the material model was successfully incorporated into finite element analysis.

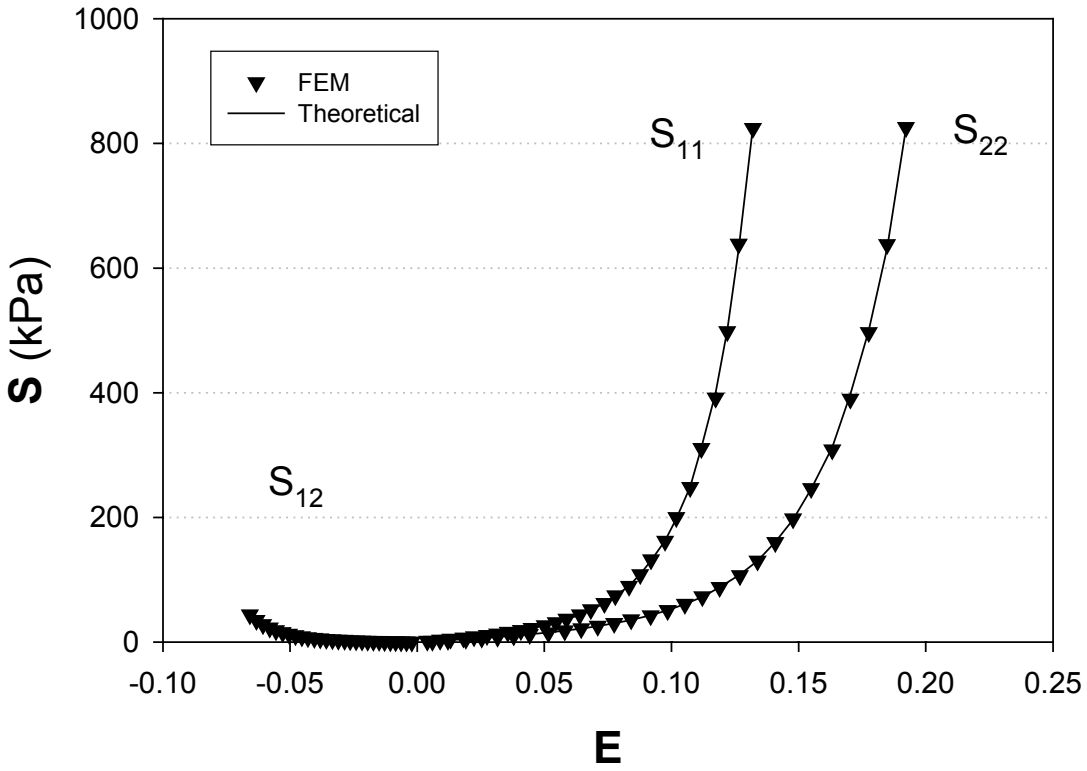

Figure 3-5 Deformations from equibiaxial protocol were input into finite element model and its outputs were compared with experimental data. Exact agreements were obtained.

Results of biaxial test finite element simulations are illustrated in Figure 3-6 for both isotropic (eqn. 3.9) and anisotropic (eqn. 3.8) cases. As in the actual experiment, the simulations exhibited symmetric deformation for isotropic model and prominent shear deformation for anisotropic model, and also different internal stress distribution.

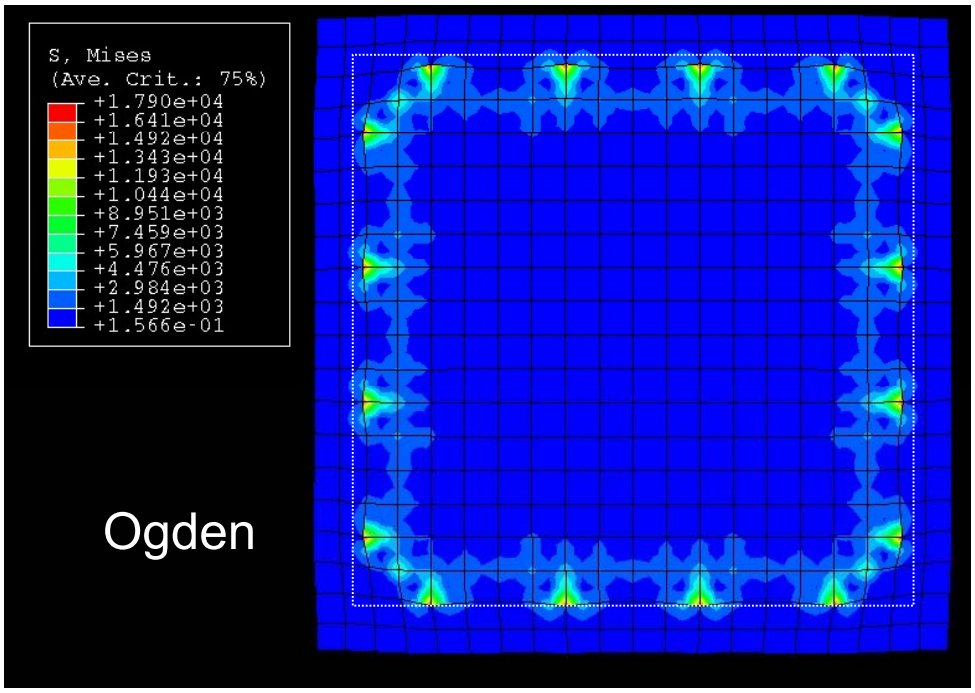

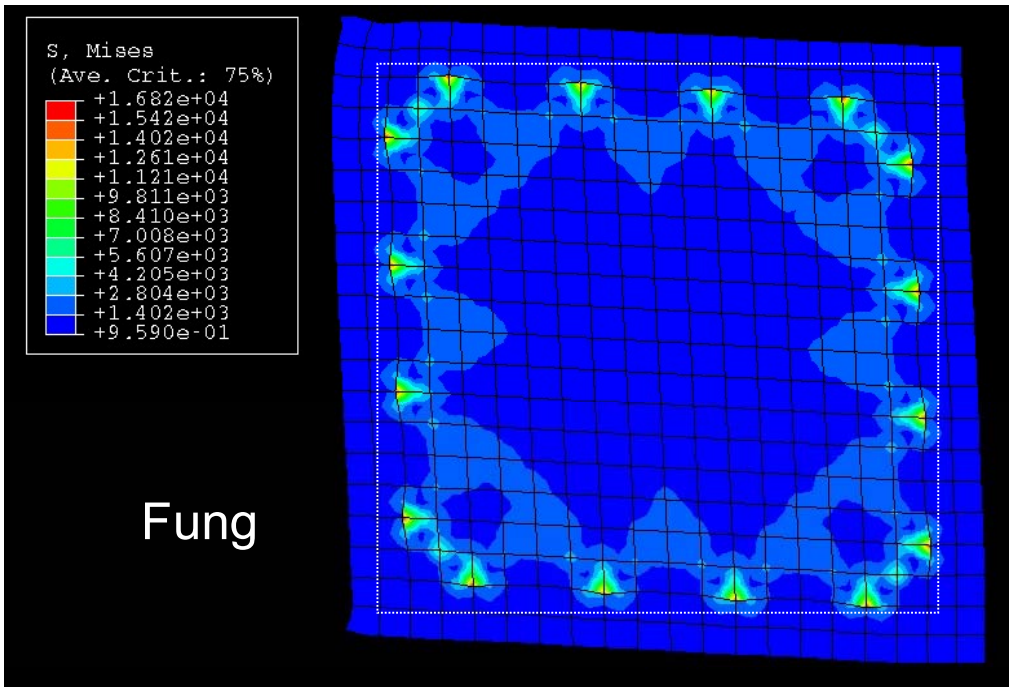

Figure 3-6 Deformation and von Mises stress distribution of biaxial testing simulations utilizing the isotropic Ogden model (a) and the anisotropic Fung model (b). The white frames in the figures indicate the original shape of the sample before deformation.

With the Fung model, stress results indicated a nearly homogenous stress distribution within the central 5 x 5 mm^2 region (a 16 element region corresponding to approximately 4% of total specimen area) could be obtained (Figure 3-6). The mean von Mises stress was 1,323.93 ± 4.31 kPa. The stress-strain output for the central region was compared with the experimental data that indicated a close match, for both normal and shear components (Figure 3-7). Also visible in Figure 3-6 are the boundary effects caused by the point loads, which propagated inside to about 7.5 – 8.75 mm from the specimen edges. This left about 10 x 10 mm^2 inner region with a relatively uniform stress distribution (comprised of sixty-four elements). For this region the mean von Mises stress was 1,332.68 ± 11.21 kPa.

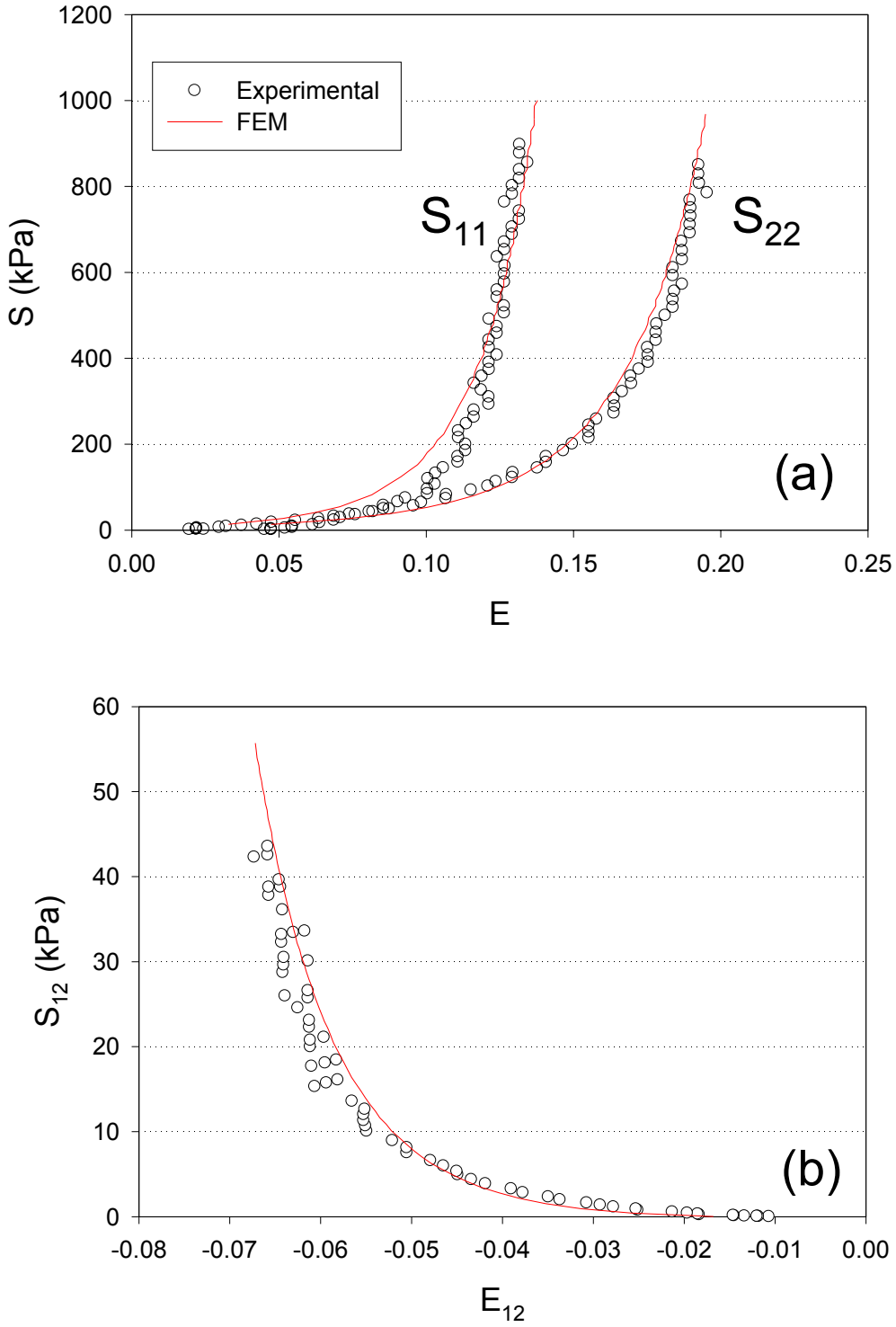

Figure 3-7 An average of sixteen elements located in the center of finite element model, delimiting ~ 25mm^2 region, was used to compare with the experimental biaxial data. A close match was obtained for both normal (a) and shear components for equibiaxial stress simulation.

For the Ogden model, the mean von Mises stress of the central sixteen elements was 1251.25±0.45 kPa. Also visible in Figure 3-6 are the boundary effects caused by the point loads, which propagated inside to about 5 mm from the specimen edges. This left about 15 x 15 mm^2 inner region with a relatively uniform stress distribution (compassed of one hundred forty-four elements). For this region the mean von Mises stress was 1,266.39 ± 26.66 kPa.

3.4 DISCUSSION

The pseudo-elastic Fung model has been shown to accurately describe the nonlinear, anisotropic behaviors of many soft tissues, and thus has many applications in biomedical research and medical device design. Taken as a whole, our previous [38, 39, 45] and current work addressed the complete process of computational implementation. This process starts from the collection of appropriate experimental data, formulating and validating the appropriate constitutive model, obtaining and refining material parameters, and finally finite element implementation and validation. Additionally, our approach is formulated within a general finite element code, and can thus be straightforwardly adopted.

3.4.1 Incompressibility

Most native and biologically-derived tissues exhibit incompressibility because of their high water content and low permeability. Incompressibility can be enforced by a Lagrange multiplier p, as second variable in addition to displacement, forming the so-called "mixed" or "hybrid" finite element approaches. However, in our application we did not explicitly enforce the incompressibility condition because our simulation is in a two-dimensional plane stress state.

For plane stress, shell and membrane elements the material is free to expand in the thickness direction, thus, special treatment of the volumetric behavior through Lagrange multiplier p is not necessary and the use of regular stress-displacement elements is satisfactory. Further, enforcing Lagrange multiplier p as second variable will render the stiffness matrix semi-definite, which is a common problem in finite elements and it leads to several numerical difficulties [101]. Nonetheless, if the tissue is modeled with three-dimensional solid element, a three-dimensional constitutive model needs to be defined and the volumetric constrains where $\det|\mathbf{F}|=1$ needs to be explicitly imposed.

3.4.2 Convergence Issues

For hyperelastic materials, the finite element convergence is always a critical issue irrespective of material anisotropy. Several techniques such as switching the finite element simulation from load-control to displacement-control, and using Line-search

and RIKS methods, may be of help. The default convergence criteria defined in ABAQUS are designed to provide reasonably optimal solutions to complex problems involving combinations of nonlinearities as well as efficient solutions of simpler nonlinear cases. If less strict convergence criteria are selected, there is a danger that results may be accepted as converged when they are not sufficiently close to the exact solution of the system. Usually this is manifested by a discrepancy between the theoretic solution and finite element output. Another alternative is to modify the model, either changing the form of the model or adjusting model parameters. While changing the form of the model is not preferable, adjusting model parameters requires that 1) the parameter estimates are not unique; 2) the accuracy of the model describing the experimental data is not compromised.

Previous work has attempted to determine proper material constants for pseudo elastic soft tissue models [39, 41, 103, 104, 110]. The general goal in finding material constants is to obtain the minimum number of parameters while adequately fitting the data [34]. However, for a highly nonlinear model it is usually difficult to determine the global minimum. If the regression started from different initial values, it is highly likely that the regression falls into a local minimum valley, thus it was found that multiple sets of constants could provide essentially equally good fits. In our case, the r^2 is changed from 0.97 to 0.96 after convexity constraints imposed on the nonlinear regression, with no perceptible impact to the quality of the fit. Non-uniqueness of parameter estimates of the Fung elastic model is probably due to the inherent co-variance of its strain components [111, 112].

A few constitutive inequalities, which have been proposed in the past, include the Baker-Ericksen inequalities, convexity, the generalized Coleman-Noll condition [97] and polyconvexity [98]. Those thermodynamic permissibility criteria are enforced on a constitutive law to ensure any response predicted by the constitutive law is physically reasonable. For nonlinear, anisotropic tissue material undergoing finite deformation, the plausibility of constitutive law may be especially acute as such unreasonable deformation may be difficulty to detect [96]. In spite of its apparent fundamental importance, it seems that little attention has been given to this issue [95, 96]. Furthermore, those constitutive inequalities are mainly been addressed from the perspective of physical considerations, rather than computational considerations. For finite element implementation of an experimentally driven hyperelastic model, as illustrated in the current work, certain constraints on the model are required for numerical convergence (eqn. 3.19). While requesting strain energy function to be convex may be too restrictive for hyperelastic materials [98], the less restrictive Legendre-Hadamard inequality has been proposed. However, its applicability to finite element analyses is unclear.

3.4.3 Fung Model and Other Models

For proper computational implementation, the Fung model requires explicitly expression of shear behavior and thus, the E_{12} term has to be included in the model. In literature, a four parameter Fung (e.g., $Q = A_1E_{11}^2 + A_2E_{22}^2 + 2A_3E_{11}E_{22}$) is often seen. This four-parameter Fung model is adequate for describing and quantifying tissue

mechanical properties, however, not adequate for any realistic numerical simulation in which element shearing is inevitable. This also suggests that biaxial testing with extension only does not provide sufficient information to constitute a strain energy function for computational implementation. Note here the argument is for anisotropic materials.

Construction of a constitutive model with physical plausibility property a priori is ideal. There are several attempts [106, 113, 114] towards this direction. For example, recently Holzapfel *et al.* [106] proposed a constitutive model for artery layers. The model is a fiber-reinforced composite model with two families of fibers. The model is discrete structural (because of the fixed fiber direction) and based on strain invariants, for which explicit expression of shear may not be needed. The model demonstrated physical plausibility (convex). The continuous structural model (has a continuous fiber distribution) proposed by Lanir [115] and used by Sacks [116] has been shown to be physical plausible [95, 96].

3.4.4 Validation with Experimental Data

Overall, we found excellent agreement between the predicted and measured stress responses. In general, the discrepancies between finite element output and experimental data could be attributed to idealization of the finite element model. Specifically, the finite element model assumed idealized conditions exist such as tissues are homogeneous, loads are evenly spaced and have exactly equal values. While it is

certainly possible to achieve this, the current simulation results suggest it is not necessary for accurate simulations.

It should be noted that our finite element analysis was conducted using tissue material axes oriented at 45° with respect to biaxial stretching axes and four-suture attachment loading boundary condition. Our findings should be interpreted in the light of these restrictions. When varying degrees of tissue anisotropy and tissue clamping methods, the region of uniform stress and strain would certainly be changed. Those effects have been addressed in Sun *et al.* [117].

3.5 SUMMARY

This study presented a finite element implementation of a general anisotropic Fung model, including in-plane shear effects. We enforced the restrictions on the model necessary to achieve numerical stability. The finite element model was validated comprehensively by both theoretical solutions and experimental data. These results suggest that accurate design and functional simulations of medical devices using realistic nonlinear anisotropic material models is both feasible and practical. The successful finite element implementation of the anisotropic Fung elastic model will eventually facilitate the medical design process.

4.0 FINITE ELEMENT SIMULATIONS – BOUNDARY EFFECTS DURING BIAXIAL TESTING OF SOFT TISSUE

"If the forces acting on an elastic body are confined to several distinct portions of its surface, each lying within a sphere of radius ε, then the stresses and strains at a fixed interior point of the body are of a smaller order of magnitude in ε as $\varepsilon \rightarrow 0$ when the forces on each of the portions are self-equilibrated than when they are not." – von Mises' interpretation (1945) of Saint-Venant's principal.

In the previous chapter, we addressed the issue of finite element implementation of the Fung pseudo-elastic model; in this chapter we will utilize the model and simulate tissue behavior under different biaxial loading conditions. To our knowledge, such simulation has not been conducted and comprehensively studied before. A previous well-referenced study of biaxial test was by Nielsen *et al.* [58], however, the material model they used is isotropic rubber type mode, which does not represent actual nonlinear, anisotropic tissue behavior. With the fact that biaxial test method is becoming an increasingly utilized technique in characterizing mechanical properties of soft tissues, more and more concerns of the reliability and repeatability of biaxial test are raised. For example, the strong influence of boundary conditions in biaxial tests

were recently underscored by Waldman *et al.* [118], wherein substantially different experimental results were obtained using different sample gripping methods on the *same* specimens. As it is not possible to directly evaluate the effects of different boundary conditions on specimen internal stress distributions, numerical simulations need to be conducted to explore these effects. We will begin this chapter by reviewing the famous Saint-Venant's principal and its applicability to soft tissue experiment (section 4.1.1). Then we will discuss how we set up our simulations to investigate the effects of different clamping methods, different tissue anisotropy and different sample shapes (sections 4.2.1 to 4.2.4). We will show the simulation results in section 4.3. The stress decay studies in sections 4.3.1 and 4.3.2 will provide the experimenters valuable information on interpreting experimental results. Finally, in section 4.4 we will give explanation of the phenomena observed in the study by Waldman *et al.* [118].

4.1 INTRODUCTION

Planar biaxial testing for soft biological tissues was first introduced by Lanir and Fung in 1974 [32, 35] who utilized it to investigate the mechanical properties of rabbit skin. Today, biaxial testing of soft tissue is becoming an increasingly utilized technique to characterize the mechanical properties of various planar biological materials, including skin, pericardium, epicardium, visceral pleura, myocardium, as well as various engineered tissues and scaffolds. Recent reviews of the biaxial testing techniques and related constitutive theories can be found in Sacks 2000 [34] and Humphrey 2002 [101]. In

spite of its growing use, biaxial testing methods have not been standardized and methodologies vary widely. Due to the complex mechanical behavior of soft tissues and the general difficulty in performing biaxial tests [34], experimental artifacts can easily be introduced. A critical factor affecting biaxial mechanical behavior are the boundary conditions used in testing, such as the uniformity of the loading along the specimen edge and the method of attachment (e.g. grip, sutures). The strong influence of boundary conditions in biaxial tests were recently underscored by Waldman *et al.* [118], wherein substantially different experimental results were obtained using different sample gripping methods on the same specimens.

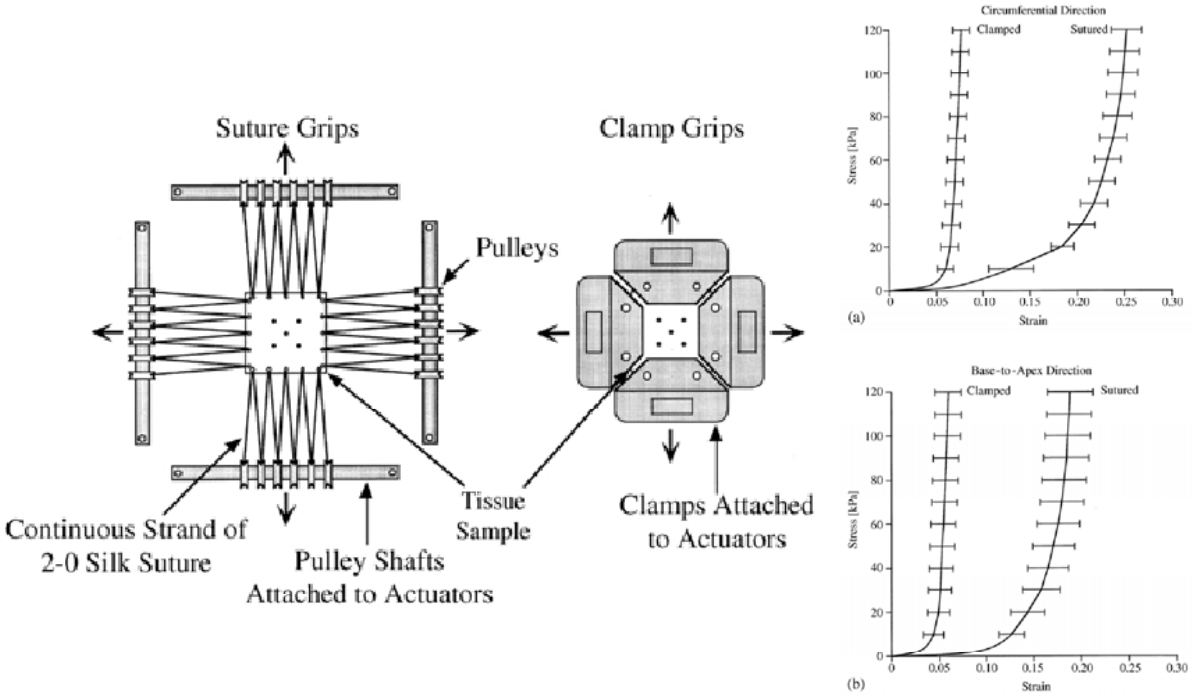

Figure 4-1 Substantially different experimental results were obtained using different sample gripping methods on the *same* specimens in a study by Waldman *et al.* [118] . Reproduced with permission.

4.1.1 Saint-Venant's Principal

Essentially all mechanical testing methods used to determine material properties are based on the assumption that Saint-Venant's principle is valid. However, the justification of the principle is largely empirical. Saint-Venant himself limited his principle to the problem of extension, torsion and flexure of prismatic and cylindrical bodies. There have been various attempts to generalized the principles, for example,

Love's Statement: The strains that are produced in a body by the application, to a small part of its surface, of a system of forces statically equivalent to zero force and zero couple, are of negligible magnitude at distances which are large compared with the linear dimensions of the part.

Sokolnikoff's Statement: If some distribution of forces acting on a portion of the surface of a body is replaced by a different distribution of forces acting on the same portion of the body, then the effects of the two different distributions on the parts of the body sufficiently far removed from the region of application of the forces are essentially the same, provided that the two distributions of forces are statically equivalent.

von Mises' Statement: If the forces acting on an elastic body are confined to several distinct portions of its surface, each lying within a sphere of radius ε, then the stresses and strains at a fixed interior point of the body are of a smaller order of magnitude in ε as $\varepsilon \to 0$ when the forces on each of the portions are self-equilibrated than when they are not.

The above statement by v. Mises was proved nine years later by E. Sternberg in 1954 for linearized elasticity. For mechanical testing of materials, Saint-Venant's

principle basically implies that the grip imposes local stresses at the grip-specimen interface and that the influence of these local stresses becomes negligible at some distance away from the grip [118]. However, the routine invocation of Saint-Venant's principle in mechanical testing of highly anisotropic or composite materials is not justified in general [119]. The validation of Saint-Venant's principle for anisotropic materials has been investigated theoretically for elastic solids subjected to self-equilibrated loads [120-122]. Utilizing a relatively simple material model and boundary conditions, the studies demonstrated a four-fold slower decay of boundary effects for a highly anisotropic transversely isotropic material compared to that of an isotropic material. [119] In light of the complex anisotropic behavior of soft tissues, we hypothesize that the stress decay pattern may be more complex. Moreover, for biaxial testing of soft tissues, such as heart valve leaflets, the boundary effects may be especially relevant due to the necessarily small sample size and strong axial coupling. Thus there is a pressing need to investigate the effects of boundary conditions in biaxial testing of biological soft tissues.

4.1.2 Our Approaches

As it is not possible to directly evaluate the effects of different boundary conditions on specimen internal stress distributions [56], and currently, there is no theoretical study to explore such effects, computational tools are required to simulate biaxial testing and to examine the stress distribution under different boundary conditions. Nielson *et al.* [58] performed a finite element simulation of sutured biaxial

experiments using an isotropic Ogden model and reported a uniform stress distribution within the central 25% of the specimen area. In Chapter 3 we successfully implemented an anisotropic Fung model, including the effects of in-plane shear, into finite element analysis. The finite element model predicted a uniform stress distribution within only the central 16% of the specimen area. While those simulations were not aimed to comprehensively study the boundary effects, in the current study we utilized the same material model implementation to simulate biaxial testing. Effects of boundary conditions under different numbers of suture attachments, different gripping methods and specimen shapes, and different degree of tissue anisotropy were examined.

4.2 METHODS

4.2.1 Biaxial Experimental Data

A detailed description of biaxial tests has been presented in Chapter 2. Note that we utilized two sets of experimental data obtained on specimen axes: I) GLBP with material axes orientation at 45 degree with respect to the biaxial stretching axes (x_1-x_2 in Figure 4-2a). II) GLBP with material axes orientation at 0 degree with respect to the biaxial stretching axes (x'_1-x'_2 in Figure 4-2a). Due to the material axes choice, experiment I contains in plane shear data, whereas experiment II has negligible shear response.

4.2.2 Constitutive Models

For data set I we applied a general Fung elastic model of eqn 3.8 , with the ability to characterize in-plane shear response. For data set II, due to negligible shear, we applied it with a simpler five parameter Fung model, where:

$$Q_5 = A_1E_{11}^2 + A_2E_{22}^2 + 2A_3E_{11}E_{22} + A_4E_{12}^2 \tag{4.1}$$

The methods for obtaining the parameters **c** and **A** through Marquardt-Levenberg nonlinear regression and corresponding constraints have been previously presented in Chapter 3. The parameters for the two data sets are listed in Table 4-1.

Table 4-1 Parameters for eqns 3.8 and 4.1 for the two set of experimental data.

Parameters	c	A1	A2	A3	A4	A5	A6	Rsqr
GLBP with shear	5.12	60.12	86.34	2.0	203.16	43.05	42.14	0.96
GLBP without shear	9.70	104.44	35.12	3.50	32.10	-	-	0.95

4.2.3 Biaxial Testing Simulation Setups

Finite element models were developed for 25 mm x 25 mm x 0.4 mm test specimens using 400 CPS8R elements. It should be noted that the 25 mm x 25 mm x 0.4 mm dimensions reflect those typically encountered in biaxial testing of heart valve biomaterials. Equibiaxial loading was simulated to examine and compare the effects of different boundary conditions. Two groups of simulations were conducted for each material axes orientation: one group explored the effects of different numbers of suture

attachments. The specimen was attached with 4, 6 or 8 points of sutures on each edge. Point loads were applied at the boundary nodes (Figure 4-2a) to exert a net total 1 MPa Lagrangian stress along each side. The other group explored the effects of different gripping methods. The gripping methods are: a) suture attachment (SA) (Figure 4-2a); b) clamps on a square specimen (CSS) (Figure 4-2b); c) clamps on a cruciform specimen (CCS) (Figure 4-2c). Two leg lengths of CCS were chosen, one with 0.5-length of 25mm (CCS05) and the other with 1.5-length of 25 mm (CCS15). As cross thickness stress is of no interest in this study, we did not model two grips in contact with the tissue enforcing a clamping force. Instead, we simplified the setup by replacing the tissue under the clamps with a linear elastic metallic material, with a Young's modulus of 2.06E+10 kPa and Poisson's ratio of 0.3. Due to the much higher stiffness of the metallic material compared to that of the tissue, a uniform distribution of in-plane tensile boundary forces could be obtained to mimic the in-plane clamp force. A 0.5 MPa Lagrangian stress was enforced on each side of specimen. Exact dimensions of the clamps and loading nodes positions were listed in Tables 4-2 and 4-3. Validation of simulations with both sets of experimental data, i.e., the 0-and 45-degress material axes data, was conducted with the four-suture attachments setup.

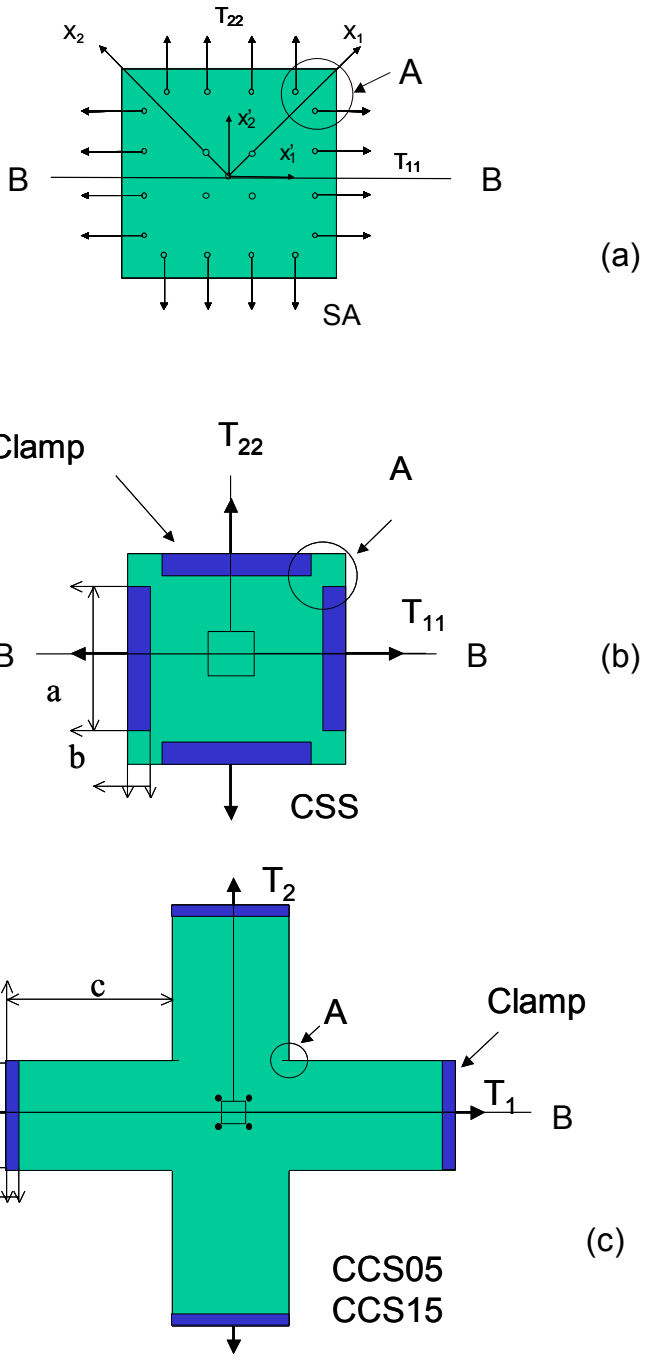

Figure 4-2 Biaxial testing setups with a) four suture attachments; b) clamp on each side of a square sample; c) clamp on each side of a cruciform sample. Dimensions of a, b and c are listed in Table 4-3. For each setup, two material axes orientations were simulated, one with material axes aligned at 45 degree with respect to the specimen axes (loading direction), the other with 0 degree. Region A is used for measuring the axial couple effects. The BB line is used for measuring the stress decay.

Table 4-2 Geometry and loadings of different number of suture attachments methods

# of sutures	Load/node	Distance between nodes	Distance from edge
4 sutures	2.50N	6.25mm	2.50mm
6 sutures	1.67N	4.17mm	1.78mm
8 sutures	1.25N	3.13mm	1.39mm

Table 4-3 Geometry and loadings of different gripping methods and the highest von Mises stress in A region.

B.C	Geometry			Axial coupling stress in A region	
	a	b	c	Data set I	Data set II
Suture (SA)	-	-	-	8.38E+03	7.72E+03
Clamp (CSS)	15.0mm	2.5mm	-	2.65E+04	1.62E+04
Cruciform05 (CCS05)	25.0mm	2.5mm	12.5mm	1.37E+04	5.74E+03
Cruciform15 (CCS15)	25.0mm	2.5mm	25.0mm	9.93E+03	5.30E+03

4.2.4 Quantification of Saint-Venant Boundary Effects

Saint-Venant boundary effects were quantified in terms of the stress decay along the centerline of the specimen (the BB lines in Figure 4-2), axial coupling effects in A region (Figure 4-2), and the stress-strain response in the inner region of the specimen which is of experimental interest. The magnitude of the stress decay was quantified by von Mises stress along the BB line (Figure 4-2). As the specimen size varied with different gripping methods, the normalized distance from the center point of the

specimen to the grip along the BB line was used for comparison. Axial coupling effects were compared for different gripping methods in terms of the highest von Mises stress in the A region (Figure 4-2). Note that the highest von Mises stress is element size dependent, therefore we chose the same element size for different grips methods, the highest von Mises stress was used for a relative comparison of the magnitude of stress concentration in the A region. Also in the region of experimental interest, (i.e., the central ~5x5mm^2 uniform stress region) the components of the second Piola-Kirchhoff stress tensor of different finite element setups were examined.

4.3 RESULTS

4.3.1 Effects of Number of Suture Attachments

The stress-strain data from the central sixteen elements from the simulation with four suture attachments were averaged and compared with the experimental data. Excellent matches were obtained (Figure 4-3) for both 45-degree and 0-degree material axes configurations, which confirmed the correctness of our simulation method. When we increased the number of sutures to six and eight, there was no difference between the suture loading conditions (Figure 4-3). As illustrated in Figure 4-4, stress decays of four, six, and eight suture attachment setups follow a similar pattern. The observation that the stress fluctuates around the ±0.4 normalized distance could be attributed to the point loading effect. The stress is relatively low between two point loads, however, it increases as the effects of the two point loads are synergistized around the ±0.4

normalized distance; Beyond ±0.4, it starts to decay and flatten. Homogenous stress distributions were observed within the central region 20% of the specimen area for all suture setups. However, it was noticed that six and eight suture attachment setups correspond with a slightly larger homogenous region than that of a four suture attachment setup for 45-degree material axes setup. For 0-degree material axes setup, no difference was observed. These results indicated that four suture attachments are sufficient for stress field uniformity in biaxial testing.

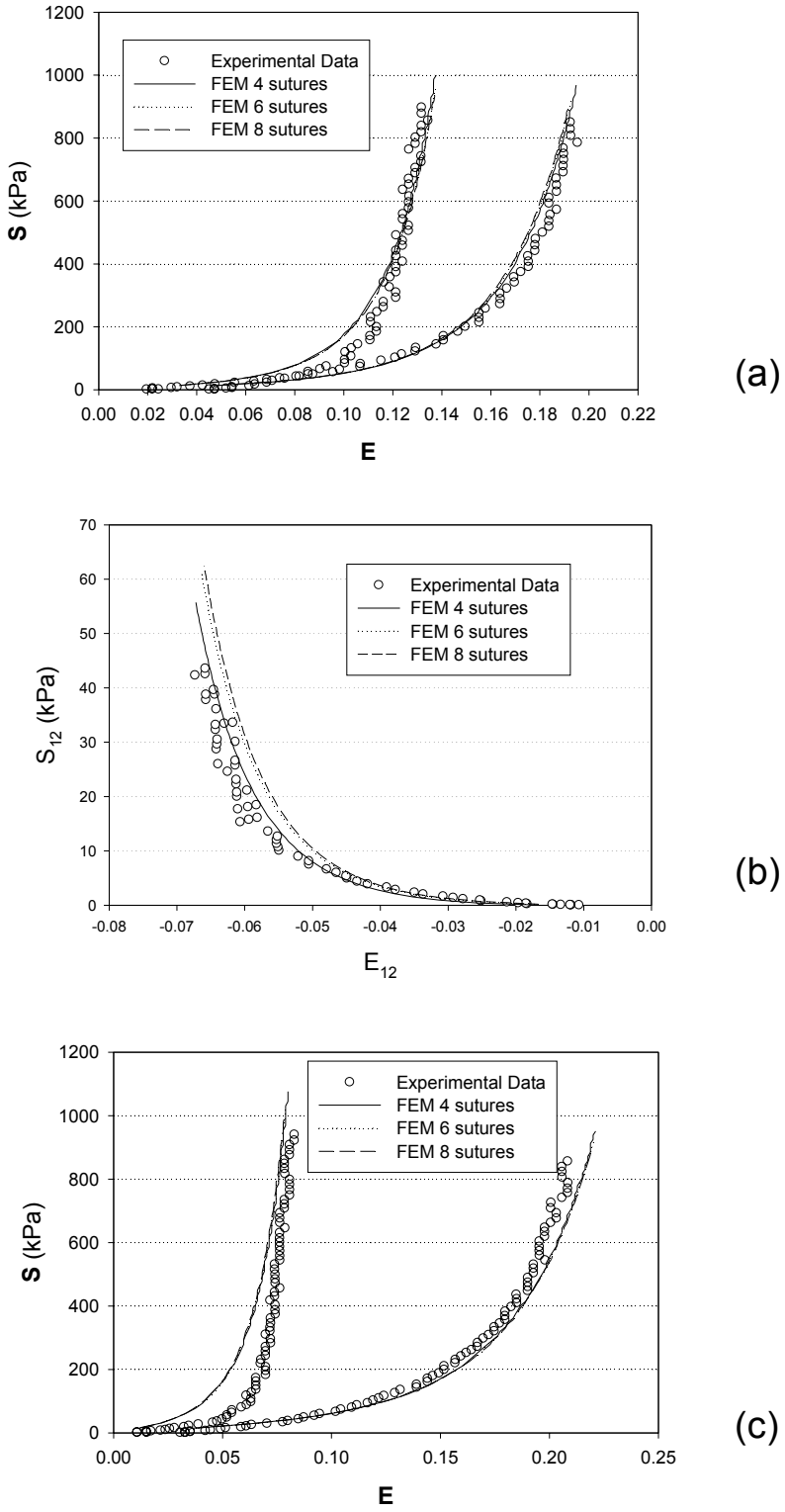

Figure 4-3 Stress-strain output of the finite element simulations with different numbers of suture attachments. a) 45-degree material axis, normal stresses, b) shear stress; c) stresses for 0-degree material axis.

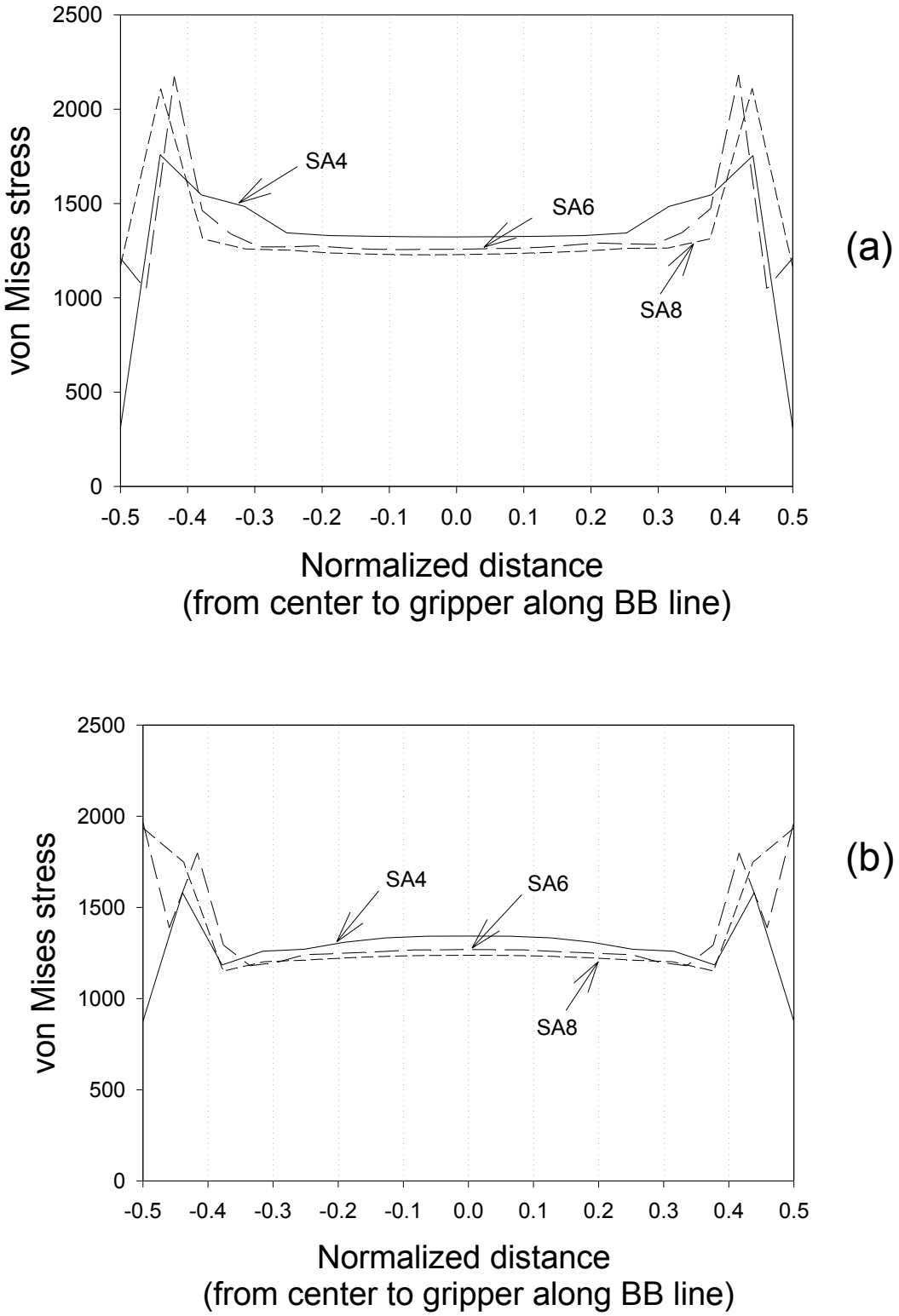

Figure 4-4 Stress decay along the BB lines of the finite element simulations with different numbers of suture attachments, a) for 45-degree material axis and b) for 0-degree material axis.

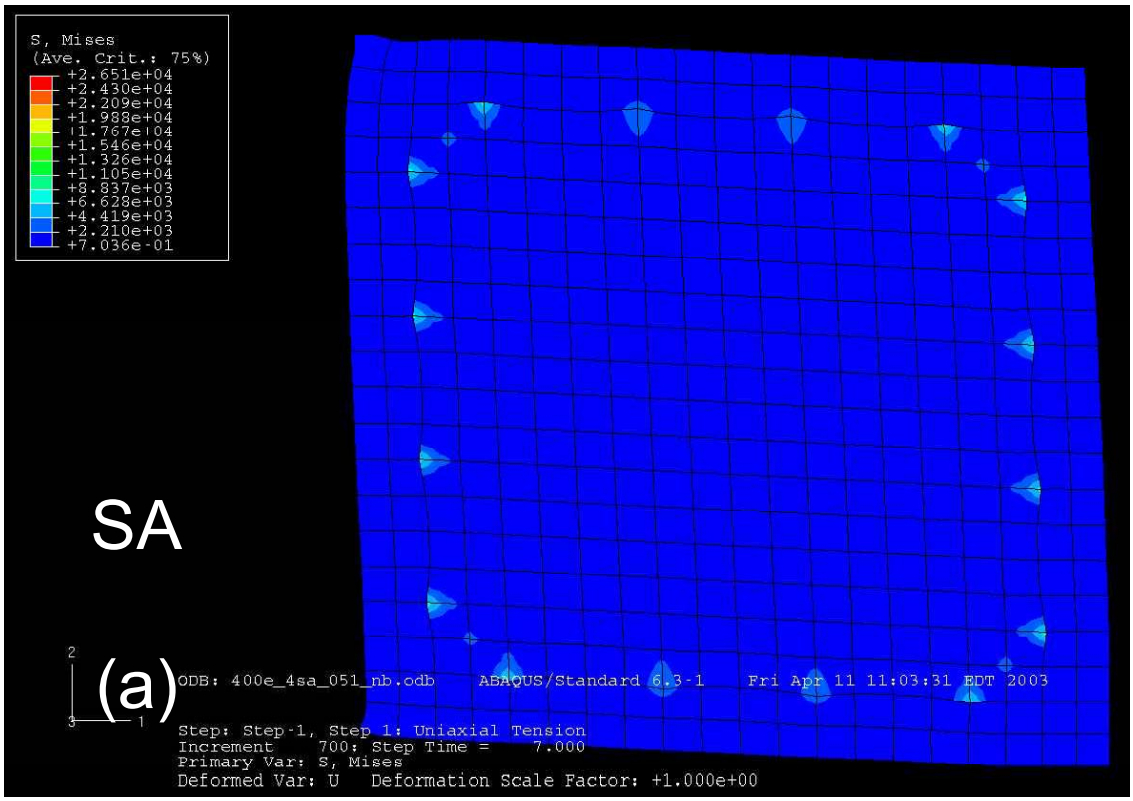
S, Mises
(Ave. Crit.: 75%)
+2.651e+04
+2.430e+04
+2.209e+04
+1.988e+04
+1.767e+04
+1.546e+04
+1.326e+04
+1.105e+04
+8.837e+03
+6.628e+03
+4.419e+03
+2.210e+03
+7.036e-01
SA
(a)
ODB: 400e_4sa_051_nb.odb ABAQUS/Standard 6.3-1 Fri Apr 11 11:03:31 EDT 2003
Step: Step-1, Step 1: Uniaxial Tension
Increment 700: Step Time = 7.000
Primary Var: S, Mises
Deformed Var: U Deformation Scale Factor: +1.000e+00

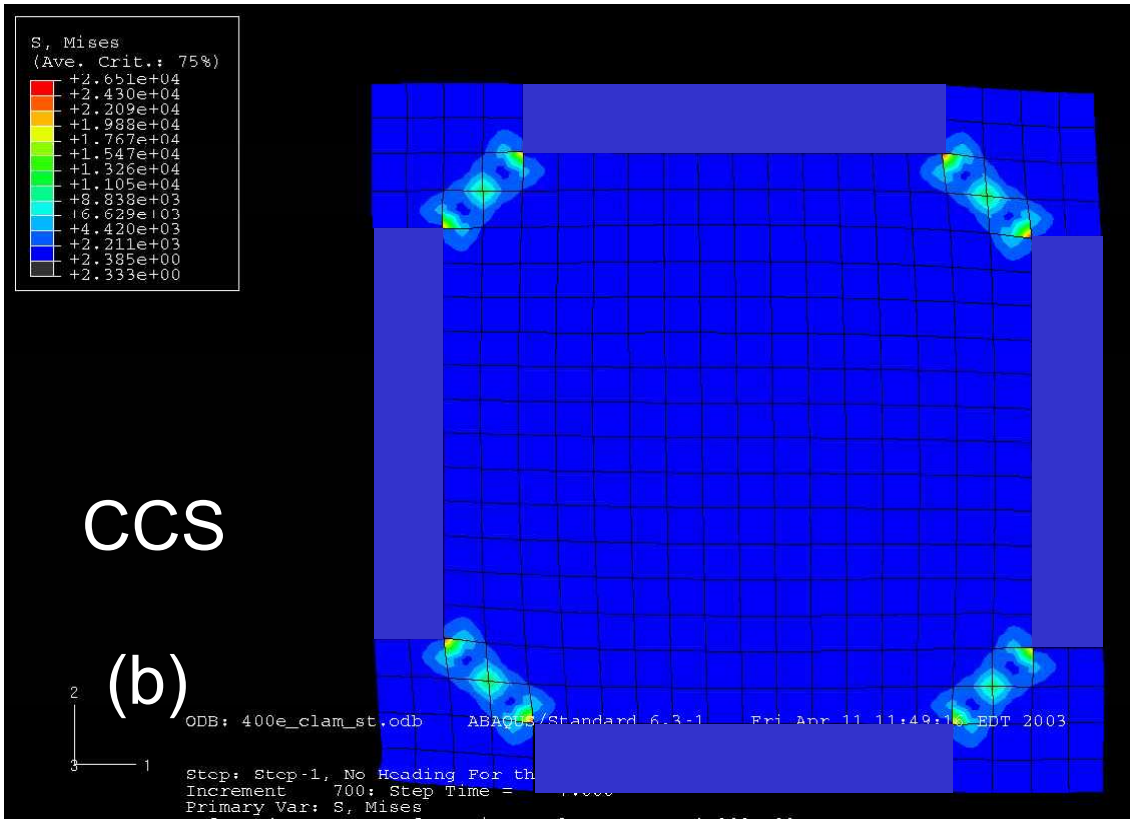
S, Mises
(Ave. Crit.: 75%)
+2.651e+04
+2.430e+04
+2.209e+04
+1.988e+04
+1.767e+04
+1.547e+04
+1.326e+04
+1.105e+04
+8.838e+03
+6.629e+03
+4.420e+03
+2.211e+03
+2.385e+00
+2.333e+00
CCS
(b)
ODB: 400e_clam_st.odb
Step: Step-1, No Heading For th
Increment 700: Step Time =
Primary Var: S, Mises

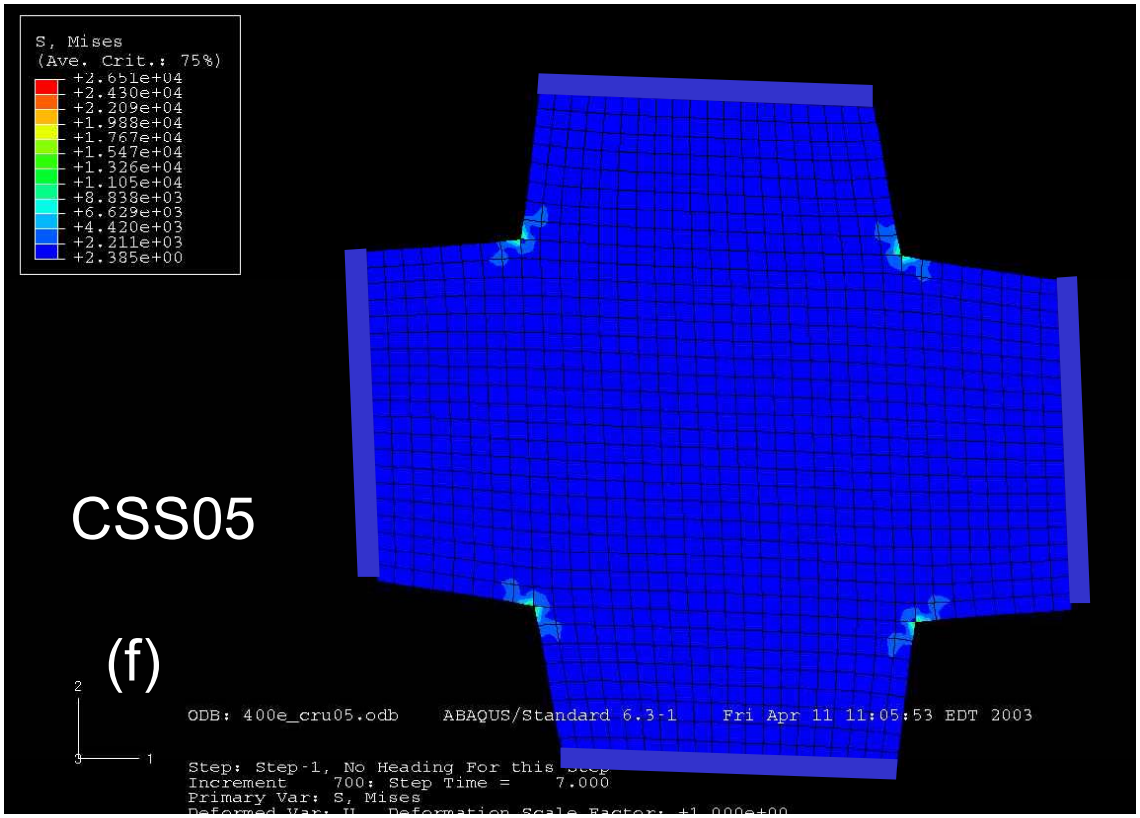
S, Mises
(Ave. Crit.: 75%)
+2.651e+04
+2.430e+04
+2.209e+04
+1.988e+04
+1.767e+04
+1.547e+04
+1.326e+04
+1.105e+04
+8.838e+03
+6.629e+03
+4.420e+03
+2.211e+03
+2.385e+00
CSS05
(f)
2
3
1
ODB: 400e_cru05.odb ABAQUS/Standard 6.3-1 Fri Apr 11 11:05:53 EDT 2003
Step: Step-1, No Heading For this Step
Increment 700: Step Time = 7.000
Primary Var: S, Mises

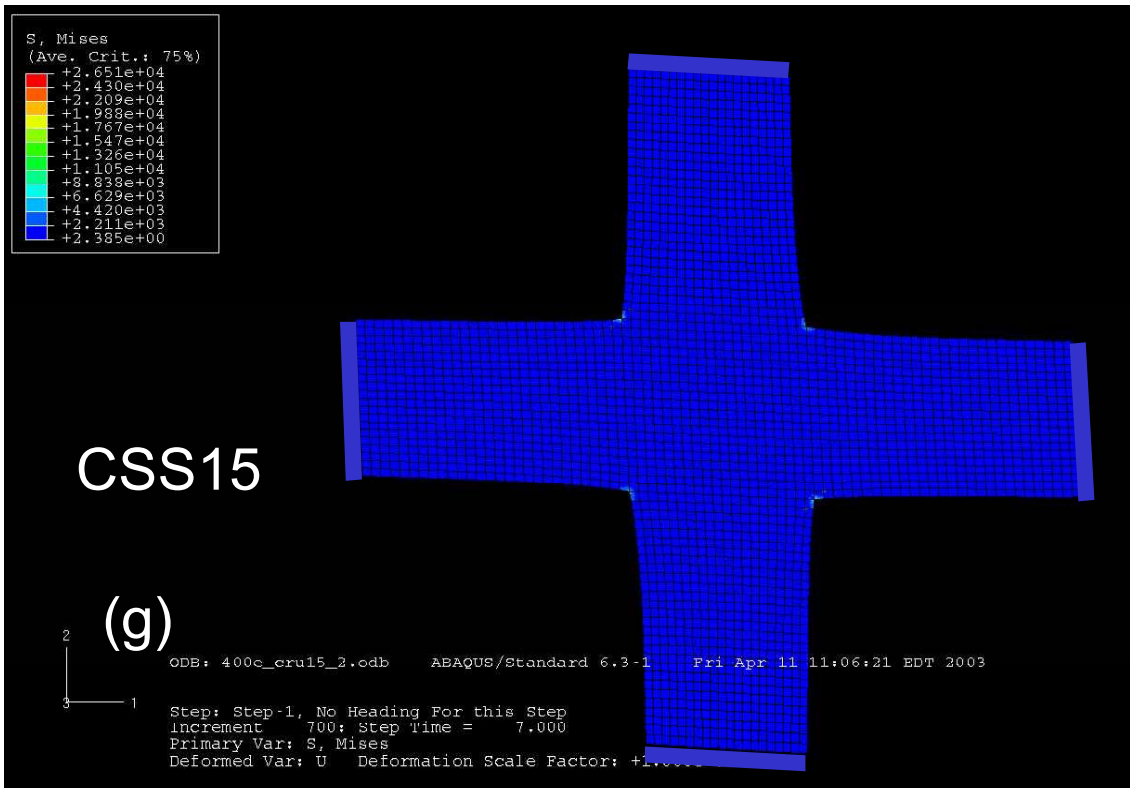
S, Mises
(Ave. Crit.: 75%)
+2.651e+04
+2.430e+04
+2.209e+04
+1.988e+04
+1.767e+04
+1.547e+04
+1.326e+04
+1.105e+04
+8.838e+03
+6.629e+03
+4.420e+03
+2.211e+03
+2.385e+00
CSS15
(g)
2
3
1
ODB: 400c_cru15_2.odb ABAQUS/Standard 6.3-1 Fri Apr 11 11:06:21 EDT 2003
Step: Step-1, No Heading For this Step
Increment 700: Step Time = 7.000
Primary Var: S, Mises
Deformed Var: U Deformation Scale Factor:

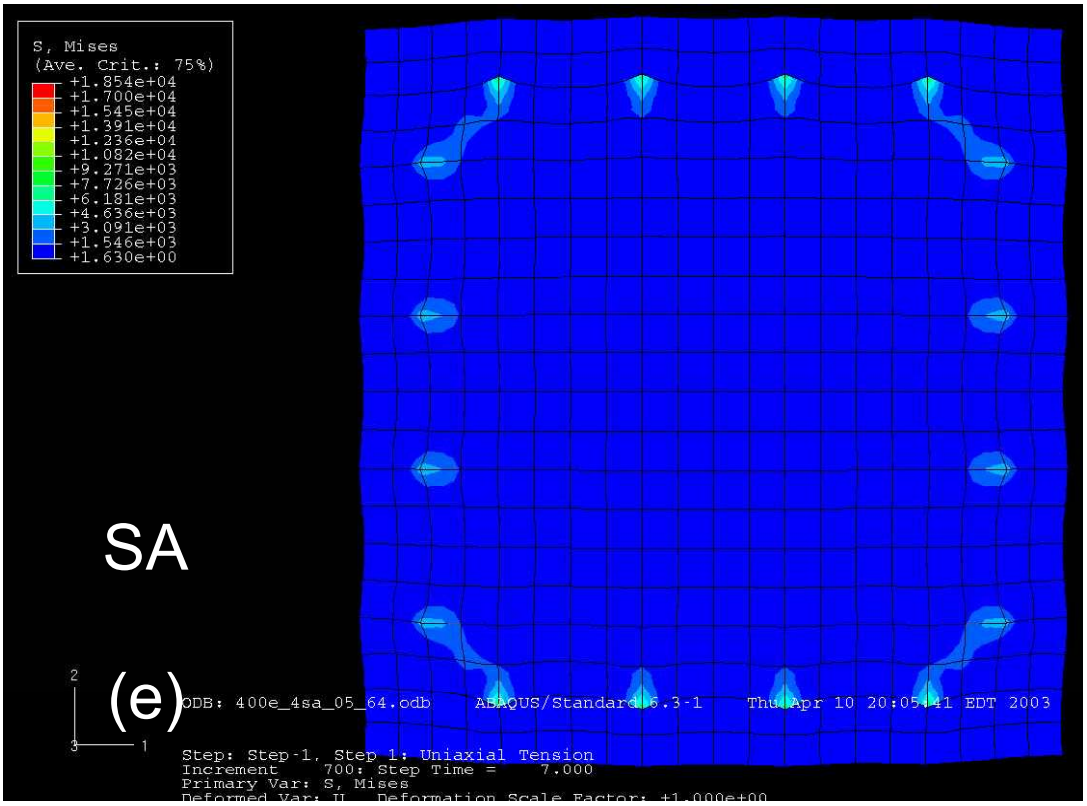
S, Mises
(Ave. Crit.: 75%)
+1.854e+04
+1.700e+04
+1.545e+04
+1.391e+04
+1.236e+04
+1.082e+04
+9.271e+03
+7.726e+03
+6.181e+03
+4.636e+03
+3.091e+03
+1.546e+03
+1.630e+00
SA
(e)
ODB: 400e_4sa_05_64.odb ABAQUS/Standard 6.3-1 Thu Apr 10 20:05:41 EDT 2003
Step: Step-1, Step 1: Uniaxial Tension
Increment 700: Step Time = 7.000
Primary Var: S, Mises

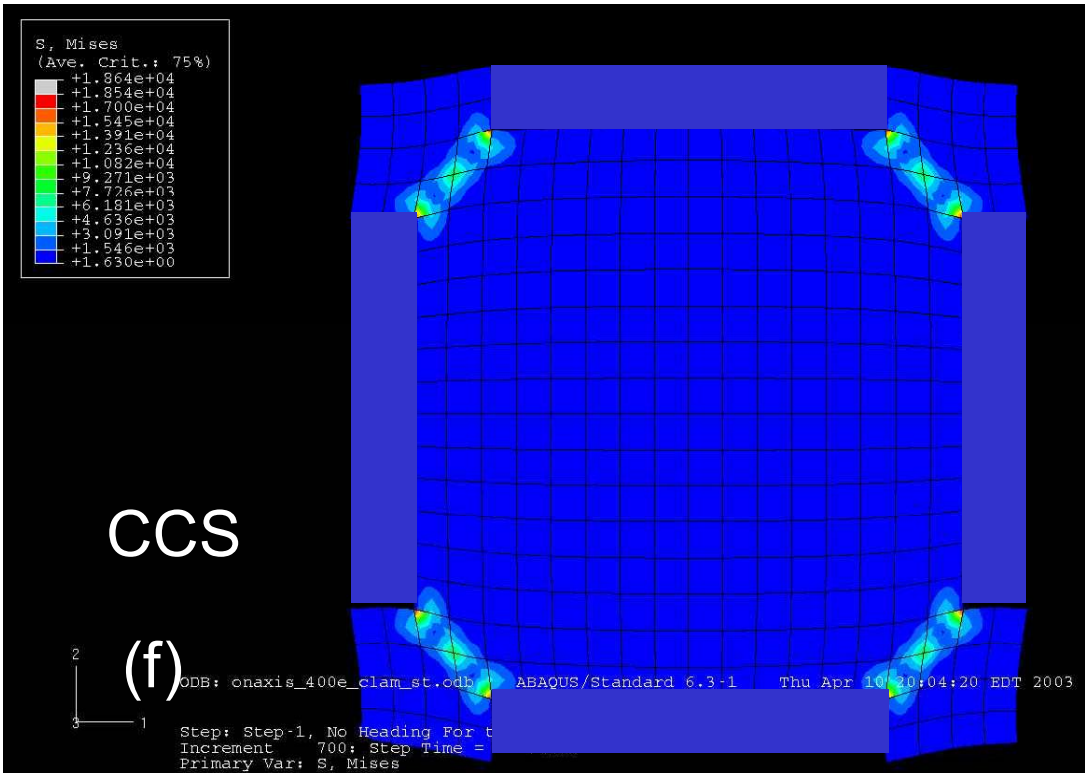
S, Mises
(Ave. Crit.: 75%)
+1.864e+04
+1.854e+04
+1.700e+04
+1.545e+04
+1.391e+04
+1.236e+04
+1.082e+04
+9.271e+03
+7.726e+03
+6.181e+03
+4.636e+03
+3.091e+03
+1.546e+03
+1.630e+00
CCS
(f)
ODB: onaxis_400e_clam_st.odb ABAQUS/Standard 6.3-1 Thu Apr 10 20:04:20 EDT 2003
Step: Step-1, No Heading For t
Increment 700: Step Time =
Primary Var: S, Mises

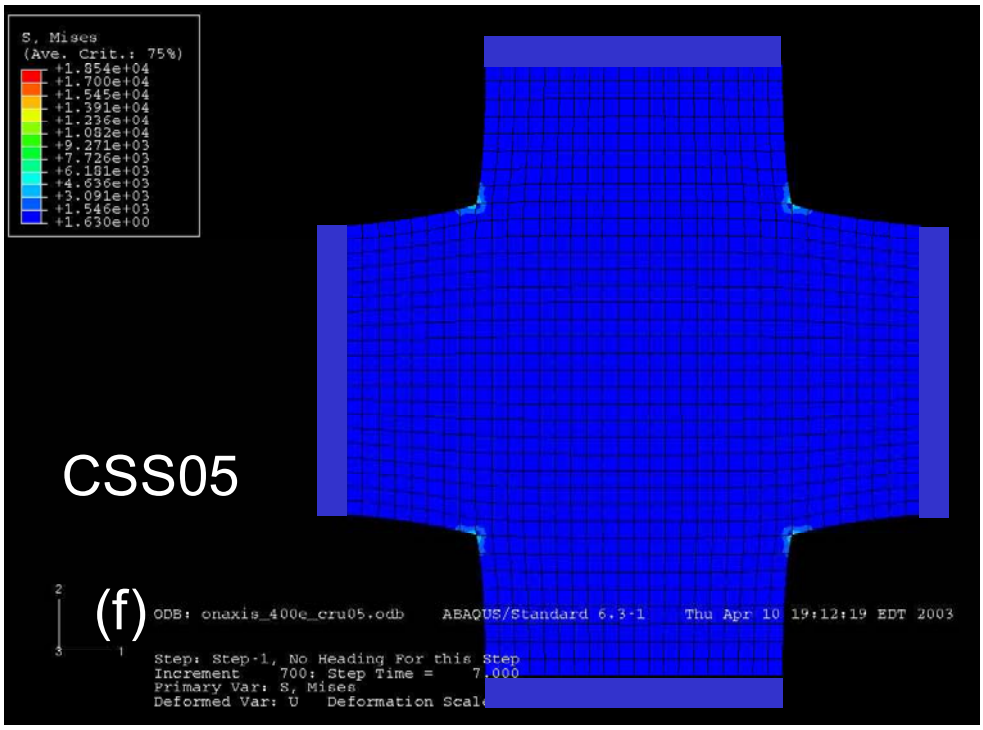

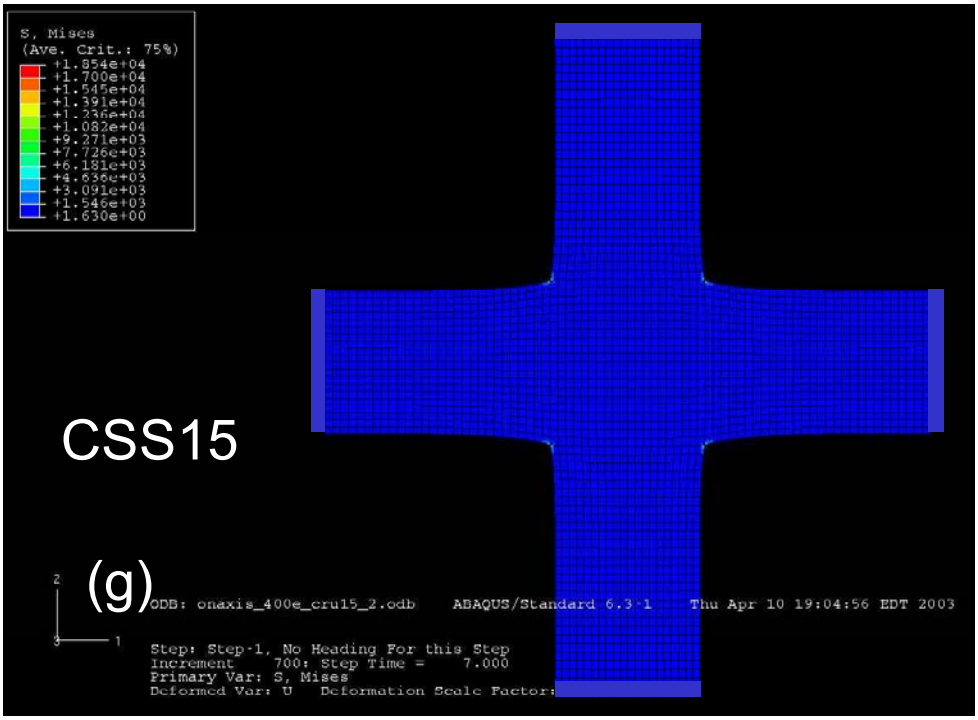

Figure 4-5 a-d) finite element simulation of effects of different gripping methods at 45-degree material axes, e-g) at 0-degree material axes. Plotted in same color scale in each group for easy comparison.

4.3.2 Effects of Different Gripping Methods

The deformation and von Mises stresses of finite element models with different gripping methods for 45-degree material axes are illustrated in Figure 4-5a-d. The SA configuration exhibited the most prominent anisotropic deformation, which is indicated by the material axis x_1 showing lesser extensibility than that of the orthogonal material axis x_2. This phenomenon corresponds with the observations from actual biaxial experiments. Similar shear deformation could be observed for CCS05 and CCS15. However, for CSS, the specimen shape remained almost square. High von Mises stresses always occurred in region A (Figure 4-2) due to the proximity of the corner and clamps (Figure 4-5b). The SA configuration exhibited the lowest stress in region A with von Mises stress of 8,382 kPa, while the CCS configuration had the highest stress of 26,510 kPa. Further investigation of the inner stress distribution of the central sixteen elements indicated that for CSS the stress and strain were only about 30 kPa and 0.045, respectively. For CCS05, CCS15 and SA, the stresses were about 220 kPa, 260 kPa and 490 kPa, respectively (Figure 4-6a).

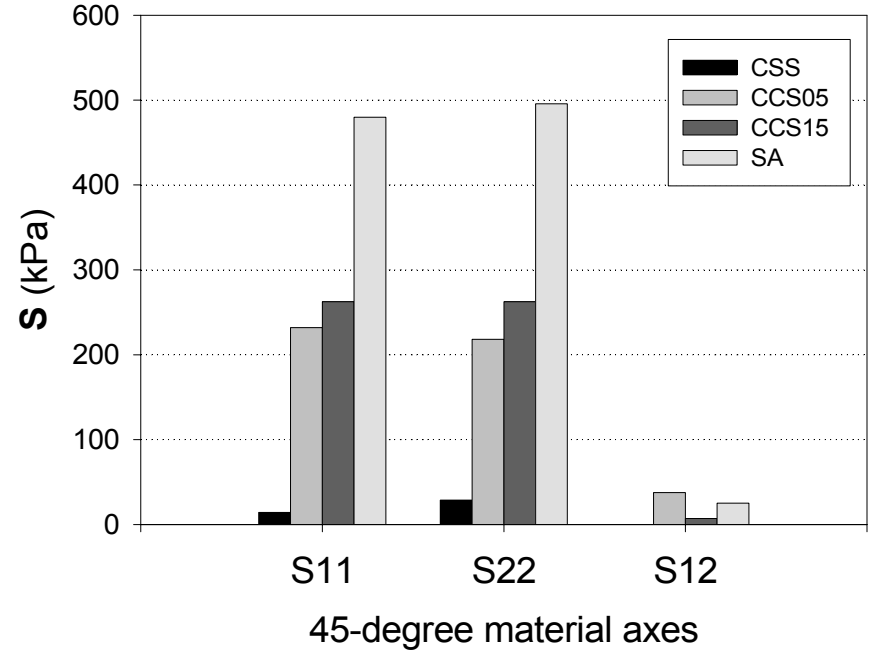

(a)

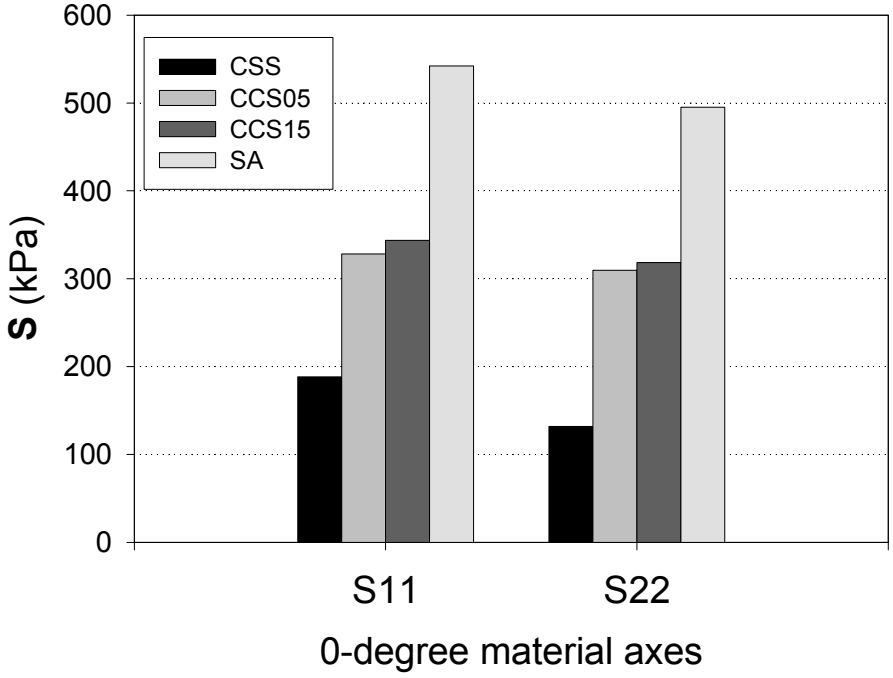

(b)

Figure 4-6 Peak stress of inner central regions for a) 45-degree and b) 0-degree material axes for different gripping methods.

For 0-degree material axes orientation (Figure 4-5, e-h), the deformations are orthogonal due to negligible shear effect when the loading axes were aligned with the material axes. High von Mises stresses also occurred in region A (Table 4-3), with lower magnitudes compared to 45-degree material axes setups. For the center region, there was a stress increase for the three clamp methods. The stress for CSS was 200 kPa, and for CCS05 and CCS15 the stresses were about 320 kPa and 340 kPa, respectively (Figure 4-6b).

Stress decay plots of different gripping methods (Figure 4-7) showed a substantial variation of the magnitude of stress decay along the BB line. For both 45- and 0-degree material axes setups, the SA configuration exhibited the least stress decay while the CSS configuration showed the most. For CCS05 and CCS15 configurations, the stress decays mainly happened in the leg region and were almost flattened in the square region of the specimen. A homogenous stress region could be obtained for the square regions of CCS05 and CCS15, which represent ~30% and ~14% of total sample areas, respectively, and the inner region of CSS configuration representing ~20% of the total specimen area. Compared to the 45-degree material axes setup (Figure 4-7a), the difference between CCS05 and CCS15 was reduced and CSS values were increased for 0-degree material axes setup.

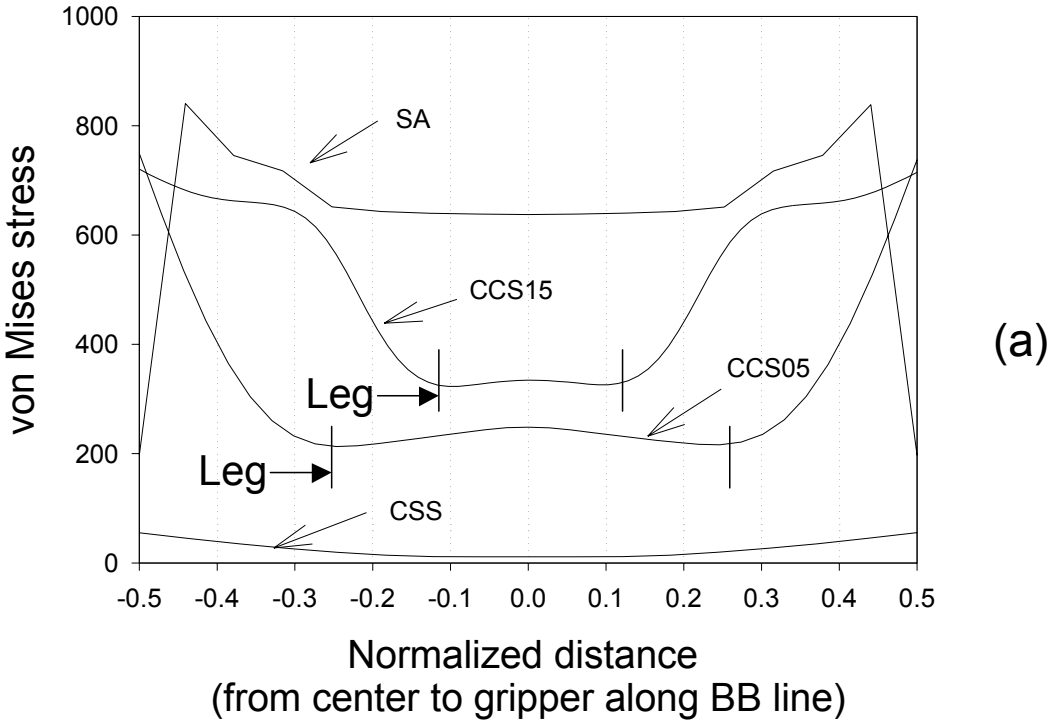

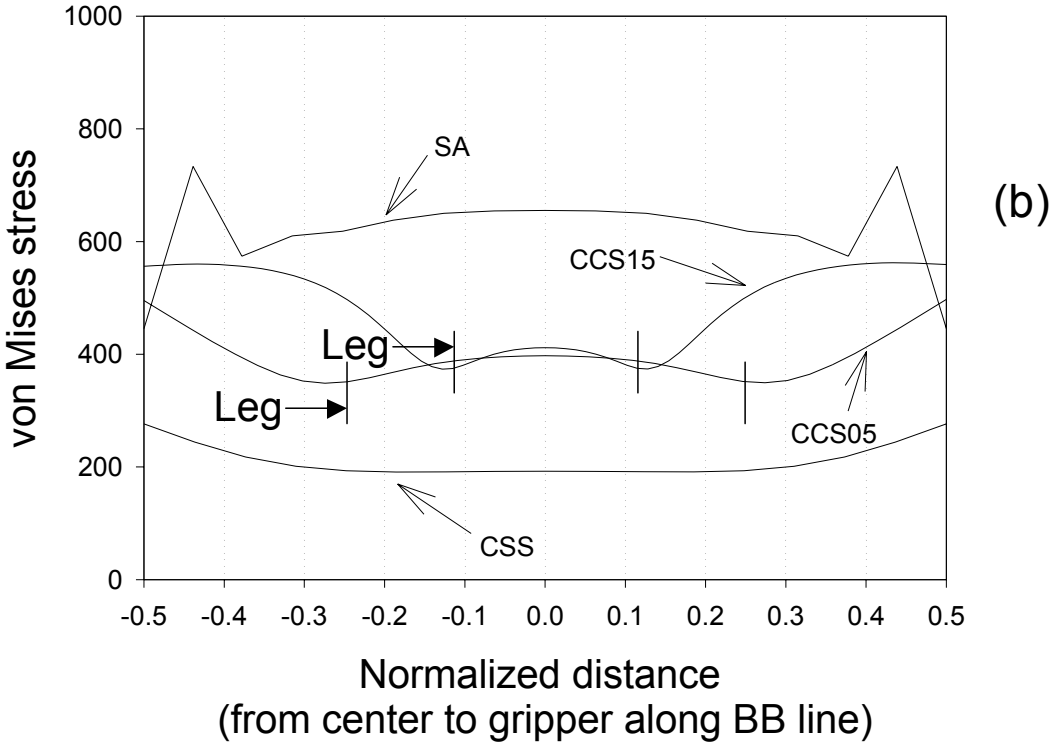

Figure 4-7 Stress decay along the BB lines of the finite element simulations for different gripping methods, a) for 45-degree material axis and b) for 0-degree material axis.

4.4 DISCUSSION

The effects of boundary conditions on biaxial tests of biological tissue were examined in this study by means of finite element simulations of biaxial tests with varied boundary conditions. Effects of different number of suture attachments, different gripping methods and specimen shapes, and different degree of tissue anisotropy were explored and compared. Numerical simulations results indicated that clamp methods had substantially lower stress in the central region of biaxial specimen compared to that of the suture attachment method, indicating that clamp methods had strong boundary condition effects. When material axes were aligned to the biaxial loading axes the clamped boundary artifacts were less severe, indicating that even under the same gripping method, material axes could play another important role affecting specimen inner stresses. These simulations, which have not been reported in the literature before, would provide experimentalists with more insight for designing experiments and interpreting experimental results

4.4.1 Experimentally, Why Do Clamped Tissues Appear to Be Stiffer Than with Suture Attachment?

In the experiments conducted by Waldman *et al.* [118], it was observed that the clamped tissue appears to be stiffer than with suture attachment. An explanation of this phenomenon has been developed by examining the local fiber orientation under different gripping methods [123]. The mechanism of load transfer to the underlying

fibrous architecture was explored qualitatively, however, not quantitatively. Our explanation is that without knowing that the Saint-Venant's principle was violated, experimentalists generally collect stress data by dividing the forces imposed on the grips by the sample undeformed cross-sectional area to obtain the Lagrangian stress. Strain data are usually collected via a non-invasive optical imaging system which tracks the deformation of a square region delimited by optical markers. If the actual loads transferred to the inner region of the tissues were affected by boundary conditions, as illustrated in Figure 4-6 and Figure 4-7, then the material would not deform as much as it supposed to be. This would result in a smaller strain. When plotting the Lagrangian stress vs. the strain, the tissue will appear to be stiffer and less extensible, which is the scenario observed by Waldman *et al.* [118].

4.4.2 Axial Coupling Effects

The substantial difference in the stress-strain response in the inner region observed with different griping methods may be attributed to the axial coupling stress in region A. The high axial coupling stress in region A will counteract boundary forces propagating into the inner region of the sample. The loads were actually "consumed" by the tissues in region A, instead of being transferred to the inner regions. The correlation between the axial coupling and the stress in the inner region can be observed by comparing the two material axes orientations for different gripping methods (Table 4-3). The 0-degree material axes setup has lower peak stresses in region A (Table 4-3) and higher stress in the inner region of the specimen. It was also observed

that, as listed in Table 4-3, SA setup has the lowest stress in region A compared to other setups and has the least boundary effects. The reason for it, we believe, is that the SA setup allows the tissue to expand lateral freely. In the SA setup, as point loads are imposed on the boundary of sample, the mobility of the collagen fiber are preserved; the tissue can expand not only along the loading direction, but also along the cross loading direction in response to the load from the other axis. This lateral expansion essentially reduces the high axial coupling stress in region A.

4.4.3 Degree of Tissue Anisotropy

Explicit comparison of the stress decay between isotropy material and anisotropy material was conducted in Chapter 3. By varying tissue material axes orientations, different stress decay behaviors were observed (Figure 4-7). The results suggest that when collagen fibers are more aligned with the loading directions, higher loads are transferred into the inner region of the specimen, probably through the collagen fibers. However, as the dominant boundary effects in our simulations are from the axial coupling, even though at 0-degree material axes orientation, we only observed the improved inner stress level for the clamp methods which were not totally free of boundary effects.

4.4.4 Concerns on Load Transfer through Local Fiber Architecture

Ever since Lanir and Fung first utilized the suture attachment method for biaxial testing of biological tissues in 1974 [32], the technique has been widely adopted by many experimentalists. However, it is not only time-consuming to put sutures on the edges of a small compliant tissue sample and but also meticulous care is required to make the sutures evenly spaced along specimen edges. Additionally, suspicions that sutures may not faithfully mimic the loading condition *in vivo* lead to other gripping methods such as clamping of a square sample and cruciform sample. These latter methods are much easier to accomplish and have been widely used in industry for mechanical testing of metallic and polymer materials. Langdon *et al.* [89] pointed out that *in vivo* fiber rearrangement under load is restricted by the attachments of the fibers at the tissue margins, for example, at the sternal or diaphragmatic attachments in the pericardium. For the SA setup, fiber mobility may be enhanced and mechanical properties may be artifactually altered. Thus cruciate geometry may offer a more realistic model of *in vivo* function since at least the fibers that run from clamp-to-clamp are restricted in their mobility. However, in theory, mechanical properties of material should be independent of testing methods, i.e., regardless of whether it is a suture attachment setup or a clamped setup. The intentionally introduced boundary effects should be treated as an application of special loading/boundary conditions to the tissue, regardless whether the Sanit-Venant's principle is justified, instead of testing the tissue in a general loading state to deduce its mechanical properties, with certainty that the Sanit-Venant's principle is not violated. In general, a careful experiment design should first avoid the

violation of the Saint-Venant's principle, and then consider more physiological conditions.

It should be noted that our finite element simulations of biaxial testing applied to a chemical treated tissue (GLBP), with specimen size of 25x25x0.4mm^3, and the dimensions of clamp and positioning of sutures as listed in Table 4-2 and 4-3, and the findings should be interpreted in the light of these restrictions.

4.5 SUMMARY

Overall the three clamp methods had substantially lower stress in the central region compared to the suture attachment method. These results indicated that the clamp methods had strong boundary condition effects. Moreover, for the clamped methods the material in the inner region of the specimen was not fully loaded and therefore would not be fully stretched. The high stress concentrations for these methods makes the tissue appear to be stiffer, which is the scenario observed by Waldman *et al.* [118]. Apparently in biaxial testing of GLBP, suture attachment method is recommended. This study presented the first finite element simulations of biaxial tests under different gripping setups and different material axes orientations. These comprehensive, even though not exhaustive, biaxial test simulations would provide experimentalists more insights into interpreting experimental results.

5.0 FINITE ELEMENT SIMULATIONS – 3D TRI-LEAFLET BIOPROSTHETIC VALVE SIMULATIONS

In the previous chapters, we have successfully implemented the Fung model into finite element and conducted biaxial test simulations under different boundary conditions. These studies act as stepping-stones that lead us to our ultimate goal, the simulation of bioprosthetic valve behaviors of this chapter. The contributions of this chapter can be divided in two parts; one is a rigorous experiment, characterizing quasi-static valve deformation under 120mmHg trans-valvular pressure. The other part is the finite element simulations of heart valve behavior, particularly the parametric study of valve stress distribution under various conditions.

The importance of experimental validation of finite element results cannot be over-emphasized. However, the experimental studies of valve deformation are relatively expensive and difficult to perform because of practical limitations in measurements very close to the leaflets and valve housing. Moreover, most finite element models used linear, isotropic material models that lead to inaccurate simulation results; consequently, a match between finite element result and experiment data is hard to achieve. Many finite element studies offered no experimental validation [67-70] or simple validations, such as comparison between images taken from pulse duplicator to

that of a finite element output[71, 72]. A rigorous validation should be the comparison of strain fields of experimental and finite element output. In this chapter we will address such an experiment in section 5.2. We will report the surface reconstruction from 3D digitized marker affixed on the surface of the leaflets and the method of how we compute in-plane membrane strain in sections 5.2.3 and 5.2.4, respectively. The finite element model was constructed based on the design geometry of leaflets and stent[§] provided by Edwards Lifesciences Inc. (Irvine, CA). Mechanical properties were obtained by biaxial testing of the leaflets dissected from the valve (section 5.3.2). After validation by the experiment, the finite element model can be used to evaluate various valve design parameters, such as with varying leaflets properties and fiber orientation (sections 5.2.7 and 5.3.5) in this study. Those finite element simulations will provide otherwise unobtainable, valuable information for optimal valve design.

5.1 INTRODUCTION

There have been many studies showing that the regions of tearing of BHV correlate with the regions of high tensile and bending stresses acting on the leaflets during opening and closing [124]. Stress concentrations within the cusp can either directly accelerate tissue structural fatigue damage, or initiate calcification by causing structural

[§] We also call it wireframe, because in finite element model the stent is simplified with only wireframe present.

disintegration, enabling multiple pathways of calcification [125] that lead to valve failure. Although details of the process are unclear, it is widely accepted that the design of the valve, which gives a stress-reduced state of the leaflets, is likely to give improved performance in long-term applications.

Finite element analysis has been the most effective method for the stress analysis and evaluation of a valve design [67, 69, 76]. Moreover, numerical analysis and simulation of BHV enable us to have better understanding of true valve behaviors. A brief summary of the previous studies on quasi-static heart valve simulations is listed in Table 5-1. The leaflet material model and experimental validation of numerical results are of particular interests to us and are therefore tabulated. Some of the interesting findings of those studies will be presented in section 5.1.2.

Table 5-1 Previous studies on quasi-static heart valve simulations.

Authors	Year	Element	Valve	Leaflet material model	Experimental validation
Cataloglu et al [126]	1977	Unknown	Human aortic valve	Linear isotropic elastic model	No
Hamid *et al.* [68]	1986	Membrane	Porcine tri-leaflets valve	Multi-step linear elastic model	No
Rousseau *et al.* [127]	1988	Membrane	Hancock porcine tri-leaflet valve, 1/6 valve simulated	Visco-elastic model for leaflet, leaflet is defined by linear elastic matrix embedded with linear elastic truss element as fiber reinforcement	Yes, commissure displacement was measured based on a voltage and distance relationship between the two attached electrical coils; leaflet center displacement was measured cinematographically.
Huang *et al.* [69]	1990	2d element	Sheffield pericardial bicuspid valve	Nonlinear isotropic hyperelastic model based on W=c1*exp(c2*I1^2+c3*I2+c4*I3)	No
Black *et al.* [67]	1991	Shell	Sheffield pericardial bicuspid valve	Nonlinear isotropic hyperelastic model based on W=c*exp(c1*I1^2+c2*I2)	No
Krucinski *et al.* [72]	1993	20-node brick element	Tri-leaflet bovine pericardial valve	Nonlinear isotropic hyperelastic model	Comparison between images taken from pulse duplicator and FEM
Patterson et al	1996	Shell	Sheffield pericardial bicuspid valve	Nonlinear isotropic hyperelastic model	No
Thornton *et al.* [128]	1997	Shell	Sheffield pericardial valve bicuspid valve	Nonlinear isotropic hyperelastic model	No
Grande *et al.* [129, 130]	1998 /9	6-node triangle shell	Human aortic valve and root	Linear anisotropic elastic model	No
Burriesci *et al* [71].	1999	Shell	Sheffield pericardial bicuspid valve	Orthotropic model defined by a finite number of points of the stress-strain curve	Comparison between images from pulse duplicator and FEM
Cacciola *et al.* [131]	2000	Shell	Synthetic fiber-reinforced tri-leaflet aortic valve	Fiber-reinforced model, with linear elastic properties for both matrix and fiber	Comparison between images from pulse duplicator and FEM
Li *et al.* [70]	2001	Shell	Porcine aortic valve, 1/2 leaflet simulated	Use strain depend E, use five elastic moduli, transversely isotropic model	No

5.1.1 Finite Element Simulations at Valve Level

Particular challenges encountered in numerical simulation of BHV include modeling of complex leaflets and stent geometry, modeling of the associated (nonlinear anisotropic) mechanical properties, contact of leaflets, and experimental validation of numerical result. Among them, the most crucial one probably is the modeling of leaflet mechanical properties. From Table 5-1, it is obvious that most of the previous studies used either linear elastic models or nonlinear isotropic material models. Using strain (or time) depend elastic moduli or fiber-reinforced material model can approximate the nonlinear anisotropic material properties of the leaflets, however, they are not accurate. We know that the material models based on a nonlinear anisotropic strain energy function can accurately capture the material responses, such as the Fung model described in Chapter 3. Nonetheless, such model has not been used for a BHV simulation in the literature.

5.1.2 Findings in the Previous Studies

Although conducted with simplified material models, studies have shown that by changing valve design, such as using difference manufacturing techniques [126], changing leaflets shapes [73, 127] and frame mounting methods [72, 126, 128, 129], the stress distribution pattern acting on the leaflets could be altered.

Numerical studies on synthetic polyurethane valves have shown that a stentless synthetic valve, which has flexible aorta base, can be a good alternative for stented valves. The results in Cacciola *et al.* [129] indicated that the stentless design reduces the stress peaks by up to 80% for a sinusoidal fiber reinforcement layout with respect to a stented valve with the same reinforcement. Moreover, a fiber-reinforcement configuration is assumed to lead to a decrease of tears and perforation as a result of reduced stresses in the weaker parts of the leaflets in their closed configuration [128].

Effects of different material models have also been investigated. Patterson *et al.* [76] compared the effects of using *linear* and *nonlinear isotropic* elastic model of the leaflets, they found that the nonlinear model was more responsive to time-varying pressure wave, and induces lower compressive but higher tensile stresses in the leaflets. Burriesci *et al*. (1999) studied the effects of *orthotropy* of a pericardium heart valve and found that even a small amount of orthotropy can significantly affect the mechanical behavior of the valve. Those studies, however, have overlooked or simplified the nonlinear *anisotropic* property of the valve material [70]. From the experimental procedure and constitutive modeling techniques we developed in Chapters 2 and 3, we have the ability to build more accurate valve models and conduct more accurate simulations. In this chapter, quasi-static valve deformation under 120 mmHg trans-valvular pressure will be investigated both experimentally and numerically. Once the numerical model is validated by the experimental data, various valve design parameters can be evaluated relatively inexpensively. In this study, we will illustrate the methodology by conducting

some readily available parametric studies, such as varying leaflets properties and fiber orientation changes.

5.2 METHODS

5.2.1 Overall Description of Valve Deformation Experiment

Valve leaflets were prepared with approximately 90 tiny graphite markers affixed over the surface. We then placed the valve in a custom-made rigid valve housing (Figure 5-1) and slowly applied an increasing trans-valvular pressure to 120 mmHg. The valve surface was imaged at 0 mmHg and 120 mmHg by two cameras simultaneously. The resulting images were digitized and the 3D marker positions reconstructed using Direct Linear Transformation (DLT) technique. Local deformation and strains were computed. After testing, the valve was disassembled. SALS and biaxial tests of dissected leaflets were conducted to quantify the leaflet mechanical properties and local collagen structure. These two important pieces of information were incorporated into finite element model. The strain space of leaflets was used to compare with the strain space from finite element output for the validation of finite element model. All three leaflets of one valve were tested in the experiment.

5.2.2 Experiment Procedure

- Valves were ordered from Edwards Lifesciences Inc.

- About 90-100 tiny graphite markers with size of about 0.2 ~0.4 mm in diameter were carefully glued on the aortic side surfaces of the leaflets.
- The valve was sutured in the mounting post such that the base of the valve was fixed.
- Two cameras were positioned angled and orthogonal to the leaflet surfaces and images were taken simultaneously. This was to record the leaflets position at 0 and 120 mmHg.
- A calibration unit was guided using a wire and gently positioned on the top surface of leaflets. Images from two cameras were recorded. These images were used as calibration images.
- The valve housing was filled with saline and trans-valvular pressures of 120 mmHg were gradually applied; the pressure level was monitored by a pressure sensor.
- At 120 mmHg, images were recorded again.
- Images were post-processed using SigmaScan (SPSS Inc., Chicago, Illinois), in which pixel locations of markers and calibration points were generated from the images to calculate the 3D coordinates of markers, by using DLT technique.
- A triangle mesh was generated based on marker locations to form a 3D surface.
- SALS testing [130] was conducted on the three leaflets to quantify the leaflet fiber architecture.

- Biaxial mechanical testing was conducted on the three leaflets, following the procedure described in Section 2.2.3, to quantify the leaflet mechanical properties.

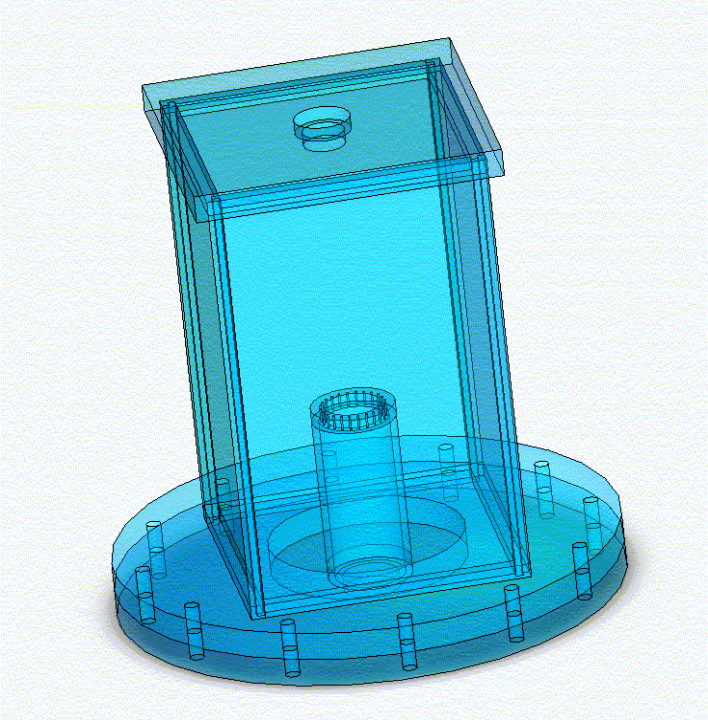

Figure 5-1 A custom-made valve housing, in which a BHV valve will be sutured in the mounting post and hydraulic pressure of 120 mmHg will be applied on the valve.

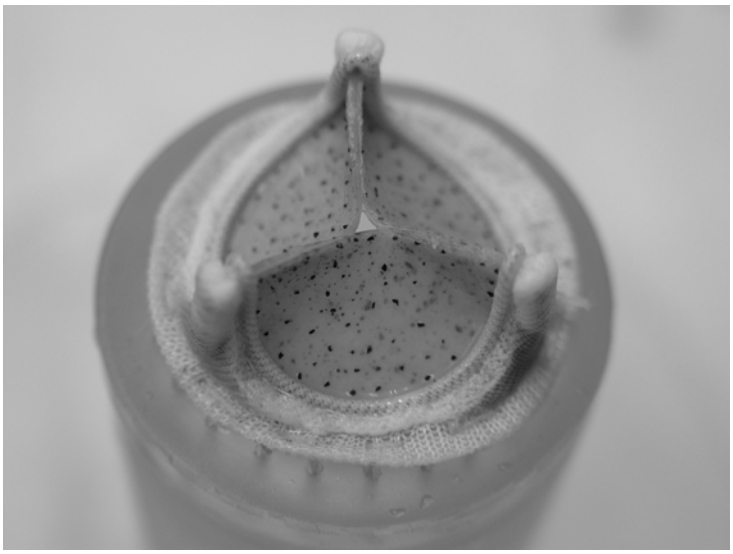

Figure 5-2 a BHV mounted in the valve deformation chamber with leaflets showing the locations of the markers. The valve size is 23mm.

5.2.3 Direct Linear Transformation (DLT)

To calculate the 3D location of objects from two different views, a process termed Direct linear transformation (DLT) was used [131]. DLT takes a calibration phantom with both the pixel coordinate from the two views and 3D coordinate of eight locations of the object (Figure 5-3). A mathematical formula calculates 11 parameters using the calibration phantom, parameters which describes the location of camera, the angle with respect to each other, focal distance, etc. These parameters when placed in the original formula form a set of 4 equations wherein pixel coordinates can translate to X, Y, Z coordinates. To solve for X, Y, Z, only 3 equations are necessary but the 4th equation can be used for error checking. After the 3D coordinates of all points were calculated, triangulation was conducted to generate a 3D mesh.

$$u1 = (aX + bY + cZ + d)/(iX + jY + kZ + 1) \tag{5.1}$$

$$v1 = (eX + fY + gZ + h)/(iX + jY + kZ + 1) \tag{5.2}$$

$$u2 = (aX + bY + CZ + d)/(iX + jY + kZ + 1) \tag{5.3}$$

$$v2 = (eX + fY + gZ + h)/(iX + jY + kZ + 1) \tag{5.4}$$

where u, v denote camera coordinates, 1, 2 denote camera number; a, b, c, d, e, f, g, h, i, j, k denote camera constants; X, Y, Z denotes 3D global coordinates.

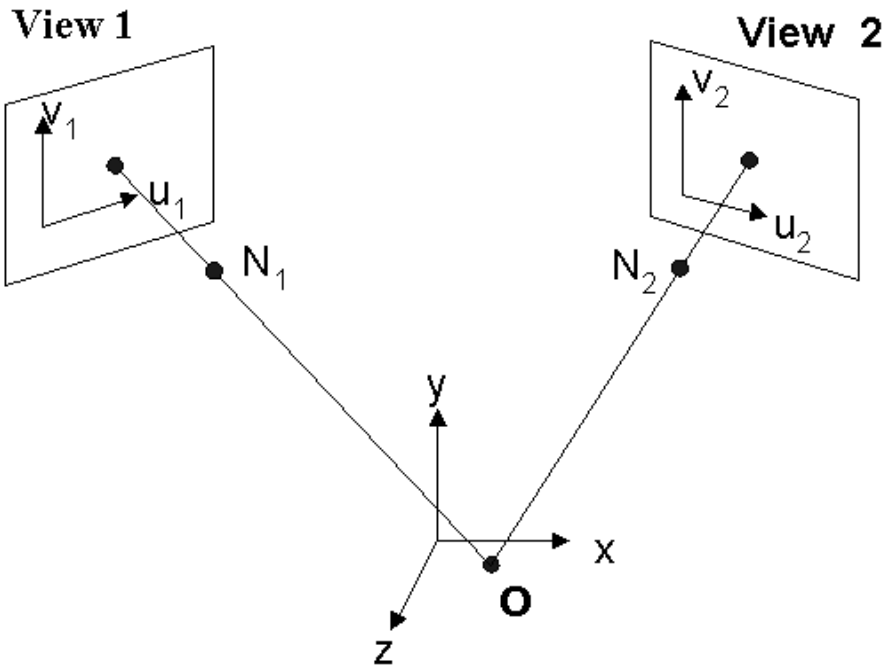

Figure 5-3 Schematic of how 3D marker position is calculated. To acquire object O's XYZ coordinates, two views, view 1 and view 2, are needed. The horizontal and vertical pixel coordinate, u, v are recorded and inserted into eqns 5.1 – 5.4 [131], reproduced from Sugimoto *et al*.[131] with permission.

5.2.4 Local Deformation and Strain Calculation

To calculate the local deformation gradient and consequently the local strain, the marker position before and after deformation and the triangulation information were input into a custom made Matlab program. From this the local coordinate system was created for each triangle and in-plane strain was calculated.

Creation of local coordinate system. For each triangle, for example the undeformed triangle ABC in Figure 5-4, a local coordinate system $o'x'y'z'$ was created following the steps described below:

- The origin of the $o'x'y'z'$ will be one of vertices, vertex A, of the triangle ABC.

- The $o'x'$ axis will be the vector of one edge, edge AB, of the triangle
- The $o'z'$ axis will be created as the cross product of the two vectors of the two edges, AB and AC.
- The $o'y'$ axis will be cross product of $o'x$ axis and $o'z'$ axis.
- The angle between the $o'z'$ axis and global oz axis will be calculated. If within 90 degree, the $o'z'$ is in the normal direction pointing towards the aortic side (this is due to the way the data collected). Otherwise, the reverse of the $o'z'$ will be calculated and $o'x'$ and $o'y'$ axes will be switched.

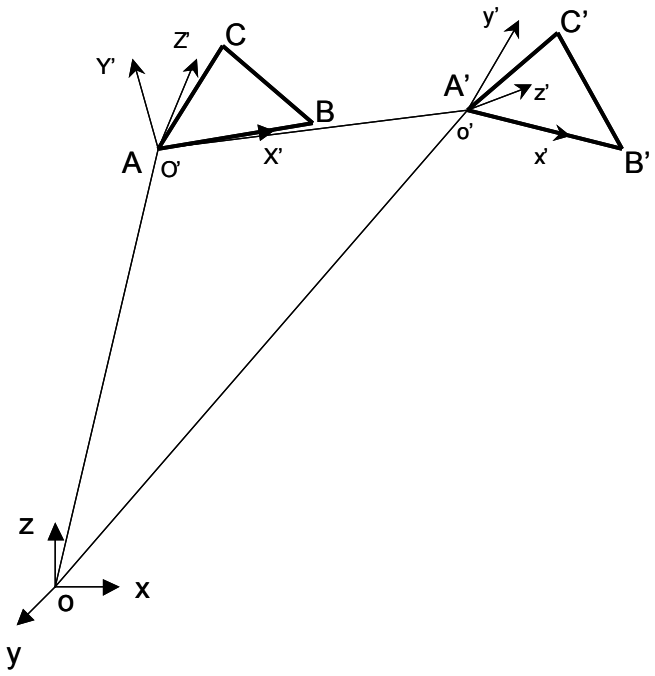

Figure 5-4 Deformation and strain calculation based on the motion of a triangle (ABC) in the reference state and (A'B'C') in the current state. The triangle has its own local coordinate system, with the oz axis aligned with its surface normal direction during the motion.

Another local coordinate system will be created in the same way for the deformed triangle A'B'C'. Note that the construction of such a local coordination

system will facilitate the calculation of in-plane membrane strain, which can be used directly to compare with finite element output, because our finite element simulation is based on the shell element.

Transformation from global to local coordinate system. 3D coordinates of the markers in the global coordinate system *oxyz* need to be transformed to the local system *o'x'y'z'* to facilitate the strain calculation.

Let the angles between *o'x'* and *ox*, *oy*, *oz* axes are a1, b1, r1, respectively; the angles between *o'y'* and *ox*, *oy*, *oz* axes are a2, b2, r3, respectively; the angles between *o'z'* and *ox*, *oy*, *oz* axes are a3, b3, r3, respectively. The transformation of a point (*x, y, z*) in the global to the corresponding point (*x', y', z'*) in the local coordinate system is obtained by:

$$x'=x*\cos(a1)+y*\cos(b1)+z*\cos(r1) \tag{5.5}$$

$$y'=x*\cos(a2)+y*\cos(b2)+z*\cos(r2) \tag{5.6}$$

$$z'=x*\cos(a3)+y*\cos(b3)+z*\cos(r3) \tag{5.7}$$

Note that after the transformation, the triangle lies in the *o'-x'-y'* plane and *z'* coordinate is vanished.

2D deformation gradient. Assuming the markers are closely placed and such, the deformation is homogenous within a triangle, the 2D deformation gradient F can be calculated:

$$F = \begin{bmatrix} AB_X & AC_X \\ AB_Y & AC_Y \end{bmatrix} \begin{bmatrix} A'B'_X & A'C'_X \\ A'B'_Y & A'C'_Y \end{bmatrix}^{-1} \tag{5.8}$$

where AB_x represents the x component of the vector AB, and AB_y represents the y component of the vector AB. Similar calculations are used for the other vectors. Note that due to the local coordinate system configuration, the deformation obtained has already "removed" the rigid body rotation, which is represented by the linear transform of AA′ and the rotation from the AB direction to the A′B′ direction.

5.2.5 FEM Model Assumptions

The finite element model must be simple enough to permit a solution for the displacements and stresses to be found using the computational resources that are available, and yet still have sufficient details for it to be an acceptable representation of the real problem. In this study, a quasi-static approach was used to analyze the deformation of the model from a stress-free position to a fully closed configuration by applying a uniform pressure, rather than a time-varying, spatially non-uniform distribution. The valve ring is fixed spatially such that no interaction with the aortic wall is taken into consideration. It is assumed that there is no heterogeneousness within a single leaflet such that one whole leaflet can be modeled with one set of material parameters. Uniform thickness of the leaflets is also assumed, as the pericardium valve usually has uniform leaflet thickness.

5.2.6 Finite Element Model Components

Geometry of the finite element model was obtained from Edwards Lifesciences Inc. based on a prototype valve developed in Edwards R&D department. The valve used in the experiment is manufactured based on the prototype. Therefore it can be reasonably assumed that the valve used in the experiment has the same geometry as the finite element model. This prototype has symmetric trileaflets and wireframe. The finite element model includes:

Wireform Wireform was modeled using beam element (ABAQUS element type B31 (2-node linear beam element)) with Young's modulus of 23.3×10^6 psi and Poisson ratio of 0.3, the wireform was "stitched" to the trileaflets (Figure 5-5).

Leaflet Tri-leaflets were modeled using mixed quadrilateral and triangular large strain shell elements (ABAQUS element type S4R (4-node, quadrilateral, finite strain with reduced integration) and S3R (3-node, triangular, finite strain with reduced integration)). Uniform thickness will be applied. Each leaflet had its own local coordinate system. Collagen fiber orientation is controlled via the constitutive law built in user subroutine UMAT.

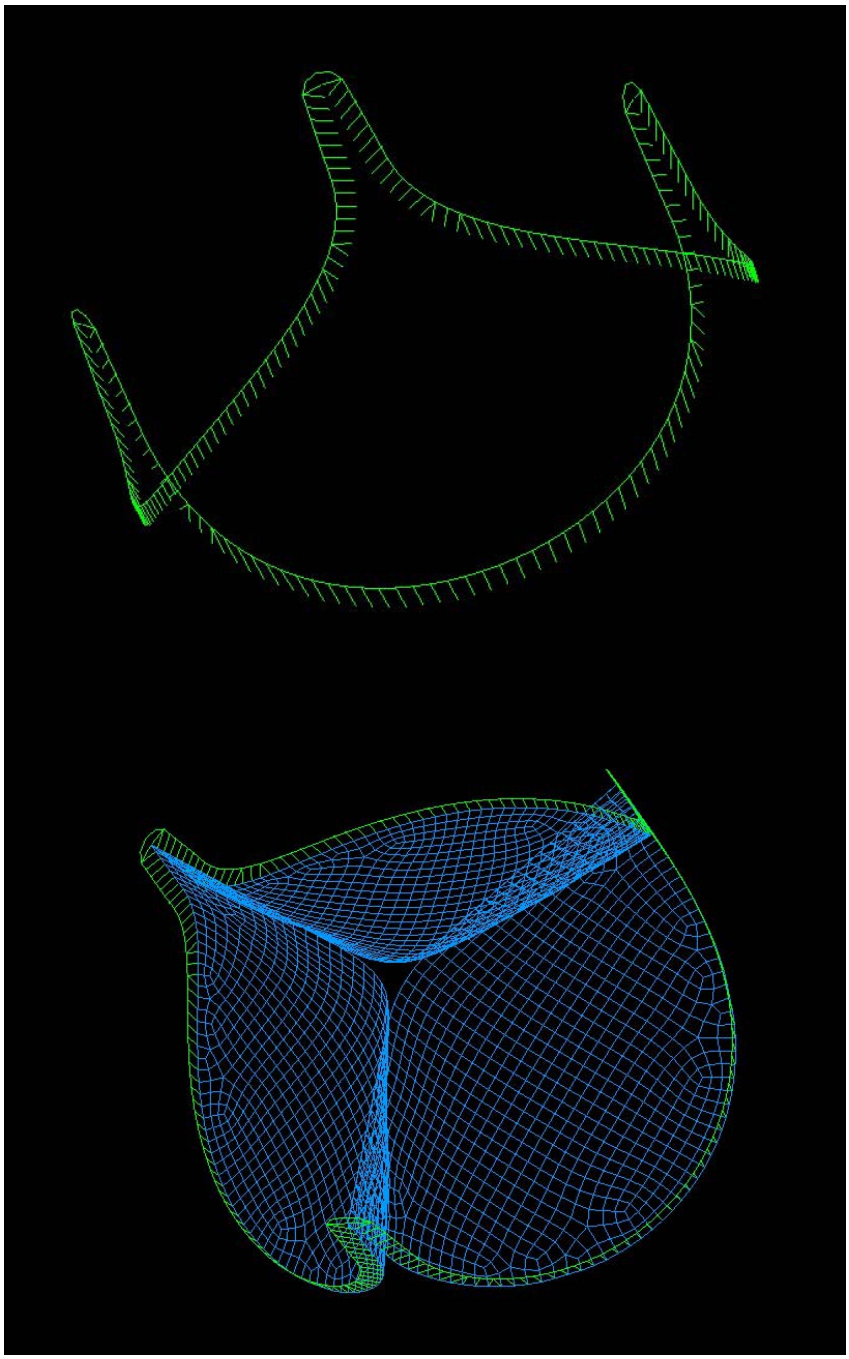

Figure 5-5 FEM model with (top) wireform, (bottom) trileaflets.

5.2.7 Finite element model variables

We have conducted a preliminary study to examine effects of various finite element variables. In that study, 120 mmHg of trans-valvular pressure was imposed on

the leaflet. A Fung-type tissue model, obtained from the biaxial testing of GLBP of the Chapter 2, was used in the simulations. The results showed that with random, uncontrolled fiber orientations, the stress-strain distribution pattern in each leaflet is different (Figure 5-6). It is suspected that the unbalanced stress-strain distribution may accelerate the damage of one leaflet. This observation motivated us to conduct a more detail study on the effects of leaflet properties, such as varying fiber orientation and degree of tissue anisotropy (will be addressed in detail in the following sections), which, to our knowledge, has not been studied before in the literature.

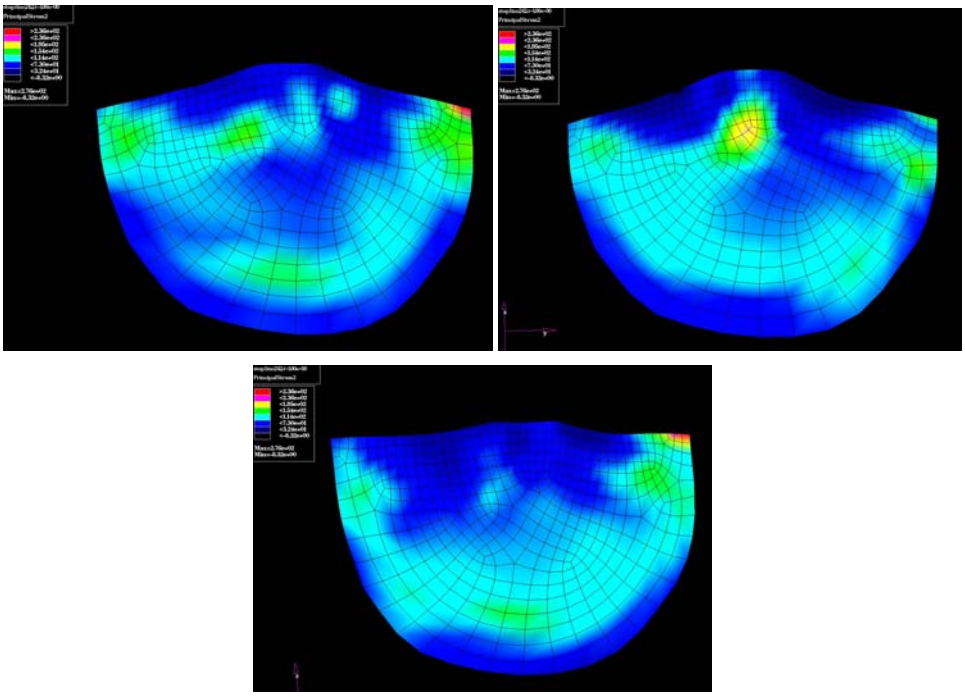

Figure 5-6 von Mises stress distribution for each of the trileaflets, even though the leaflets are modeled symmetrically, however, due to the random material properties of each leaflet, the high stress occurred in different locations.

5.2.8 Effects of Engineered Tissue Anisotropy

Engineering tissue anisotropy is not a well-known concept. We briefly recap its underlying mechanism as follows: it is widely accepted that glutaraldehyde fixation introduces a large number of stable crosslinks between the amino acid groups of the polypetide chains of collagen [132]. It has been observed that the collagen fiber architecture – and the corresponding mechanical behavior- are changed with different pressure of chemical fixation. SALS data for a bovine pericardial sample (Figure 5-7a) before and (Figure 5-7b) after undergoing biaxial stretch also indicated collagen fiber re-orientation and alignment. If the pericardial sample was chemically fixed at a pre-loaded state, the collagen fiber structure at that state will be locked; the corresponding mechanical behavior will be consequently changed. Therefore we can manipulate GLBP tissue properties and "make" a tissue with desired properties. For example, one has one direction stiffer and the other direction more compliant (Figure 5-8). Of particular interest will be the ability to simulate valve stress-strain distribution by varying the degree of anisotropy with engineered GLBP tissue and evaluate how much we can benefit by using those engineered tissues.

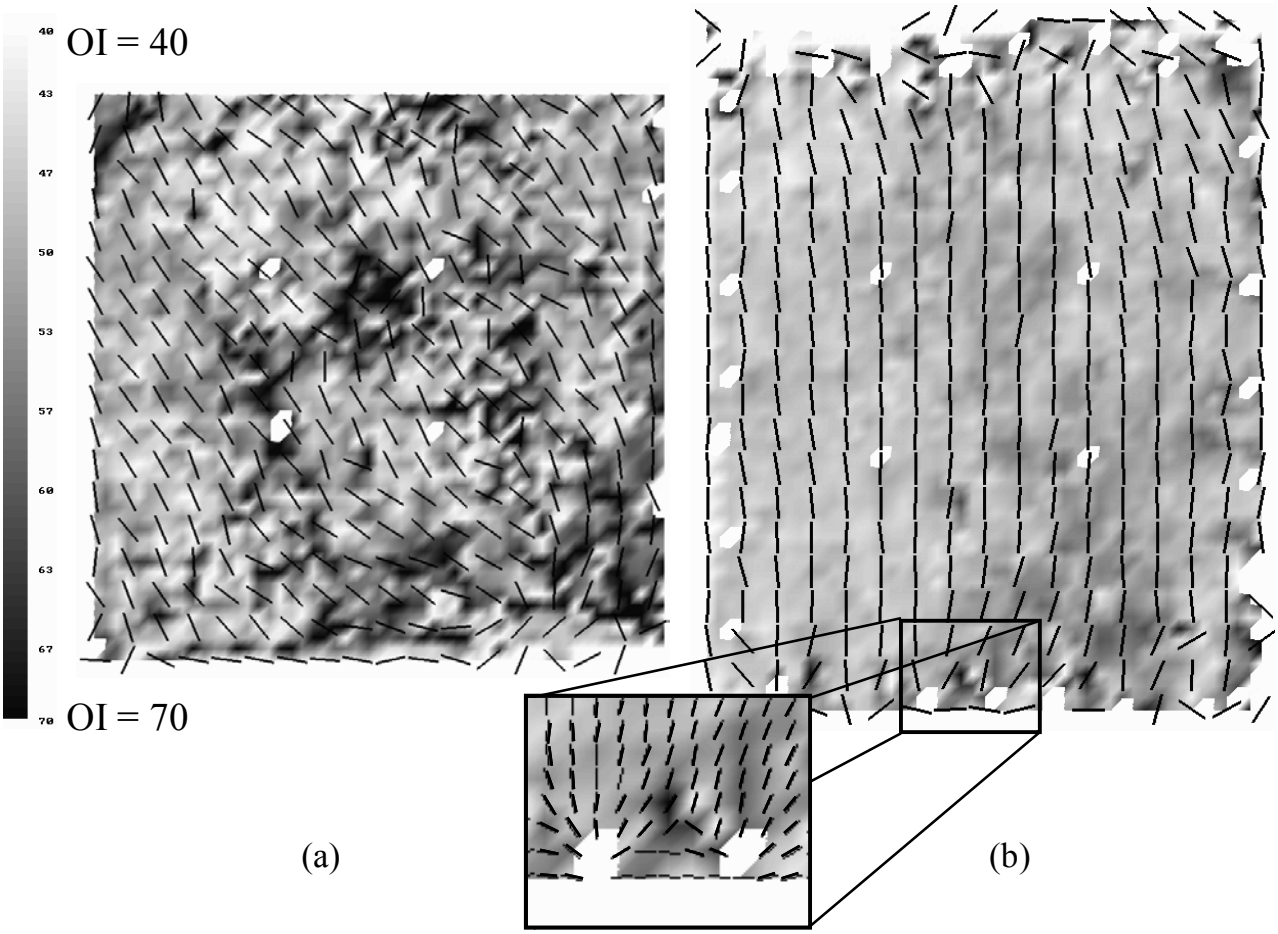

Figure 5-7 SALS data for a bovine pericardial sample (a) before and (b) after undergoing biaxial stretch (λ_1=1.1, λ_2=1.3, shear=0). The vectors represent the local preferred fiber orientations; only every third data point is displayed for clarity. The background shading indicates the degree of orientation (lighter = more highly aligned fiber population). The white areas occur due to suture attachment points or markers. Note the substantial reorientation of the fibers and decrease in variability of tissue structure with stretch, and the local reorientation around the attachment points (inlay).

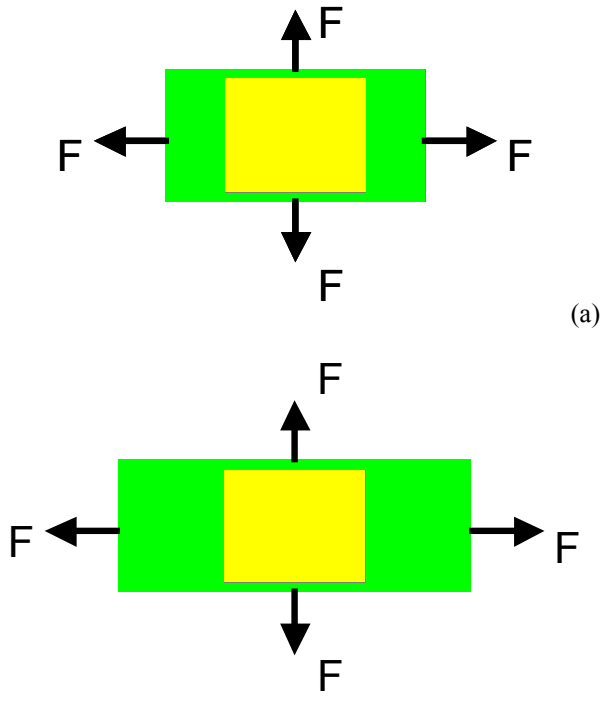

Figure 5-8 Effects of engineered tissue anisotropy. (a) before changing tissue properties, corresponding to the state in Figure 5-7a; (a) after changing tissue properties, corresponding to the state in Figure 5-7b.

5.3 RESULTS

5.3.1 3D Mesh of the Valve Deformation

Representative 3D triangle mesh was shown in Figure 5-9. Two meshes, one for the valve under 0 mmHg and the other for 120 mmHg, with same marker sequence were generated for each leaflet. The principal strain was calculated based on corresponding triangles of these two meshes. Out of the three leaflets, we were able to obtain strain fields for two leaflets, i.e., leaflet0 and leaflet1.

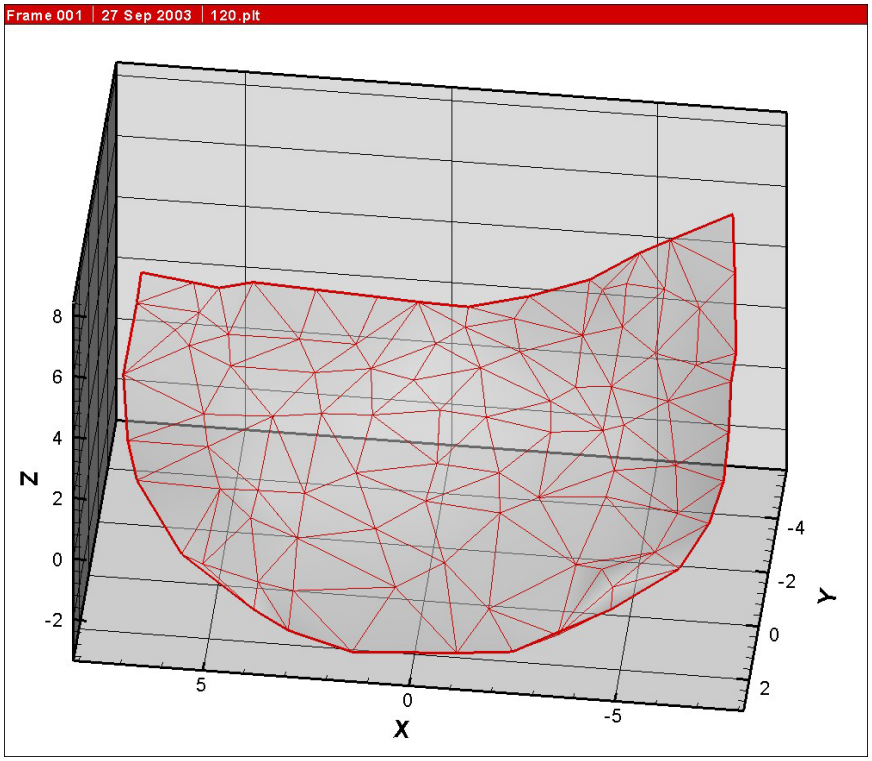

Figure 5-9 The 3D reconstruction/triangulation of the makers obtained from the two images when the valve is deformed under 120 mmHg pressure.

5.3.2 SALS Results

SALS scanning data showed a relatively homogenous fiber distribution with the preferred fiber orientation along the 45-degree angle for leaflet2 and 135-degree for leaflet0 and leaflet1. This indicated that the pericardium tissue used in Edwards Lifesciences Inc. underwent pre-sorted and controlled selection procedure. This homogenous fiber distribution enabled us to easily manipulate the material axes of leaflets in the finite element model.

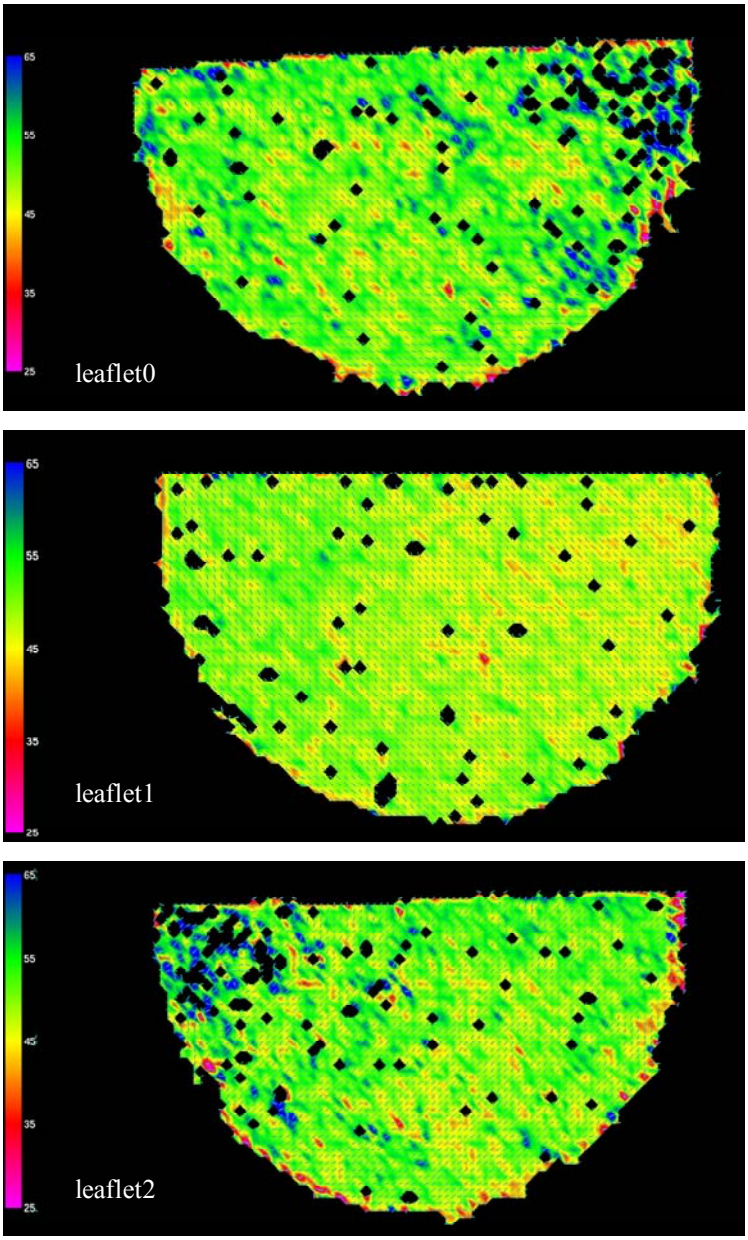

Figure 5-10 SALS scans of the three leaflets. The green vectors represent the local preferred fiber orientations. The background color shading indicates the degree of orientation (OI) (warmer color = more highly aligned fiber population). Black dots were caused by markers or air bubbles that the laser cannot penetrate. Note that the preferred fiber orientation is along the 45-degree angle for leaflet2 and 135-degree for leaflet0 and leaflet1.

5.3.3 Biaxial Mechanical Properties

Biaxial testing was conducted following the procedure previously described (Section 2.2.1). Biaxial experiment data with tissue material axes oriented at 45-degree or 135-degree angle with respect to specimen axes were shown in Figure 5-11. Results indicated that one leaflet (leaflet0) was nearly isotropic, and the other two leaflets (leaflet1 and leaflet2) were very anisotropic.

If let us define the degree of anisotropy (DA) as: under 1MPa equibiaxial stress loading condition, degree of anisotropy of the tissue equals the ratio of two peak strains of two axes,

$$DA=E_{11}:E_{22} \tag{5.9}$$

then for leaflet 0, 1, and 2, the DAs of them are 1.03, 2.69 and 5.61, respectively. Note that the shearing behavior of leaflet2 is different to that of the other two leaflets. This is due to the fiber orientation of leaflets is at 45 degree while the other two are at 135 degree (Figure 5-10). They sheared at an opposite direction causing one to give a positive value while the others demonstrated negative shearing.

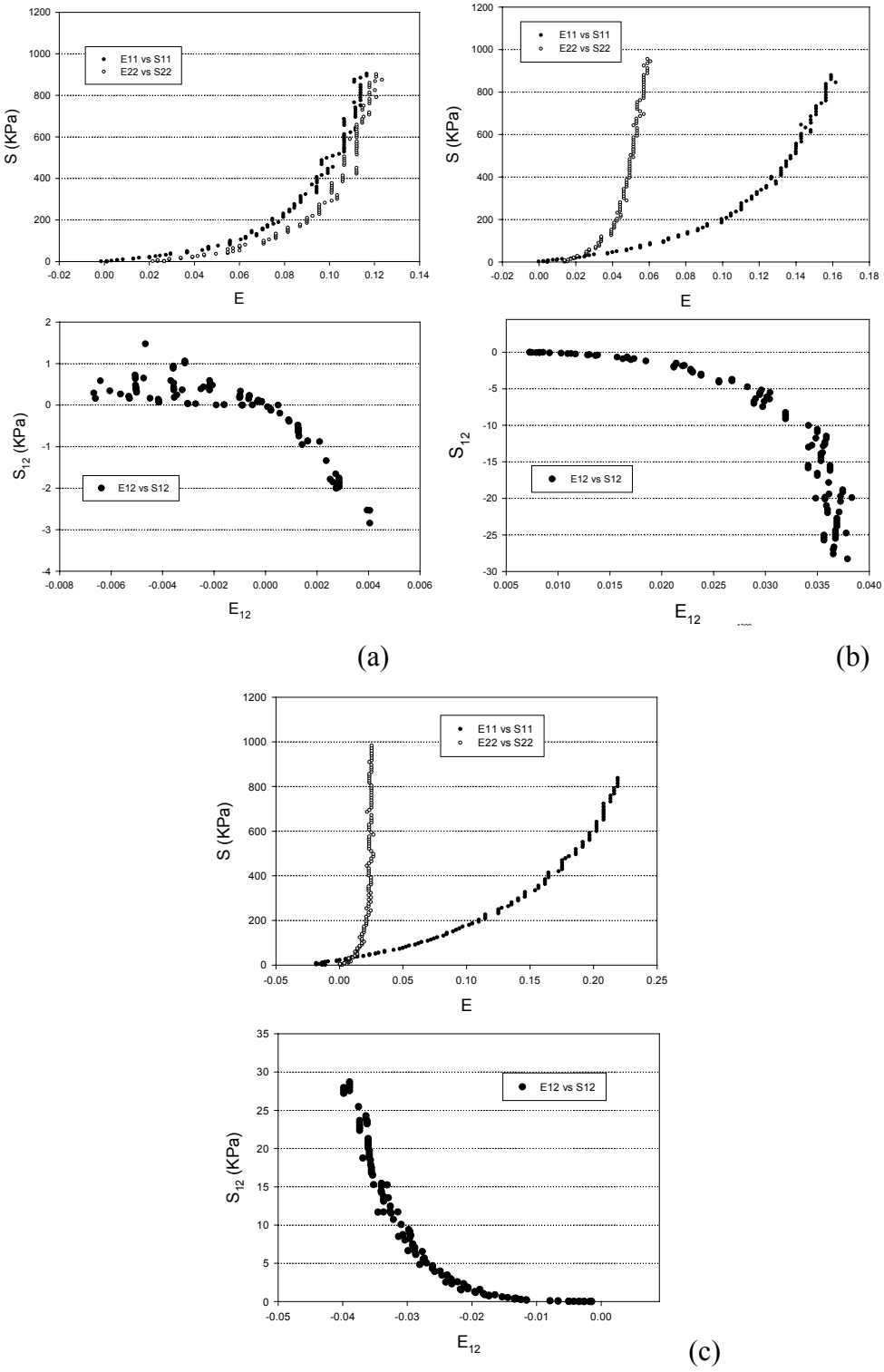

Figure 5-11 The biaxial test stress-strain data for (a) leaflet0, (b) leaflet1 and (c) leaflet2 under the equibiaxial testing protocol with the material axes of the specimen oriented at 45-degree or 135-degree with respect to the specimen axes.

The biaxial testing data were fitted with the Fung model of eqn. 3.8, followed the procedure described in the section 3.2.1 with convexity condition imposed and condition number checked. The parameters such obtained for the three leaflets were listed in Table 5-2.

Table 5-2 Parameter estimates for the three leaflets, fitted with eqn. 3.8.

	c (kPa)	A1	A2	A3	A4	A5	A6
Leaflet0	14.42	61.27	70.37	5.11	14.20	3.10	2.01
Leaflet1	9.95	56.85	192.18	1.00	34.00	2.00	4.00
Leaflet2	25.32	21.82	274.77	15.66	50.41	2.00	41.86

5.3.4 Comparison of Experiment Strain Fields to That of Finite Element Output

Material properties from the biaxial testing of the three leaflets (Figure 5-11) were input into the finite element model such that each finite element leaflet had its corresponding actual leaflet properties. The strain field from the aortic side surfaces of the finite element output was compared with the strain field of the experimental result. For the two leaflets that we were able to obtain strain fields, we presented experimental data and finite element results *in the same color scale* and next to each other for easy comparison (e.g., from Figure 5-12 to Figure 5-15). The max. in-plane principal strain was plotted as index for the comparison because its objectivity, invariant to the local coordinate system. From Figure 5-12 to Figure 5-15, it could be observed that the experimental strain fields did not show a smooth strain distribution exhibited by finite

element results. This is due to experimental error that will be elaborated in the section 5.4.1. Nonetheless, there were major obvious agreements between experimental and finite element results. One example is the belly region, where the magnitude of experimental strain was comparable to that of the finite element output. Also the high strain regions were similar in both of them. The same six regions in the experimental strain field for leaflet0 and leaflet1 are compared to the corresponding regions of the finite element output (Table 5-2 and 5-3). The peak strains of the two leaflets were different, underscoring the importance of using accurate material properties for each leaflet to faithfully replicate an experimental setup and enable an accurate validation.

Table 5-3 comparison of finite element strain output to that of experimental strain for leaflet0. Value illustrated is Max. in-plane principal strain.

Leaflet0	Locations					
	1	2	3	4	5	6
FE	0.1058	0.1509	0.0990	0.0687	0.0876	0.1014
Experiment	0.1427	0.1888	0.1017	0.0644	0.1466	0.1056
Difference	***0.0369***	***0.0379***	***0.0027***	***-0.0043***	***0.0590***	***0.0042***

Table 5-4 comparison of finite element strain output to that of experiment strain for leaflet1. Value illustrated is Max. in-plane principal strain

Leaflet1	Locations					
	1	2	3	4	5	6
FE	0.0861	0.1069	0.0810	0.0571	0.0793	0.0623
Experiment	0.1187	0.1474	0.0783	0.0592	0.0804	0.0629
Difference	***0.0326***	***0.0405***	***-0.0027***	***0.0021***	***0.0011***	***0.0006***

The averaged differences between finite element and experimental output were 0.0242 and 0.0133 for leaflet0 and leaflet1, respectively, thus we would estimate the overall discrepancy is about 0.0187. Based on our error estimates (in section 5.4.1) the above differences are within the experimental error range (within 1 pixel off the targeted marker centroid). We therefore concluded that our finite element model is accurate and represents the actual valve behavior. Consequently, parametric study of finite element simulations can be conducted.

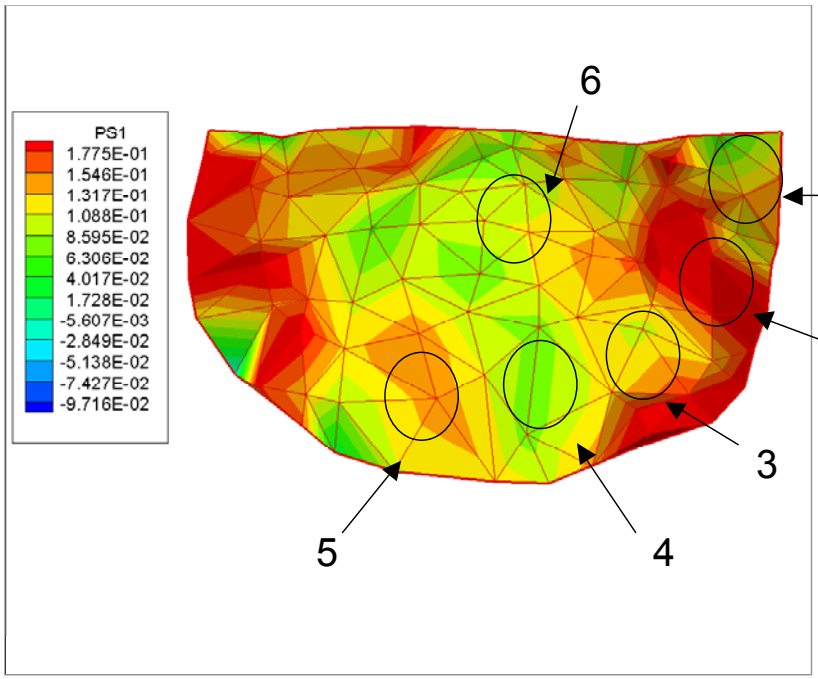

Figure 5-12 Experiment strain field for leaflet0, plotted in max. in-plane principal strain. Circles indicate the regions where strains are computed to compare with finite element output.

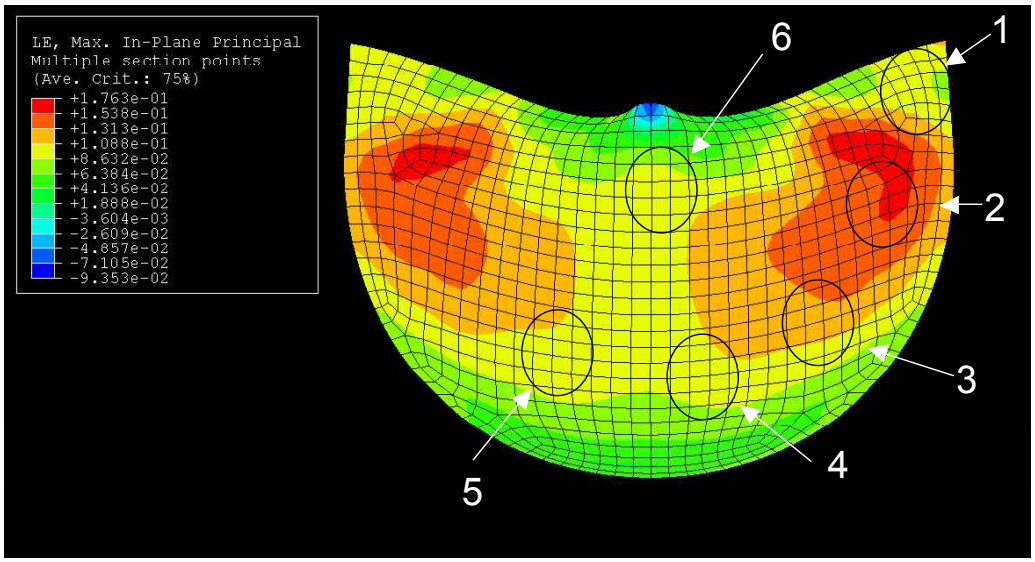

Figure 5-13 Finite element strain field for leaflet0, plotted in max. in-plane principal strain. Circles indicate the regions where strains are computed to compare with corresponding experiment data.

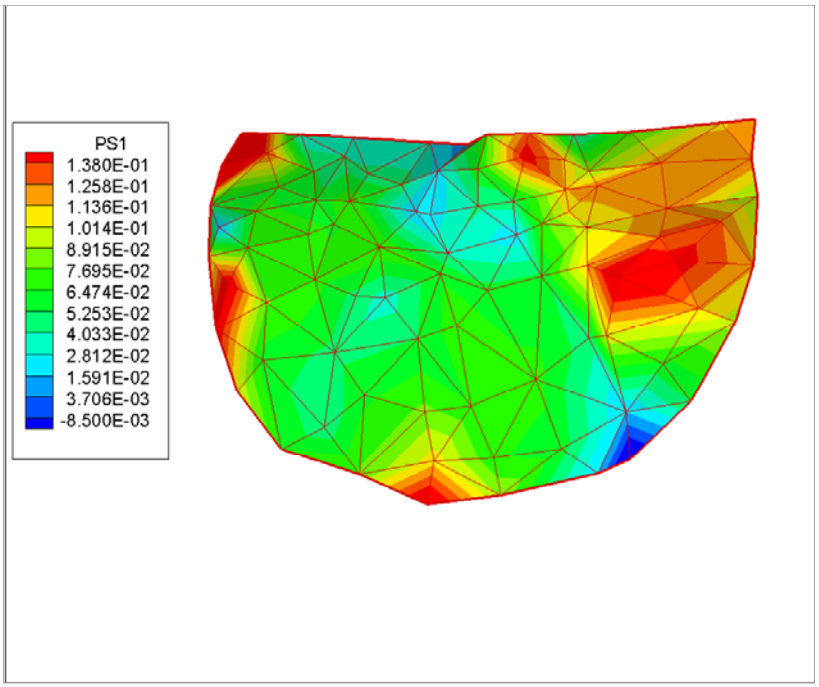

Figure 5-14 Experiment strain field for leaflet1, plotted in max. in-plane principal strain. Strains of the regions similar to Figure 5-12 are computed to compare with finite element output.

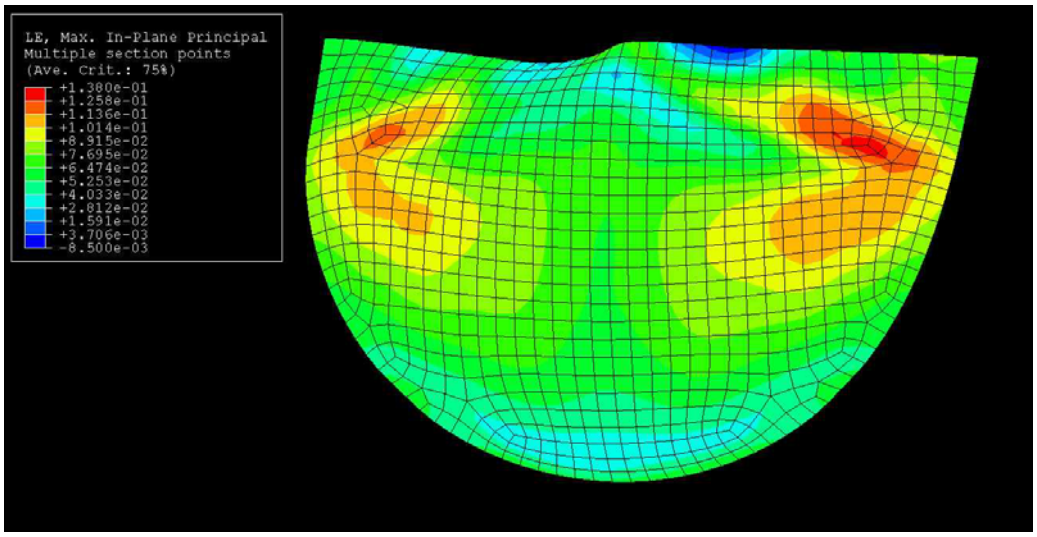

Figure 5-15 Finite element strain field for leaflet1, plotted in max. in-plane principal strain. Strains of the regions similar to Figure 5-13 are computed to compare with corresponding experiment data

5.3.5 FEM Simulations with Different Degree of Tissue Anisotropy

Since from our biaxial testing of the three leaflets (Figure 5-11), we already found that the three leaflets had substantial different degree of anisotropy, varying from 1.03 (nearly isotropic), 2.69 to 5.61 (very anisotropic). Without bothering to obtain such data from other sources, such as manipulating the tissues (refer to section 5.2.8 for details), we directly utilized the mechanical properties of these three leaflets to examine effects of degree of tissue anisotropy. Therefore, three simulations were conducted, (a) with leaflet0 material properties for all three leaflets, degree of anisotropy is 1.03; (b) with leaflet1 material properties for all three leaflets, degree of anisotropy is 2.69; (c) with leaflet2 material properties for all three leaflets, degree of anisotropy is 5.61.

The simulations results of both the aortic and ventricular sides of the leaflet surface were illustrated in Figure 5-16 and Figure 5-17, respectively. Max. in-plane principal stress of different regions for both the aortic side and ventricular side of the leaflet surface were tabulated in Table 5-5 and Table 5-6, respectively. It is interesting to note that on the aortic side the peak stress always occurred in the vicinity of commissure and the lowest stress always occurred around the free edge. When the degree of anisotropy was 5.61, the peak stress also appeared in the vicinity of the nodulus of Arantii. In general, for aortic side of the surface the peak stress increased with the increase of degree of anisotropy. However, for the ventricular side of the leaflet surface, when the degree anisotropy increased from 1.03 to 1.69, the peak stress was reduced by over 10%, however, when it went to extreme anisotropy, the peak stress increased by about 10%. The peak stress was also shifted from the commissure region

to the belly region when anisotropy increased. The lowest stress always happened at the free edge, which was same as the aortic side. It was most likely due to the contact of the leaflets that leaded to the compression stress at the free edge. Above observations indicated that the degree of anisotropy had a confounding impact to the stress distribution of the leaflet.

Table 5-5 Max in-plane principal stress (psi) of different degree of tissue anisotropy (DAs) on the aortic side of the leaflet surface.

DAs	Highest Stress		Lowest Stress		Stress of other regions	
	in psi	location	in psi	location	Belly	Commissure
1.03	90.2	Vicinity of Commissure	-0.6	Free edge	61.6	87.6
1.69	110.0	Vicinity of Commissure	-0.6	Free edge	68.6	67.5
5.61	131.8	Vicinity of Commissure	-0.1	Free edge	83.6	103.9

Table 5-6 Max in-plane principal stress (psi) of different degree of tissue anisotropy (DAs) on the ventricular side of the leaflet surface.

DAs	Highest Stress		Lowest Stress		Stress of other regions	
	in psi	location	in psi	location	Belly	Commissure
1.03	91.20	Commissure	0.04	Free edge	67.28	-
1.69	80.21	Belly	-0.75	Free edge	-	69.80
5.61	100.65	Belly	-5.98	Free edge	-	100.38

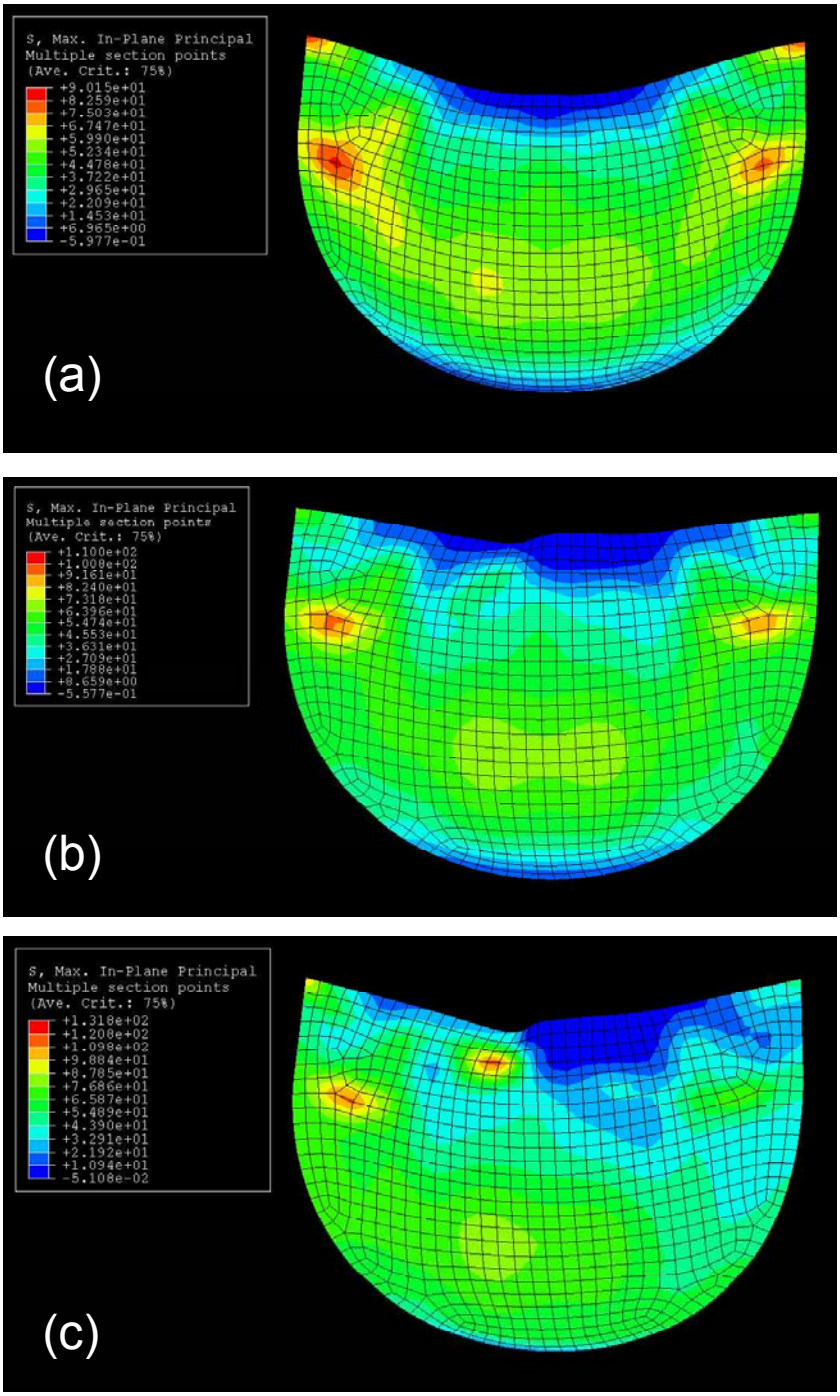

Figure 5-16 Finite element simulation results on the aortic side of the leaflet surface. (a) with leaflet0 material properties for all three leaflets, degree of anisotropy is 1.03; (b) with leaflet1 material properties for all three leaflets, degree of anisotropy is 2.69; (c) with leaflet2 material properties for all three leaflets, degree of anisotropy is 5.61. Stress illustrated is max. in-plane principal stress in psi.

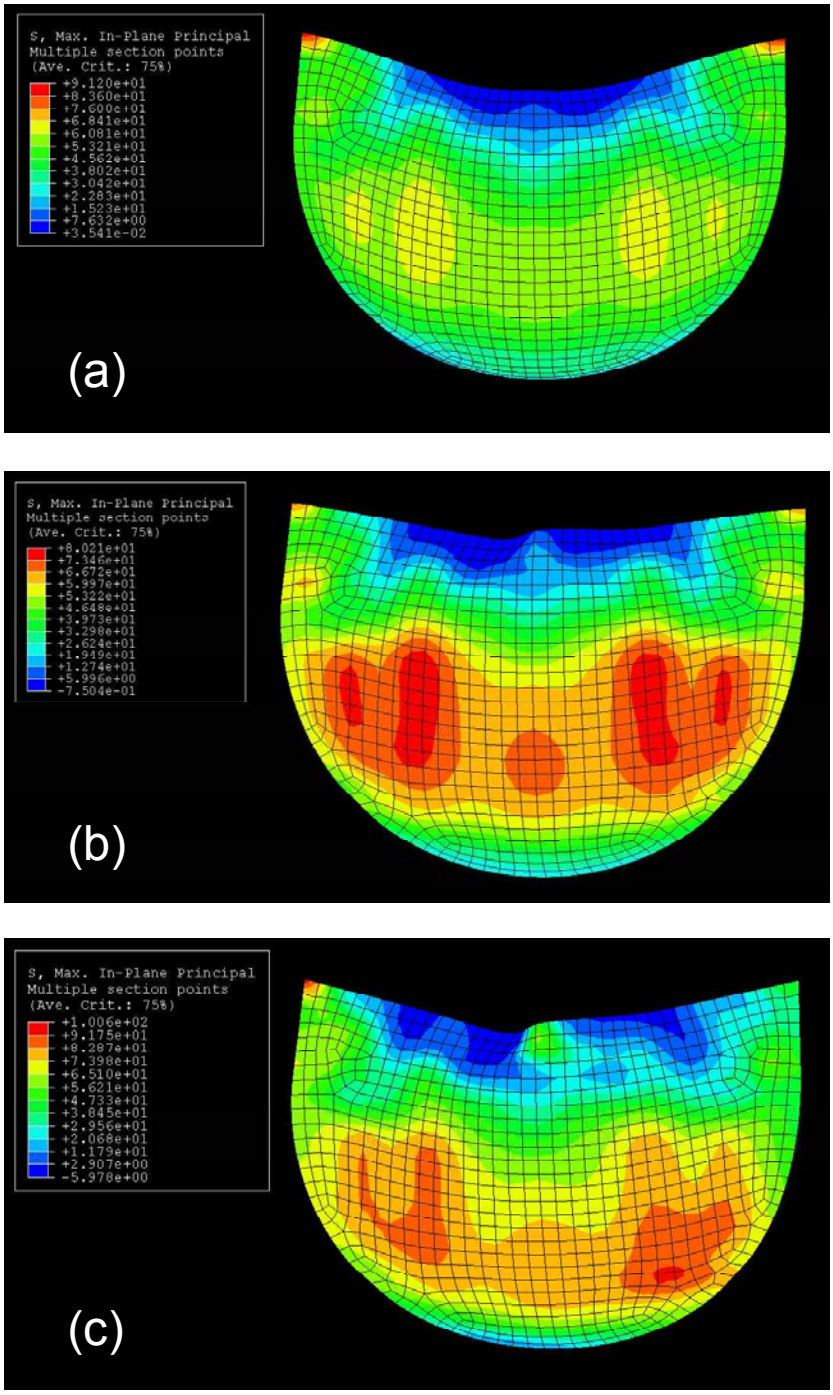

Figure 5-17 Finite element simulation results on the ventricular side of the leaflet surface. (a) with leaflet0 material properties for all three leaflets, degree of anisotropy is 1.03; (b) with leaflet1 material properties for all three leaflets, degree of anisotropy is 2.69; (c) with leaflet2 material properties for all three leaflets, degree of anisotropy is 5.61. Stress illustrated is max. in-plane principal stress in psi.

5.3.6 FEM Simulations with Different Angle of Fiber Orientations

Fiber orientation changes were realized by changing the local coordinate system of each leaflet. Because the default fiber orientation of leaflet1, for example, is at 135-degree with respect to the leaflet circumferential direction, if we rotate the local coordinate system by positive 45-degree, then the fiber orientation will be parallel to the circumferential direction. Likewise, if we rotate the local coordinate system by negative 45-degree, then the fiber orientation will be vertical to the circumferential direction, or that is the radial direction.

We used leaflet1 properties for all three leaflets of the finite element model, and varied the local orientation system to simulate 1) fiber in the radial direction, 2) fiber in the circumferential direction. The simulation results for the aortic side and ventricular side are shown in Figure 5-18 and Figure 5-18, respectively and listed in Table 5-7 and Table 5-8. The results indicated that when fiber orientation is at 45-degree the valve has significant lower peak stress than that of circumferential and radial fiber orientations for both aortic and ventricular sides of the surface. The influence of leaflet anisotropy was conducted by Burriesci *et al.* [71] on the Sheffield biocuspid valve. They used a nonlinear orthotropic material model defined on a finite number of points on the material stress-strain curves. They found that the axial model, when the fiber (stiffer) direction was aligned along with the axial (radial) direction, achieved a peak value of max. principal stress some 15% smaller than the circumferential model. Cacciola *et al.* [129] studied the influence of fiber orientation based on a fiber-reinforced valve model.

Two type of fiber reinforcement for the leaflets were considered. One was the unidirectional layout mimicked the circumferential distribution of the collagen fibers. The other was the sinusoidal layout reinforcing the leaflets in both radial and circumferential directions. They found that the peak stress values for the sinusoidal layout were significantly lower than that of the unidirectional circumferential layout. We know that the native aortic valve has collagen fibers predominately in the circumferential direction, however, those abovementioned studies and our simulations indicated that the leaflet with predominate circumferential fiber orientation might not have the lowest stress state. It appeared that the interaction between the fiber and its surrounding matrix was complex and the stress distribution change due to the fiber structure variation is significant and not intuitive.

One of the potential problems in our simulations is that the fiber orientation detected by SALS (Figure 5-7) is in a stress-free state, and that during biaxial testing of the leaflet the fiber orientation may rotate as the loading is applied. The actual biaxial testing data used in simulation, especially at high stress state, may represent a fiber orientation other than the 45-degree fiber orientation. To verify it and more accurately define fiber orientation, a SALS device coupled with a biaxial loading device is required.

Table 5-7 Max in-plane principal stress (psi) of different fiber orientations on the aortic side of the leaflet surface

Fiber orientation	peak stress	region	lowest stress	region
45 degree to circumferential direction	110.0	Vicinity of commissure	-0.6	free edge
circumferential direction	286.4	commissure	-3.3	free edge
radial direction	318.5	commissure	-3.2	free edge

Table 5-8 Max in-plane principal stress (psi) of different fiber orientations on the ventricular side of the leaflet surface

Fiber orientation	peak stress	region	lowest stress	region
45 degree to circumferential direction	80.2	belly	-0.8	free edge
circumferential direction	282.3	commissure	-2.3	free edge
radial direction	316.2	commissure	-3.6	free edge

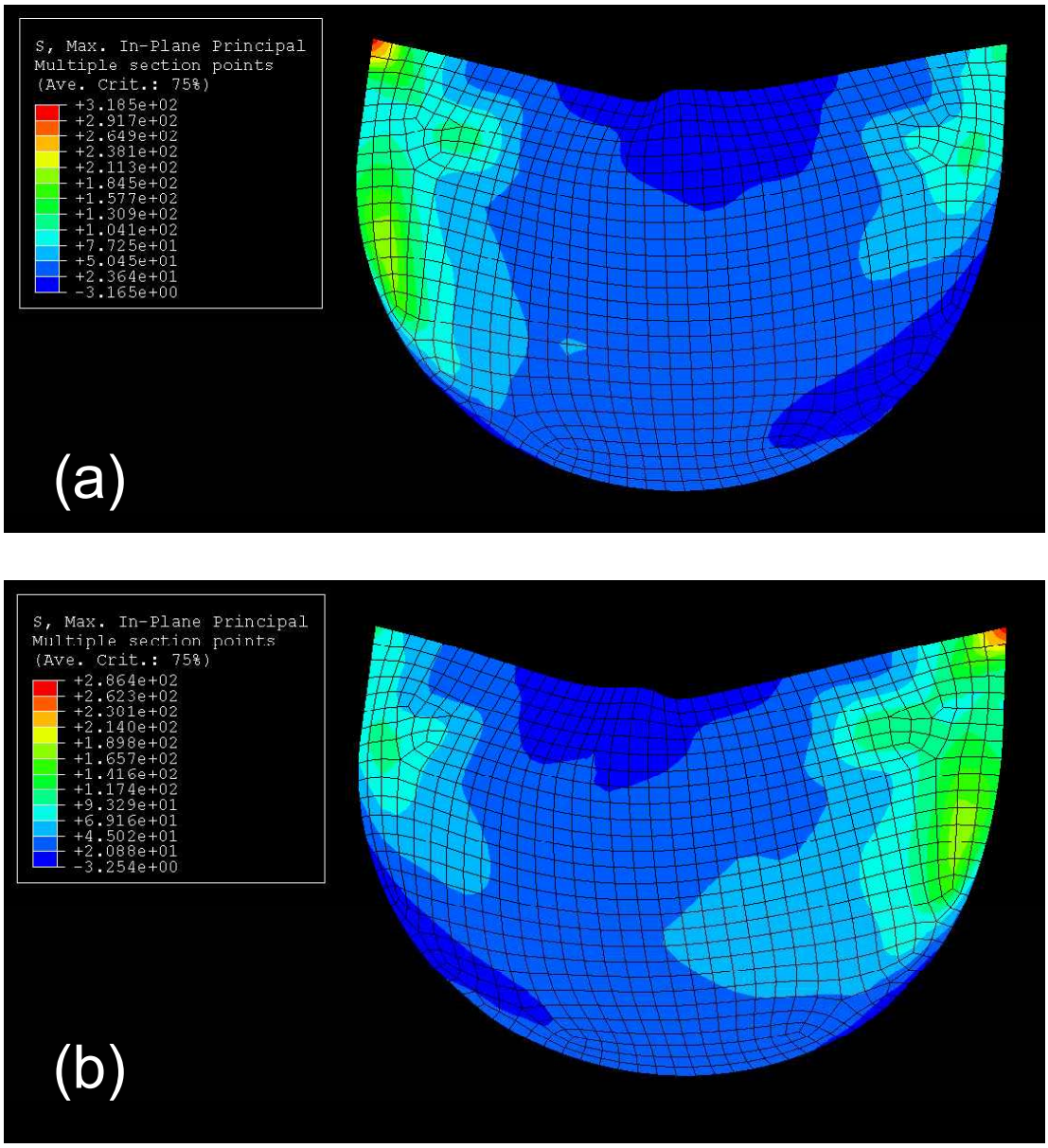

Figure 5-18 Finite element simulation results on the aortic side of the leaflet surface, with different angle of fiber orientations, (a) fiber vertical to leaflet circumferential direction; (b) fiber parallel to leaflet circumferential direction. Stress illustrated is max. in-plane principal stress in psi.

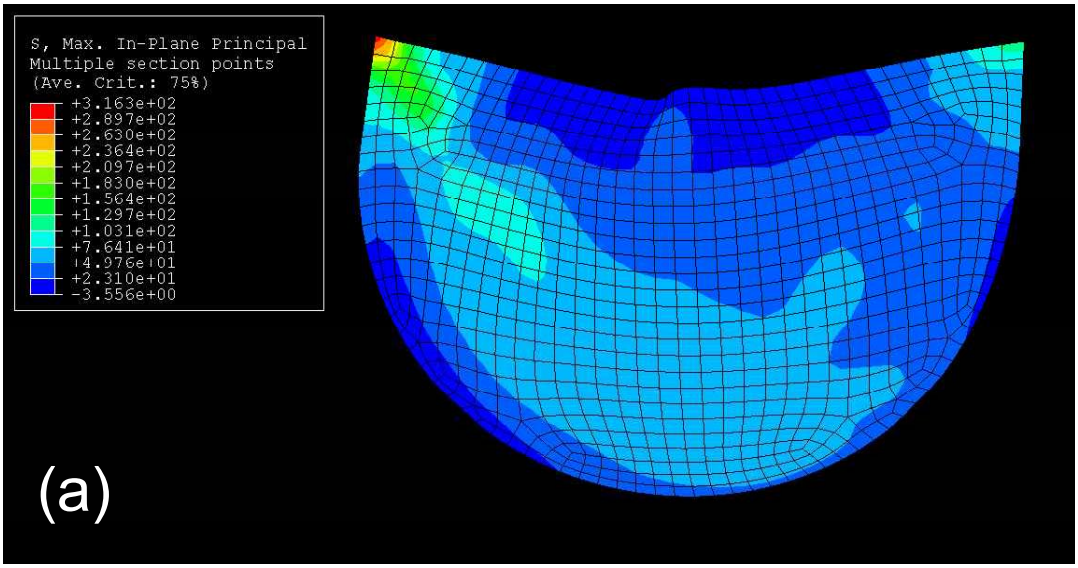

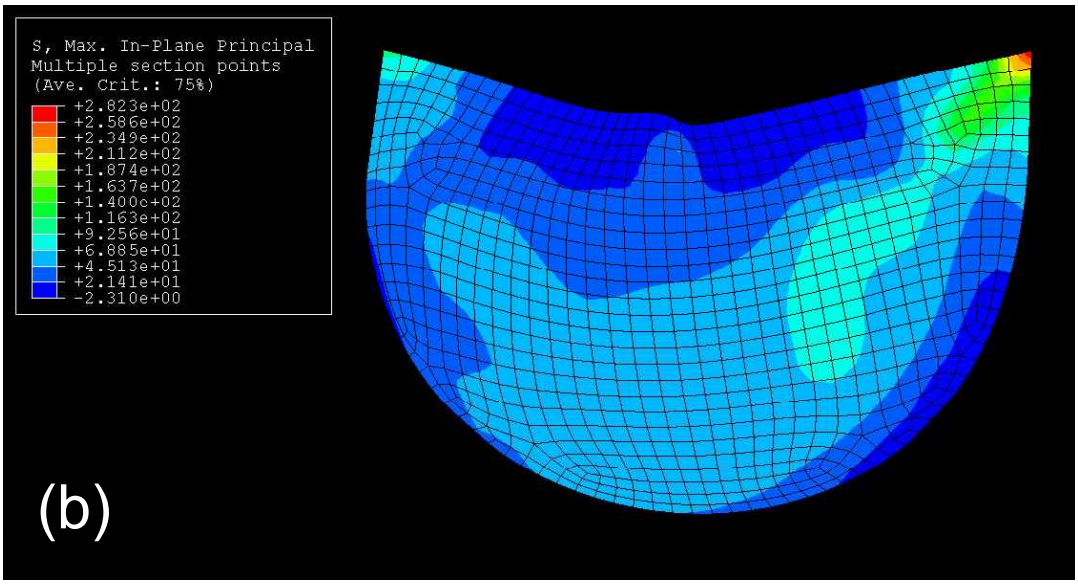

Figure 5-19 Finite element simulation results on the ventricular side of the leaflet surface, with different angle of fiber orientations, (a) fiber vertical to leaflet circumferential direction; (b) fiber parallel to leaflet circumferential direction. Stress illustrated is max. in-plane principal stress in psi.

5.4 DISCUSSION

5.4.1 Source of Experiment Errors

Experimental studies, either in vitro or in vivo, can provide valuable information on the opening and closing dynamics of artificial heart valves. But the studies are relatively expensive and difficult to perform. For the experiment we conducted, we put about 90 tiny markers in a leaflet area similar to the size of an adult thumbnail. Imaging of the markers in such a small area requires high-resolution cameras and meticulous care needs to be given for the digitization of those images. In other words, the experiment is prone to human error. After careful examination of the experiment procedure, the sources of experiment errors are identified as:

Digitization process (manual). The size of one leaflet is at about 23x 12 mm in circumferential and radial directions, respectively. From the image taken for digitization (Figure 5-20), the length of the free edge, marked by x1 and x2, corresponds to the total pixel length of about 542. From the Figure 5-9, there are about 12 line segments on the free edge. The averaged pixel length of those line segments is 524/12=43.6 pixels. The averaged actual length of those segments is 23mm/12=1.9mm. The marker size on the image is about 4 ~ 10 pixels in diameter (corresponding to 0.18 to 0.44mm). Please note that the ratio of the size of marker to the length of the line segment is high. Due to the manual digitization process, one may not pick the actual centroid of a marker. If the centroid is by 1 or 2 pixels, the imposed error accounts for

0.023 to 0.045 strain errors. This is the reason why we concluded that the differences listed in Table 5-3 and Table 5-4 are within the experiment error range.

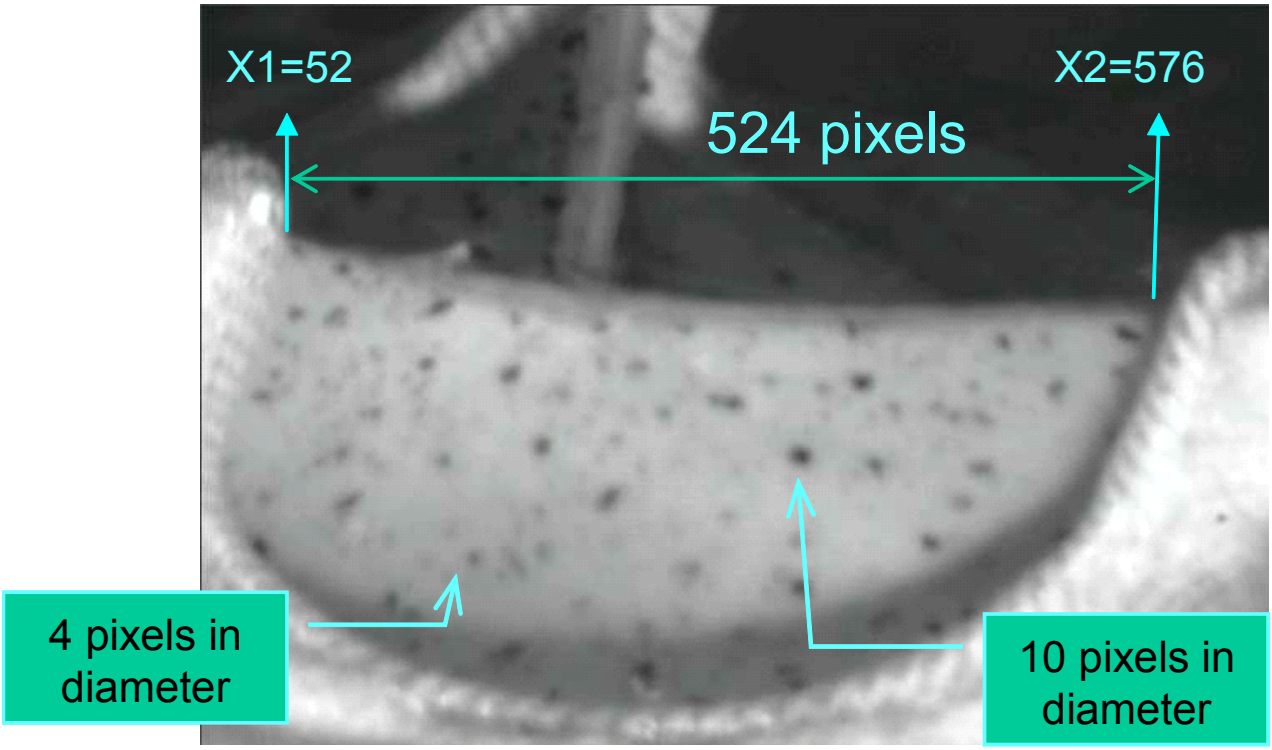

Figure 5-20 Image from one camera showing one leaflet and markers on it, x1 represents the free edge starting location in pixel at x axis; x2 represents the free edge ending location in pixel at x axis. Two representative marker sizes are also indicated in diameter.

For better understanding the source of errors, we summarize the calculation as below:

Measurements:

- Pixels between x2 and x1 are 524.
- 12 line segments in between.
- Marker has about 4 - 10 pixels in diameter.

Error Estimate:

- One line segment has: 524/12 = 43.6 pixels.

- If 1 pixel off,
    - then 1/43.6 = 0.023 strain error
- If 2 pixels off, t
    - then 2/43.6= 0.046 strain error.

Image quality. Due to practical limitations in the measurement of markers very close to the leaflets and valve housing, the quality of images cannot be guaranteed. For example, the images of Figure 5-21 taken from two cameras showed that some markers can only be seen by one camera. Therefore at some boundary areas no marker can be selected, possibly resulting in loss of information of that region. Also during valve deformation motion, markers may be out of focus and thus images may be blurred which creates difficulty during digitization. Those limitations need to be improved in future experiments.

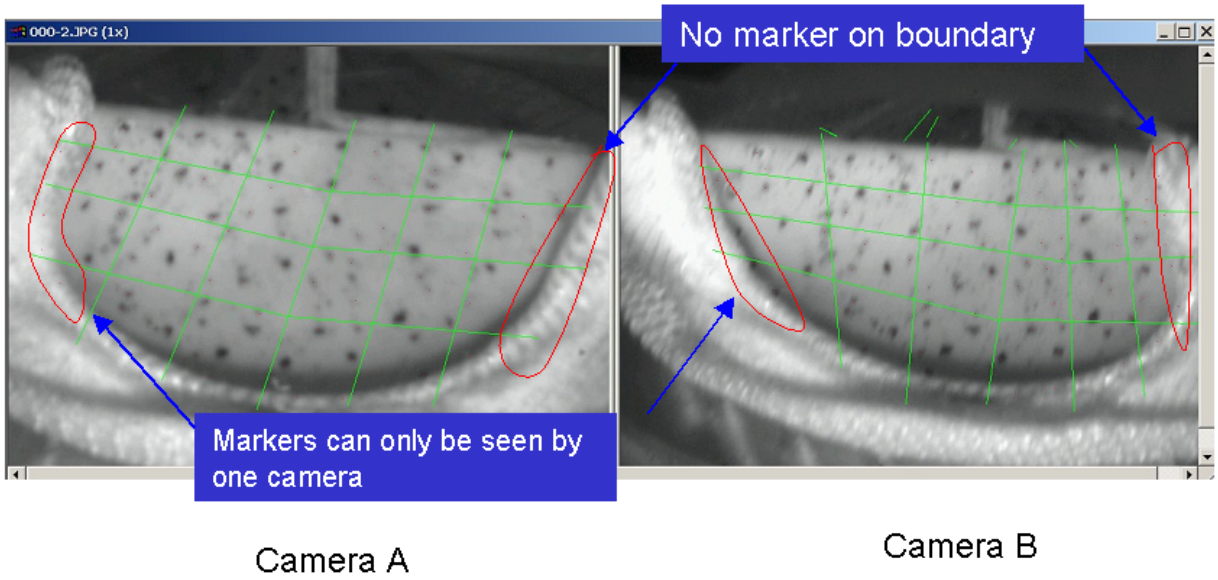

Figure 5-21 Images from two cameras showing that some markers can only be seen by one camera and at some boundary area no marker can be selected that could result in loss of information of that region. The green lines are grids used to aid in digitization.

5.4.2 Considerations for Element Type Selection

Valve leaflets are thin-walled structures that have sometimes been modeled as membranes [75, 133-135]. However, many studies [136] have shown that bending damage is one of the main causes of valve mechanical damages. Modeling leaflets as tension-only membrane structure essentially eliminates the bending effects. Whilst the analysis [67, 69] using shell elements did show that the leaflets were subjected to bending. This observation motivates us to use shell elements in our simulations. Another alternative is to use three dimensional brick elements. Complex systems of stress are often best modeled using three dimensional brick elements, and this approach has been taken in the study of tissue heart valves by Krucinski *et al.* [72]. However, it was noticed [137] that there are severe problems of modeling thin structures with brick elements, such as "a balance required between the very large number (of elements) needed to keep the bricks well-shaped, and the numeric problem that results from bricks with highly disparate dimensions". Also using brick element requires a 3D constitutive modeling and a 3D Fung model could be an ill-posed, non-convex model (personal communications with Dr. Criscione of the Texas A&M University). Another concern is the enforcement of incompressibility. Imposing incompressibility constraint via Lagrange multiplier p is rather complex for 3D element; however, it is relatively easy for a shell element and can be realized by kinetic constraints. Based on those considerations, we built our model by using shell elements.

5.4.3 Material Model for Leaflet

To our knowledge, the Fung material model used in this study is, up to now, the most accurate model that has ever been implemented for BHV simulations. However, this is not meant to imply that the Fung model is the best model for BHV simulation. The limitation of the model is revealed in the simulations conducted in section 5.3.6. The Fung model has the disadvantages inherited in phenomenological models, it can only describe a pre-defined state and cannot describe the underlying mechanism of fiber structure changes. Therefore, it is not surprising to see that the fiber reorientation scenarios cannot be captured by the Fung model either in experiment or in the simulations of section 5.3.6. Alternative models that have better prediction ability should be either based on individual fiber strain energy law, such as the structural model by Lanir [115] and Sacks [116], or has the ability to incorporate the specimen material axes changes, such as fiber-reinforced composite models with two families of fibers proposed by Holzapfel *et al.* [106]. However, those models have not been utilized in BHV simulations yet.

5.4.4 Correlation Between the Calculated Stress Distribution and Common Regions of Failure in Tissue Valves

The simulations we conducted in sections 5.3.4, 5.3.5 and 5.3.6, could be used to investigate correlations between the calculated stress distribution and common regions

of failure in tissue valves. The failure phenomena of leaflets in valve prostheses basically may be divided into the following three types:

1) Cusp calcification, tear and laceration [138]

2) Tears in the leaflets in the vicinity of the commissure [139]

3) Cusp tears associated with the holding suture attached to stents [139, 140]

From the simulation results (Figure 5-16 and Table 5-5) it can be observed that the highest tensile stress happened at the central portion of leaflets and the vicinity of commissure region. It is possible that the tears and perforations occurred at those regions are due to the high tensile stress. Valves during closed states also experience bending stress especially at the coaptation area. Negative values for the minimum principal stress are found in the coaptation area and edges where leaflets are attached to the stent (Figure 5-22). Those compression stresses, even small, may cause fiber wrinkling, and lead to the flexure damage of collagen fibers and consequently, damage of leaflets [136, 141].

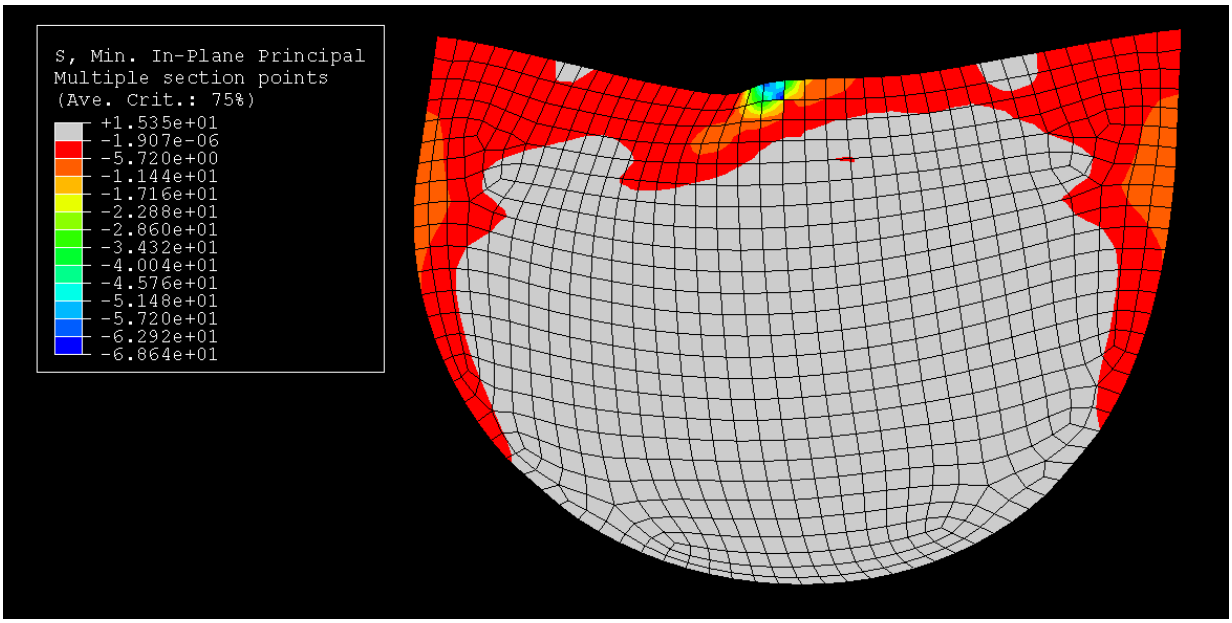

Figure 5-22 Min. in-plane principal stress of the aortic side of the leaflet, plotted with only negative values to show the compression stress occurred at the coaptation area and edges where the leaflets are attached to the stent.

5.4.5 Limitations

BHV finite element model. In this study, the simulations were conducted with quasi-static deformation only. The dynamic loading conditions, such as "water hammer" effects during valve closure, would cause higher stresses than that of a quasi-static state. The study conducted by Sacks 2000 [34] also demonstrated that GLBP responded differently under varied strain rates (Figure 5-23). To account for the dynamic loading conditions, the finite element model may need to incorporate fluid-structural interaction and a viscoelastic model may be needed to accommodate the strain rate effect. In addition in this finite element model we did not consider the effects

of cyclic loading that ultimately resulted in BHV failure. However, we will present some of our preliminary work in this direction in the Chapter 6.

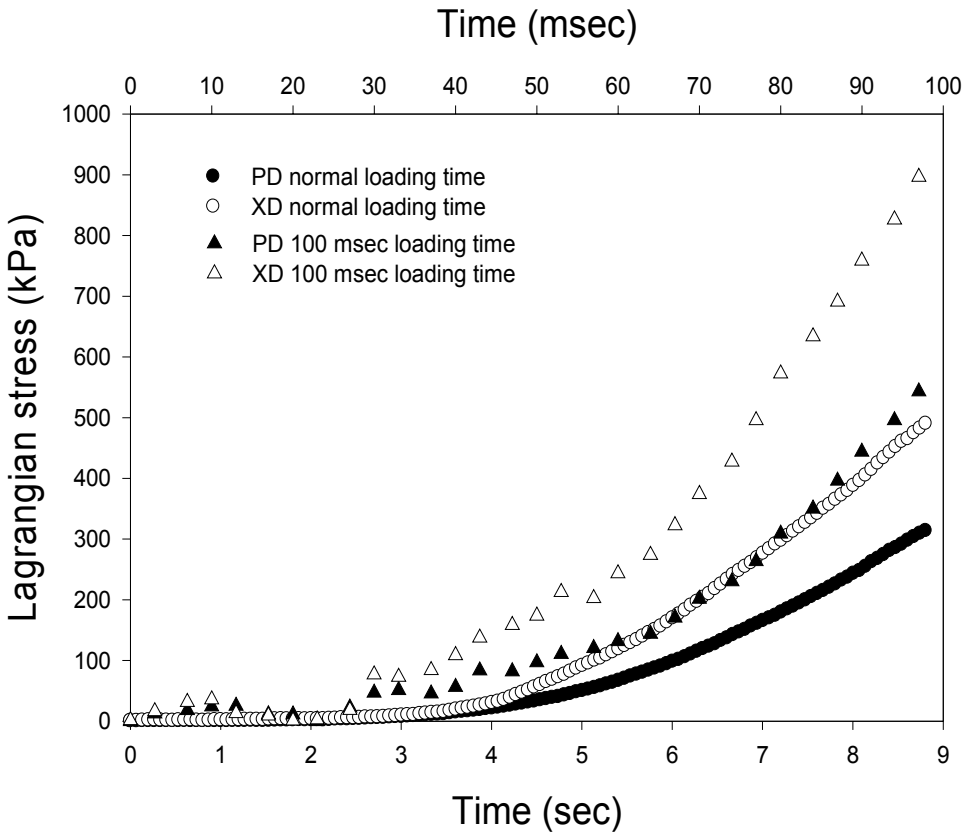

Figure 5-23. Effects of strain rate on the equibiaxial ($E_{11} = E_{22}$) mechanical properties of GLBP. A change in loading time from 1 sec to 100 msec resulted a near doubling of stress levels. Adapted from Sacks 2000 [34].

Note that the constitutive model used in this study is a continuum model at tissue level. Even though we simulated different fiber orientation effects, the continuum scale that our stress-strain measurement based on is still at tissue level. To quantify individual fiber stress, a structural model [105] needs to be employed, which is capable to describe the interaction between the fiber and its surrounding matrix. The stress in a fiber-reinforced material should be synergic effect of both the fiber and the matrix, i.e.,

$S=P_f/A_f+P_m/A_m$, where P is the load, A is the cross section area and the subscript f and m stand for the fiber and the matrix, respectively. If matrix is not considered to be a load-bearing constitute, then $S=P_f/A_f$, where A_f should be the total cross section area of all fibers instead of the macro specimen cross section area. Note here that specimen cross section area can only be used if the tissue is fully packed with fibers, otherwise the stress such calculated is not the fiber stress and but the stress of both the fiber and matrix components.

Experiment methods As indicated in the section 5.4.1, the image resolution needs to be improved as well as the digitization process. Currently we estimated an experimental error of about 1-2 pixels. An automatic marker centroid detection program needs to be employed to eliminate such error, and thus high quality images are required to ensure consistent centroid detection. Furthermore, since the measuring resolution of a system using a CCD (charge-coupled device) camera is in principle limited to the pixel size, to obtain better resolution such as sub-pixel resolution, the output data from the CCD must be interpolated in some way. Typical interpolating methods use digital data processing methods, which first convert the output data of the CCD into digital data using an A/D (analogue-to-digital) converter and subsequently perform mathematical calculations using a computational algorithm. The images with sub-pixel resolution are desirable in the valve deformation experiment for the accurate strain measurement. It is hoped that in the future some studies could be conducted in this area.

Only one valve (three leaflets) was used in the study, more experiments are needed to examine effects of different valve, geometry and material properties. The sensitivity analysis (SA) for the model has not been conducted. ABQUS provides a design sensitivity analysis function that enables one to perturb various design parameters to obtain the different response of the model. This information will be valuable for a designer to evaluate the reliability, the robustness, and the efficiency of the model. Apparently, more studies need to be conducted in this direction.

Effects of the tissue pre-sorting procedure on the applicability of the techniques developed here. The material properties of GLBP in the chapters 2, 3 and 4 were obtained from pre-sorted GLBP tissues. The pre-sorting procedure is aimed to prepare structurally consistent biaxial specimens from the bovine pericardial sac and the areas with high degree of fiber alignment were chosen. This high degree of fiber alignment represented an upper bound of degree of anisotropy. For the other areas with low degree of fiber alignment, the specimens would behave more towards isotropic. Our constitutive models (eqn 2.16 and eqn 3.8) were therefore developed to be able to capture a high degree of tissue anisotropy. It was not surprised that the models could also capture the non-sorted more isotropic tissue properties. This is demonstrated in chapter 5 that the non-sorted leaflet properties could be modeled accurately.

5.5 SUMMARY

In this chapter, we investigated quasi-static valve deformation under 120 mmHg trans-valvular pressure experimentally and numerically. The novelty of this study lies in two parts, 1) rigorous experimental validation of numerical results; 2) accurate material model in describing the leaflets' material properties. These two key elements are essential for a finite element model to give a reliable prediction. The BHV finite element model integrated the techniques developed in the previous chapters, e.g., rigorous biaxial experiment including inducing tissue in-plane shear response for characterizing leaflet properties, and finite element implementation of user-defined material model with convexity and condition number constraints imposed. We have not only illustrated the processes of how to build and validate the finite element model, but also demonstrated needs for such rigorous experimentation and constitutive modeling that make a close match between FE and experiment output possible. The BHV model, to our knowledge, is the most rigorously validated model to date in the literature (Table 5-1). The model can be used to evaluate various valve design parameters and is hoped to be able to greatly facilitate optimal BHV design.

6.0 SUMMARY AND FUTURE STUDIES

In this chapter, we will summarize main findings of the previous chapters (2 to 5). Then we will propose some of the areas for the future studies and present some of preliminary works that have been done in those directions.

6.1 SUMMARY

Chapter 1 presented an up-to-date overview from the biomechanics perspective of what is currently known about heart valve replacement. This review includes the experimental data collection, constitutive modeling, numerical implementation of the associated model and numerical simulations of BHV behavior. Some of the limitations of those components were identified and improvements were given in the later chapters.

In Chapter 2, we generated a comprehensive experimental biaxial mechanical dataset that included high in-plane shear stresses. Compared to our previous study [38], GLBP demonstrated a substantially different response under high shear strains. This finding was underscored by the inability of the standard Fung model, applied successfully in our previous GLBP study, to fit the high-shear data. To develop an

appropriate constitutive model, we utilized an interpolation technique for the pseudo-elastic response to guide modification of the final model form. An eight parameter modified Fung model utilizing additional quartic terms was developed, which fitted the complete dataset well. Model parameters were also constrained to satisfy physical plausibility of the strain energy function. The results underscore the limited predictive ability of current soft tissue models, and the need to collect experimental data for soft tissue simulations over the complete functional range.

Chapter 3 focused on the numerical implementation of a generalized Fung pseduo-elastic model. finite element simulations of soft tissue behavior, including simulating shear behaviors, using accurate material models have been limited. In addition to difficulties in development, the high nonlinearity of soft tissue models leads to numerical instability and related convergence problems. To address these issues, in Chapter 3, we developed model restrictions necessary to achieve numerical stability. Two restrictions were imposed: 1) convexity of the strain energy function W; 2) the condition number of material stiffness matrix is restricted to be less than a set value. These restrictions lead to a set of bounds that can be enforced in nonlinear regression for material model parameter estimates. In the current approach, we utilized ABAQUS as a computational platform to implement a generalized Fung pseudo-elastic constitutive model. Planar biaxial mechanical tests were simulated and validated using theoretical solutions and experimental data. Results indicated that in addition to parameter constraints required for physical plausibility [39], the numerical constraints presented in this study are required for numerical convergence. The successful

implementation of the Fung pseudo-elastic constitutive model presented in Chapter 3 suggests that accurate simulations using realistic nonlinear anisotropic material models of soft native and biologically-derived tissues are both feasible and practical.

Chapters 4 and 5 focused on the numerical simulations of heart valve biomaterials at tissue and valve levels, respectively. At tissue level, numerical simulations of planar biaxial testing were conducted and accessed. Effects of boundary conditions under different numbers of suture attachments, different gripping methods and specimen shapes, and different tissue anisotropy were examined. Simulation results clearly indicated that there are strong boundary effects with the clamped methods, while suture attachment methods had minimal boundary effects. Moreover, the simulations demonstrated that the stress decay behavior depends on the material axes orientation, even with the same gripping method. While not exhaustive, these comprehensive simulations provide experimentalists with more insight into the stress-strain fields associated with different biaxial testing boundary conditions, and may be used as a rational basis for the design of biaxial testing experiments.

At valve level, 3D tri-leaflets bioprosthetic valve deformation under 120 mmHg trans-valvular pressure was simulated and validated against experimental data. We reported our approaches to obtain the 3D surface reconstruction from markers affixed on the surface of the leaflets and the method of how we compute in-plane membrane strain. We also constructed tri-leaflets BHV finite element model with the same geometry of the actual valve and mechanical properties obtained by biaxial testing of the actual leaflets to ensure accuracy of the finite element model. After validating with

the experiment, the finite element model can be used to evaluate various valve design parameters, such as varying leaflets properties and fiber orientation. Those finite element simulations will provide, otherwise unobtainable, valuable information for optimal BHV design.

Major contributions of this dissertation are:

1. Developed a novel stress-control biaxial experimental method to generate an extensive experimental database that included tissue response under high in-plane shear and the techniques for constitutive modeling of the dataset.
2. Formulated a set of model constraints necessary for numerical stability and successfully implemented generalized Fung elastic model into finite element.
3. Simulated complex boundary effects during biaxial testing of soft tissue using accurate nonlinear, anisotropic material model.
4. Constructed an accurate BHV finite element model that integrated the techniques of abovementioned 1 and 2. And developed a rigorous experimentation for the validation of the BHV finite element model. The model offers great potential for optimal BHV design.

6.2 FUTURE STUDIES

Native valves can withstand 80-120 mmHg of trans-valvular pressure and will operate in excess of 3 billion cycles during an individual's lifetime. However, all BHV continue to suffer from limited durability due to structural failure [2, 16]. Moreover, tissue

engineered heart valve scaffolds require decellurized scaffolds to withstand physiological mechanical loading until enough new tissue has been laid down. This clearly poses a need for understanding the mechanisms of collagenous tissue degradation under long-term cyclic loading. This demanding application also necessitates some potential research areas:

i. Characterize the mechanisms of tissue fatigue damage under tensile and flexural deformation;

ii. Develop structural constitutive models to predict fatigue behavior

iii. Implement fatigue damage model into computational framework for utilization in device design [142].

6.2.1 Response of Heterograft BHV Biomaterials to Moderate Cyclic Loading

While not the focus of this dissertation, we have conducted an experimental study to quantify the response of heart valve biomaterials subjected to moderate levels of cyclic loading. This study was intended to illustrate the challenges and form groundwork for future finite element simulations of BHV fatigue. In this study, changes in specimen dimensions, anisotropic mechanical properties, and molecular- and fiber level structural changes to collagen were quantified. Mechanisms of mechanical property changes were postulated. Please see Appendix C for details.

Application of the structure model on fatigued tissues. Our preliminary experimental fatigue study indicated that at moderate cyclic loading stage tissue undergoes conformation changes at fiber level. If our hypothesis that the change of mechanical

properties was due to permanent increase in collage crimp period and fiber kinematical re-orientation induced by cyclic loading is correct, the structural finite element model could be theoretically very easy to catch the phenomena by just changing the fiber distribution function (see section 6.2.2 for details about structural model). The approach is to use experimental data at 0 cycle state to fit the structural model. Parameters of fiber distribution function, i.e., the mean and standard derivation, can be adjusted to mimic the fiber structure re-orientation and individual fiber strain energy law can be changed to mimic the fiber crimp change. If they are matched with 30, $65x10^6$ cycles data, then a BHV finite element model using the structural model could simulate and predict a valve behavior at a fatigued stage. If such model is available, it will be a major step towards the ultimate understanding of BHV failure.

6.2.2 Incorporation of Structural Model into Finite Element

With the limitation of the Fung model (eqn. 3.8), for the fatigue study and future applications, structural modeling approaches developed in our lab [8, 105] offer an alternative approach to accurately describe the tissue response with fewer parameters. More importantly, this approach can clarify the underlying physical basis for complex mechanical behavior of BHV biomaterials. For example, collagen fiber structural changes for a fatigued tissue can be explicitly described in a structural model, which gives the model the potential to predict a fatigue state.

Structural model essentials. A structural approach towards constitutive modeling for planar tissues is summarized [45, 115]. Briefly, it is assumed that the tissue can be

modeled as a hyperelastic solid, so that $S_{ij}=\partial W/\partial E_{ij}$, where S_{ij} and E_{ij} are the second Piola-Kirchhoff stress and Green strain tensors, respectively, and W is the tissue strain energy density per unit volume. W is expressed as

$$W = \int_{-\frac{\pi}{2}}^{\frac{\pi}{2}} R(\theta) w_f(E_f) d\theta \tag{6.1}$$

where w_f is the fiber strain energy function, and E_f is the fiber strain computed from the global tissue strains (E), which can be expresses as $E_f = N^T \bullet E \bullet N$, in which $N=\begin{bmatrix} \cos(\theta) \\ \sin(\theta) \end{bmatrix}$ is the fiber direction in the tissue space and $R(\theta)$ is the fiber orientation distribution function. The expressions for the S_{ij} are:

$$\begin{aligned} S_{11} &= \int R(\theta) S_{11}^f(\varepsilon) \cos^2\theta \, d\theta \\ S_{12} &= \int R(\theta) S_{11}^f(\varepsilon) \cos\theta \sin\theta \, d\theta \\ S_{22} &= \int R(\theta) S_{11}^f(\varepsilon) \sin^2\theta \, d\theta \end{aligned} \tag{6.2}$$

where $S_{11}^f(\varepsilon)$ is the fiber stress-strain law with material constants A and B, for which the following exponential form is used:

$$S_{11}^f(\varepsilon) = A\,[\exp(B E_f) - 1] \tag{6.3}$$

where A and B are positive constants. As in our previous study [8], we will assume that $R(\theta)$ follows a Gaussian distribution given by:

$$R(\theta) = \frac{1}{\sigma\sqrt{2\pi}} \exp\left[\frac{-(\theta-\mu)^2}{2\sigma^2}\right] \tag{6.4}$$

where σ is the standard deviation and μ is the mean of the distribution.

Structural model implementation. Following the procedure in section 3.1.2, biaxial testing data of fresh bovine pericardium was fitted with the structural model. The structural model was also coded into ABAQUS/UMAT. The correctness of the coding was validated by single element finite element testing. Illustrated here in Figure 6-1 is the experimental data and the single element finite element simulation results for the equibiaxial protocol (protocol 4), which the ratio of the applied tension in the circumferential and radial directions is T_{cc}:T_{rr} = 60:60,.

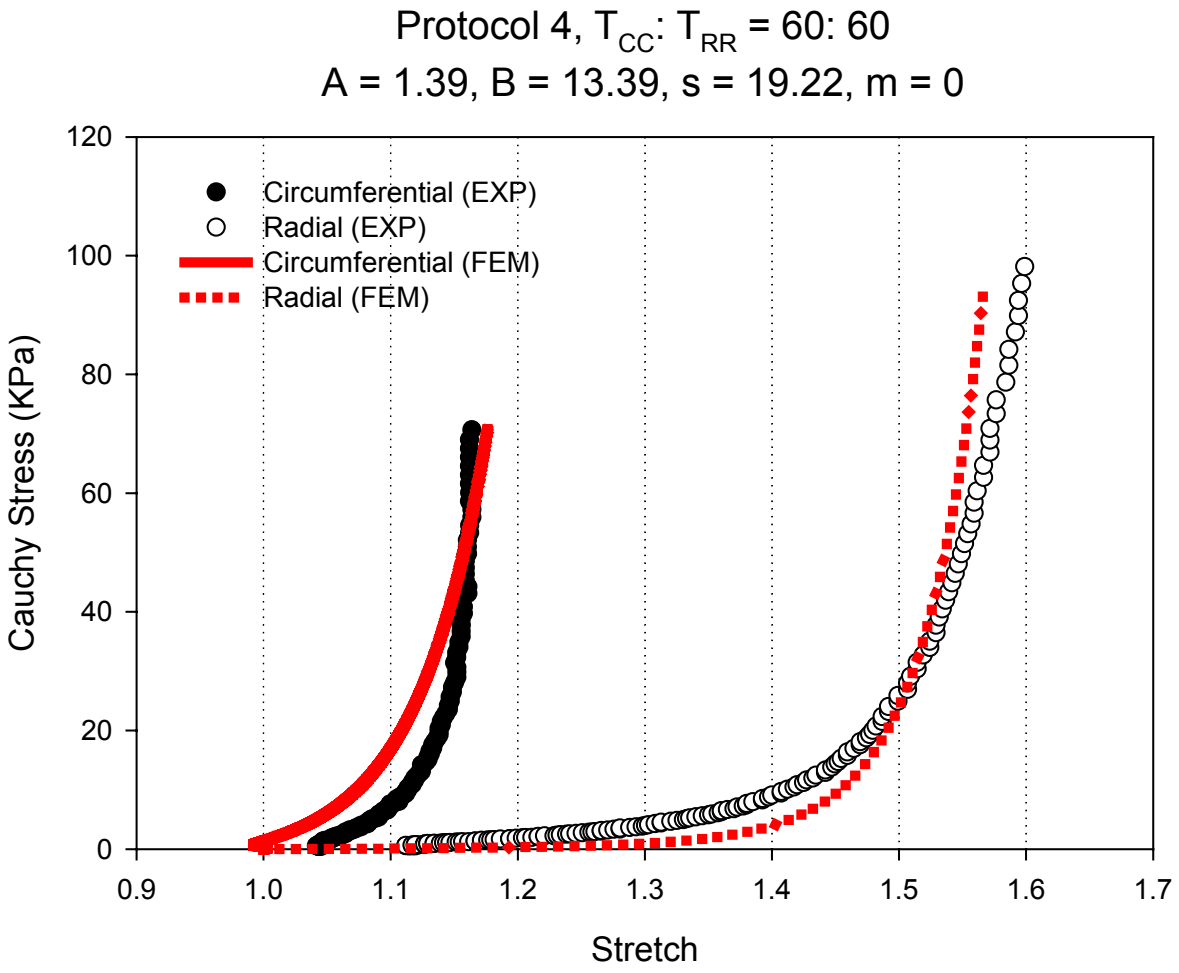

Figure 6-1 Experimental data of fresh bovine pericardium and single element finite element simulation, whereas protocol 4 indicates an equibiaxial tension protocol. T_{cc} and T_{rr} stand for the tensions applied in circumferential and radial directions, respectively.

However, when we tried to incorporate the model into multi-element simulations, a numerical convergence problem was encountered. Careful evaluation of the convergence problem has been conducted by looking at the ABAQUS nonlinear solution method – Newton's methods (section 3.1.2) and related convergence criteria. However, with limited methods to interact with ABAQUS solver, we could not get the problem solved. We estimated that possible solutions might include shifting the project into another finite element software package that has a more transparent finite element solver that a user have more controls, or reforming the constitutive model, such as adding a matrix term.

6.3 CONCLUSION

In the long term, chemically treated BHV will be supplanted by tissue engineered valve prostheses. Regardless of the specifics of chemically treated BHV design and biomaterial design for tissue engineered valve prosthesis, all BHV will have to duplicate natural tissue mechanics to some extent in order to properly simulate their *in vivo* function. Biomechanical simulations can contribute significantly to this process by integrating the disparate findings of structural properties measured experimentally *in vitro* and theoretical studies of biomechanics and forming a unifying tool to predict BHV functions *in vivo*. This is the goal of biomechanical simulations and the research effort in this study is one step towards it. With the rapid development of biotechnology,

we have no doubt that a numerical simulation that includes functional coupling between many physiological processes, such as cell growth and signaling, tissue damage, growth and remodeling, metabolism, transport and electrophysiology could be available in a foreseeable future and benefit millions of lives.

APPENDIX A: PHYSICAL CONSTRAINTS

In the following we present material parameter restrictions for eqn. 2.16. While the following is not an exhaustive analysis, the derived constraints are sufficient for physically realistic strain energy functions, and extend similar relationships derived by Humphrey [93] to include the presence of shear strains. The derived restrictions were applied to simpler forms used in the current study by the eliminating the additional terms.

Following eqns. 2.13 and 2.16, we have

$$W=\frac{c}{2}(e^{Q}-1) \tag{A1}$$

and from eqn. 2.12

$$S_{11}=\frac{c}{2}(2A_1E_{11}+2A_3E_{22}+2A_5E_{12})e^{Q} \tag{A2}$$

$$S_{12}=\frac{c}{2}(2A_4E_{12}+2A_5E_{11}+2A_6E_{22}+2BE_{12}E_{22}^{2})e^{Q} \tag{A3}$$

$$S_{22}=\frac{c}{2}(2A_2E_{22}+2A_3E_{11}+2A_6E_{12}+2BE_{12}^{2}E_{22})e^{Q} \tag{A4}$$

We first require that W vanish in the reference configuration and increase with deformation, i.e. $W \geq 0$ so that $c \geq 0$. Next, the parameters used in the current model must also satisfy the following simple deformations:

Case 1: $S_{11}>0$, when $E_{11}>0$, $E_{12}=E_{22}=0$, leading to $A_1E_{11}+A_3E_{22}+A_5E_{12}>0$, or $A_1>0$.

Case 2: $S_{22}>0$, when $E_{22}>0$, $E_{12}=E_{11}=0$, leading to $A_2E_{22}+A_3E_{11}+A_6E_{12}+BE_{12}^2E_{22}>0$, or $A_2>0$.

Case 3: $S_{12}>0$, which is sub-divided into the following two sub-cases:

(a) $E_{11}=0$, $E_{12}>0$ and $E_{22}\neq 0$ (i.e. simple shear in X_1 direction), so that $A_4E_{12}+A_6E_{22}+BE_{12}E_{22}^2>0$.

(b) $E_{22}=0$, $E_{12}>0$ and $E_{11}\neq 0$ (i.e. simple shear in X_2 direction), so that $A_4E_{12}+A_5E_{11}>0$.

These conditions were validated during the regression procedure. Please note that based on above constraints the material constant A_3 is not restricted, so that A_3 will occasionally have negative values (Tables 2-1 and 2-2).

APPENDIX B: RESPONSE FUNCTION

In the following the formulae used for interpolation of the complete pseudo-elastic response is described. First, each stress component was *individually fit* to the following functions:

$$S_{11} = c(2D_1E_{11} + 2D_3E_{22} + 2D_5E_{12} + 4D_7E_{11}^3)e^P \tag{B1}$$

$$S_{22}=c(2D_2E_{22}+2D_3E_{11}+2D_6E_{12}+4D_9E_{22}^3)e^P \tag{B2}$$

$$S_{12}=c(2D_4E_{12}+2D_5E_{11}+2D_6E_{22}+4D_8E_{12}^3)e^P \tag{B3}$$

where

$$P=D_1E_{11}^2+D_2E_{22}^2+2D_3E_{11}E_{22}+D_4E_{12}^2+2D_5E_{11}E_{12}+ 2D_6E_{22}E_{12}+D_7E_{11}^4+D_8E_{12}^4+D_9E_{22}^4 \tag{B4}$$

and c and D_i are material constants. Thus, each stress component had its unique parameter set, and resulted in very accurate fits ($r^2 \geq 0.99$).

Next, the value of each stress component was expressed as a function of two strain components while the other was kept at a prescribed constant value. This allowed us to simulate the response of each **S** component against various combinations of **E** and

guide the choice of the functional form of **Q**. All together nine response functions were generated, using strain ranges of experimental data.

APPENDIX C: RESPONSE OF BHV BIOMATERIALS TO MODERATE CYCLIC LOADING**

Currently, the durability of candidate BHV biomaterials is assessed through costly, time-consuming accelerated durability tests and animal implantation studies. Accelerated durability tests may approximate the tissue stress fields for intact valve and induce some forms of tissue damages. However, damage mechanisms are difficult to analyze from these tests due to the complexity of the BHV leaflet deformations and the confounding influences of specific valve designs. There is clearly a need for a comprehensive understanding of the intrinsic response of BHV biomaterials subjected to cyclic loading. Moreover, heterograft biomaterials are composed of fibrous collagen and other extra-cellular proteins with additional exogenous cross-links that exhibit complex anisotropic mechanical behaviors [34]. Thus, traditional approaches to material

---

** Some of the results are from the manuscript:

W. Sun, M.S. Sacks, G. Fulchiero, J. Lovecamp, N. Vyavahare, and M. J Scott, "response of heterograft heart valve biomaterials to moderate cyclic loading", ***Journal of Biomedical Materials Research***. (in review)

fatigue, originally developed for metallic materials, may not be applicable to BHV biomaterials. This suggests the need for a more fundamental understanding of the response of heterograft biomaterials to long-term cyclic loading.

As a starting point, we choose to study the *early* responses of BHV biomaterials to cyclic loading. This based on our previous work on porcine BHV [143] which indicated large changes in mechanical behavior occur relatively early in valve operation (between $1x10^6$ and $50x10^6$ cycles, corresponding to ~1.4 patient years at 70 bpm). Moreover, it is likely that once the BHV biomaterial is at or near material failure (occurring after several hundred million cycles), there is little that can be done (with regard to the material) to mitigate the failure process. Minimizing the early degeneration processes of heterograft biomaterials would presumably lead to improved long-term heart valve durability.

Based on these considerations, we have elected to focus our studies on the mechanisms of structural and mechanical changes BHV biomaterials subjected to moderate levels of cyclic loading. We hypothesize that an improved understanding of these initial responses can guide the development of novel chemical modifications to minimized these processes and ultimately produce more durable heart valve biomaterials. For the current study, we utilized GLBP as the representative BHV heterograft biomaterial and quantified its response to moderate levels of cyclic loading. Changes in specimen dimensions, anisotropic mechanical properties, and molecular- and fiber level structural changes to collagen were quantified. In addition, we present a

generalized framework for 2 dimensional kinematic analyses to account for the effects of permanent set on strain calculations.

Specimen preparation. For this study, we used GLBP as the representative heart valve biomaterial. Specimens were presorted by SALS [38, 45]. Twelve 25 mm x 25 mm GLBP specimens exhibiting a high degree of structural uniformity were selected; six used for fatigue testing and six for uncycled control.

Cyclic testing apparatus. The cyclic testing apparatus used in the study was a custom-made tensile fatigue tester capable of testing six specimens simultaneously (Figure C-1). Displacement and frequency was adjustable within a stroke range of 0-6mm and frequency range of 0-40Hz. A specially designed tissue grips were used for mounting the specimens with the edges of the grips rounded to avoid abrasion of the edges to the specimens during fatigue. In addition, the grips had four pins on both upper and lower grips for each specimen; the pins went through the suture holes used for biaxial testing of the specimen.

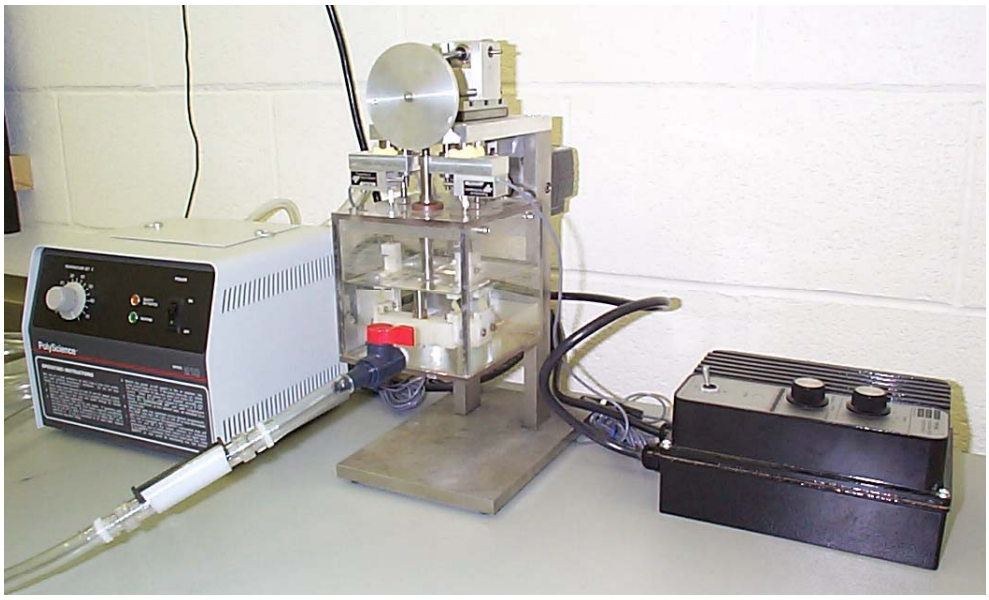

Figure C-1 The custom-made tensile fatigue testing apparatus

Six fatigue specimens were mounted on the tester with the direction of strain aligned to tissue preferred fiber direction (PD), while the cross-preferred fiber direction (XD) left load-free. Cyclic tests were conducted under strain control at room temperature with the specimens completely submerged in phosphate buffered saline (PBS) plus 0.5% sodium azide to prevent bacteria growth. Specimens were then cycled at 30 Hz to a maximum strain level of 16% (peak stress level about 1 MPa). Six control specimens were put into the same testing bath, without any loading imposed on, for characterizing the time and solution effects. Specimens were cycled to 0, 30×10^6 (low) and 65×10^6 (moderate) cycle levels. After each cycle level, each specimen was removed from the fatigue tester and biaxial tested to quantify changes in anisotropic biaxial mechanical properties.

Kinematic analysis methods. To quantify mechanical property changes during cyclic loading, the biaxial mechanical testing data was analyzed with respect to both (i) the current reference marker positions, and (ii) the original un-cycled reference marker positions (See Appendix D). This approach allows examinations of current tissue mechanical properties with respect to both the permanent deformation caused by the cyclic loading and the loading deformation due to the application of 1 MPa in biaxial testing. The stretch ratios along the preferred (λ_{PD}) and cross-preferred (λ_{XD}) directions under 1 MPa equibiaxial stress was used to qualify the tissue extensibility. The net tissue compliance was represented by the areal stretch that was computed ($=\lambda_{PD}\lambda_{XD}$) under 1 MPa equibiaxial stress. Comparisons between cyclic loading levels were performed using t-tests, with statistically significant difference level set to $p<0.05$. All data are represented as the mean ± standard error.

Methods of quantifying fiber and molecular-level changes to collagen. Mechanical properties of collagenous tissues are a function of the structural organization collagen, from the molecular– to fiber-level structural levels. In this study, we examined changes in collagen molecular conformation and fiber uncrimping as measures at these two structural levels. To examine the collagen fiber structure changes with cyclic loading, histological sections were prepared parallel to the preferred collagen fiber direction and stained with picro-sirius red. Polarized light microscopy (Nikon Eclipse Microscope) was performed on each specimen and 3-6 digitized images were recorded, at each magnification (e.g. 10x, 20x, and 40x). Collagen crimp analysis, based on the previous work by Hilbert [53], was performed on the digital polarized photomicrographs [144].

Briefly, the images were imported as N (rows) by M (columns) matrices of grayscale pixel intensities into MATLAB® (MathWorks, Inc., Ver. 7.0). The images were then averaged along the columns, creating a vector of averaged intensities having the dimension of 1 (row) by M (columns). This vector was next entered as a discrete intensity versus distance signal into the MATLAB Signal Processing Toolbox®, where a fast Fourier transform (FFT) and power spectral density (PSD) were subsequently performed. Spectral decomposition of a signal using PSD is able to reveal a distinct peak of the dominant frequency of collagen crimp in the digital image.

We have previously used FTIR spectra to examine the collagen structure changes at molecular level for fatigued glutaraldehyde crosslinked porcine aortic cusps [145]. In this study, we applied the same technique for the first time to cyclically loaded GLBP. These specimens were equilibrated in sterile water prior to obtaining FT-IR spectra. The IR spectra (64 scans at 2 cm^{-1} resolution) of specimens in the hydrated state were obtained using Fourier transform IR spectroscopy (FTIR, Jasco 480 Plus) with a fixed 45^{o} angle attenuated total reflectance (ATR, ZnSe) cell attachment. Water was used as a background reference and water spectrum was subtracted from the specimen spectra by the computer program. For both the FTIR and collagen crimp studies, two control and three cycled specimens were analyzed.

Key results. A summary of the key results of the study are is listed in Table C-1. As anticipated, permanent deformations were induced with cyclic loading. On average, specimen geometry was changed by 7.1% in the PD direction and 7.7% in the XD

direction at $30x10^6$ cycles (Figure C-2). There were no statistically significant changes between $30x10^6$, $65x10^6$ cycles, as well as no statistically significant changes for the control specimens for all cycles.

Table C-1 Summary of the key results

Methods	Results	Level
FT-IR	Collagen conformational change	Molecular
Collagen crimp period	Increase collagen crimp period with cycling	Fiber
Specimen dimension change	+7.1% strain in PD direction, -7.7% in XD direction	Tissue
Biaxial mechanical testing: Strain referenced to current state	Decreased extensibility in PD direction; increased extensibility in XD direction.	Tissue
Biaxial mechanical testing: Strain referenced to un-cycled state	Stabile areal strain, overall tissue compliance unchanged	Tissue

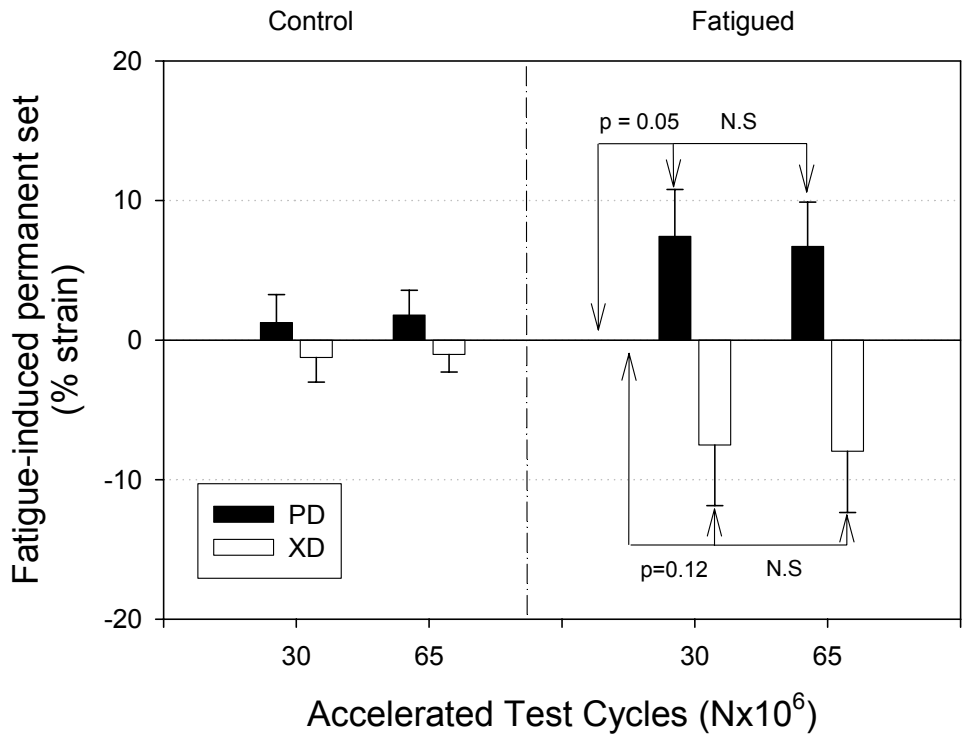

Figure C-2 Fatigue-induced permanent tissue deformation. The fatigued specimen geometry was changed by about +7.1% in the PD direction and about –7.7% in the XD direction for both measurements at $30x10^6$, $65x10^6$ cycles.

Mechanical property changes referred to the current state. When the biaxial mechanical data were analyzed with respect to the current cycle level, decreasing extensibility along the PD direction with cycling was observed (Figure C-3a). For the XD direction, there was a corresponding increase in extensibility with cycle numbers (Figure C-3b). When examining peak stretch ratios, the PD direction decreased significantly ($p<0.05$) by 0.05 (=5% strain) from 0 cycle to $30x10^6$ cycles (Figure C-4a). There were no statistically significant differences between $30x10^6$ cycles and $65x10^6$

cycles. In the XD direction, there was a statistically significant increase of stretch ratio from 0 cycle to $65x10^6$ cycles (Figure C-4a). However, no significant changes occurred from 0 cycles to $30x10^6$ cycles and from $30x10^6$ cycles to $65x10^6$ cycles. For control group there is no statistically significant difference among all cycle levels (Figure C-4b).

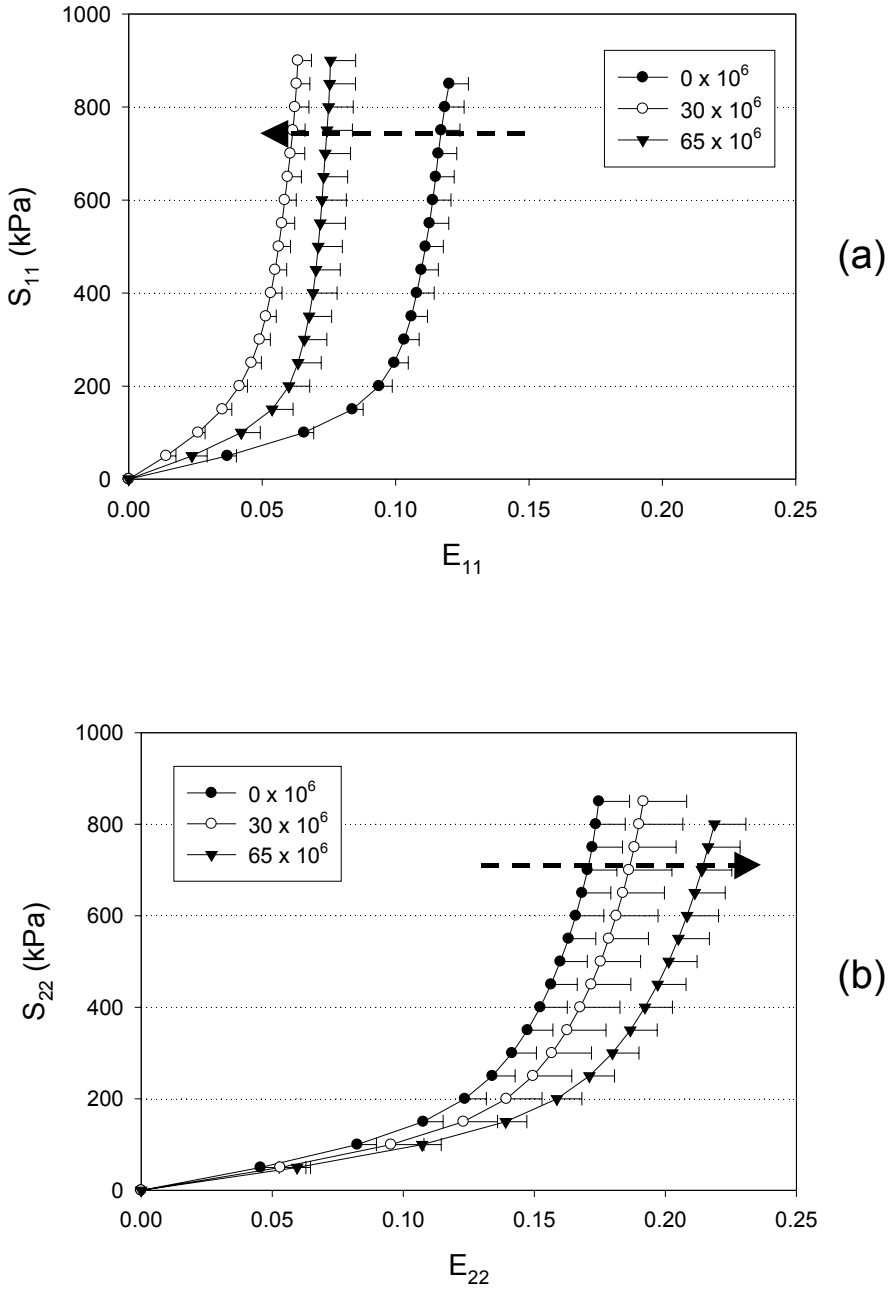

Figure C-3 Biaxial testing data at 0, $30x10^6$ and $65x10^6$ cycles levels, analyzed with each individual current fatigue state, showed a decreasing extensibility in PD direction and increasing extensibility in XD direction.

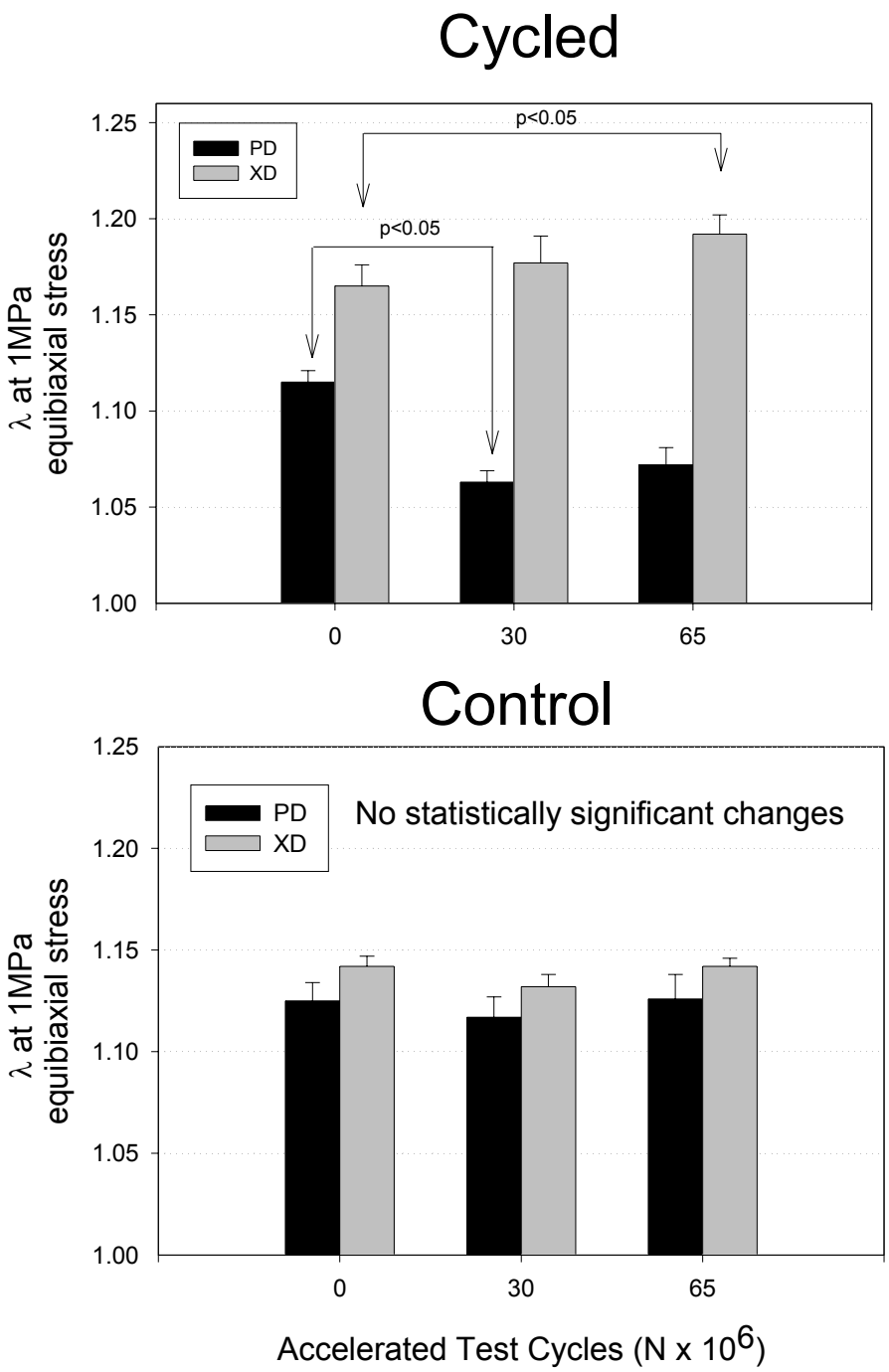

Figure C-4 (a) The peak stretch ratios at 1MPa equibiaxial stress, analyzed at each individual current fatigue reference state, for fatigued tissue. Stretch ratios were decreased in the PD direction and increased in XD direction with fatigue cycles. (b) The peak stretch ratios at 1MPa equibiaxial stress, analyzed at each individual current fatigue reference state, for control tissue, showing no statistically significant changes.

Biaxial mechanical properties referred to the uncycled state. When the biaxial experimental data were re-analyzed with respect to the un-cycled reference marker state (see Appendix D), there were no statistically significant changes in the peak stretch ratios for both PD and XD directions (Figure C-5a). Areal stretch values indicated a trend toward decreasing extensibility with cycling. However, the peak values were not statistically different nor were the slopes were statistically different from zero (Figure C-5b). For the control group, there were no statistically significant changes with time.

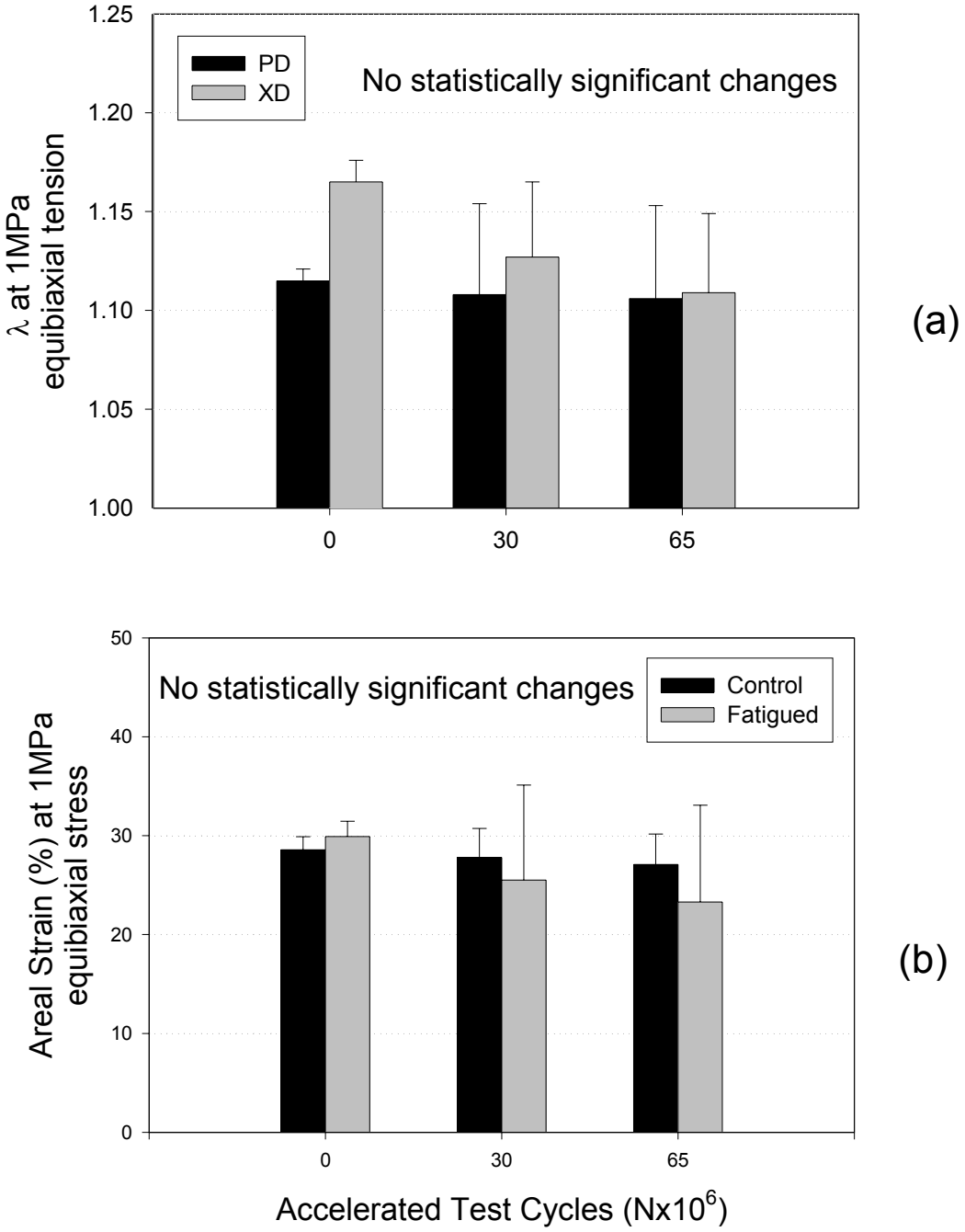

Figure C-5 (a) The peak stretch ratios at 1MPa equibiaxial stress, analyzed at 0 cycle PP reference state, for fatigued tissue. There is no statistically significant change at all cycle stops; (b) The areal strain at 1Mpa equibiaxial stress, analyzed at initial, un-cycled reference state, for both control and fatigued tissue. There is no statistically significant change at all cycle stops. However, there is a "declining" trend for fatigued tissue.

Fiber and molecular-level changes to collagen. Representative digital polarized photomicrographs for both control specimen and fatigue specimens at $65x10^6$ are illustrated in Figure C-6. Collagen crimp period increased from 40.55 μm for un-cycled control specimens to 45.22 μm for $65x10^6$ cycles fatigued specimens ($p=0.05$) (Figure C-6c). Conformational changes accessed by ATR-FTIR spectroscopy showed typical spectrum for Type I collagen, the major protein in the pericardium, for control specimens (Figure C-7). Two major peaks were found, one at 1660-1630 (Amide I peak from C=O stretching vibrations) and other at 1553 cm^{-1} (Amide II peak for amide N-H bending vibrations coupled with C-N stretching). Amide I peak at 1660-1630 cm^{-1} was separated into three peaks, viz. 1653, 1643, and 1632 cm^{-1} showing carbonyls in different environments. After $65x10^6$ cycles, fatigued specimens showed significant changes in the amide I region. The peaks at 1655 and 1643 cm^{-1} were reduced in intensity and the peak at 1631 cm^{-1} was increased in the intensity. There was also a new peak found at 1728 cm^{-1} (for esters probably from phospholipids), which was absent in the control specimens. All other peaks in cycled specimens were similar to that of control specimens (Figure C-7).

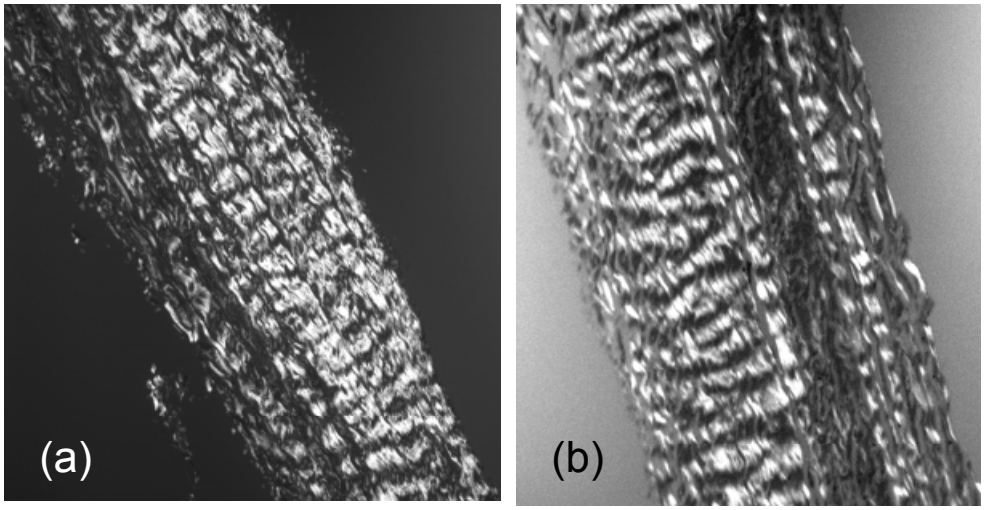

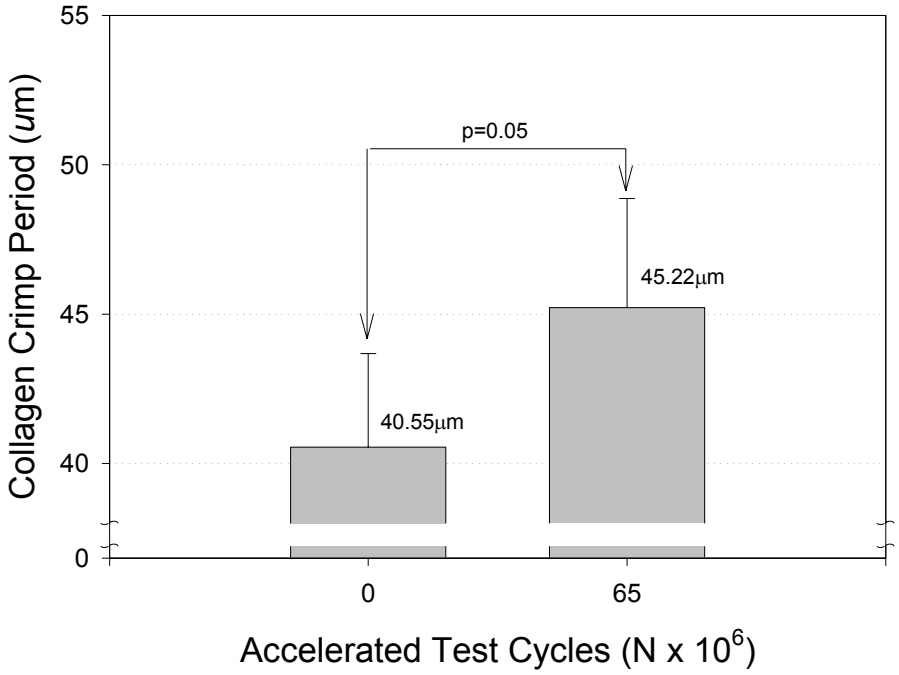

(c)

Figure C-6 a) digital polarized photomicrographs for control tissue; b) for fatigued tissue at 65 x 10^6 cycles; c) The crimp analysis from digital polarized photomicrographs for both control and fatigued specimens showed that the collagen crimp period increased from 40.55 μm for un-cycled control specimens to 45.22 μm for 65x10^6 cycles fatigued specimens.

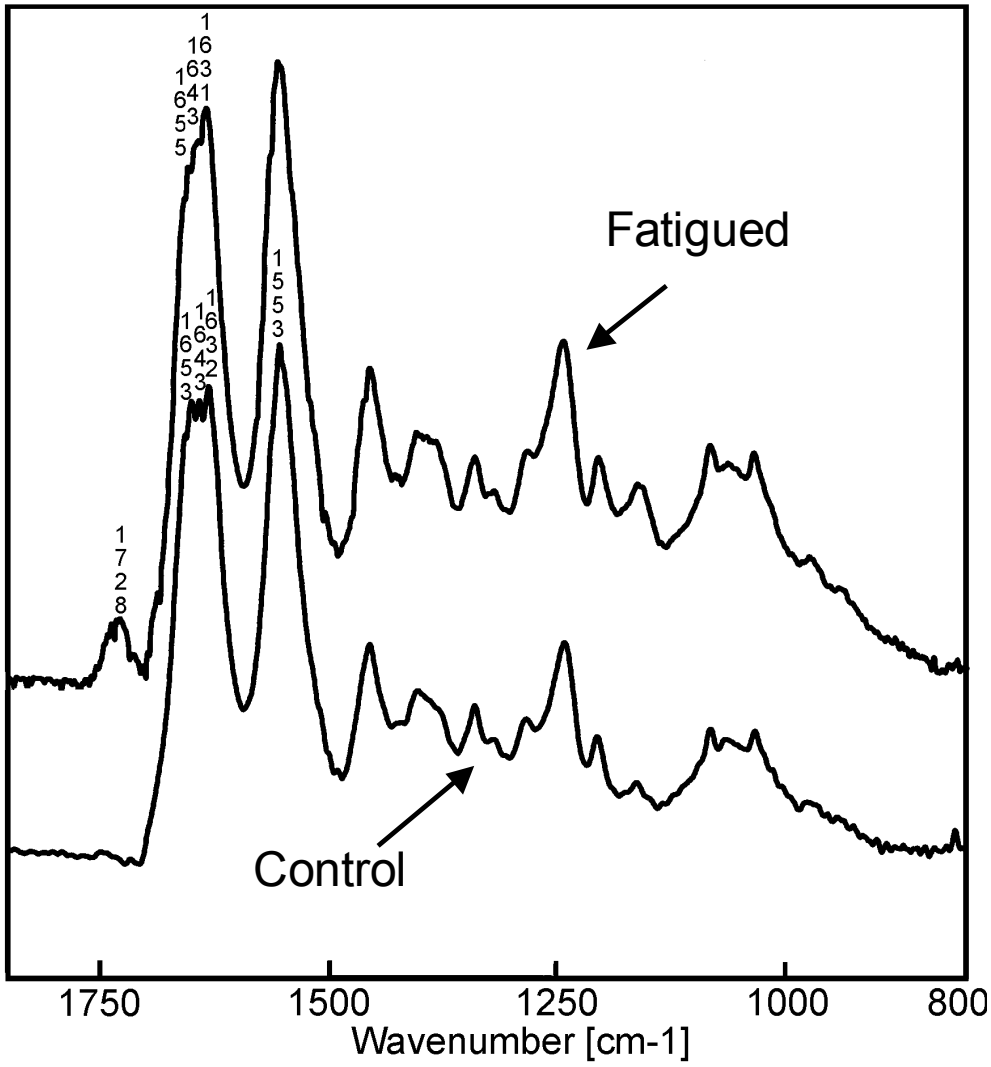

Figure C-7 FT-IR spectra for both control and fatigued specimens.

Discussion. This study was aimed at improving our knowledge of the mechanisms of fatigue of biologically derived collagenous BHV biomaterials. There have been relatively few related studies, with most dependent on a particular valve design [55, 143, 146-148]. However, the profound influence of complex leaflet deformations during valve operation makes it difficult to elucidate fundamental fatigue damage mechanisms. Broom *et al*. [55] conducted the first efforts to characterize the isolated tissue

behavior under a combined tensile and buckling fatigue studies. However, to fully elicit the mechanisms of tissue degeneration, isolation of the contributions of individual loading states (e.g. tension, flexure) is a necessary first step in understanding the fatigue process as a whole.

Our previous work on porcine BHV [143] indicated large changes in mechanical behavior occur relatively early in valve operation (between $1x10^6$ and $50x10^6$ cycles, corresponding to ~1.4 patient years at 70 bpm). Thus, in the present study we investigated the response of GLBP to medium-term tensile-only cyclic loading, and have examined the tissue degeneration through the methods of FT-IR analysis (for molecular level collagen conformational change), collagen crimp analysis (for fiber level collagen fiber un-crimping) and biaxial mechanical testing (for tissue mechanical properties changes.).

Fatigue induced collagen conformational changes. Infrared spectroscopy has been used extensively to study protein conformation. In particular, infrared spectrum of Type I collagen has been thoroughly investigated [149-154]. The amide I carbonyl stretching region (1700-1600 cm^{-1}) has been shown to be very sensitive to the changes in collagen's triple helical tertiary structure during fibrillogenesis and denaturation [152-154]. The amide I peak is made up of three distinct bands; a band at 1655 cm^{-1} is assigned to the carbonyls that are within the triple helix, which are associated intra-molecularly with weaker hydrogen bonds. A band at 1643 cm^{-1} was assigned to the solvent hydrogen bonded glycine residues in the triple helix and a band at 1630 cm^{-1} was assigned to amide carbonyls protruding out from the triple helix and are associated inter-

molecularly with water molecules [153, 154]. Thus, increase in the intensity of 1630 cm^{-1} band as compared to the 1655 cm^{-1} as observed after $65x10^6$ cyclic loading of GLBP suggest that cyclic loading leads to collagen conformational changes and denaturation probably due to change in helicity caused by mechanically induced molecular fatigue. Similar increase in the intensity of peak at 1630 cm^{-1} for collagen to gelatin transitions has been reported for pure Type I collagen [154]. We have also shown similar collagen denaturation occurring after cyclic fatigue of glutaraldehyde treated porcine aortic cusps [145].

GLBP also showed a new prominent peak at 1728 cm^{-1} that was not present in the control non-fatigued specimens (Figure C-7). This peak could be assigned to the ester bonds of phospholipids [155]. At this time we do not know how the phospholipids appear at the surface of the tissues after in vitro cyclic fatigue. However, it is possible that because of the subsurface damage caused by mechanical fatigue, the remnants of devitalized cellular debris may leach out to the surface. We have also seen increase in this peak after cyclic fatigue of glutaraldehyde crosslinked porcine aortic valve cusps [145]. Overall FT-IR studies suggested that cyclic fatigue of GLBP caused collagen denaturation and beginnings of progressive deterioration as early as $65x10^6$ cycles.

Possible mechanisms for mechanical behavior with fatigue. Glutaraldehyde fixation introduces a large number of stable crosslinks between the amino acid groups of the polypeptide chains of collagen [132]. It has been assumed that the collagen fiber architecture and the corresponding mechanical behavior are locked in place with chemical fixation and remain unchanged during valve operation. However, if

mechanical properties are altered, there are two possible reasons: 1) collagen fiber architecture is changed, i.e. there is a spatial rearrangement of collagen fiber architecture (fiber un-crimping and reorientation) and/or 2) intrinsic properties of collagen fibrils are changed, possibly due to collagen molecule conformation change and denaturation. In the case of collagen un-crimping, when stretched tissue will exhibit lesser extensibility compared to its original crimp state. In the case of collagen reorientation, it has been shown [8] that tissue will exhibit more anisotropic and PD direction will be stiffer and XD direction more compliance.

Based on those considerations, our mechanical testing results (Figure C-2) can be explained in terms of collagen fiber un-crimping and fiber reorientation in the direction of loading. When the specimens were cycled in PD direction, the undulated collagen fibers were straightened along the loading direction, which was manifested by the permanent changes in tissue dimensions at tissue level (Figure C-2) and the increase of collagen fiber crimp period at fiber level (Figure C-6). It was therefore not surprising that the specimens would appear to be less extensible (Figure C-3a) when biaxial strains were referenced to the marker position of current cycle level. What is more interesting is in the XD direction the specimens appeared more extensible as the cycles increased (Figure C-3a). We speculated that since collagen fibers re-orient direction towards the loading direction [130, 156], under cyclic loading some of collagen fibers originally at an angle to the PD direction would be forced to rotate towards the loading direction and thus result in even less amount of fibers oriented in the XD direction. As a result the XD direction became more extensible (Figure C-3a). In this study, we are not able to

explicitly separate the effects of collagen fiber un-crimping and reorientation. However, we hypothesize that the fiber reorientation in the loading direction was the major contributor to the changes of tissue anisotropy. Similar fiber kinematics have been demonstrated in the mitral valve leaflet [5, 156], coronary artery [157] and bovine pericardium [130] as transient fiber configuration change (Note that in these case when stretch is removed, the fibers relax to their original configuration). However, in this study these fiber configuration changes were permanent changes induced by cyclic loading.

When the biaxial test data were referenced to the un-cycled marker position, no statistical significant difference was found for all cycle levels (Figure C-5). This result indicated that there was no overall tissue compliance change with respect to 0 cycle state (see Appendix D). In theory, a single cleavage in a protein chain can result in a decrease in mechanical integrity that can be detected by mechanical testing [148]. We speculated that even though there were conformational changes of type I collagen, those changes were not significant to alter overall tissue compliance and the overall tissue mechanical integrity was still intact after 65×10^6 cycles. These observations suggest that deterioration of collagen begin immediately, but the fiber straightening and reorientation dominate changes in mechanical behavior in the early (up to 65×10^6 cycles) phase of fatigue. However, as showed in Figure C-5b, the areal strain had the trend of declining for the fatigued tissue. The declining trend was not statistically significant and could be caused by the artifacts during the repetitive biaxial and fatigue testing, or intrinsic tissue properties changes similar to "strain hardening" effect that is unclear now. Even though different BHV biomaterials were used, our finding here is

consistent with our previous finding that the mechanical properties of zero-pressure-fixed porcine BHV cusps were not stabile with long-term cyclic loading [143] and large changes in mechanical behavior occur relatively early in valve operation (between $1x10^6$ and $50x10^6$ cycles).

Limitations. As an initial study, establishing proper and feasible experimental methods and protocols was also part of our goal. The accuracy of repetitive tissue deformation measurements at each cycle level is dependent on the integrity of the optical markers glued on the central region of the specimens. After 65 x 10^6 cycles, optical markers stayed on all cycled specimens and five control specimens, suggesting the feasibility of using optical marker for strain measurement in tissue fatigue study. Specimen griping may need to be slightly modified to allow for sandpaper sandwich clamping so that lesser force born by suture hole. Reliance on suture holes tore a few suture holes of the specimens. No significant mechanical property change for control specimens indicated that the effects of time and solution contamination over the fatigue period were not significant. Fatigue testing was conducted under strain control, which might be one of the drawbacks of the experiment. As physiologically BHV is deformed under hydraulic pressure that is equivalent to stress-driven deformation. Current fatigue tester however does not allow us to conduct stress control experiments. At 30 million cycles, fatigue may already consume the possible crimp effects and that might be the reason that we did not see the alteration of tissue mechanical properties after $30x10^6$ cycles. In addition, in current study we only examined the effects of cyclic loading with the loading direction parallel to the PD direction, a more rigorous study

with the loading direction perpendicular to the PD direction and with constitutive modeling of fatigue effects is current ongoing in our lab.

Summary. The response of GLBP to medium-term cyclic tensile loading was quantified in this study to elucidate the mechanisms of tissue degeneration in BHV biomaterials. After $65x10^6$ cycles, we found permanent changes in tissue dimensions as well as collagen crimp period increase, which indicated cyclic loading induced permanent configuration changes in fiber level and manifested in tissue level. Biaxial mechanical testing indicated that tissue became less extensible in the PD direction and more extensible in the XD direction. We hypothesized that this change was due to permanent increase in collage crimp period and fiber kinematical re-orientation induced by cyclic loading. Moreover, no significant areal strain change indicated that there is no significant fiber fracture and tissue change to alter overall tissue compliance. Taken as a whole, these results indicate that while molecular level damage to collagen occurs very early, these changes are secondary to fiber straightening and reorientation effects resulting from geometric changes to the specimen as a resulting from permanent set.

APPENDIX D: KINEMATICAL ANALYSIS OF FATIGUE

To rigorously quantify multi-dimensional tissue deformation during fatigue, we rely on the kinematic framework of finite strain theory with multi-configurations. These relations can be explained as follows. Consider the relations between the three configurations of interest: the initial, stress-free uncycled configuration β^o, the stress-free but fatigued configuration β^1, and the loaded configuration β^2 for the state when the tissue is stressed to 1 MPa (Figure D-1). The deformation gradient tensor $\mathbf{F}$ associated with the any finite deformation is given by $\mathbf{F}=\begin{bmatrix}\lambda_1 & \kappa_1\\ \kappa_2 & \lambda_2\end{bmatrix}$, where λ_i are the stretch ratios and κ_i measures of in-plane shear. When deforming from β^o to β^1, β^1 to β^2, β^o to β^2 (Figure D-1), the associated deformation gradient tensors are $\mathbf{F}^{0\text{-}1}$, $\mathbf{F}^{1\text{-}2}$, and $\mathbf{F}^{0\text{-}2}$, respectively. Extending this approach to the current study, we adopt the notation F_0, F_{30}, and F_{65} for the deformations at 0, 30 and 65x10^6 cycles, respectively. Thus, F_{30}^{1-2} and F_{65}^{1-2} represent the deformations due the application of 1 MPa equibiaxial loading analyzed with respect to the current reference marker position. In contrast, $F_{30}^{0-2}=F_{30}^{0-1}\bullet F_{30}^{1-2}$ and $F_{65}^{0-2}=F_{65}^{0-1}\bullet F_{65}^{1-2}$ represent the data analyzed by referenced to the initial, un-cycled reference marker position. As an illustration of the kinematic approach, the

stretches (λ_1, λ_2) of one specimen during the cyclic loading process are shown here. Please be noted that for demonstration propose we ignore the shear components, which is usually very small, however, shear components should be included during the actual calculation to ensure accuracy.

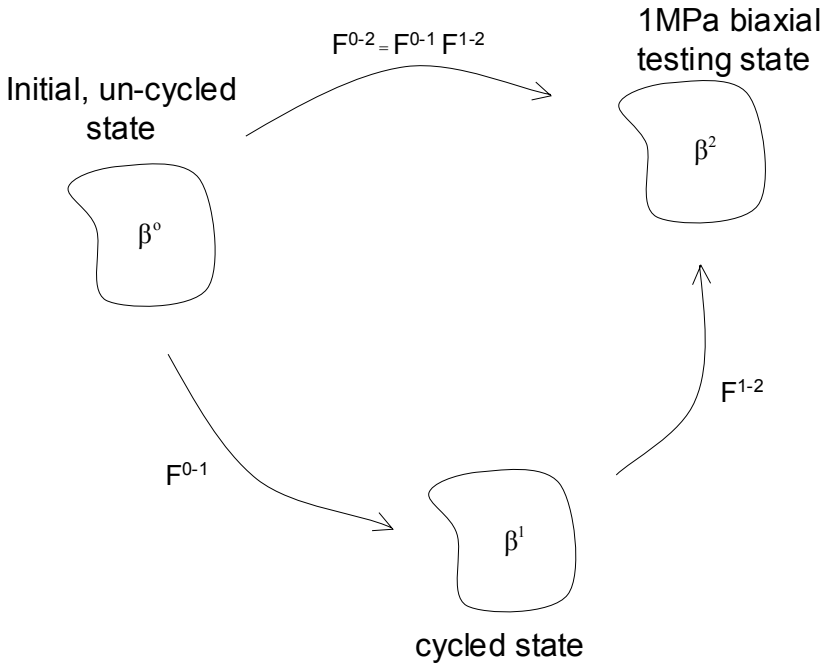

Figure D-1 Schema of deformations from uncycled reference configuration β^0 to a cycled configuration β^1, and then to configuration β^2 following 1 MPa stress. In finite strain theory, successive deformations are accounted by multiplication of **F** for each state, rather than summing the strains as done in infinitesimal strain theory.

The stretches (λ_1, λ_2) of two axes due to the application of 1 MPa equibiaxial loading analyzed with respect to the current 0, 30 and $65x10^6$ cycles reference marker position are (1.14, 1.21), (1.05, 1.15), and (1.08, 1.17), respectively. The stretches (λ_1, λ_2) of two axes induced by the cyclic loading at 0, 30 and $65x10^6$ cycles are (1.0, 1.0), (1.09,

1.06), and (1.06, 1.03), respectively. The data analyzed by referenced to the initial, un-cycled reference marker position are calculated by:

$$F_0^{0-2} = F_0^{0-1} \bullet F_0^{1-2} = \begin{bmatrix} 1.0 & 0.0 \\ 0.0 & 1.0 \end{bmatrix} \bullet \begin{bmatrix} 1.14 & 0.0 \\ 0.0 & 1.21 \end{bmatrix} = \begin{bmatrix} 1.14 & 0.0 \\ 0.0 & 1.21 \end{bmatrix} \quad \text{(D1)}$$

$$F_{30}^{0-2} = F_{30}^{0-1} \bullet F_{30}^{1-2} = \begin{bmatrix} 1.09 & 0.0 \\ 0.0 & 1.06 \end{bmatrix} \bullet \begin{bmatrix} 1.05 & 0.0 \\ 0.0 & 1.15 \end{bmatrix} = \begin{bmatrix} 1.14 & 0.0 \\ 0.0 & 1.22 \end{bmatrix} \quad \text{(D2)}$$

$$F_{65}^{0-2} = F_{65}^{0-1} \bullet F_{65}^{1-2} = \begin{bmatrix} 1.06 & 0.0 \\ 0.0 & 1.03 \end{bmatrix} \bullet \begin{bmatrix} 1.08 & 0.0 \\ 0.0 & 1.17 \end{bmatrix} = \begin{bmatrix} 1.14 & 0.0 \\ 0.0 & 1.21 \end{bmatrix} \quad \text{(D3)}$$

It can be observed that F_0^{0-2}, F_{30}^{0-2} and F_{65}^{0-2} are very close to each other.

In the present study, when mechanical testing data are referred to the initial, stress-free uncycled configuration β^o and statistically no changes are observed, it can be concluded that there are no intrinsic changes in the mechanical properties of the tissue, and that the observed changes in the current state represent "permanent set" effects only.

BIBLIOGRAPHY

1. Biosci, The history of heart disease. http://www.fi.edu/biosci/history/history.html, 2003.

2. Schoen, F. and R. Levy, Pathology of Substitute Heart Valves. Journal of Cardiac Surgery, 1994. **9**: p. 222-227.

3. Sacks, M.S. and F.J. Schoen, Collagen fiber disruption occurs independent of calcification in clinically explanted bioprosthetic heart valves. J Biomed Mater Res, 2002. **62**(3): p. 359-71.

4. Schoen, F.J. and R.J. Levy, Founder's Award, 25th Annual Meeting of the Society for Biomaterials, perspectives. Providence, RI, April 28-May 2, 1999. Tissue heart valves: current challenges and future research perspectives. J Biomed Mater Res, 1999. **47**(4): p. 439-65.

5. Clark, R.E. and E.C. Finke, Scanning and light microscopy of human aortic leaflets in stressed and relaxed states. Journal of Thoracic Cardiovascular Surgery, 1974. **67**: p. 792-804.

6. Sacks, M.S., D.B. Smith, and E.D. Hiester, The aortic valve microstructure: effects of transvalvular pressure. J Biomed Mater Res, 1998. **41**(1): p. 131-41.

7. Billiar, K.L. and M.S. Sacks, Biaxial mechanical properties of the natural and glutaraldehyde treated aortic valve cusp--Part I: Experimental results. J Biomech Eng, 2000. **122**(1): p. 23-30.

8. Billiar, K.L. and M.S. Sacks, Biaxial mechanical properties of fresh and glutaraldehyde treated porcine aortic valve cusps: Part II - A structurally guided constitutive model. Journal of Biomechanical Engineering, 2000. **122**(4): p. 327-335.

9. Schoen, F.J., Pathology of heart valve substitution with mechanical and tissue prostheses, in *Cardiovascular Pathology*, M.D. Silver, A.I. Gotlieb, and F.J. Schoen, Editors. 2001, Livingstone: New York.

10. Turina, J., O.M. Hess, M. Turina, and H.P. Krayenbuehl, Cardiac bioprostheses in the 1990s. Circulation, 1993. **88**(2): p. 775-81.

11. Aupart, M., D. Babuty, L. Guesnier, Y. Meurisse, A. Sirinelli, and M. Marchand, Double valve replacement with the carpentier-edwards pericardial valve: 10 year results. Journal of Heart Valve Disease, 1996. **5**: p. 312-316.

12. Cosgrove, D., Carpentier Pericardial Valve. Seminars in Thoracic and Cardiovascular Surgery, 1996. **8**(3): p. 269-275.

13. Frater, R., P. Furlong, D. Cosgrove, J. Okies, L. Colburn, A. Katz, N. Lowe, and E. Ryba, Long-term durability and patient functional status of the carpentier-edwards perimount pericardial bioprosthesis in the aortic position. Jounral of Heart Valve Disease, 1998. **7**: p. 48-53.

14. Grunkemeier, G.L. and E. Bodnar, Comparative assessment of bioprosthesis durability in the aortic position. J Heart Valve Dis, 1995. **4**(1): p. 49-55.

15. Pelletier, L., M. Carrier, Y. Leclerc, and I. Dyrda, The carpentier-edwards pericardial bioprosthesis: Clinical experience with 600 patients. Annals of Thoracic Surgery, 1995. **60**: p. S297-302.

16. Schoen, F.J. and R.J. Levy, Calcification of bioprosthetic heart valves, in *Replacement Cardiac Valves*, E. Bodnar and R.W.M. Frater, Editors. 1991, Pergamon Press, Inc.: New York. p. 125-148.

17. Ferrans, V.J., S.L. Hilbert, S. Fujita, M. Jones, and W.C. Roberts, Morphologic Abnormalities in Explanted Bioprosthetic Heart Valves, in *Cardiovascular Pathology*, R. Virmani, J. Atkinson, and J. Fenoglio, Editors. 1991, W.B. Saunders: Philadelphia. p. 373-398.

18. Harasaki, H., M. Baker, and D. Zona, Cross-linking agents, degree of crosslinkage and calcifiability in bioprosthetic heart valves. Transactions of the Society for Biomaterials (abstract), 1990. **13**: p. 25.

19. Pereira, C.A., J.M. Lee, and S.A. Haberer, Effect of alternative crosslinking methods on the low strain rate viscoelastic properties of bovine pericardial bioprosthetic material. Journal of Biomedical Materials Research, 1990. **24**: p. 345-361.

20. Petite, H., I. Rault, A. Huc, P. Menasche, and D. Herbage, Use of acyl azide method for cross-linking collagen rich tissues such as pericardium. Journal of Biomedical Materials Research, 1990. **24**: p. 179-187.

21. Vasudev, S. and T. Chandy, Effect of alternative crosslinking techniques on the enzymatic degradation of bovine pericardia and their calcification. Journal of Biomedical Materials Research, 1997. **35**: p. 357-369.

22. Bengtsson, L., R. Phillips, and A. Haegerstrand, In-vitro endothelialization of photooxidatively stabilized xenogenic pericardium. Annals of Thoracic Surgery, 1995. **60**: p. S365-S368.

23. Moore, M., I. Bohachevsky, D. Cheung, B. Boyan, W. Chen, R. Bickers, and B. McIlroy, Stabilization of Pericardial Tissue by Dye-Mediated Photooxidation. Journal of Biomedical Materials Research, 1994. **28**: p. 611-618.

24. Moore, M., W. Chen, R. Phillips, I. Bohachevsky, and B. McIlroy, Shrinkage Temperature versus Protein Extraction as a Measure of Stabilization of Photooxidized Tissue. Journal of Biomedical Materials Research, 1996. **32**: p. 209-214.

25. Moore, M., B. McIlroy, and R. Phillips, Nonaldehyde sterilization of biologic tissue for use in implantable medical devices. ASAIO, 1997. **43**: p. 23-30.

26. Schoen, F.J., Pathologic findings in explanted clinical bioprosthetic valves fabricated from photooxidized bovine pericardium. J Heart Valve Dis, 1998. **7**(2): p. 174-9.

27. Broom, N.D., Simultaneous morphological and stress-strain studies of the fibrous components in wet heart valve leaflet tissue. Connective Tissue Research, 1978. **6**: p. 37-50.

28. Kunzelman, K.S. and R.P. Cochran, Stress/strain characteristics of porcine mitral valve tissue: parallel versus perpendicular collagen orientation. J Card Surg, 1992. **7**(1): p. 71-8.

29. Wineman, A.S., Large axisymmetric inflation of a nonlinear viscoelastic membrane by laterial pressure. Transactions of the society of rheology, 1976. **20**(2): p. 203-225.

30. Yang, W.H. and C.H. Lu, General deformations of neo-hookean membranes. Journal of Applied Mechanics, 1973. **March**: p. 1-12.

31. Sacks, M.S. and W. Sun, Multiaxial Mechanical Behavior of Biological Materials. Annu Rev Biomed Eng, 2003. **5**: p. 251-284.

32. Lanir, Y. and Y.C. Fung, Two-dimensional mechanical properties of rabbit skin. II. Experimental results. J Biomech, 1974. **7**(2): p. 171-82.

33. Nielsen, P.M., P.J. Hunter, and B.H. Smaill, Biaxial testing of membrane biomaterials: testing equipment and procedures. J Biomech Eng, 1991. **113**(3): p. 295-300.

34. Sacks, M.S., Biaxial mechanical evaluation of planar biological materials. Journal of Elasticity, 2000. **61**: p. 199-246.

35. Lanir, Y. and Y.C. Fung, Two-dimensional mechanical properties of rabbit skin. I. Experimental system. J Biomech, 1974. **7**(1): p. 29-34.

36. Vawter, D.L., Y.C. Fung, and J.B. West, Elasticity of excised dog lung parenchyma. J Appl Physiol, 1978. **45**(2): p. 261-9.

37. Choi, H.S. and R.P. Vito, Two-dimensional stress-strain relationship for canine pericardium. J Biomech Eng, 1990. **112**(2): p. 153-9.

38. Sacks, M.S., A method for planar biaxial mechanical testing that includes in-plane shear. J Biomech Eng, 1999. **121**(5): p. 551-5.

39. Sun, W., M.S. Sacks, T.L. Sellaro, W.S. Slaughter, and M.J. Scott, Biaxial mechanical response of bioprosthetic heart valve biomaterials to high in-plane shear. Journal Biomechanical Engineering, 2003. **125**: p. 372-380.

40. Yin, F.C., R.K. Strumpf, P.H. Chew, and S.L. Zeger, Quantification of the mechanical properties of noncontracting canine myocardium under simultaneous biaxial loading. J Biomech, 1987. **20**(6): p. 577-89.

41. Humphrey, J.D., R.K. Strumpf, and F.C. Yin, Determination of a constitutive relation for passive myocardium: II. Parameter estimation. J Biomech Eng, 1990. **112**(3): p. 340-6.

42. Humphrey, J.D., R.K. Strumpf, and F.C. Yin, Determination of a constitutive relation for passive myocardium: I. A new functional form. J Biomech Eng, 1990. **112**(3): p. 333-9.

43. May-Newman, K. and F.C. Yin, A constitutive law for mitral valve tissue. J Biomech Eng, 1998. **120**(1): p. 38-47.

44. May-Newman, K. and F.C. Yin, Biaxial mechanical behavior of excised porcine mitral valve leaflets. Am J Physiol, 1995. **269**(4 Pt 2): p. H1319-27.

45. Sacks, M.S. and C.J. Chuong, Orthotropic mechanical properties of chemically treated bovine pericardium. Ann Biomed Eng, 1998. **26**(5): p. 892-902.

46. Lee, J., C. Pereira, D. Abdulla, W. Naimark, and I. Crawford, A multi-sample denaturation temperature tester for collagenous biomaterials. Medical Engineering and Physics, 1995. **17**: p. 115-121.

47. Lee, J.M., D.R. Boughner, and D.W. Courtman, The glutaraldehyde-stabilized porcine aortic valve xenograft. II. Effect of fixation with or without pressure on the tensile viscoelastic properties of the leaflet material. Journal of Biomedical Materials Research, 1984. **18**: p. 79-98.

48. Lee, J.M., R. Corrente, and S.A. Haberer, The bovine pericardial xenograft: II. Effect of tethering or pressurization during fixation on the tensile viscoelastic properties of bovine pericardium. Journal of Biomedical Materials Research, 1989. **23**: p. 477-489.

49. Lee, J.M., D.W. Courtman, and D.R. Boughner, The glutaraldehyde-stablized porcine aortic valve xenograft. I. Tensile viscoelastic properties of the fresh leaflet material. Journal of Biomedical Materials Research, 1984. **18**: p. 61-77.

50. Lee, J.M., S.A. Haberer, and D.R. Boughner, The bovine pericardial xenograft: I. Effect of fixation in aldehydes without constraint on the tensile properties of bovine pericardium. Journal of Biomedical Materials Research, 1989. **23**: p. 457-475.

51. Lee, J.M., M. Ku, and S.A. Haberer, The bovine pericardial xenograft: III - Effect of uniaxial and sequential biaxial stress during fixation on the tensile viscoelastic properties of bovine pericardium. Journal of Biomedical Materials Research, 1989. **23**: p. 491-506.

52. Khanna, R.A. and J.M. Lee, Fatigue damage accelerates enzymatic degradation of glutaraldehyde-crosslinked bovine pericardium. Transactions of the Sixth World Biomaterials Congress, 2000. **2**: p.???

53. Hilbert, S.L., L.C. Sword, K.F. Batchelder, M.K. Barrick, and V.J. Ferrans, Simultaneous assessment of bioprosthetic heart valve biomechanical properties and collagen crimp length. J Biomed Mater Res, 1996. **31**(4): p. 503-9.

54. Purinya, B., V. Kasyanov, J. Volkolakov, R. Latsis, and G. Tetere, Biomechanical and Structural Properies of the Explanted Bioprosthetic Valve Leaftets. Journal of Biomechanics, 1994. **27**: p. 1-11.

55. Broom, N.D., An 'in vitro' study of mechanical fatigue in glutaraldehyde-treated porcine aortic valve tissue. Biomaterials, 1980. **1**(1): p. 3-8.

56. Fung, Y.C., Biomechanics: Mechanical Properties of Living Tissues. 2nd ed. 1993, New York: Springer Verlag. 568.

57. Kyriacou, S.K., A.D. Shah, and J.D. Humphrey, Inverse finite element characterization of nonlinear hyperelastic membranes. Journal of Applied Mechanics, 1997. **64**(June): p. 257-262.

58. Nielsen, P.M.F., P.J. Hunter, and B.H. Smaill, Biaxial Testing of Membrane Biomaterials: Testing Equipment and Procedures. Journal of Biomechanical Engineering, 1991. **113**: p. 295-300.

59. Weiss, J.A., B.N. Maker, and S. Govindjee, Finite element implementation of incompressible, transversely isotropic hyperelasticity. Comput Methods Biomech Biomed Engin, 1996. **135**: p. 107-128.

60. Gardiner, J.C. and J.A. Weiss, Simple shear testing of parallel-fibered planar soft tissues. J Biomech Eng, 2001. **123**(2): p. 170-5.

61. Tong, P. and Y.C. Fung, The stress-strain relationship for the skin. J Biomech, 1976. **9**(10): p. 649-57.

62. Humphrey, J.D., D.L. Vawter, and R.P. Vito, Pseudoelasticity of Excised Visceral Pleura. Journal of Biomechanical Engineering, 1987. **109**: p. 115-120.

63. Chew, P.H., F.C. Yin, and S.L. Zeger, Biaxial stress-strain properties of canine pericardium. J Mol Cell Cardiol, 1986. **18**(6): p. 567-78.

64. Fung, Y.C., Biomechanics: Motion, Flow, Stress, and Growth. 1990, New York: Springer-Verlag. 569.

65. Fung, Y.C., Biodynamics:circulation. 1984, New York: Springer-Verlag. 404.

66. Holzapfel, G.A. and R.W. Ogden, Biomechanics of Soft Tissue in Cardiovascular Systems, in *International Center for Mechanical Sciences - Courses and Lectures - No. 144*. 2003, Springer-Verlag Wien New York: New York.

67. Black, M.M., I.C. Howard, X.C. Huang, and E.A. Patterson, A Three-dimensional Analysis of a Bioprosthetic Heart Valve. Journal of Biomechanics, 1991. **24**: p. 793-801.

68. Hamid, M.S., H.N. Sabbah, and P.D. Stein, Influence of Stent Height upon Stresses on the Cusps of Closed Bioprosthetic Valves. Journal of Biomechanics, 1986. **19**(9): p. 759-769.

69. Huang, X., M.M. Black, I.C. Howard, and E.A. Patterson, A Two Dimensional Finite Element Analysis of a Bioprosthetic Heart Valve. Journal of Biomechanics, 1990. **23**: p. 753-762.

70. Li, J., X.Y. Luo, and Z.B. Kuang, A nonlinear anisotropic model for porcine aortic heart valves. J Biomech, 2001. **34**(10): p. 1279-89.

71. Burriesci, G., I.C. Howard, and E.A. Patterson, Influence of anisotropy on the mechanical behaviour of bioprosthetic heart valves. J Med Eng Technol, 1999. **23**(6): p. 203-15.

72. Krucinski, S., I. Vesely, M.A. Dokainish, and G. Campbell, Numerical Simulation of Leaflet Flexure in Bioprosthetic Valves Mounted on Rigid and Expansile stents. Journal of Biomechanics, 1993. **26**: p. 929-943.

73. Gould, P.L., A. Cataloglu, A. Chattopadyhay, G. Dhatt, and R.E. Clark, Stress analysis of the human aortic valve. Computers and Structures, 1973. **3**: p. 377.

74. Ghista, D. and Y. Lin, Statistical analysis of longevity of prosthetic aortic valves. Journal of Applied Mechanics, 1976. **98**(1): p. 2-7.

75. Hamid, M., H. Sabbah, and P. Stein, Finite element evaluation of stresses on closed leaflets of bioprosthetic heart valves with flexible stents. Finite Elements in Analysis and Design, 1985. **1**: p. 213-225.

76. Patterson, E.A., I.C. Howard, and M.A. Thornton, A comparative study of linear and nonlinear simulations of the leaflets in a bioprosthetic heart valve during the cardiac cycle. J Med Eng Technol, 1996. **20**(3): p. 95-108.

77. Downs, J., H. Halperin, J. Humphrey, and F. Yin, An Improved Video-based Computer Tracking System for Soft biomaterials Testing. IEEE Transactions on Biomedical Engineering, 1990. **37**: p. 903-907.

78. Humphrey, J., D. Vawter, and R. Vito, Quantification of Strains in Biaxially Tested Soft Tissues. Journal of Biomechanics, 1987. **20**(1): p. 59-65.

79. Hoffman, A.H. and P. Grigg, A Method for Measuring Strains in Soft Tissue. Journal of Biomechanics, 1984. **10**: p. 795-800.

80. Treloar, L.R.G., The physics of rubber elasticity. 1975, London: Oxford University Press. 310.

81. Rivlin, R.S. and A.D. Thomas, Rupture of rubber: I. Characteristic energy for tearing. Journal of Polymer Science, 1957. **10**: p. 291-318.

82. Rivlin, R.S. and D.W. Saunders, Large Elastic Deformations of Isotropic Materials, VII. Experiments on the Deformation of Rubber. Philosophical Transactions of the Royal Society, 1951. **A243**: p. 251-288.

83. Rivlin, R.S., Large elastic defomations of isotropic materials IV. Further developments of the general theory. Philosophical Transactions of the Royal Society, 1948. **A241**: p. 379-397.

84. Spencer, A.J.M., Continuum Mechanics. 1980, New York: Longman Scientific & Technical. 183.

85. Yin, F.C., W.R. Tompkins, K.L. Peterson, and M. Intaglietta, A video-dimension analyxer. IEEE Trans Biomed Eng, 1972. **19**(5): p. 376-81.

86. Sacks, M.S., Biomechanics of native and engineered heart valve tissues, in *Functional Tissue Engineering*, F. Guilak, D.L. Butler, S. Goldstein, and D. Mooney, Editors. 2003, Spring-Verlag: New York.

87. Vito, R.P., The Mechanical Properties of Soft Tissues-I. A Mechanical System for Biaxial Testing. Journal of Biomechanics, 1980. **13**: p. 947-950.

88. Sacks, M.S., D.B. Smith, and E.D. Hiester, A small angle light scattering device for planar connective tissue microstructural analysis. Ann Biomed Eng, 1997. **25**(4): p. 678-89.

89. Langdon, S.E., R. Chernecky, C.A. Pereira, D. Abdulla, and J.M. Lee, Biaxial mechanical/structural effects of equibiaxial strain during crosslinking of bovine pericardial xenograft materials. Biomaterials, 1999. **20**(2): p. 137-53.

90. Brossollet, L.J. and R.P. Vito, A new approach to mechanical testing and modeling of biological tissues, with application to blood vessels. Journal of Biomechanial Engineering, 1996. **118**(November): p. 433-439.

91. Rousseeuw, P.J. and A.M. Leroy, Robust regression and outlier detection. Wiley series in probability and mathematical statistics. Applied probability and statistics,. 1987, New York: Wiley. xiv, 329.

92. Zioupos, P., J.C. Barbenel, and J. Fisher, Anisotropic Elasticity and Strength of Glutaraldehyde Fixed Bovine Pericardium for use in Pericardial Bioprosthetic Valves. Journal of Biomedical Materials Research, 1994. **28**: p. 49-57.

93. Humphrey, J.D., R.K. Strumpf, and F.C. Yin, A constitutive theory for biomembranes: application to epicardial mechanics. J Biomech Eng, 1992. **114**(4): p. 461-6.

94. Curnier, A., Q.C. He, and P. Zysset, Conewise Linear Elastic-Materials. Journal of Elasticity, 1995. **37**(1): p. 1-38.

95. Lanir, Y., Plausibility of structural constitutive equations for isotropic soft tissues in finite static deformations. Journal of Applied Mechanics, 1994. **61**: p. 695-702.

96. Lanir, Y., Plausibility of structural constitutive equations for swelling tissues - implications of the C-N and S-E conditions. Journal of Biomechanial Engineering, 1996. **118**: p. 10-16.

97. Truesdell, C. and W. Noll, The Nonlinear Field Theories, in *Handbuch der Physik*, S. Flugge, Editor. 1965, Springer-Verlag: Berlin. p. 119-126.

98. Marsden, J.E. and T.J.R. Hughes, Mathematical Foundations of Elasticity. 1983, Don Mills: Dover. 556.

99. Simon, B.R., M.V. Kaufmann, M.A. McAfee, and A.L. Baldwin, Finite Element Models for Arterial Wall Mechanics. Journal of Biomechanical Engineering, 1993. **115**: p. 489-496.

100. Holzapfel, G.A., R. Eberlein, P. Wriggers, and H.W. Weizascker, Large strain analysis of soft biological membranes: Formulatin and finite element analysis. Comput. Methods Appl. Mech. Engrg, 1996. **132**: p. 45-61.

101. Humphrey, J.D., Cardiovascular solid mechanics : cells, tissues, and organs. 2002, New York: Springer. xvi, 757.

102. ABAQUS, ABAQUS/Standard User's Manual, Version 6.3. 2002: Hibbitt, Karlsson & Sorensen, Inc.

103. Criscione, J.C., M.S. Sacks, and W.C. Hunter, Experimentally tractable, pseudo-elastic constitutive law for biomembranes: II. Application. J Biomech Eng, 2003. **125**(1): p. 100-5.

104. Criscione, J.C., M.S. Sacks, and W.C. Hunter, Experimentally tractable, pseudo-elastic constitutive law for biomembranes: I. Theory. J Biomech Eng, 2003. **125**(1): p. 94-9.

105. Sacks, M.S., Incorporation of experimentally-derived fiber orientation into a structural constitutive model for planar collagenous tissues. J Biomech Eng, 2003. **125**(2): p. 280-7.

106. Holzapfel, G.A. and T.C. Gasser, A new constitutive framework for arterial wall mechanics and a comparative study of material models. Journal of Elasticity, 2000. **61**: p. 1-48.

107. Humphery, J.D., Cardiovascular Solid Mechanics. 2002: Springer Verlag.

108. Ogden, R.W., Non-linear elastic deformations. 1997, Toronto: Dover. 532.

109. Holzapfel, G.A., Nonlinear solid mechanics : a continuum approach for engineering. 2000, Chichester ; New York: Wiley. xiv, 455.

110. Humphrey, J.D., R.K. Strumpf, and F.C.P. Yin, A Constitutive Theory for Biomembranes: Application to Epicardial Mechanics. Journal of Biomechanical Engineering, 1992. **114**: p. 461-466.

111. Criscione, J.C., J.D. Humphrey, A.D. Douglas, and W.C. Hunter, An invariant basis for natural strain which yields orthogonal stress response terms in isotropic hyperelasticity. Journal mechanics physics of Solids, 2000. **48**: p. 2445-2465.

112. Costa, K.D., J.W. Holmes, and A.D. MeCulloch, Modelling cardiac mechanical properties in three dimensions. Phil. Trans. R. Soc. Lond., 2001. **359**: p. 1233-1250.

113. Ogden, R.W., Nonlinear elasticity, anisotropy, material stability and residual stresses in soft tissue, in *Biomechanics of soft tissue in cardiovascular system*, G.A. Holzapfel and R.W. Ogden, Editors. 2003, Springer Wien New York: New York.

114. Schroder, J. and P. Neff. Aspects of the formulation of hyperelastic soft tissues with polyconvex anisotropic energies. in *The Second MIT Conference on Computational Fluid and Solid Mechanics*. 2003. MIT.

115. Lanir, Y., Constitutive Equations for Fibrous Connective Tissues. journal of biomechanics, 1983. **16**: p. 1-12.

116. Sacks, M.S., A structural constitutive model for chemically treated planar connective tissues under biaxial loading. Computational Mechanics, 2000. **26**(3): p. 243-249.

117. Sun, W., M.S. Sacks, and M.J. Scott. Numerical simulations of the planar biaxial mechanical behavior of biological materials. in *ASME Summer Bioengineering*. 2003. Miami, FL: ASME.

118. Waldman, S.D. and J.M. Lee, Boundary conditions during biaxial testing of planar connective tissues: Part 1: Dynamic behavior. J. Materials Science: Materials in Medicine, 2002. **in-press**.

119. Choi, I. and C.O. Horgan, Saint-Venant's principle and end effects in anisotropic elasticity. Journal of Applied Mechanics, 1977. **44**: p. 424-430.

120. Horgan, C.O. and J.K. Knowles, Recent developments concerning Saint-Venant's principle, in *Adv Appl Mech*, T.Y. Wu and J.W. Hutchinson, Editors. 1983, Academic: New York. p. 179-269.

121. Horgan, C.O., Recent developments concerning Saint-Venant's principle: An update. Appl Mech Rev, 1989. **42**(11): p. 295-302.

122. Miller, K.L. and C.O. Horgan, End effects for plane deformation of an elastic anisotropic semi-infinite strip. Journal of Elasticity, 1995. **38**: p. 261-316.

123. Waldman, S.D., M.S. Sacks, and J.M. Lee, Boundary conditions during biaxial testing of planar connective tissues: Part 2: Fiber orientation. J. Materials Science: Materials in Medicine, 2002. **in-press**.

124. Hilbert, S.L., V.J. Ferrans, Y. Tomita, E.E. Eidbo, and M. Jones, Evaluation of explanted polyurethane trileaflet cardiac valve prostheses. J Thorac Cardiovasc Surg, 1987. **94**(3): p. 419-29.

125. Love J.W., P.W. Willems, and C.S. Love, New Horizons and the future of heart valve prostheses, ed. S. Gabbay and F. R.W. 1994, Austin: Silent Partners.

126. Leat, M.E. and J. Fisher, The influence of manufacturing methods on the function and performance of a synthetic leaflet heart valve. Proc Inst Mech Eng [H], 1995. **209**(1): p. 65-9.

127. Leat, M.E. and J. Fisher, A synthetic leaflet heart valve with improved opening characteristics. Med Eng Phys, 1994. **16**(6): p. 470-6.

128. Cacciola, G., G.W. Peters, and F.P. Baaijens, A synthetic fiber-reinforced stentless heart valve. J Biomech, 2000. **33**(6): p. 653-8.

129. Cacciola, G., G.W. Peters, and P.J. Schreurs, A three-dimensional mechanical analysis of a stentless fibre-reinforced aortic valve prosthesis. J Biomech, 2000. **33**(5): p. 521-30.

130. Billiar, K.L. and M.S. Sacks, A method to quantify the fiber kinematics of planar tissues under biaxial stretch. J Biomech, 1997. **30**(7): p. 753-6.

131. Sugimoto, H., K. Shimada, and M.S. Sacks, Dynamic Geometry of the native aortic heart valve leaflet. Journal of Biomechanics, submitted.

132. Bowes, A. and C.W. Cater, The Interaction of Aldehydes with Collagen. Biochimica et Biophysica Acta, 1968. **168**: p. 341-352.

133. Cataloglu, A., R.E. Clark, and P.L. Gould, Stress analysis of aortic valve leaflets with smoothed geometrical data. Journal of Biomechanics, 1977. **10**: p. 153-158.

134. Christie, C.W. and I.C. Medland, A non-linear finite element stress analysis of bioprosthetic heart valve, in *Finite element in Biomechanics*, R.H. Gallager, B.R. Simon, P.C. Johnson, and J.F. Gross, Editors. 1982, John Wiley: Chichester. p. 153-179.

135. Rousseau, E., A. van Steenhoven, and J. Janssen, A mechanical analysis of the closed Hancock heart valve prosthesis. Journal of Biomechanics, 1988. **21**(7): p. 545-562.

136. Gloeckner, D., K. Billiar, and M. Sacks. The bending behavior of fixed porcine aortic cusp. in *Third World Congress of Biomechanics*. 1998. Hokaiddo, Japan.

137. Thornton, M.A., I.C. Howard, and E.A. Patterson, Three-dimensional stress analysis of polypropylene leaflets for prosthetic heart valves. Med Eng Phys, 1997. **19**(6): p. 588-97.

138. Gabbay, S., U. Bortolotti, F. Wasserman, S. Factor, J. Strom, and R.W. Frater, Fatigue-induced failure of the Ionescu-Shiley pericardial xenograft in the mitral position. In vivo and in vitro correlation and a proposed classification. J Thorac Cardiovasc Surg, 1984. **87**(6): p. 836-44.

139. Trowbridge, E.A., P.V. Lawford, C.E. Crofts, and K.M. Roberts, Pericardial heterografts: why do these valves fail? J Thorac Cardiovasc Surg, 1988. **95**(4): p. 577-85.

140. Walley, V.M., F.D. Rubens, M. Campagna, A.L. Pipe, and W.J. Keon, Patterns of failure in Hancock pericardial bioprostheses. J Thorac Cardiovasc Surg, 1991. **102**(2): p. 187-94.

141. Gloeckner, D.C., K.L. Billiar, and M.S. Sacks, Effects of mechanical fatigue on the bending properties of the porcine bioprosthetic heart valve. Asaio J, 1999. **45**(1): p. 59-63.

142. Sacks, M.S., The biomechanical effects of fatigue on the porcine bioprosthetic heart valve. Journal of long-term effects of medical implants, 2001. **11**(3&4): p. 231-247.

143. Wells, S.M. and M.S. Sacks, Effects of fixation pressure on the biaxial mechanical behavior of porcine bioprosthetic heart valves with long-term cyclic loading. Biomaterials, 2002. **23**(11): p. 2389-99.

144. Fulchiero, G., S.M. Wells, T.L. Sellaro, E. Rabkin, F.J. Schoen, and M.S. Sacks, Alterations in Collagen Fiber Crimp morphology with Cyclic Loading in Zero and Low Pressure-Fixed porcine bioprosthetic heart valves. Biomaterials, submitted.

145. Vyavahare, N., M. Ogle, F.J. Schoen, R. Zand, D.C. Gloeckner, M. Sacks, and R.J. Levy, Mechanisms of bioprosthetic heart valve failure: fatigue causes collagen denaturation and glycosaminoglycan loss. J Biomed Mater Res, 1999. **46**(1): p. 44-50.

146. Christie, G.W., J.F. Gross, and C.E. Eberhardt, Fatigue-induced changes to the biaxial mechanical properties of glutaraldehyde-fixed porcine aortic valve leaflets. Semin Thorac Cardiovasc Surg, 1999. **11**(4 Suppl 1): p. 201-5.

147. Sacks, M. and K. Billiar, Chapter 3: Biaxial Mechanical Behavior of Bioprosthetic Heart Cusps Subjected to Accelerated Testing, in *Advances in Anticalcific and Antidegenerative Treatment of Heart Valve Bioprostheses*, S. Gabbay and R. Frater, Editors. 1997, Silent Partners: Austin.

148. Ellsmere, J.C., R.A. Khanna, and J.M. Lee, Mechanical loading of bovine pericardium accelerates enzymatic degradation. Biomaterials, 1999. **20**: p. 1143-1150.

149. Susi, H., J.S. Ard, and R.J. Carroll, The infrared spectrum and water binding of collagen as a function of relative humidity. Biopolymers, 1971. **10**(9): p. 1597-604.

150. Doyle, B.B., E.G. Bendit, and E.R. Blout, Infrared spectroscopy of collagen and collagen-like polypeptides. Biopolymers, 1975. **14**(5): p. 937-57.

151. Jakobsen, R.J., L.L. Brown, T.B. Hutson, D.J. Fink, and A. Veis, Intermolecular interactions in collagen self-assembly as revealed by Fourier transform infrared spectroscopy. Science, 1983. **220**(4603): p. 1288-90.

152. Lazarev, Y.A., B.A. Grishkovsky, and T.B. Khromova, Amide I band of IR spectrum and structure of collagen and related polypeptides. Biopolymers, 1985. **24**(8): p. 1449-78.

153. Payne, K.J. and A. Veis, Fourier transform IR spectroscopy of collagen and gelatin solutions: deconvolution of the amide I band for conformational studies. Biopolymers, 1988. **27**(11): p. 1749-60.

154. George, A. and A. Veis, FTIRS in H2O demonstrates that collagen monomers undergo a conformational transition prior to thermal self-assembly in vitro. Biochemistry, 1991. **30**(9): p. 2372-7.

155. Jackson, M., M.G. Sowa, and H.H. Mantsch, Infrared spectroscopy: a new frontier in medicine. Biophys Chem, 1997. **68**(1-3): p. 109-25.

156. Broom, N.D., The stress/strain and fatigue behaviour of glutaraldehyde preserved heart-valve tissue. Journal of Biomechanics, 1977. **10**: p. 707-724.

157. Bigi, A., A. Ripamonti, N. Roveri, G. Jeronimidis, and P.P. Purslow, Collagen Orientation by X-ray Pole Figures and Mechanical Properties of Media Carotid Wall. Journal of Material Science, 1981. **16**: p. 2557-2562.